COMPUTATIONAL FLUID DYNAMIC MODELING
OF AORTIC BLOOD FLOW

COMPUTATIONAL FLUID DYNAMIC MODELING OF AORTIC BLOOD FLOW

By

SUZIE BROWN, B.ENG. & MANAGEMENT

A Thesis
Submitted to the School of Graduate Studies
In Partial Fulfillment of the Requirements
For the Degree
Master of Applied Science

McMaster University

MASTER OF APPLIED SCIENCE (2013) McMaster University
(Department of Mechanical Engineering) Hamilton, Ontario

TITLE: Computational Fluid Dynamic Modeling
of Aortic Blood Flow
AUTHOR: Suzie Brown, B.Eng. & Management
(McMaster University)
SUPERVISOR: Stephen Tullis, Ph.D.
NUMBER OF PAGES: xvii, 171

Abstract

Computational fluid dynamic (CFD) models of aortic blood flow have developed over the past decade from rigid one dimensional models to three dimensional models that include wall flexibility. Although anatomically correct, these models have been significantly idealized as compared to their physiologic in vivo conditions. This thesis investigates the effect of addition of four dimensional MRI inlet flow, motion of the heart at the aortic inlet and addition of wall elasticity coupled with tissue backing support. Results show that the addition of MRI inlet data and aortic inlet motion of the heart significantly change flow in the aorta and should be included in future aortic CFD simulations.

Acknowledgements

For the opportunity to pursue this thesis and support and guidance through the project, I would like to thank Dr. Stephen Tullis.

For their support in debugging my simulations, many thanks go to Mike Tooley (ANSYS technical support) and Talal and Szymon Buhajczuk (Simutech Engineering). Thanks also to Earl, Alex and Thuan-Le for their assistance with geometry creation and Dr. Gregory Wohl for his input and direction on the biomedical aspect of this work. Finally, thanks go to Dr. M. Markl for his donation of MRI inlet data and Joei from the McMaster Echocardiography lab for the inlet motion data used in this thesis.

For believing in me and offering unconditional support, I would like to thank my family and friends who have carried me through the entirety of this thesis. I could not have done it without you.

Table of Contents

List of Figures

List of Tables

Nomenclature

AAo - Ascending aorta

APWV - Aortic Pulse Wave Velocity {m/s}

CFD - Computational Fluid Dynamics

CT - Computed Tomography

DAo - Descending aorta

DArch - Descending aortic arch

$E_{combined}$ - Combined Elastic Modulus of the Vessel Wall and Surrounding Tissue {MPa}

E_{wall} - Elastic Modulus of the Vessel Wall {MPa}

Echo - Echocardiography

EFS - Elastic Foundation Stiffness {MPa/m}

FEA - Finite Element Analysis

FSI - Fluid Structure Interaction

L - Total Blood Vessel Length {mm}

MRI - Magnetic Resonance Imaging

NS - Navier-Stokes Equations

P - Pressure {Pa}

d - Diameter {mm}

h - Thickness {mm}

r - Radius {mm}

t - Time {s}

u - Velocity in x-direction {m/s}

v - Velocity in y-direction {m/s}

w - Velocity in z-direction {m/s}

K-ω - Turbulent model {-}

μ - Blood Viscosity {cP}

ρ_f - Blood Density {kg/m^3}

ρ_w - Vessel Wall Density {kg/m^3}

τ - Wall Shear Stress {Pa}

For those who believe and never give up.

Wall-E

1 Introduction

The aorta is an important blood vessel responsible for delivering oxygenated blood from the heart to peripheral arteries. It can become compromised with many diseases including atherosclerosis, aneurysms and stenoses where plaque build-up, ballooning and artificial narrowing of the vessel can occur. Surgical reconstruction is often needed to mediate the effects of these diseases. Until recently, imaging techniques have not been able to provide sufficient information on the blood flow and repercussions of these diseases. In an effort to more fully understand the role of blood flow in the development of disease and in its management, computational fluid modeling (CFD) has been used. Initially, simplified frameworks were used, but have now progressed to incorporate a larger number of variables affecting the flow. Several different boundary conditions have been investigated in order to establish physiological flow patterns; however, consensus has yet to be reached on the appropriate condition to apply. Interaction of the blood with the elastic vessel wall is also an important consideration that received little attention until recently due to its extremely high computational modeling cost. Perhaps the most important effects; motion of the aorta induced by the heart and proper placement of the aorta in surrounding tissues have yet to be investigated.

The objective of this thesis is to model the aorta as physiologically relevant as possible to the human aorta and determine the blood flow affects as a result of this. Motion of the heart imparted on the aorta are investigated for the first time in literature. In addition, elasticity of the aortic walls and elastic foundation stiffness of the surround tissue is included. CFD model results are validated with blood flow data obtained from Magnetic Resonance Imaging (MRI) and values used in the CFD model are obtained from physiologic data where possible.

2 Background and Literature Review

This section gives background on both aortic modeling and aorta anatomy and physiology. Background on the heart and aorta is given first as an introduction to the biological side of this work for mechanical engineers who may not have knowledge of the circulatory system. Following the review of the circulatory system, an in depth literature review of past and present work, both computationally and experimentally is given.

2.1 The Heart and Circulatory System

The circulatory system is a closed circuit blood distribution network made up of three main systems; the heart, the systemic arterial system and the pulmonary arterial tree. The heart is responsible for pumping blood through both the systemic and pulmonary systems. The pulmonary system oxygenates the blood via the lungs while the systemic system delivers the oxygenated blood to the rest of the body for use by organs and other structures. The aorta is the beginning of the systemic arterial system and connects to the heart, shown in Figure 1.

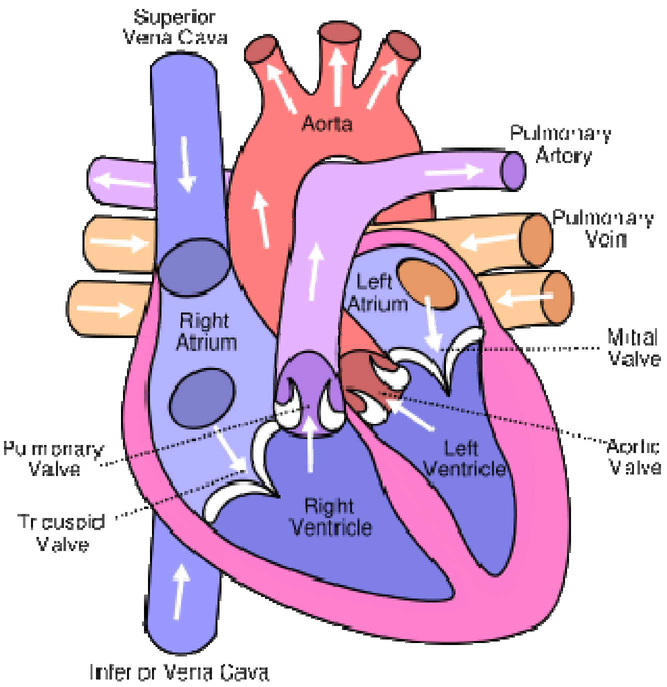

Figure 1: General anatomy of the heart [1]

The heart pumps blood through the body by repeated rhythmic contractions. De-oxygenated blood stored in the veins travels to the right atrium where it flows through the tricuspid valve (TV) into the right ventricle. The right ventricle expels the de-oxygenated blood through the pulmonary valve (PV) into the pulmonary arteries where it travels to the lungs. The lungs oxygenate the blood through diffusion and return the blood to the heart (left atrium) through the pulmonary veins. The blood then moves from the left atrium through the mitral valve (MV) into the left ventricle where it is pumped out through the aortic valve (AV) into the aorta. The oxygenated blood is delivered via the arterial system to organs and the rest of the body where oxygen is extracted for use in metabolic processes. The de-oxygenated blood then enters the venus system and the cycle repeats.

The cardiac cycle, also known as a 'pulse' describes the flow and pressure changes of blood through the heart from one beat to the next. The cycle consists of four stages; ventricular filling, isovolumetric ventricular contraction, ventricular ejection and isovolumetric ventricular relaxation, shown in Figure 2. The second two stages (2-4 in Figure 2) are known as the systolic phase or contraction phase of the cycle and the first and last stages (4-2 in Figure 2) make up the diastolic phase.

During ventricular filling, the MV and PV open and blood moves from the atria to the ventricles. There is an increase in blood volume, but no pressure change within the heart. Isovolumetric ventricular contraction follows when the ventricular muscles contract. Since all valves are closed during this step, a pressure increase is seen, but no change in volume. The next stage, ventricular ejection occurs when the pressure peaks and the AV and PV valves open to expel blood out of the ventricles and into the systemic and pulmonary systems. There is a decrease in blood volume and subsequent decrease in pressure during this step. Isovolumetric ventricular relaxation begins when the valves close and the heart muscle relaxes. There is no change in volume, but a decrease in pressure is observed during this stage. The cycle then repeats, beginning again with ventricular filling [2].

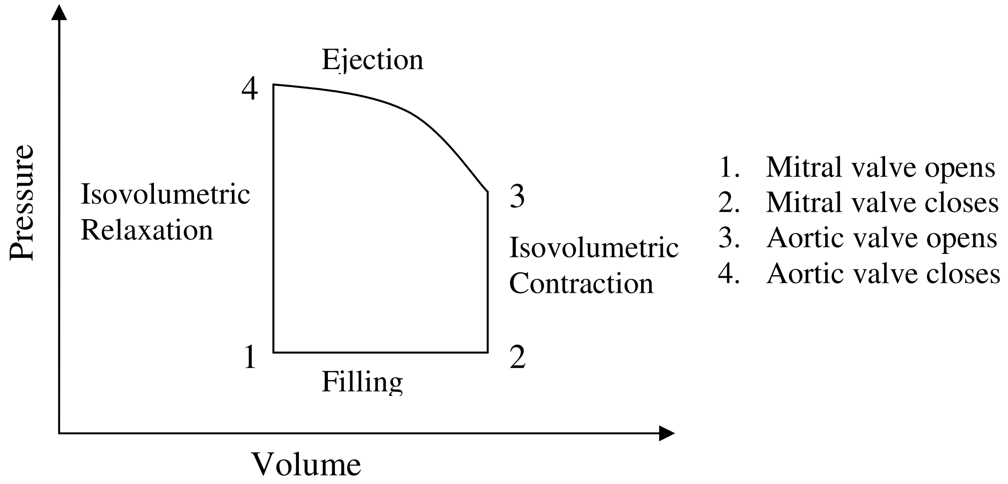

Figure 2: Pressure- volume flow loop for the heart.

Blood pressure is generated by the contraction of ventricles and resistance of the arterial system. It is the hydrostatic pressure the blood exerts on the vessel walls and is highest in the aorta reaching 120 mmHg during systole and 80 mmHg during diastole. Pressure fluctuations decrease as blood travels into the capillaries, eventually reaching 0 mmHg into the right ventricle.

2.2 The Aorta

2.2.1 Anatomy

The aorta stems from the aortic valve of the heart and extends down through the torso to the iliac bifurcation where it splits into the iliac arteries, which deliver blood to both legs. The aorta can be split into three main sections, the ascending aorta, the aortic arch and the descending aorta, which includes both the thoracic and abdominal aorta, shown in Figure 3.

The inlet of the aorta, located at the outlet of the left ventricle of the heart is approximately level with the costal cartilage of the third rib and deep to the left half of the sternum. The ascending aorta travels proximally to the aortic arch, which begins at a plane slightly superior to the costal cartilage of the second right rib. Following the arch, the thoracic aorta begins at the fourth thoracic vertebra on the left side and travels down the spinal column, gradually shifting to the midline of the body ending at the twelfth thoracic vertebra where the abdominal aorta begins. The iliac bifurcation, which signifies the end of the aorta, is located distal to that at the fourth lumbar vertebra [3].

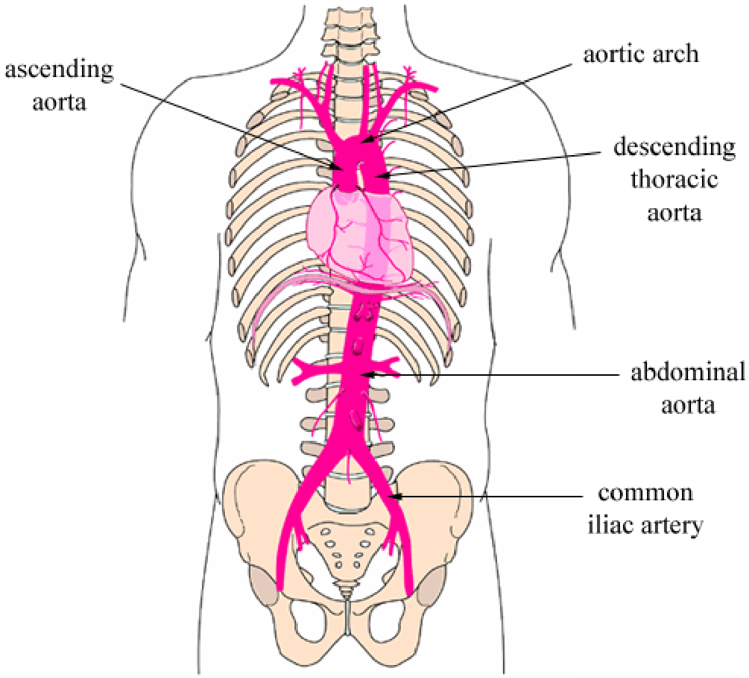

Figure 3: Location of aorta in body [4].

The aorta begins at the aortic valve is tricuspid shaped, consisting of three triangular valve leaflets approximately 120 degrees apart. The leaflets are close to equal in size and open with the increased pressure build-up in the left ventricle to expel blood into the aorta. Following the systolic pulse phase they close and return to their initial position. This leaflet formation is important for inlet flow profile consideration. Just above the aortic valve, the aorta expands into the aortic sinuses, which bulge out to a slightly larger diameter than the valve. The sinuses contain the orifices of the coronary arteries, which feed oxygenated blood to the heart muscles. Following the sinuses, the aorta extends slightly anteriorly and laterally to the right before continuing superiorly while bending laterally left and posteriorly. This section, the ascending aorta, is approximately five cm in length and two and a half cm in diameter in adults [5, 6].

The aorta continues into the aortic arch, extending superiorly, curving laterally left a full 180 degrees and slightly posteriorly. The arch is typically four to five cm in length with a slightly smaller diameter than the ascending aorta. Three major arteries branch from the superior aspect of the arch, seen in Figure 4. In order from right to left they are the brachiocephalic trunk, left common carotid and left subclavian. Typical branch diameters are 12 mm, 7 mm and 9 mm respectively [7]. These arteries are responsible for delivering oxygenated blood to the head, neck and arms. At the centre of the underside of the arch, the arterial ligament connects the aorta to the left pulmonary artery. The ligament, also known as the ligamentum arteriosum is the remains of the patent arterial duct in the fetus, which until birth, allows blood from the right ventricle to bypass the lungs. The fibrous ligament tethers the aorta to the pulmonary artery to prevent opposing motion of the two vessels. The aortic isthmus is the section of aorta located between the insertion of the ligamentum arteriosum and the inlet of the left subclavian artery.

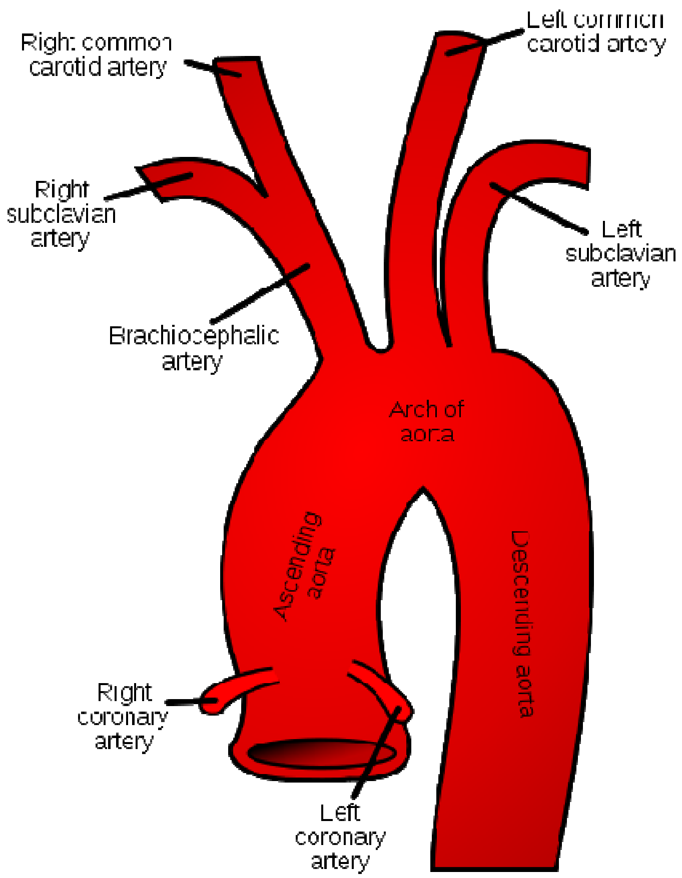

Figure 4: Branch arteries of the aortic arch [8].

The descending aorta, which can be broken into two regions: the thoracic aorta and abdominal aorta, begins after the aortic arch. The thoracic aorta is approximately 20 cm in length in adults and tapers slightly along its length to end at a typical diameter of 1.5 cm. Numerous arteries branch off along the length of the thoracic aorta including the intercostal arteries and several visceral arteries. A continuation of the thoracic aorta; the abdominal aorta is approximately 10 centimetres in length and also tapers significantly along its length reaching a typical outlet diameter of 1 centimetre. The abdominal aorta supplies the majority of the internal organs with blood via numerous branch visceral arteries. The abdominal aorta truncates at the iliac bifurcation where it splits into the iliac arteries [9].

X, y and z directions for orientation of the aorta in simulations have been defined based on the location of the aorta in the body. The z-direction is defined parallel to the long axis of the body (superior, inferior directions). The x and y directions are parallel to the short axis of the body, with the x-direction going back to front (anterior, posterior) and the y-direction side to side.

2.2.2 Structure

Artery walls consist of three layers from deep to superficial - tunica intima, tunica media and tunica adventitia, shown in Figure 5. The tunica intima is the inner most layer and contains the endothelium, a base membrane and a layer of elastic tissue; the internal elastic lamina. The endothelium is the only tissue that makes contact with blood; it lines the entire cardiovascular system including the heart and all blood vessels. The middle layer, the tunica media is the thickest of the three layers. It is composed of elastic fibres and smooth muscle fibres that extend in rings around the vessel. The outer most layer, the tunica adventitia consists of a combination of elastin and collagen fibres. At low pressure, the elastin dominates the wall behaviour, making it highly elastic, while at high pressures the collagen dominates resulting in a stiffer wall response. This pressure-compliance relationship is frequently seen in diseased aortic walls where pressure is increased and wall elasticity is significantly decreased from baseline [2].

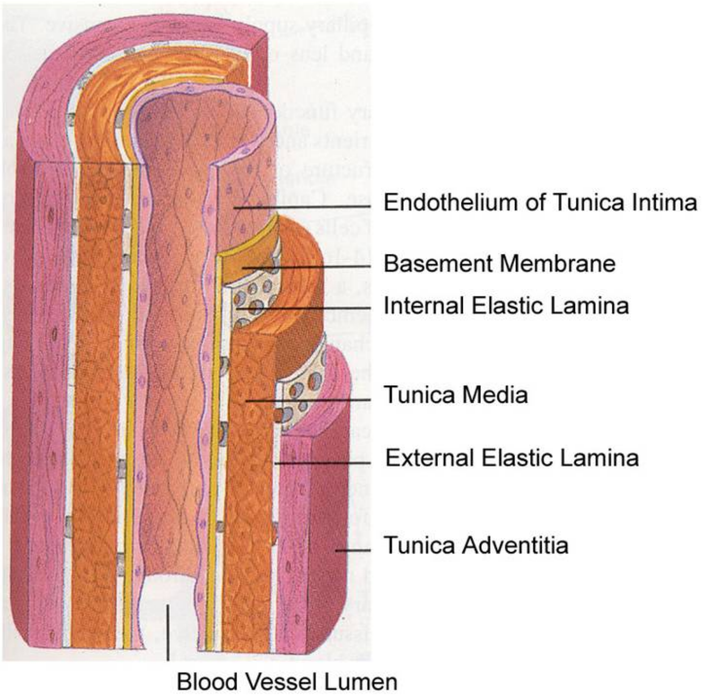

Figure 5: Aortic wall layers

The aorta is an elastic artery, meaning it contains a high proportion of elastin fibres and has relatively thin walls in comparison to the vessel diameter. This combination of elastin and thin walls permitting the aorta wall to easily stretch in response to small increases in pressure, is known as compliance and allows the aorta to propel blood away from the heart while the ventricles relax. As blood enters the aorta from the heart, the aortic wall expands to accommodate the blood surge. The elastin in the wall stretches and stores mechanical energy for a short period of time. When the fibres relax, the mechanical energy of the elastin is converted into kinetic energy of the blood allowing the blood to flow to the peripheral arteries after the heart has relaxed. The amount of elastin in the aorta varies with location and is highest in the ascending aorta and lowest in the abdominal aorta [10].

Aortic wall stretch during the cardiac cycle has been recorded with both computed tomography (CT) and MRI imaging techniques [11, 12]. Typical diameter changes are in the range of 8% in the aortic root, [13] 10% in the ascending aorta [12] and 11% in the descending aorta.[11] These values are affected by cardiac output, patient age, gender and health; however, a change of 10% is generally accepted to occur along the aorta [11, 14].

Numerous tests, summarized in Table 1, have been conducted on aortic tissue in an effort to find its wall elasticity value. Many of these tests were conducted at high strain rates, greater than 40s^{-1} and resulted in high elasticity values of 1.1-12.7 MPa [15-19].

Author	Year	Strain Rate (s^{-1})	E_{circ} (MPa)
Tremblay [23]	2009	$6.67x10^{-4}$	0.03
Choudhury [22]	2008	$6.67x10^{-4}$	0.167
VandeGeest [24]	2004	$6.67x10^{-4}$	0.667
VandeGeest [25]	2006	$6.67x10^{-4}$	0.1
Craiem [21]	2008	0.01	0.36
Vorp [19]	2003	0.014	1.5
Mohan [16]	1983	20	7
Shah [17]	2005	44	9.95
Shah [17]	2005	91	12.7
Mohan [15]	1982	100	1.12
Shah [18]	2006	136	8.46

Table 1: Tensile test elasticity values and corresponding strain rates for aortic wall specimen.

These strain rate values; however, are not representative of those experienced by the aorta in vivo. The typical strain seen by the aorta in this scenario is on average 8-10% and translates to a strain rate of 3s^{-1} when a normal value of systolic time (0.29 sec, 60 bpm) is used [20]. Several tensile test studies conducted using much lower strain rates were examined [21-25]. These studies calculated elastic modulus values in the range of 0.03-0.667 MPa. The lower strain values used are lower than the typical strain expected to be experienced by the aorta and elastic stiffness is a function of strain; however, there is a high variance in the sample preparation and elastic stiffness location variation along the aorta that can skew the results. Elastic stiffness variation can also be attributed to the age, size and health of the person, creating an additional scatter in the data.

The aortic wall has been modeled in CFD studies as a uniform, isotropic membrane with constant elasticity [26-32] although this is not the case in vivo [18, 20]. Studies have been conducted using multiple wall layers [33, 34] and multiple elasticity values [35]. The value used for wall elastic modulus in the case of the multiple wall layers was significantly larger than documented in vivo (2.0-9.0 MPa vs. 0.5 MPa). Results showed that peak wall shear stress values occurred in the same location as with a single layer aortic wall; however, stress values were higher in the three layer model (tunica media layer only) than the single layer model. Changes in flow were not documented [33, 34]. More realistic elastic modulus values were used for the varying wall elasticity study (0.4-1.2 MPa). The model was created from 4D CT scans and motion in the thoracic aorta agreed well with in vivo imaging. Flow was not documented in this study [35].

2.2.3 Motion

In addition to wall stretch, large motion of the aorta is possible and occurs as seen in echocardiographic data. This large motion is imparted on the aorta from the heart during the cardiac cycle, where due to contraction the heart moves in all three planar directions. Displacements range from one cm in the longitudinal z (superior/inferior) direction to half a cm in the transverse x (anterior/posterior) and y (lateral) directions [36].

The descending aorta is almost rigidly fixed in all directions due to its tether points along the spine and 360 degree encasement by surrounding spinal muscles. The arch is tethered by the three branch arteries (which are securely fixed by the surrounding neck muscles and tissue), but has some degree of motion due to the slack at the distal end of the branch arteries. The ascending aorta is free to move as the heart moves. The majority of the motion is seen in the ascending aorta and the arch since they are free to move with the heart [37].

Motion of the aorta is seen in CT scans of the ascending aorta and aortic root as motion artefacts [38-40]. The presence of motion artefacts confirms that the aorta is a different shape and in a different position between two phases of the cardiac cycle [39]. Motion artefacts are commonly seen during systole in more than 60% of CT images [38]. Left anterior and right posterior motion were observed when the aorta was imaged in the xy plane, with an amplitude in the ascending aorta ranging from 0-8 mm [38, 40] and at the aortic root a mean amplitude of 3.5 mm [40]. A mean motion amplitude of 3.3 mm approximately 30 mm above the aortic root and 2.2 mm amplitude at the pulmonary trunk bifurcation approximately 60 mm above the aortic root were also seen [40]. This data indicates the maximum motion occurs at the aortic root and diminishes along the length of the ascending aorta.

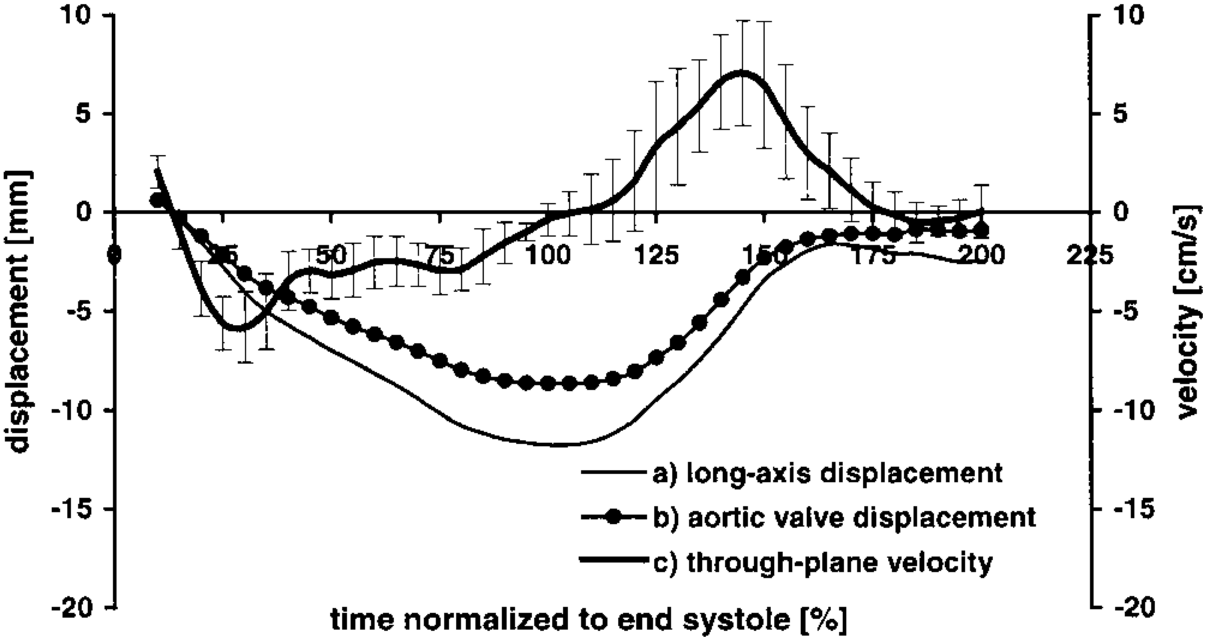

Figure 6: Aortic root motion in the z-direction during the cardiac cycle [12].

MRI has also been used to image motion of the aortic root [12]. In the z-direction it was observed that the aortic root moved distally in the cardiac cycle, 9 mm [12, 14] with the majority of motion occurring during systole. Motion of the aortic root in systole can be seen in Figure 6.

Considerable heart motion has been observed in other studies [41], but not quantified. Translation of the aorta on the xy plane has been shown to occur [41] with 6 mm translation in the x-direction and 8 mm translation in the y-direction [14]. Tracking of the aortic root along the xy plane by [14] is shown in Figure 7.

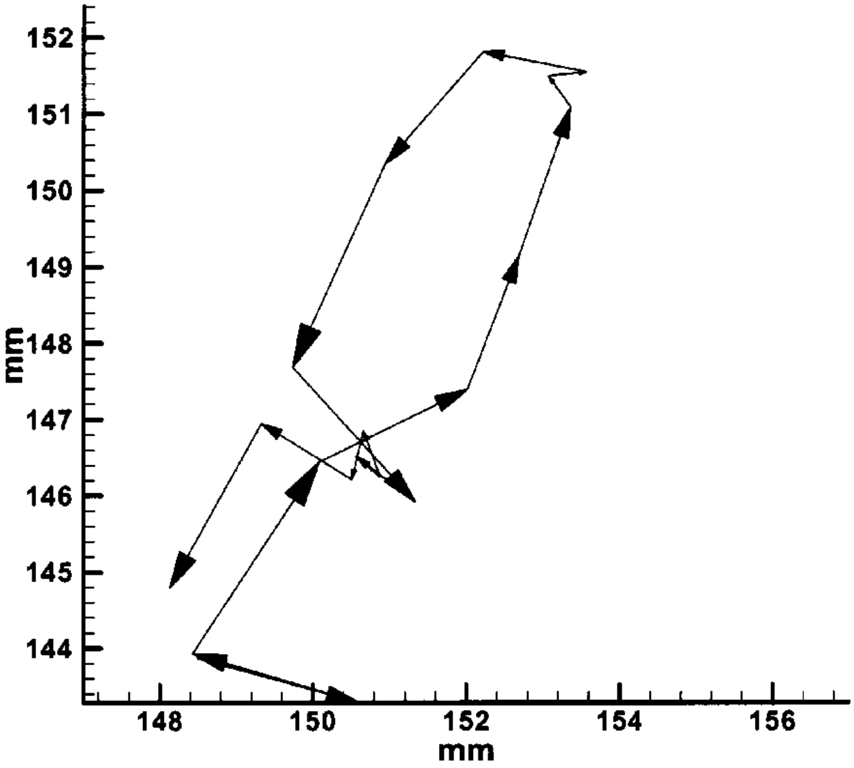

Figure 7: Aortic root motion in the xy plane during the cardiac cycle [14].

2.3 Aortic Hemodynamics

The first documented in vivo results used hot film anemometry [42] to determine velocity profiles in healthy individuals. It was found that flow was highly disturbed at the aortic valve and through the ascending aorta. Non-disturbed flow was noted to occur in the mid-ascending and proximal arch. Descending flow was not measured due to geometric constraints. In recent years, in vivo MRI imaging has been used to validate CFD flow models in addition to providing patient flow profiles for disease management [41].

In vivo 3D blood flow patterns were first documented in the early 1990's through use of angioscopy, a technique whereby a fibre optic catheter is inserted into the blood vessel for visualization of the vessel wall. Dye injection allowed for flow visualization revealing clockwise rotations (when viewed from the anterior direction, looking inferior on the defined plane) in the abdominal aorta with secondary spiral flow patterns [43]. A few years later, technology had evolved such that Doppler ultrasound was able to image 3D flow patterns in vivo. In [44], a sample group of young healthy males were imaged at several locations along the aorta for four different points in the cardiac cycle. Spiral flow patterns were seen at all locations; approximately 50% of the patients demonstrated clockwise flow versus anti-clockwise flow [44]. Recently, MRI has been used for flow visualization in the aorta [41, 45]. Velocity components were measured along a single plane, with multiple planes obtained to create a 3D profile. Results were then post processed to view velocity vectors, streamlines and particle traces. Results from these MRI flow studies have been used for disease prognosis and are used for validation of the results presented in this thesis.

2.3.1 Magnetic Resonance Imaging and the Aorta

Magnetic resonance imaging, (MRI), uses nuclear magnetic resonance to dynamically visualize internal body structures noninvasively. MRI is useful for imaging the aorta because of the superior definition provided between tissue (vessel wall) and fluid (blood). Images can be acquired in multiple planes with a wide field of view, allowing for the entire aorta to be captured. Combining gradient-echo and phase mapping to MRI enables blood flow volume and velocity to be visualized. The overall image acquisition is time consuming, but allows for the construction of three and four dimensional images used to visualize blood flow patterns and aortic compliance [46].

Several studies have been conducted with both 3D and 4D MRI in an attempt to determine typical aortic flow patterns [11, 41, 45, 47-49]. Helical flow patterns have been found in both the ascending and descending aorta as seen in Figure 8.

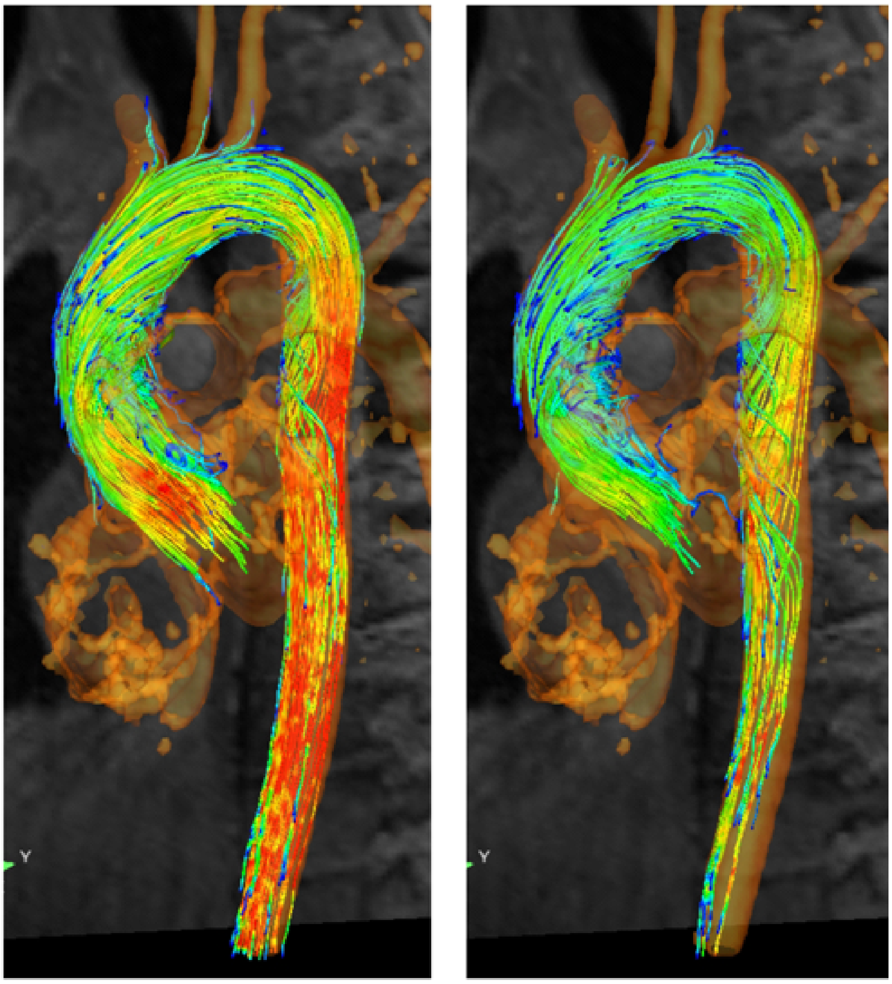

Figure 8: Typical 4D MRI aortic blood flow patterns showing helical flow, late systole on the left and early diastole on the right [41].

During early systole, no helical flow was observed in the ascending aorta or the aortic arch [49]. A right hand flow, or counter clockwise helicity was observed in the distal ascending aorta extending into the arch along the inner arch wall at peak systole [41, 45, 47-49]. The development of helical flow was thought to compensate for the space left by the flow separation that began to occur at the distal end of the arch during peak systole and early diastole (thus limiting the amount of flow separation that occurred). The flow pattern was also determined to be responsible for the decreased amount of turbulent kinetic energy in early diastole and lead to a shorter turbulent time frame than in a straight pipe [49]. Helical and bi-helical flow patterns persisted into diastole in the ascending aorta [49]. Conversely, in the descending aorta, left handed flow, or clockwise helicity was observed following the systolic phase [48].

2.3.2 Echocardiography and the Aorta

Echocardiography is a non-invasive medical procedure used to create images of the heart and its surrounding structures using ultrasound and is clinically used to detect heart disease or heart abnormalities in individuals. Images are usually 2D based on a sweep of the transducer beam along an arc. Doppler echocardiography uses frequency shifting of the returned echo to give information on flow direction and magnitude.

There are several typical views used to examine the heart with Echocardiography. These include the left parasternal (LP) long axis, short axis aortic valve (AV), two chamber and four chamber views, shown in Figure 9. The LP long axis provides image information on AV and MV leaflet motion in addition to posterior wall and anterior septum proportions. The short axis AV depicts the aortic root, AV leaflet motion head on and both the TV and PV cross sections. MV motion and left ventricle proportions can be seen in the two chamber view. The four chamber view shows both ventricles and atria and also cross sectional views of the MV and TV. Of interest to the aorta are the LP long axis and short axis AV views that provide information on the aortic root function.

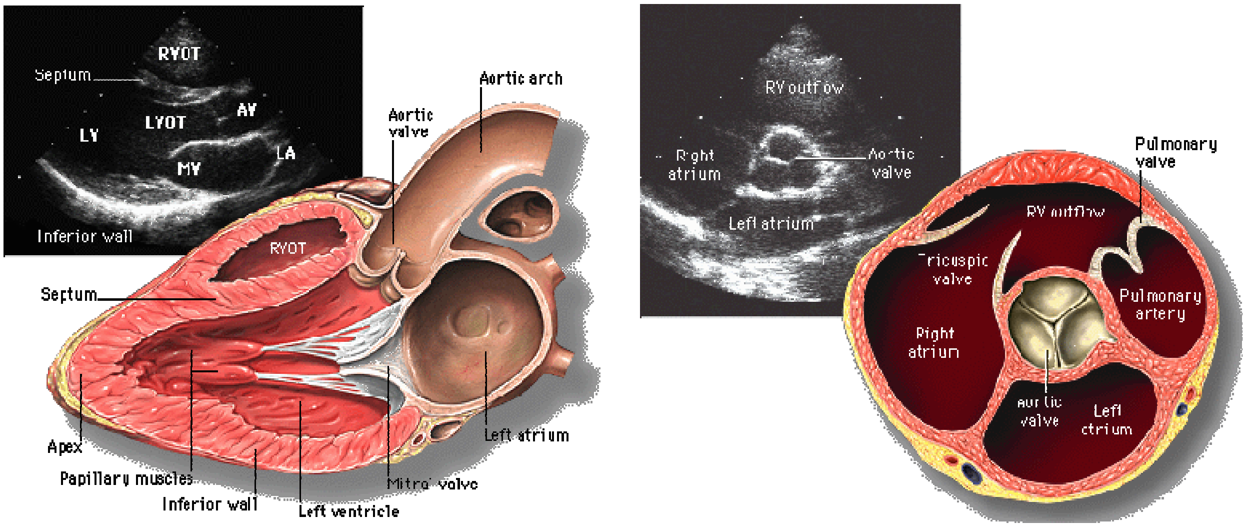

LP Long Axis Short Axis AV

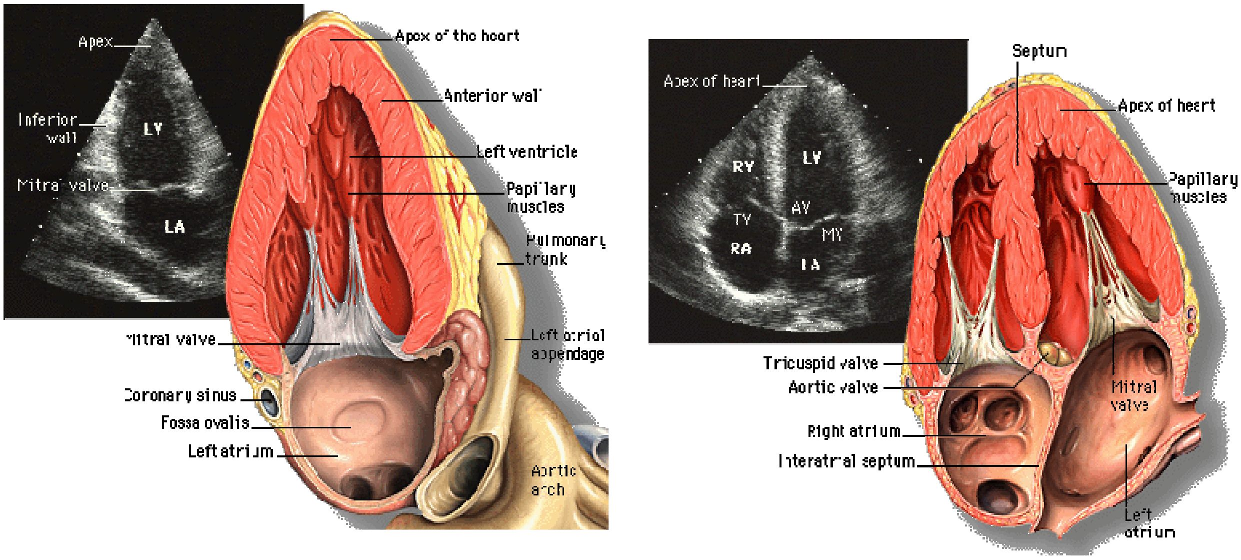

Two Chamber Four Chamber

Figure 9: Echocardiography views of the heart [50].

Echocardiography has been used to view the geometry of the aortic valve and its motion during the cardiac cycle [51, 52]. It has been observed that the aortic root moves toward the apex of the left ventricle during systole [52]. This procedure is quick and efficient, but is limited to aortic valve and heart motion. Information on whole vessel motion and 3D flow patterns are usually qualitative and quantitative measurements are unavailable in the literature.

2.3.3 Wall Elasticity and Windkessel Effect

During systole the elastic aorta acts as a reservoir by distending to accommodate the surge of blood from the heart. It then recoils during diastole to ensure blood flow surges and pressure surges are not experienced in the rest of the systemic system. The volume change helps reduce the amount of turbulence during systole and the length of time in which turbulence can occur [53]. Damping the flow also maintains organ perfusion during diastole when the heart no longer ejects blood. This concept is modeled by assuming the aorta is a uniform elastic tube and peripheral vessels are rigid tubes and that pressure fluctuations occur synchronously so the pressure pulse propagates with infinite velocity. The result is a lumped compliance (artery) - resistance (vein) mode that is limited by the lack of pressure pulse propagation.

Several studies have been conducted on Windkessel boundary conditions in the aorta [54-59]. As an alternative to outlet pressure boundary conditions, Windkessel boundary conditions attempt to model the resistance and capacitance of the downstream arterial network that has been removed from the truncated aorta. Kung [55] modeled the descending aorta using a silicone piping ex vivo model with computer controlled pulsatile flow input. A four element windkessel model using inductance, capacitance and proximal and distal resistance was applied to the outlet. Hemodynamic results agreed well with in vivo data with an average error of 2.4% between simulated and measured pressure curves and average error of 12% between flow velocity curves [55].

Shi [59] conducted an ex vivo study with whole body circulation, a ventricular assist device and artificial aortic valve. The 1D model was composed of three parts - the heart, the systemic circulation loop and the pulmonary circulation loop. In both loops, resistance, compliance and inductance were modeled. The reference values used for each variable were calculated from human subjects where possible, otherwise canine models were adjusted to fit the human scale. It was found that pressure fluctuations were accurately representative of physical data of pressure in the heart and aorta [59].

Similar to Shi [59], Fogliardi [57] also created a 1D model using canine models as justification for results. This study defined a three element model using both a linear constant compliance and non-linear pressure dependant compliance. It was found that the non-linear model had an improved data fit, but overall lower accuracy compared to the linear model. It was concluded that linear constant compliance is the preferred choice for three element Windkessel models [57].

Building on the previous work of Shi [59] and Fogliardi [57], Spilker [56] created a 2D finite element analysis (FEA) model using Womersley's elastic tube theory to determine impedance outflow conditions. Custom software was used to generate a pulmonary tree using data sets from patient artery diameters and lengths. Impedance was calculated from the applied lengths and diameters. The results were compared to both porcine and human data; they matched well to the hemodynamic measurements and determined that resistance was extremely sensitive to artery diameter. The model assumed the use of a stenosis and was computationally expensive [56].

Park [58] introduced the first 3D CFD model using a pseudo-organ model with resistance and compared it to a 3D pulsatile model with pressure outlet conditions. The organs in Park's model were created as cylindrical elements with a permeability function defined for each organ. This method was accurate within 10% of reference values for pressure and flow with all branches except for the coronary arteries and within 2% for the aorta [58]. While this was an improvement on previous work, a simplified pipe geometry was used and artery compliance not accounted for.

A 3D CFD study of the descending aorta using Windkessel outlet conditions was performed by Vignon-Clementel [54]. In this model, the effects of constant pressure, singular resistance and singular impedance at the outlet were studied. It was found that a constant pressure condition resulted in both a pressure phase lag and incorrect pressure amplitude compared to in vivo conditions. Similarly, the resistance outlet boundary condition led to large pressure pulse amplitudes, but no phase lag was noticed. The impedance condition resulted in realistic pressure values and only a slight pressure lag and was thus determined to be the best match. This model failed to consider vessel wall compliance, or lumped parameter variables that better simulate pressure conditions [54].

Although Windkessel boundary conditions have been validated in several different studies [54-59], a 3D CFD model using realistic geometry and arterial compliance has yet to be created. Reasons for this include the high computational cost of modeling Windkessel outlet conditions as compared to physiological pressure conditions and the lack of human data for reference values used in the calculation of Windkessel variables. The majority of aortic CFD studies apply a simplified pressure outlet condition as a result of these limitations [26, 60-69].

2.3.4 Blood Rheology

Blood is a non-Newtonian fluid, meaning its fluid properties are not described by a constant viscosity value; the relationship between shear stress and strain rate is non-linear. Since the apparent viscosity of blood decreases with increased stress, it is considered to be a shear thinning liquid. This results in low flow at slow rates of deformation and free flow at higher rates. Blood is a suspension of small particles (red blood cells, white blood cells, nutrients, etc.) in aqueous solution and in tubes with large internal diameters when compared to the size of the red blood cells, the change in viscosity can be neglected and blood behaves as a Newtonian fluid

[20]. However, in tubes with an internal radius less than 0.5 mm, changes in apparent viscosity are evident [20]. In the aorta, the artery travelled by the blood is large and has high enough shear rates that it has been generally accepted to model blood flow as Newtonian [20, 26]. Values of blood viscosity and density used in aortic modeling are shown in Table 2.

Author	Date	ρ_f (kg/m³)	μ (cP)	Study Type
Stein [42]	1976	Not stated	5.3	Physiologic
Xu [115]	1999	Not stated	3.4	CFD
Wood [68]	2001	1050	4	CFD
Leuprecht [90]	2002	1044	3.7	CFD
Nicosia [97]	2003	1060	3.5	CFD
Morris [66]	2005	1050	3.5	CFD
Canic [105]	2006	1050	3.5	1D model
Figueroa [27]	2006	1060	4	CFD
Gao [33]	2006	1050	3.5	CFD
Nakamura [85]	2006	1050	3.5	CFD
Park [58]	2006	1060	3.5	CFD
Svensson [67]	2006	1060	3.5	CFD
Spilker [56]	2007	1060	4	CFD
Tan [60]	2008	1060	2.8	CFD
Xiao [112]	2008	1056	4	CFD
Yang [69]	2008	1121	3.8	CFD
Fu [65]	2009	1050	3.5	CFD
Kim [32]	2009	1060	4	CFD
Kim [32]	2009	1050	4	2D model
Paul [84]	2009	1060	3.7	CFD
Vasava [88]	2009	1060	5	CFD
Cheng [61]	2010	1060	4	CFD
Wen [89]	2010	1121	3.8	CFD
Benim [82]	2011	1060	-	CFD
Brown, A. [29]	2011	1056	3.5	CFD
Lantz [26]	2011	1080	3.5	CFD
Lantz [91]	2011	1080	2.6	CFD
Stalder [79]	2011	1055	4.6	CFD
Stalder [140]	2011	1050	4.5	CFD
Tay [28]	2011	1000	3.1	CFD
Midulla [31]	2012	1050	4	CFD

Table 2: Fluid properties of blood used in aortic modeling

The majority of studies conducted using blood as a non-Newtonian fluid take place in either stenosed or bifurcated arteries. It is intuitive to include the non-Newtonian properties of blood in both of these cases as the size of the artery is significantly smaller than that of the aorta and downstream results vary due to the diameter change [70-73].

2.3.5 Turbulence

In pipe flows the flow remains laminar for Reynolds numbers less than 2300, even if disturbed. In small arteries the Reynolds number is less that this so flow is always laminar; however, in large vessels such as the aorta, turbulence can occur. It is most common to see turbulent fluctuation during early systole when peak flowrates are achieved [42]. During systole the aorta distends as a reservoir to accommodate the surge of blood, reducing the Reynolds number and helping reduce the amount of turbulence during systole.

Turbulence in the aorta was first documented in 1976 in vivo study conducted by Stein [42] where flow in the human aorta was directly measured with a hot film anemometer probe[42]. In healthy individuals, peak Reynolds numbers of 5700-8900 were calculated [42]. A similar study conducted in 1994 in porcine specimens also revealed evidence of systolic turbulence [74]. Since then, imaging techniques have been used to investigate turbulence in the aorta. Doppler ultrasound has been used to measure turbulent intensity near stenoses in flow phantoms [75] and in vivo in carotid arteries during systole [76]. Turbulence in the arch and ascending aorta during systole has also been well documented using magnetic resonance techniques to measure turbulent kinetic energy in young healthy patients [77-79]. Additionally, ex vivo [80, 81] and CFD studies of straight pipes [72, 82] have been used to visualize and quantify turbulence in the aorta. CFD models of stenosed arteries [83, 84] and aneurysms [60, 61] have also been conducted; however, shear stresses and turbulence values are significantly higher in these models than in the healthy aorta. In 2012, the first turbulent CFD model [26] was created using a physiologic geometry, inlet pulse and resistance pressure outflow. The model was rigid and saw disturbed and separated flow in the aortic arch and descending aorta [26].

It is acknowledged that turbulence occurs in the aorta at peak flow, as evidenced by the peak Reynolds numbers of 5700-8900 calculated in healthy individuals [42] and turbulent flow seen in vivo using Doppler ultrasound [75, 76]. During the remainder of the cardiac cycle; however, flow is laminar. Since turbulence models themselves do not contain a transition to laminar, the vast majority of CFD studies performed with healthy aortic geometries have been conducted with laminar flows [26, 61-69] and it has been generally accepted by the medical profession that laminar flows are valid for aortic CFD modeling [85].

2.3.6 Wall Shear Stress

In the aorta, measuring the amount of wall shear stress (WSS),

$$\tau_w = \mu \left(\frac{\partial u}{\partial y} \right)_{y=0} \tag{1}$$

is important for determining atherosclerosis, a disease where fat and plaque build-up causes arterial hardening [79]. MRI has been used to measure WSS with limited success [45, 48, 67, 69] and has led to the use of CFD models to provide WSS values in both diseased and healthy aortas. In a rigid model of the aorta with an input flow and output pressure specified from MRI data, high values of WSS were found on the right side of the ascending aorta, with moderate WSS along the right side of the arch and distal descending aorta [79]. Other rigid wall CFD models found high WSS values at the branch attachment locations [69, 86-89] and along the inner wall of the arch [66, 69, 85-87, 89, 90]. The high WSS was found to flip during diastole to the posterior wall and then diminish [90]. Minimum values occurred along the inner wall of the descending aorta and along the proximal walls of the branch arteries [87]. Typical peak WSS values seen at the arch and branch inserts are shown in Table 3.

Time Period	WSS Value (N/m^2)
Early Systole	15
Peak Systole	26
Early Diastole	20
Late Diastole	3

Table 3: Peak WSS values seen at the inner aortic arch and branch inserts [89].

Flexible wall studies have also been conducted to observe WSS during the cardiac cycle. Locations of high and low WSS remained the same as the rigid cases; however, magnitude of the stress changed significantly with the addition of flexible walls. In systole, WSS values were 23-29% lower than the rigid wall case and in diastole, 2-12% lower [29][29][29]. The opposite was noticed in a similar study [91] where flexible walls resulted in higher values of WSS. The descending and thoracic aorta were seen to have higher WSS values in the flexible model during peak systole and early diastole, an effect attributed to the elastic volume storage of blood [91]. WSS results from flexible wall studies are contradictory and so not of use in validation to CFD studies; however, are increasingly important to the medical profession due to the role of shear stress in atherosclerosis.

2.4 Aortic Modeling

Flow in the aorta has been studied in a variety of mediums including ex vivo and CFD studies to investigate the effects of wall and boundary conditions [92-104]. Early studies focused on the effects of applying constant inflow versus a pulsatile inflow in straight pipes that more closely mimicked physiological conditions in the aorta. Models evolved over time to more anatomically correct geometries obtained from imaging. Later, models developed to investigate the effects of modeling flexible walls in comparison to previous rigid wall models. Addition of inlet motion has been the most recent topic of discussion, but has yet to be modeled completely. in CFD studies. On the fluids side, the effects of laminar versus turbulent flow modeling have been compared with recent developments allowing the addition of turbulent modeling in complex computer simulations. Outflow conditions of back pressure versus resistance boundary conditions have been investigated numerous times, while comparison of the effects of Newtonian and non-Newtonian fluid properties have been sparsely studied. This section provides an overview of the majority of aortic flow studies completed, summarizing them in Table 4.

2.4.1 Aortic Valve Modeling and Outflow

Characterization of aortic valve flow has been performed in different mediums including CFD, ex vivo and in vivo imaging studies in an attempt to fully understand aortic inflow profiles to assist with modeling prosthetic valves used for valve replacement in humans. The aortic inflow field has been found to affect the velocity field in the ascending aorta, but not the descending aortic flow patterns [85].

Early CFD studies included rigid aorta geometries with laminar flow and artificial heart valves [92, 93]. Later, models were expanded to include Fluid Structure Interaction (FSI) of prosthetic valves [94, 95] and physiologic aortic valves [96-98]. The most recent CFD simulations have applied non-linear elasticity to the valve wall structure [99, 100]. Although these studies provide insight into flow patterns entering the aorta, they are not full physiologic models and are thus limited in their findings.

Ex vivo studies of aortic valve flow have also been conducted to view aortic inlet flows using particle image velocimetry (PIV) [101] and high speed flow video capture [102]. Both imaging studies compared various tri- and bi-leaflet prosthetic valve designs in silicone aorta models using a water/glycol fluid mixture. Recirculation flow, leakage flow and flow patterns in systole and diastole were visualized downstream of the valve. As with the CFD studies, these ex vivo models are limited by their assumptions of a rigid walled aorta with laminar flow.

3D Doppler echocardiography [103] and 3D phase contrast MRI [41, 104] have been used to characterize physiologic aortic inflows in healthy patients. The flow patterns obtained have been used to compare to root replacement patients [104].

2.4.2 Ex Vivo Models

Ex vivo [77, 80] and in vivo models [42, 74] were used prior to mainstream CFD aortic models and more recently have been used in combination with CFD models as flow validation [63, 75, 79, 81].

Several rigid wall ex vivo models with pulsatile, turbulent, Newtonian flow and uniform pressure outlet conditions have been used to visualize aortic blood flow. Additionally, ex vivo models using stenosed arteries were performed [75, 77] with high levels of turbulent flow developing post stenosis. Healthy models [63, 81] were also completed with real aortic geometries constructed by rapid prototype. Exact creation of an inlet flow profile was challenging and significant model limitation occurred due to wall stiffness and pressure buildup [63].

2.4.3 Early CFD Models

Initial models of blood flow were performed in 1D rigid pipe networks by averaging the 3D incompressible Navier-Stokes (NS) equations. Compliance was later added to the walls to investigate the effect of wall elasticity on the velocity and pressure pulses travelling through the vessel [105]. Blood was considered to be a viscous fluid in a compliant cylinder with no slip at the walls and an inlet velocity pulse and outlet pressure pulse applied as boundary conditions. A

3% difference in velocity and time lag of the pressure pulse occurred when compared to the rigid model [105]. 1D models have also been used in the past decade to model the resistance of the full arterial tree [106, 107] based on inlet flow data and geometry measurements from ex vivo sources. Pressure and velocity curves have shown agreement within 10% error of in vivo measurements, with most of the uncertainty resulting from measurement of the experimental data [107].

To further research, 2D models were conducted to study both blood flow and wall shear stress [32, 108, 109]. Pulsatile flow in an elastic vessel was modeled using immersed boundary techniques due to the significantly reduced computation time as compared to solving the NS equations. It was found that the vessel wall deformed 5% in diameter in response to the inlet velocity pulse, resulting in subsequent changes in wall shear stress compared to a rigid case [109]. The vessel motion acted to smooth the flow field by expanding to accommodate the influx during systole and contracting to inhibit boundary layer separation during diastole [109]. Small vortical sheddings were noticed during systole with large vortices developing during diastole to create double eddy flow downstream from the inlet [32]. Computed velocities agreed well with ex vivo measured velocities (within 15%) [32, 108]. Although an improvement of 1D models; 2D models lacked the 3D blood flow patterns experienced by the aorta, a key factor in how the blood flows from the heart through the vessel.

2.4.4 Rigid Wall CFD Models

The first 3D simulations of the aorta were performed using uniform flow of a Newtonian fluid in a rigid pipe with an outlet pressure boundary condition of zero relative pressure applied to the outlet [110-112]. In a simplified 'candy cane' geometry of the aorta with branches excluded, large right hand rotational vortices were found in the descending arch with a transition to left hand rotational vortices in the descending aorta occurring during early diastole. Small backward flow at the inner wall of the arch was observed at peak systole [86, 111].

Subsequent models followed with more realistic pulsatile flow applied to the inlet [58, 72, 82, 84, 85, 87-89, 113, 114]. For models applying laminar, Newtonian flow in a rigid pipe with a zero relative pressure applied to the outlet, blood flow was found to be axial and hug the inner curve of the arch during early systole [85]. This pattern continued into peak systole with spiral (helical) flow developing in the ascending aorta and extending to the descending aorta as flow progressed through the cardiac cycle [85]. Following the end of systole, axial flow had been replaced by a secondary flow helix [85]. Around the aortic arch, flow was drawn from the outside of the arch towards the centre of the descending aorta [114]. Symmetric flow swirls moved towards the posterior wall in the descending aorta, with the ascending aorta experiencing a counter-clockwise spiral at the inner wall, moving posteriorly through the diastolic phase [85, 87, 114]. What is called an 'M-shaped' velocity profile (Figure 10) was seen to occur in the arch and descending aorta throughout the entire cardiac cycle [87, 114]. Recirculation zones were noted to occur on the inner wall of the branch arteries [89]. The addition of an outlet pulsatile pressure condition [88, 89] resulted in identical flow patterns developing through the cardiac cycle.

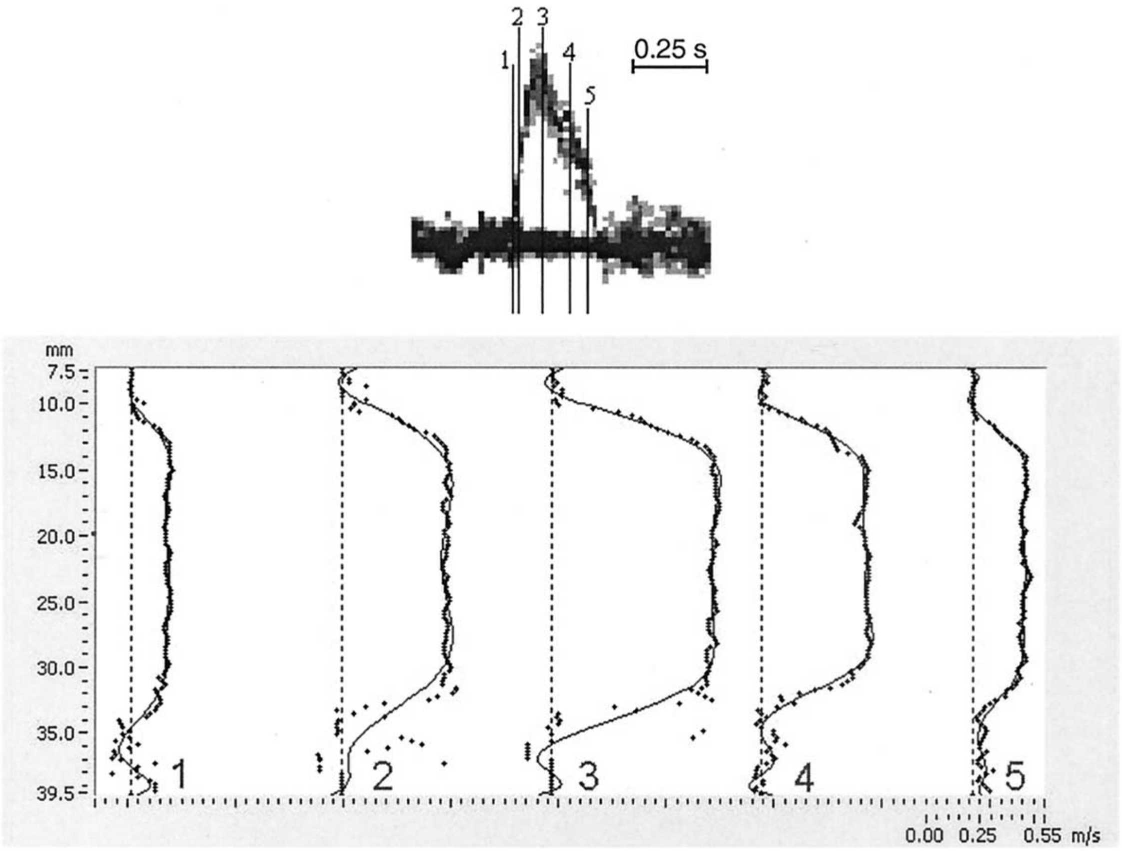

Figure 10: M-shaped velocity profiles seen in the descending aorta in a healthy patient. Time intervals correspond to spectrogram on top [20].

Imaging techniques evolved during this time such that physiological patient specific aortic geometries could be added to CFD studies to further investigate blood flow patterns. Models were still rigid with laminar, pulsatile, Newtonian flow and an outlet pressure boundary condition [26, 60-69]. In a model constructed with a prosthetic bi-leaflet valve, parallel flow was observed in early systole with small scale chaotic vortical structures developing in the ascending aorta at peak systole. Turbulent flow was found to develop more slowly in the physiologic model as compared to the aortic pipe model and viscous shear stresses were lower in the physiologic model [62]. Similar to the pipe models, right hand helical flow developed in the ascending aorta [63, 111]. In early systole, axial flow in the ascending aorta and arch was skewed toward the inner wall with recirculation flow occurring during early diastole [66]. Flow in the descending aorta was skewed towards the outer wall [66, 69]. A dominant counter-clockwise vortex and small clockwise vortex were observed in the descending aorta, originating from the flow separation in the distal arch at peak systole [68]. These complex secondary flows created a clockwise helical flow in the descending aorta after peak systole [26, 68]. Counter-clockwise helical flow was also seen to occur in the proximal branch walls [69]. M-shaped velocity profiles were evident in both the ascending aorta and descending aorta during the entire cardiac cycle [69].

Addition of a resistance outlet boundary condition yielded inconclusive results [26, 56]. Flow in the descending aorta was found to be highly disturbed during diastole, but not helical, with clockwise flow occurring through the entire aorta during systole [26]. However, a similar study indicated only slight flow changes occurred when resistance outlet boundary conditions were added [56].

When inlet flow was modeled from 3D MRI data instead of a uniform sinusoidal inlet pulse, flow results in the ascending aorta were significantly different [79, 90, 115]. In an ascending aorta model, velocity profiles during early systole were flat; considerably different from the previously suggested M-shaped profiles [90]. Flow was skewed towards the inner arch wall during early systole and flow reversal occurred at the same location during early diastole, both patterns consistent with earlier studies [90]. The importance of modeling inlet flow as 3D was also seen in a descending aorta study [115]. Early systolic flow was parallel and centered, skewing to the posterior wall in late systole. Early diastole showed the emergence of secondary flow patterns with flow axially centered at the anterior wall. Late diastolic flow had migrated back to the posterior wall as in late systole [115]. The only model to date that incorporated inlet motion was performed on a flexible ascending aorta with rigid arch and descending aorta sections [14]. 3D inlet flow from MRI data was used as the laminar, Newtonian inlet flow condition. A large axially elongated vortex was present in late systole and early diastole, similar to previous study findings [14]. Good agreement with MRI flow was seen during systole with the velocity magnitudes and location of flow patterns matching in vivo MRI data. It was concluded that heart inlet motion should be included in future studies in order to obtain accurate flow information and that the effect of vessel wall flexibility needed to be investigated [14].

Recently, MRI has been used to validate CFD flow models. In a rigid CFD model of the aorta, it was found that flow curves were phase delayed in comparison to the MRI data [79]; however, velocity profiles showed good agreement to the in vivo data [67].

2.4.5 Flexible Wall CFD Models

A significant step forward in aortic modeling has been the inclusion of flexibility to the aortic walls, making models more physiologically representative of in vivo conditions. Initial flexible studies were performed with pulsatile, laminar, Newtonian flow in simplified aortic pipe geometries with constant outlet pressure conditions and with fixed inlet and outlets [27, 28, 33]. A 5% change in diameter was recorded over the cardiac cycle when a wall elasticity of 0.407MPa was applied. Compared to rigid models, pressures at the inlet and outlet were lower in the flexible case by approximately 20% [27]. An outlet pressure and outlet flow time lag compared to the inlet was noticed due to the addition of wall elasticity. The volume outflow was the same for both rigid and flexible models; however, outflow during diastole in the deformable case was larger as it received the flow 'stored' by the elastic membrane during systole [27]. In a model with higher wall elasticity values in the range of 2-6.5 MPa, similar trends were observed, but with less of a significant change over the rigid case [33].

The most recent addition to aortic modeling has been the inclusion of anatomically correct geometries with flexible walls. In the past few years, several studies have been performed using a flexible aortic geometry with laminar, pulsatile, Newtonian flow [26, 29-32, 116]. In comparison to a rigid model, the mass flow curves were observed to be similar at both the inlet and outlet [29]. Velocity was lower in the flexible case by 20-30% in systole and 5% in diastole. This was attributed to the storage of blood in the flexible aorta in systole, as noted in other studies. Outlet pressure remained the same for both cases; however, inlet pressure was higher at peak systole in the rigid case [29]. In a study that included both wall elasticity (0.5, 0.75, 1.0 MPa) and elastic foundation stiffness of 10 MPa/m, during both peak systole and early diastole; the rigid model overestimated the amount of recirculation flow [91]. A decrease in wall deformation was noticed as the value of wall elasticity increased. Helicity of the flow was recorded and during early systole, early diastole and end diastole was found to be 10%, 12% and 15% larger in the flexible case. In peak systole and late systole; however, a slightly higher (2-3%) helical index was seen in the rigid case [91]. On the structural side, radial wall expansions of 15% [30] and 10% [29] were recorded in the flexible models. Although more anatomically and physiologically correct, the computational efforts required for these complex models were significant and time consuming [29, 32, 117].

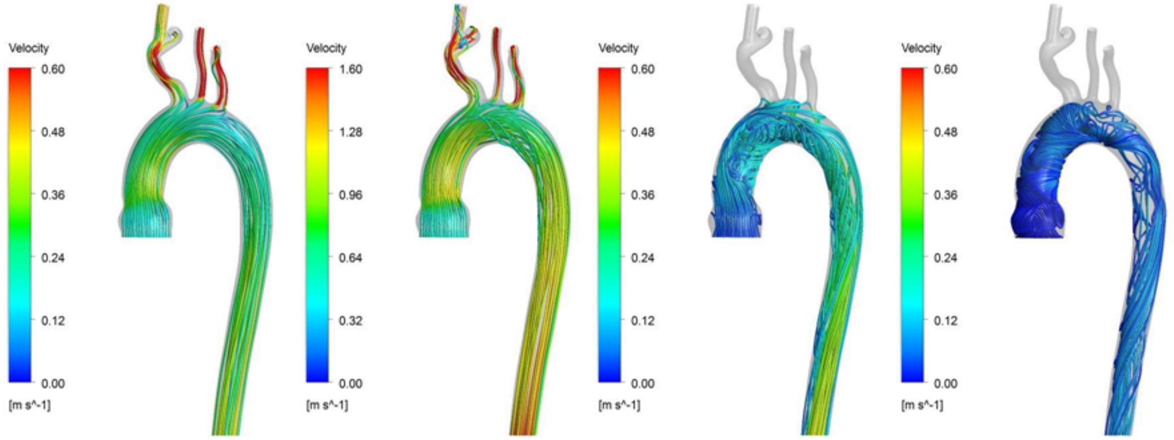

Figure 11: Development of helical flow in the aorta; from left to right: early systole, peak systole, early diastole and late diastole [116].

Through the comparative analysis of previous CFD models, it has been possible to quantify the result of anatomic and physiologic changes made to the aortic studies. Starting with the 1D and 2D models, it was found that changing the resistance outflow condition from a zero uniform applied pressure to a physiologic pressure curve had no effect on the flow. The addition of pulsatile flow to originally steady flow conditions changed the location and development of vortices formed through the cardiac cycle, shown in Figure 11. The direction of vortical flow; however, remained the same. Adding an anatomically correct aortic geometry resulted in a decrease in turbulence and shear stress and no change of the helical flow direction in the ascending and descending aorta. Addition of a resistance outlet condition was inconclusive with opposing results obtained from two models. The most significant changes came with the addition of 3D inlet flow, heart motion and flexible walls. Incorporating 3D flow at the inlet changed the velocity profile in the ascending aorta and resulted in skewing of flow patterns in the descending aorta. Addition of heart motion was seen to change systolic flow patterns and should be included in future CFD studies. Including flexibility in the model geometry resulted in diameter changes, outlet flow and pressure time lags, overall lower pressures and velocities and larger diastolic outflow. The helical flow index was also changed with the addition of flexibility and resulted in larger indices during early systole and throughout diastole. It is concluded that flexibility, 3D inlet flow and heart motion should be included in future anatomically correct, pulsatile aortic CFD simulations.

Previous to the work in this thesis, flexible flow simulations were completed by Brown, Wang, et, al [116] and presented at several conferences. The simulations included flexible walls, blood as a Newtonian fluid, fixed inlet and outlets, low intensity turbulent flow and inlet uniform flow. Results showed increased mass flow in the ascending aorta during systole due to the addition of flexibility. Maximum wall displacement was seen in the ascending aorta with a value of 2 mm diameter stretch. Values for wall flexibility were approximated based on values used in previous flexible case studies. The aim of the work in this thesis was to expand on the previous work from Brown, Wang, et al [116] to include more physiologically realistic flexibility values, a 3D inlet pulse and aortic inlet motion.

	Input Flow			Flow Conditions			Fluid Conditions		Geometry		Wall Conditions		Outflow		Inlet Motion		Study Type			
Author	Steady	Pulsatile	3D	Laminar	Turbulent	T - Model	Non-Newtonian	Newtonian	Pipe	Real	Rigid	Flexible	Pressure	Resistance	None	Included	Ex Vivo	CFD	In vivo	Detail
Nygaard, 1994		√			√		√			√		√		√		√			√	porcine
Stein, 1976		√			√		√			√		√		√		√			√	healthy
Stalder, 2011		√			√		√			√		√		√		√			√	healthy
Oshinski, 1995		√			√			√	√		√		√ (atm)		√		√			stenosis
Yellin, 1966		√			√			√	√		√		√ (atm)		√		√			pipe
Fukuda, 2009	√				√			√		√	√		√ (0 Pa)		√		√			healthy
Wong, 2009		√			√			√		√	√		√ (atm)		√		√			stenosis
Canstein, 2008		√		√				√		√	√		√ (0 Pa)		√		√			healthy
Xiao, 2008	√	√			√	κ-ω		√	√		√		√ 0 Pa)		√			√		stenosis
Sultanov, 2009		√			√	?	√		√		√		?		√			√		pipe
Paul, 2009		√			√	LES		√	√		√		√ (atm)		√			√		stenosis
Benim, 2011		√			√	κ-ε/κ-ω		√	√		√			√ (to calc P)	√			√		pipe
Park, 2006		√		√				√	√		√			√	√			√		pipe
Mori, 2002	√			√				√	√		√		√ (0 Pa)		√			√		simplified aorta
Mori, 2010	√	√ (sin wave)		√				√	√		√		√ (0 Pa)		√			√		no branches
Nakamura, 2006		√ (ventricle)		√				√	√		√		√ (0 Pa)		√			√		no branches, heart with orifice valve
Shahcheraghi, 2002		√		√				√	√		√		√ (0 Pa)		√			√		simplified aorta
Vasava, 2009		√		√				√	√		√		√ (curve)		√			√		simplified aorta
Vasava, 2009		√		√				√	√		√		√ (curve)		√			√		simplified aorta
Wen, 2010		√		√				√	√		√		√ (curve)		√			√		healthy
Weston, 1998		√		√				√	√		√		√		√			√		pipe bend
Figueroa, 2006		√		√				√	√			√	√ (100mmHg)	√	√			√		healthy
Gao, 2006		√		√				√	√			√	√ (0 Pa)		√			√		high E, healthy
Tay, 2011		√	√	√				√	√			√	?		√			√		full CFD heart included
Jin, 2003			√	√				√		√	√	√	√			√		√		Healthy, ascend only

	Input Flow			Flow Conditions			Fluid Conditions		Geometry		Wall Conditions		Outflow		Inlet Motion		Study Type			Detail
Author	Steady	Pulsatile	3D	Laminar	Turbulent	T - Model	Non-Newtonian	Newtonian	Pipe	Real	Rigid	Flexible	Pressure	Resistance	None	Included	Ex Vivo	CFD	In vivo	
Tan, 2009		√			√	κ-ε/κ-ω		√		√	√		√ (0 Pa)		√			√		aneurysm
Cheng, 2010		√			√	κ-ε/κ-ω		√		√	√		√ (0 Pa)		√			√		aortic dissection
Lantz, 2012		√			√	LES		√		√	√			√ (to calc P)	√			√		healthy
Spilker, 2007		√		√				√		√	√			√	√			√		healthy
Borazjani, 2011		√		√				√		√	√		√ (0 Pa)		√			√		bileaflet valve
Canstein, 2008		√		√				√		√	√		√ (0 Pa)		√			√		healthy
Cheer, 2011		√		√				√		√	√		√ (0 Pa)		√			√		abdominal only
Fu, 2009		√		√				√		√	√		√ (0 Pa)		√			√		aneurysm
Liu, 2011		√		√			√			√	√		√ (0 Pa)		√			√		02 mass transport
Morris, 2005		√		√				√		√	√		√ (0 Pa)		√			√		no branches
Stalder, 2011		√	√	√				√		√	√		√ (MRI data)		√			√		healthy
Svensson, 2006		√		√				√		√	√		√ (0 Pa)		√			√		healthy
Wood, 2001		√		√				√		√	√		√ (uniform)		√			√		descending Aorta
Xu, 1999		√	√	√				√		√	√		√ (MRI data)		√			√		descending Aorta
Yang, 2008		√		√				√		√	√		√ (curve)		√			√		healthy
Leuprecht, 2002		√	√	√				√		√	√		√ (0 Pa)		√			√		ascending only
Lantz, 2011		√	√		√	κ-ε/κ-ω		√		√		√		√ (to calc P)	√			√		healthy
Brown, 2012		√			√	κ-ε/κ-ω		√		√		√	√ (curve)		√			√		healthy
Bongert, 2009		√		√				√		√		√	√ (0 Pa)		√			√		healthy
Brown, A., 2011		√		√				√		√		√		√	√			√		healthy
Kim, 2009		√		√				√		√		√		√	√			√		healthy, exercise
Midulla, 2012		√		√				√		√		√	√ (0 Pa)		√			√		aortic lesions

Table 4: Summary of aortic flow studies completed from 1976 to 2012

2.5 Summary

As can be seen from the literature review, many CFD studies have been conducted investigating the effects of various anatomical and physiological factors on aortic blood flow, with the most significant effects resulting from the addition of 3D inlet flow, heart motion and flexible walls. The studies conducted with these variables were limited in their scope; 3D inlet flow was only investigated in rigid aorta geometries, or only in separate descending and ascending flexible aortic sections, inlet motion was only included in one study and was simulated with a partially flexible, partially rigid aortic geometry and flexible walls were modeled with unvalidated elastic moduli. The objective of the work in this thesis was to investigate the effects of flexibility, a 3D inlet flow profile and addition of inlet motion on the aortic blood flow patterns using published data on aortic tissue testing to find the correct elastic modulus of the aortic tissue and echo and MRI data to validate the inlet flow profile and inlet motion.

3 Methods

Flow simulations were run using a combination of computational fluid dynamics, finite element modeling and fluid structure interaction to couple the aortic fluid domain with the aortic wall. Boundary conditions for the fluid and solid domains were varied depending on the simulation performed and values were taken from literature and previous work. Details of the flow simulations and boundary conditions are presented in this section.

3.1 Solid Model

The following section describes in detail the properties and boundary conditions used in the solid finite element model of the aorta.

3.1.1 Geometry

CT is commonly used to acquire anatomic aortic geometries for use in CFD models. MRI can also be used and is beneficial over CT because velocity, flow and geometric data can be obtained simultaneously [35, 117]; however, at the time of modeling, MRI data was not available for this study so CT data was used. A patient specific aortic model was used in the simulation, shown in Figure 12. The model was taken from the public vascular model repository of Cardiovascular Simulation Inc [118].

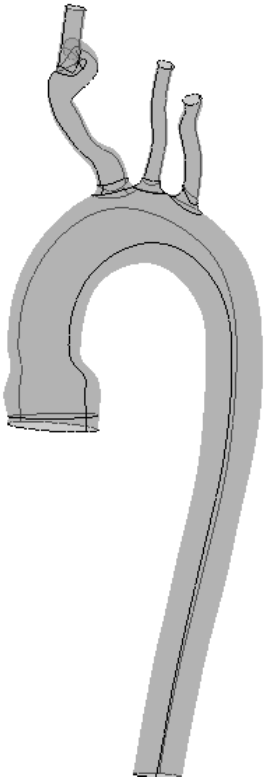

Figure 12: Aortic geometry used for the CFD model [118].

The geometry is a digitized 3D image from a CT scan of a young (20-25 year old) male. The aortic model is truncated in the distal region slightly superior to the renal hepatic arteries. It includes the three major branch arteries off the arch; the brachiocephalic, left common carotid and left subclavian arteries. The unloaded inlet diameter is 25.8 mm and corresponding outlet diameter is 14.0 mm. This geometry was used for both the FEA and CFD models, with the FEA model incorporating the outer shell only and the CFD model incorporating the full solid domain.

3.1.2 Wall Properties

The aorta walls were assumed to be isotropic with a constant density of 1070 kg/m^3, as done by [20, 26, 32]. Using an isotropic wall is a gross approximation; however, it allows for simple description of the artery wall mechanical properties.

The Poisson's ratio for the aortic wall was taken as 0.48 [2, 119]. This value is close to 0.5 and as such, the walls are assumed to be incompressible [20], implying that there is no volume change of the wall material when the wall is stretched.

The wall thickness was taken as 1.1 mm, approximately 4% of the unloaded aortic diameter. This value was chosen as it is between the measured range of 1-2 mm thickness of several aortic measurement studies [20] and has also been used in other CFD studies as seen in Table 5.

Wall Thickness (mm)	Author	Year
1.59	Bongert [30]	2009
0.8	Brown, A. [29]	2011
2.0	Canstein [63]	2008
2-4	Gao [33]	2006
1.0	Kim [32]	2009
1.0	Lantz [26]	2011

Table 5: Wall thickness values used in aortic CFD studies.

The thin walled cylinder assumption can be used if ratio of *h/r* is less than 1/10 (0.1) [2]. The aorta wall thickness is 1.1 mm and inlet radius 12.9 mm, giving a ratio of thickness to radius of 0.09. It is therefore assumed that the aorta vessel acts as a thin walled cylinder.

3.1.3 Wall Elasticity

Young's modulus is defined as the relationship between tensile stress and tensile strain. If the relationship is linear, the material is said to abide by Hooke's law of elasticity, which normally applies to purely elastic materials. Blood vessels are by nature non-Hookian materials due to their complicated biological composition and layered walls. They can, however, be approximated as Hookian if radial deformations are small compared to the respective vessel diameter. If the change is less than ten percent it is generally accepted that a linear elastic approximation can be used [2]. This approximation has been used for the model in this thesis, supported by the diameter change data in Section 2.4.5.

In addition to the wall elasticity tensile tests performed in literature and described in Section 2.2.2, typical stresses and strains were calculated from published physiologic data [20] to give a typical combined Young's modulus (the effects of wall elasticity and elastic foundation stiffness combined, but reported as just a wall elasticity value) in the range of 0.29-0.69 MPa. These data were calculated using the thin walled cylinder assumption that is valid when considering the diameter and wall thickness of the aorta. Aortic pulse wave velocity (APWV) data [120-127] also yielded a similar combined Young's modulus value of less than or equal to 0.80 MPa. A similar combined elasticity value calculated based on cine PC-MRI data at a strain of 11% was found to be 0.60 MPa [32]. Combined elastic modulus values can be seen in Table 6, values that depend on separating out the contributions of the wall elasticity itself and the elastic foundation stiffness discussed in the next section.

Author	Location	Pressure (mmHg)	Dd (mm)	Ds-Dd (mm)	Age (yrs.)	Strain (%)	Stress* (kPa)	$E_{combined}$ (MPa)
Stefanadis	Ascending Aorta	124/80	32.3	2.2	40-50	6.8	47.4	0.70
Patrianakos	Ascending Aorta	125/74	28	2.8	58	10.0	47.6	0.48
Pearson	Descending Aorta	125/78	21.1	1.8	47	8.5	33.0	0.39
Pearson	Descending Aorta	123/75	18.2	1.8	43	9.9	29.1	0.29
Lanne	Abdominal Aorta	116//64	15.5	1.5	19-38	9.7	26.9	0.28
Lanne	Abdominal Aorta	117/70	15.6	1.4	25	9.0	24.4	0.27
Sonesson	Abdominal Aorta	120/76	13.2	1.6	27	12.1	19.4	0.16
Kawasaki	Abdominal Aorta	120/69	11.7	1.1	20-39	9.4	19.9	0.21

Table 6: Typical stress and strains in the aorta in vivo [20]. *assuming thin walled cylinder

A value of 0.17 MPa was selected for the aortic wall elasticity based on the tensile tests described in Section 2.2.2. This value is valid for the small strain values seen be the aorta during normal blood flow. It is important to note that elasticity of the aortic wall varies with age, being more pliable when young and stiffer when older. For the model in this thesis, the subject is a young adult (20-25 years), so a value lower in the range was selected.

3.1.4 Elastic Foundation Stiffness

In vivo, the aorta is surrounded by tissues, organs and body fluids that provide a cushion and also support the vessel. To model this in the FSI simulation, an elastic foundation stiffness (EFS) is imposed on the aortic wall to tether it in space and also simulate tissue support. The EFS then partially acts to constrain the vessel dilation and compliance, but is more a resistance to large translations and rotations of the aorta during the cardiac cycle. The EFS acts in combination with the aortic wall elasticity, providing a combined elastic modulus. A combined value of elasticity for the aorta was found from aortic impact trauma studies, APWV measurements, simple stress strain calculations and cine PC-MRI data.

Aortic trauma studies have been conducted to analyze the effect of body impact on the aorta in motor vehicle collisions [128, 129]. Both Cavanaugh [128] and Nusholtz [129] performed impact testing on cadavers using 32 and 48 kilogram impactors and a 25 kg impactor respectively. Specimens were placed sitting in an upright position and received a blow to the abdomen. Deflection was measured using string potentiometers and accelerometers attached to the impactor and 12th thoracic vertebrae. Figure 13 illustrates the results for both experiments. Calculations were performed using the force displacement curves and the surface area of the aortic model. Results gave a combined stiffness value between 1.58 MPa/m and 4.75 MPa/m.

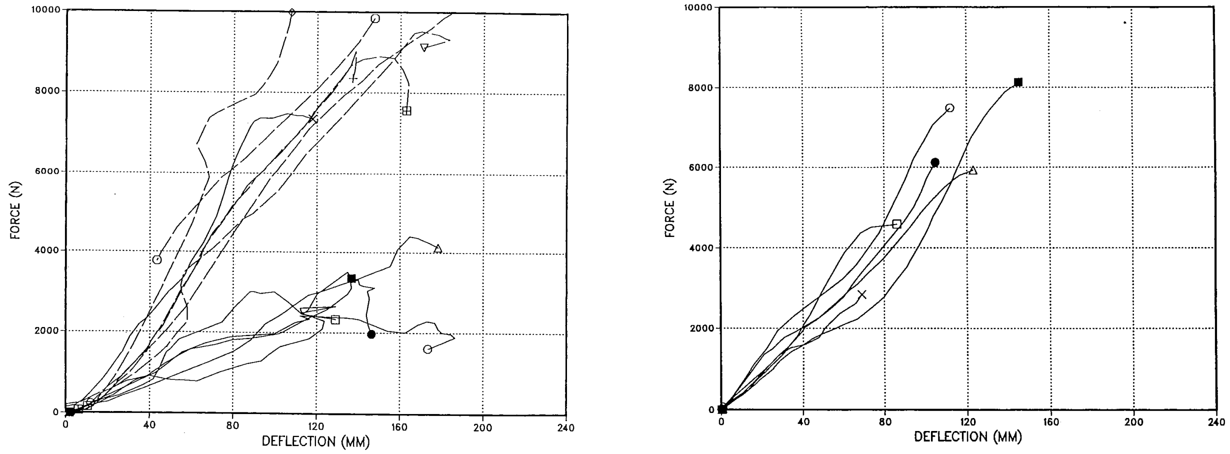

Cavanaugh 1986 Nusholtz 1988

Figure 13: Force deflection curves for the abdominal aorta during impact [129].

Pulse wave velocity is a measure of arterial stiffness used to diagnose hypertension. Two transducers are placed on the surface of the body above the carotid artery-aorta junction (A) and the femoral artery split (B). The distance between transducers is measured and a correction factor applied to account for the curvature of the aorta. An average transit time of the pulse from transducer A to transducer B is then measured and divided by the distance between A and B to give the APWV. In a hypertensive population, the APW travels faster [120]. Similarly, older patients record higher APWVs because their arteries are less elastic than their younger counterparts [20]. APWV data can be used to calculate a combined elastic modulus for the aorta. It is well documented that the relationship between APWV and $E_{combined}$ depends on aortic wall thickness (h), blood density (ρ_f) and aortic radius (r) [2, 20, 126, 130].

$$APWV = \sqrt{\frac{E_{combined}h}{2r\rho_f}} \tag{2}$$

Many studies [120-127] have documented APWV values for individuals and found correlations based on age, gender and medical conditions as seen in Table 7.

Author	Year	Age	Gender	$APWV_{avg}$ (m/s)	Health
Luzardo [120]	2012	45.6 +/- 16.4	M	7.4 +/- 2.7	General population*
			M	8.3 +/- 3.5	General population*
			F	6.9 +/- 1.9	General population*
			F	7.0 +/- 1.8	General population*
			M/F	7.3 +/- 1.9	General population*
			M/F	7.0 +/- 2.2	General population*
Inoue [103]	2009	61 +/- 5.5	M/F	8.3	General population*
Hansen [121]	2006	40-70	F	10.8 +/- 3.2	General population*
			M	11.8 +/- 3.6	General population*
Shokawa [122]	2005	64 +/- 8	M/F	9.5 +/- 1.8	Non-diabetic
			M/F	9.5 +/- 1.7	Non ECG normal
			M/F	9.2 +/- 1.5	Non-hypertensive
Nagui [20]	1999	56 +/- 15	M	7.6 +/- 3.0	General population*
			F	7.0 +/- 2.9	General population*
			M/F	7.3 +/- 2.9	General population*
Belz [125]	1995	25	M/F	7.1	General population*
		35	M/F	7.5	General population*
Laogun [126]	1982	20-30	M/F	6.9	General population*
Radhakrishnan [127]	1981	Unknown	M/F	7.0	General population*

Table 7: APWV values. * Attempts made to include only healthy volunteers.

For this thesis, the patient specific data is from a young (20-25 year old) male. The APWV data that meets this criteria is 7.0 m/s, which leads to a value of 0.80 MPa combined elasticity.

Recently, MRI has also been used to determine APWV as an alternative to the traditional transducer method. This method is significantly more time consuming in both post processing of results and data collection; however, is more accurate than the transducer method [131-134]. Results from several studies conducted on young adults [131-134], documented in Table 8 show significantly lower values that the transducer values.

Author	Year	Age	$APWV_{avg}$ (m/s)	Health
Markl [131]	2010	25 +/- 3	4.4 +/- 0.3	General population*
Fielden [132]	2008	29 +/- 7	4.5 +/- 0.5	General population*
Yu [133]	2006	34 +/- 11	5.4 +/- 0.9	General population*
Vulliemoz [134]	2002	34	4.4 +/- 0.9	General population*

Table 8 : MRI Calculation of APWV

Rough averages of elasticity for healthy young adults for each study types are summarized in Table 9.

Study Type	Calculation	$E_{combined}$ (MPa)
APWV - transducer	$E_{combined} = \frac{APWV^2 2\rho r}{h}$	0.80
APWV – MRI	$E_{combined} = \frac{APWV^2 2\rho r}{h}$	0.32
Stress/Strain Calculations	$E_{combined} = \frac{\Delta P d^2}{2h\Delta d}$	0.35
Cine PC-MRI	Measured	0.60
Trauma (Cavanaugh)	Stiffness*deformation	0.29
Trauma (Nusholtz)	Stiffness*deformation	0.57

Table 9: Combined elasticity values for healthy young males from various measurement techniques.

An appropriate value of the combined elasticity values was chosen as 0.49 MPa. With a wall elasticity value of 0.17 MPa selected, the contribution of the EFS to the combined wall elasticity is simply the remaining 0.32 MPa. Converting this into a stiffness value by dividing by the aortic radius gives an elastic foundation stiffness of 20 MPa/m. The elastic foundation stiffness value of 20 MPa/m was applied uniformly along the aorta. Although the aorta is not uniformly supported in place by the same tissue along its length in vivo, this approximation is justified for the FSI simulation. The descending aorta is fixed in space and during a cardiac cycle experiences expansion of the aortic walls only (see Section 4), so the amount of EFS applied does not change the large motion of the descending aorta. Uniform application of EFS to the ascending aorta and arch,, which are both relatively free to move with heart motion, is also representative of in vivo conditions. It is important to note that the ligamentum arteriosum tether was not included in the model (it is a defined attachment point; however, the stiffness of the anchor at the left pulmonary artery is not well defined other than its unlikely significance at large deformations).

3.1.5 Outlet Boundary Conditions

Several visits to the McMaster University Anatomy Lab [37] were taken such that the aorta could be viewed in situ. Two cadavers were examined, one with the internal thoracic cavity removed such that the thoracic aorta was visible (A) and one with the complete thoracic cavity; lungs, heart and pleura present (B).

In specimen A, the abdominal and thoracic aorta were present along with the spine. All other internal tissues had been removed. The aorta was firmly attached posteriorly to the spine via the intercostal arteries. When palpated, the aorta was free to rotate about the intercostal artery attachments.

In Specimen B, the descending aorta was fixed in space with very little motion achieved upon palpation. It was constrained by the pleura of the lungs and other thoracic cavity tissue that prevented the aorta from rotating about the spine. The three branch arteries were also fully constrained by the soft tissues in the neck approximately 5-10 mm superior to their attachment to the aorta. The aortic arch on the other hand was free to translate laterally (y-direction) and anteriorly/posteriorly (x-direction). It was constrained superiorly/inferiorly (z-direction) by the three branch arteries and also the ligamentum arteriosum,, which attached it to the relatively fixed pulmonary artery. The arch was also constrained in space by the trachea and esophagus, which prevented excessive motion of the vessel in the y-direction and also z-direction, see Figure 14. When palpated, the arch experienced minimal rotation. The most unconstrained segment of the aorta was the ascending portion that was free to move with the heart in all directions.

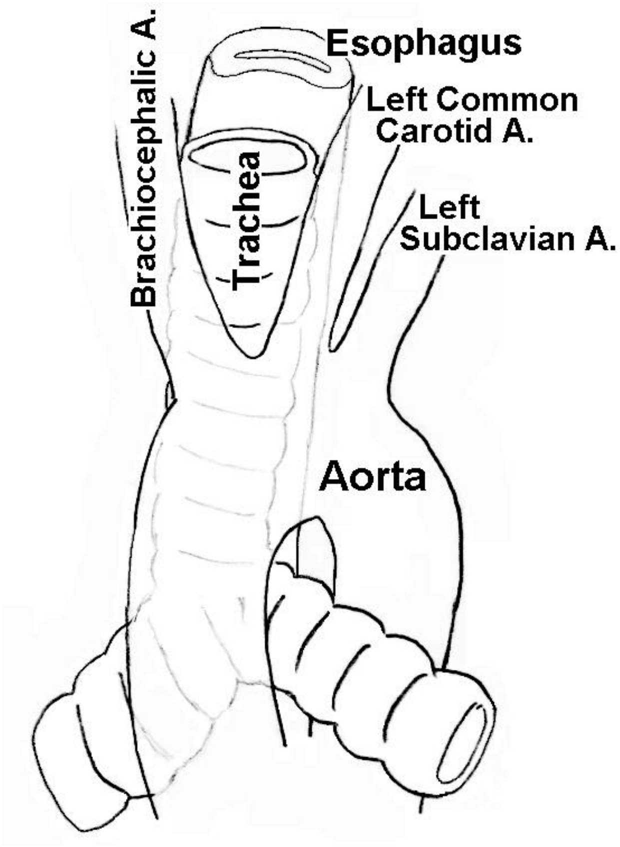

Figure 14: Location of the aorta with respect to the trachea and esophagus [135].

The information obtained from the cadaveric sample was used to impose boundary conditions on the solid domain in the FSI model. The branch arteries were fully constrained at their outlets, simulating the condition of entrapment by the neck tissues. Since the outlet was also bound by thoracic cavity tissues, it was fully constrained in the simulation as well. The inlet was assumed free to move with heart motion for the FEA case and was fixed in space for the CFD/FSI cases where inlet motion was not applied.

3.1.6 Inlet Boundary Conditions

A key part of this work was the inclusion of heart motion at the inlet. To model this in the FEA simulation, the ascending aorta was free to move with heart motion. Motion of the aortic inlet was quantified using from data obtained from the McMaster University Echocardiography Laboratory [36].

Several views of aortic valve motion were provided from a healthy, young (20-25 year old) male. From these motion captures, aortic valve motion was measured in the x, y and z directions for each time step of the cardiac cycle. Each timestep was 0.0625 seconds, giving 16 motion points for each direction. The short axis AV view was used to obtain aortic inlet motion in the x and y directions while the long axis LP was used for the z direction. For the short axis AV, the measurements were taken by orienting the view with respect to the aortic cusps as in Figure 15.

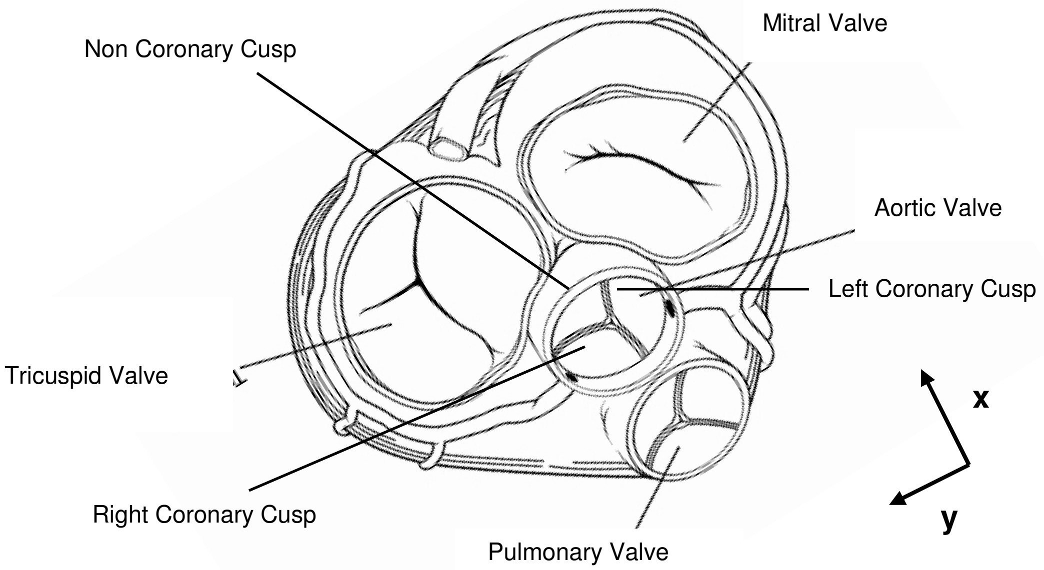

Figure 15: Orientation of aortic valve for echo data [141] .

The y axis was oriented along the right coronary/non coronary cusp boundary and the negative x axis along the right coronary cusp/left coronary cusp boundary. When relating the boundaries to the echo short axis AV images, it is important to note that the view is from inside the left ventricle looking up (Figure 16), whereas the view in the schematic (Figure 15) is from the aorta looking down towards the aortic valve. For LP long axis images, orientation of the z direction was determined by the aligning and centring the y axis at the inlet of the valve cross section and locating the z axis perpendicular to the centre of the valve (to correspond with the z direction in the FSI model).

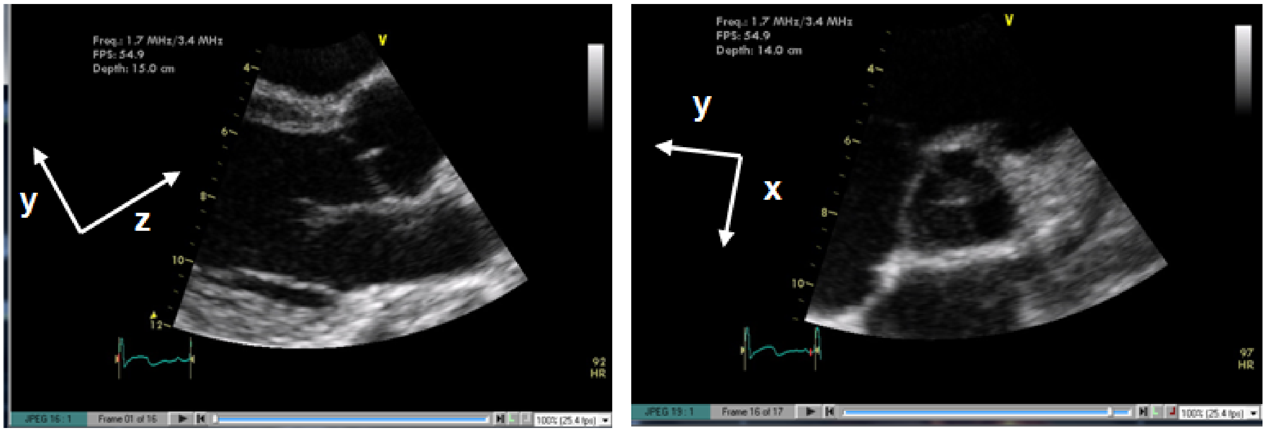

LP Long Axis View Short Axis AV View

Figure 16 : Echo views and orientations

Resulting changes in inlet motion in the x, y and z directions were tabulated frame by frame, as shown in Table 10 and applied to the inlet of the FEA motion simulation. A graphical representation of the 3D aortic inlet motion can be seen in Figure 17.

Frame	Time (s)	Δx (cm)	Δy (cm)	Δz (cm)
0	0.00	0.00	0.00	0.00
1	0.0625	0.00	0.06	-0.33
2	0.125	0.00	0.06	-0.17
3	0.1875	0.25	0.22	-0.17
4	0.25	-0.33	0.06	-0.25
5	0.3125	-0.25	0.06	0.17
6	0.375	-0.08	-0.11	0.17
7	0.4375	-0.17	-0.11	0.04
8	0.5	-0.08	-0.19	0.04
9	0.5625	0.08	-0.03	0.00
10	0.625	0.08	0.14	0.08
11	0.6875	0.08	-0.03	0.00
12	0.75	0.17	-0.03	0.17
13	0.8125	0.25	-0.11	0.17
14	0.875	0.00	-0.03	0.00
15	0.9375	0.00	-0.03	0.00
16	1.00	0.00	0.06	0.08

Table 10: Inlet motion obtained from echocardiographic data in the x, y and z directions.

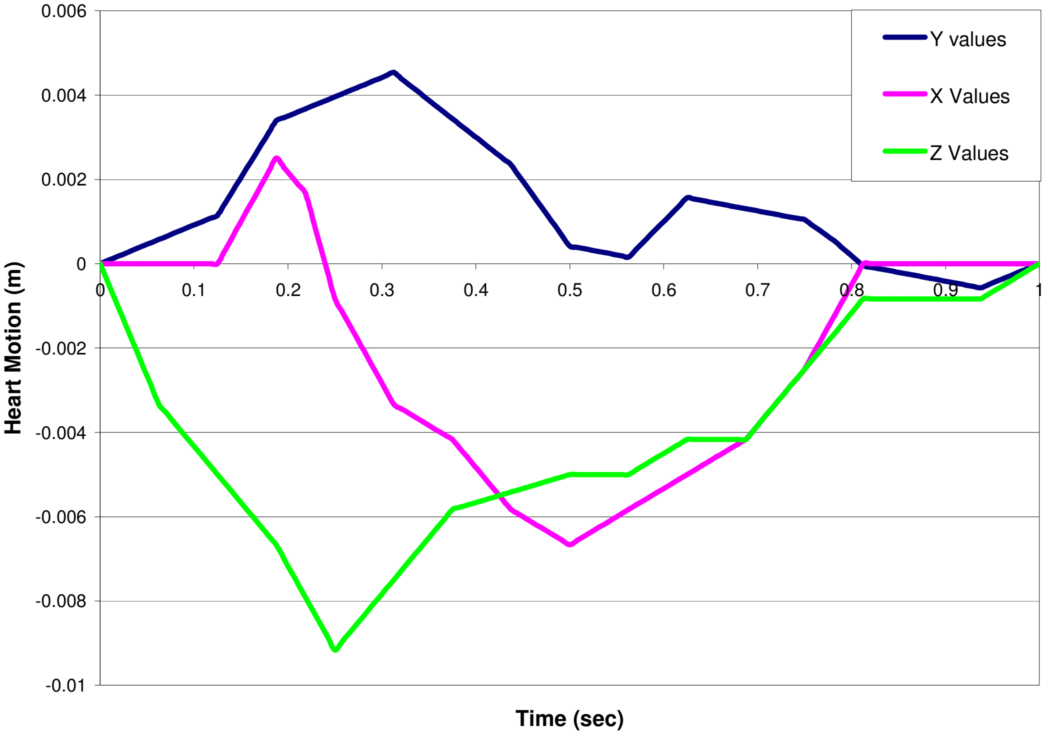

Figure 17: XYZ motion at the aortic inlet over one cardiac cycle, taken from echocardiographic data [36].

3.1.7 Mesh

The solid domain (aorta wall) required a 1 mm maximum edge length mesh for the aorta and 0.5 mm mesh for the branches in order to converge with the applied inlet motion and achieve less than 1% variance in results. Since the elements have a 1 mm edge length and the thickness of the shell is 1.1 mm, it was necessary to use solid shell elements such that the shell would be able to be sliced into multiple layers to keep with conventional shell theory. The solid domain consisted of approximately 31 000 elements and was created using SOLSH190 elements, shown in Figure 18.

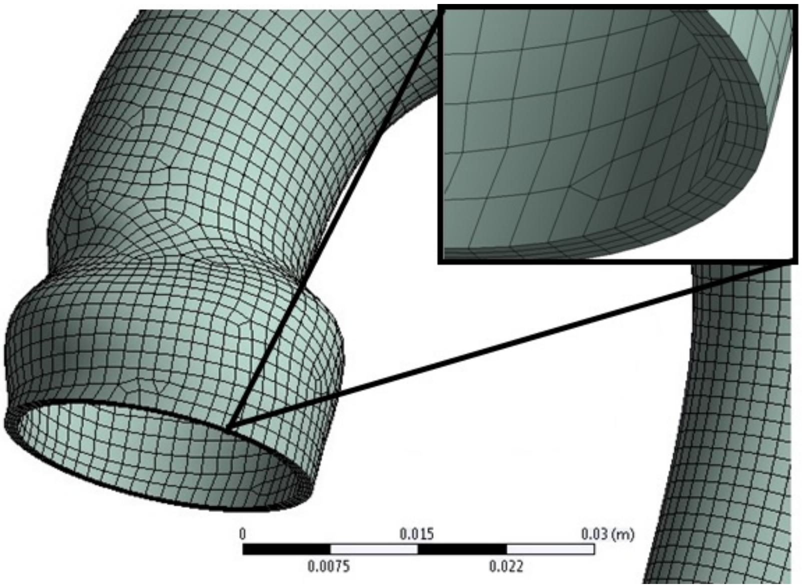

Figure 18 : Aorta wall mesh consisting of solid shell elements (SOLSH190).

3.1.8 Finite Element Method Numerics

Finite element analysis (FEA) [136] was used to provide structural analysis of the solid domain. Numerical methods were used to solve ordinary and partial differential equations (ODEs and PDEs) to provide a solution to the solid. Solid shell elements (stacked shell elements) used to mesh the aortic wall were governed by the Kirchoff-Love theory, which applies to thin plate elements with small bending deformations.

3.2 Fluid Model

The following section describes in detail the boundary conditions and properties used in the fluids CFD model of the aorta. Fluids simulations were done with either fixed boundaries (rigid walls) or moving boundaries (compliant walls), the later simulated using fluid structure interaction.

3.2.1 Geometry

The geometry used for the fluid domain was a solid model of that used in the FEA simulation, as described in Section 3.1.1.

3.2.2 Fluid Properties and Flow

Blood in nature is non-Newtonian; however, these effects only come into play in small artery hemodynamics and as such the blood was assumed to be Newtonian. Blood was used as the fluid with a density of 1060kg/m^3 and viscosity of 0.0039 Pas. These values are commonly used for blood properties in CFD studies as shown in Table 2.

Blood flow was defined as laminar throughout the entire cardiac cycle of the simulation. It has been found through both calculation and imaging that turbulence can occur in the aortic arch during systole [42, 74-78]; however, most simulations [32, 58, 63, 64, 67, 68, 83, 85, 86, 137] are performed under the assumption of laminar flow, since this concept is generally accepted by the medical profession. For this work, the main investigation was the effect of inlet motion and a real time inlet profile, so turbulence and transition to turbulence were neglected.

3.2.3 Inlet Boundary Conditions

Two inlet flow conditions were used for the CFX simulation; a time varying but spatially uniform flow profile and a time and spatially varying profile from a patient specific 4D MRI.

The spatially uniform inlet volumetric flowrate waveform was adopted from Olufsen et. al [138] and represented as Fourier analysis with the first 10 harmonics by [116]. The cardiac cycle in this waveform is 1.0 second with the division between systole and diastole at approximately 0.4 seconds. The mean flowrate is 4.94 litres per minute, which is the approximate cardiac output of a healthy adult [6, 89, 116]. A plot of the uniform velocity function used is shown in Figure 19. As seen from the figure, the harmonics are apparent in diastole, along with occasional small negative flow excursions, both of which are not seen physiologically in aortic blood flow. However, specifying the waveform in this manner easily defines the flowrate as an equation in time that can be applied uniformly across the entire defined inlet surface of the aorta at each timestep.

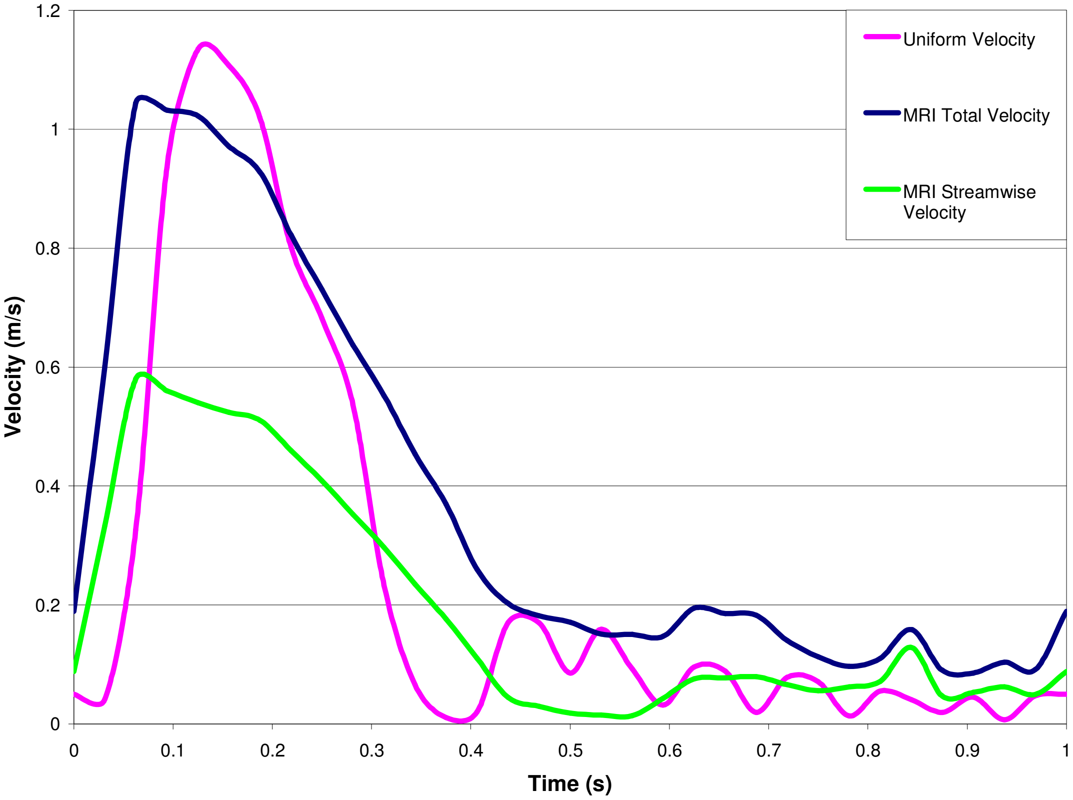

Figure 19: Uniform profile (pink), total MRI inlet profile (blue) and streamwise MRI inlet velocity (green) functions used in simulations [46], [116].

MRI data was also acquired [46] such that a spatially non-uniform flowrate driven from in vivo data could also be modeled and investigated. Data was provided in EnSight CFD file form [46] from a 4D MRI with a spatial resolution of 1.7x2.2x2.0 mm and temporal resolution of 40.8 ms. The mean flow was reported to be 4.24 L/min,, which is slightly lower than the uniform profile, but still within the physiologic range of a health adult [6, 89, 116].

Some aorta geometry was available from the MRI during systole, defined by the edges of the flow regions (ie. aorta walls). During diastole, with its much lower flow velocities, the geometry could not be clearly identified. Consequently the CT geometry [118] was used both because it is the fully available geometry, and to directly compare the effects of uniform and non-uniform inlet velocity. The geometries and flowrates are compared in Table 11. The MRI geometry has both a smaller cross-section and total flowrate. Transposing the MRI inlet velocities onto the CT geometry would then give an excessively large total flowrate. However, the streamwise (inlet normal) velocities from the MRI are substantially lower than the peak uniform velocities, with the excess presumably due to the spread of high flowrates over a longer portion of systole, see Figure 19. Based on this, no velocity scaling was done in transposing inlet velocities from the MRI to CT geometries. Compounding this data transpose is potential non-alignment of the orientation of the inlet geometries. While this alignment was done based on the observed aorta geometry during systole, the flow data suggests that non-alignment did occur.

Measurement	MRI Geometry	Geometry from [118]	Difference
Aorta inlet diameter	20 mm x 22 mm	24 mm x 26 mm	17%, 15%
Aorta inlet area	346 mm^2	490 mm^2	29%
Aortic arch diameter	21 mm	22 mm	5%
Distance from inlet to branch arteries (z-dir)	63.8 mm	58.8 mm	-8%
Volume flowrate	4.24 L/min	4.94 L/min	14%
Average inlet velocity (volume flowrate/inletarea)	0.204 m/s	0.168 m/s	-17%

Table 11: Differences in geometry measurements and flowrates between the MRI data and the geometry and flowrate from [118] and [138] respectively.

A timestep of 0.03125 seconds was selected after conducting a timestep independence study. It was found that decreasing the timestep to a value lower than 0.03 seconds had less than a 1% change on the velocity profiles at nine locations along the length of the aorta. Since the MRI data provided had a timestep of 0.0625 seconds, the data was interpolated linearly to the required 0.03125 second timestep for the simulations.

During systole, flow was visible and distinguishable from other tissues in the MRI images. For diastole when the flow was not as visible in the MRI data, the centre of the aortic inlet was found using a combination of the echo motion data and the location of the inlet centroid during systole. The inlet was located using the flow profile just after the start of the cardiac cycle when leaflet induced jet flow was visible. A plane was set at the determined inlet and moved each timestep in the x, y and z directions according to the heart motion amounts from the echocardiographic data from the McMaster Lab [36]. Velocities in the x, y and z direction (u, v, w) were then recorded for each timestep. On the plane selected, the spatial resolution of the points was 1.4x2.0x1.7 mm due to the tilt of the plane. The data was applied to the inlet at 0.03125 second intervals in the x, y and z directions (u,v,w) on a 0.55 mm by 0.35 mm xy grid shown in Figure 20. A CFX expression language (CEL) function was written to combine the u, v and w timesteps into a pulse sequence. The u, v and w velocities were then applied to the inlet as Cartesian velocity components.

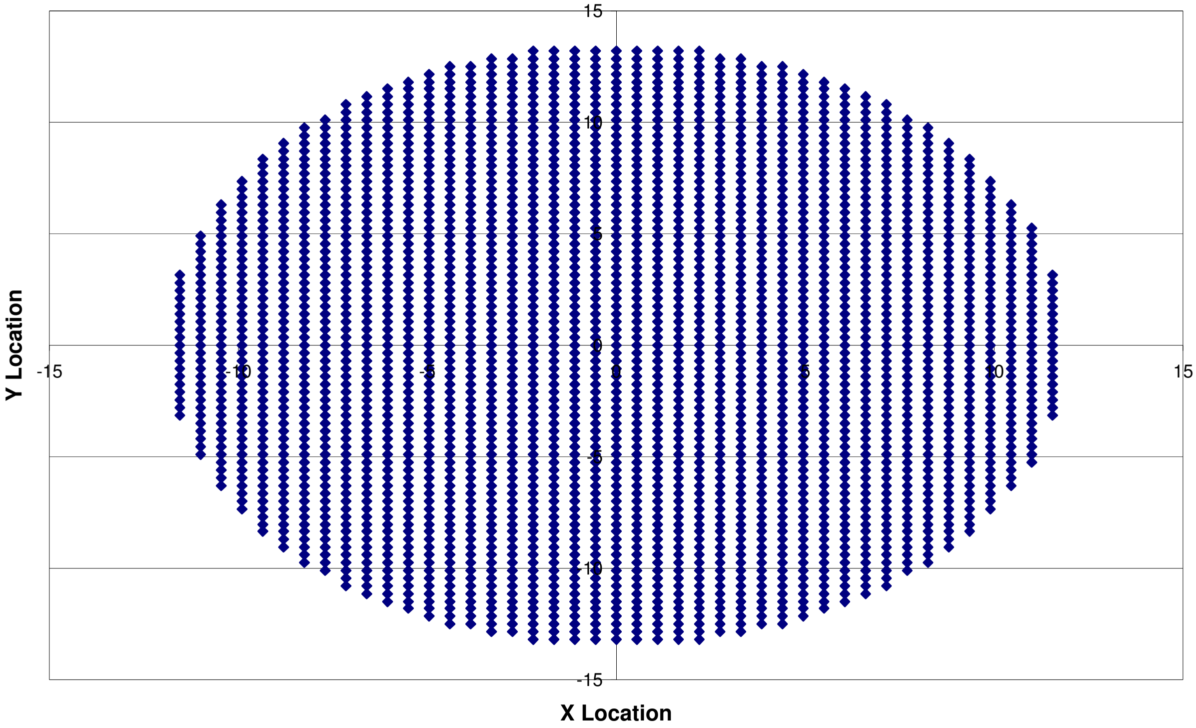

Figure 20: MRI data points shown on a 0.55 mm by 0.35 mm grid at inlet of aorta, taken from the first timestep at zero second.

Velocities at the aortic inlet for the first nine timesteps are shown in Figure 21. Velocity contours are for normal flow (w), with velocity vectors plotted as cross stream (u-v) vectors. All plots are on the same scale. It is important to note that streamwise velocities are approximately half those of the uniform profile imposed in the compliant and rigid wall simulations due to the likely non-alignment of the orientation of the inlet geometry. The mass flow through the simulation is expected to be decreased by the same amount, along with the corresponding area averaged velocities along the aorta and at the outlets.

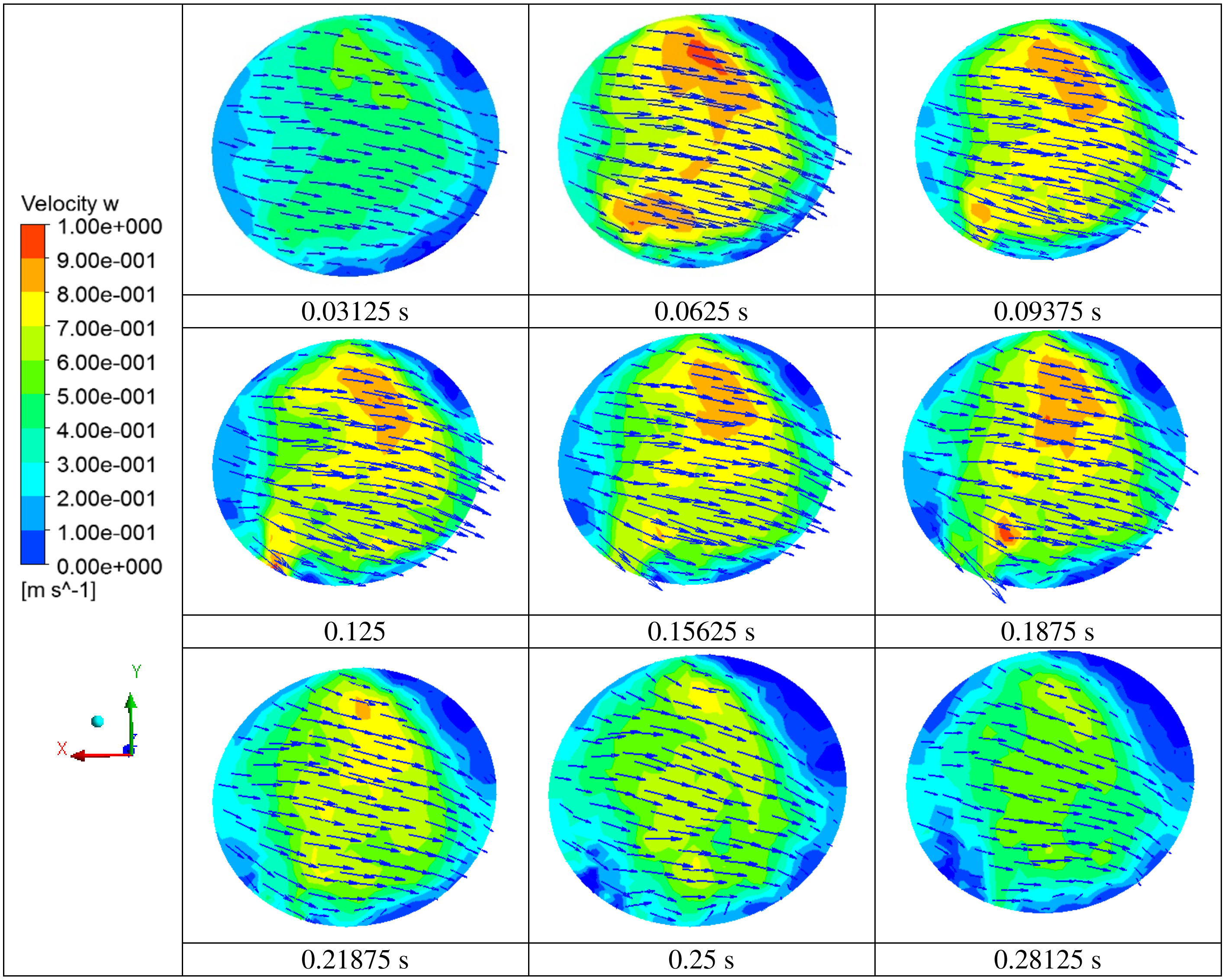

0.03125 s 0.0625 s 0.09375 s

0.125 0.15625 s 0.1875 s

0.21875 s 0.25 s 0.28125 s

Figure 21 : Inlet flow profiles from MRI data.

The degree of inlet flow non-uniformity was calculated at each timestep using the variance in the streamwise (z direction) and also total velocity using the following formulae, where N is the number of velocity points:

$$Var(v_{zinlet}) = \int_{inletarea} [v_{zinlet}(x, y) - \bar{v}_{zinlet}]^2 dA \qquad (3)$$

$$Var(v_{zinlet}) = \frac{1}{N} \sum [v_{zinlet}(x, y) - \bar{v}_{zinlet}]^2 \qquad (4)$$

The variance was calculated at each timestep to determine the variability in the flow as compared to the uniform inlet case and is shown in Figure 22. Variance is higher in systole, as expected due to the jet flow profile, as can be seen in Figure 21. In diastole, when the flow is fairly uniform and constant, variance is low and the flow mimics a uniform inlet flow profile.

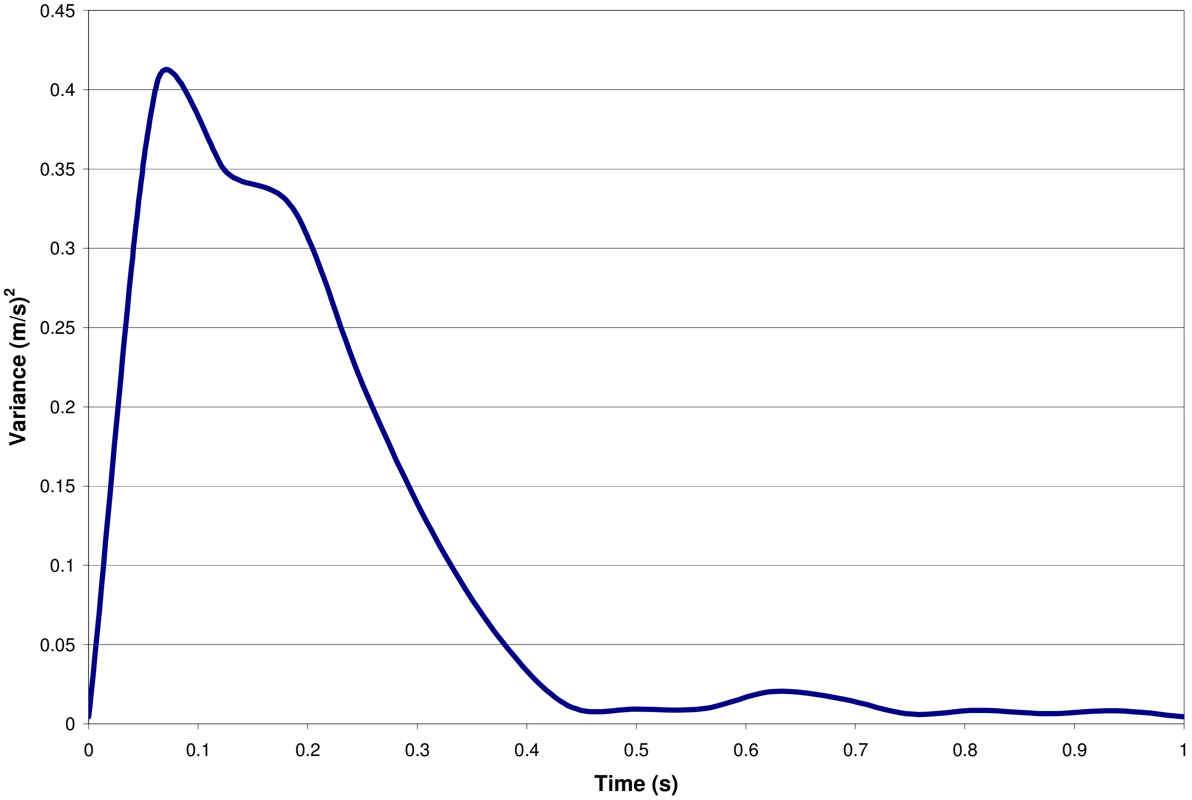

Figure 22: Normal flow (z-direction) variance of the 3D MRI inlet flow.

The number of pulse sequences required for the simulation was also validated through a pulse independence study. A simulation was run for a total of four pulse sequences and the velocity values on different xy planes along the length of the aorta were compared. The first pulse sequence was required for numerical stabilization of the simulation, so sequences 2, 3 and 4 were compared for values. There was less than 1% difference in the results between pulses 2 and 4 (likely due to the pipe flow nature of the flow with low residence times) and as such, the use of three pulse sequences was selected for the simulations.

3.2.4 Outlet Boundary Conditions

A real time back pressure [116], shown in Figure 23 was imposed as the outlet boundary condition. The pressure profile was synchronized to the inlet flow cycle and transformed by Fourier analysis to 10 harmonics in a similar manner to the inlet flow so it could be entered into the simulation in equation form [116]. The pressure differences between outlets were assumed to be negligible, so the profile was applied equally to all outlets. The pressure profile at each outlet was sensitive to the length of the applied artery; however, a previous study determined the branch lengths for this geometry were adequate such that the bulk flowrate split between the outlet and branch arteries was realistic [116].

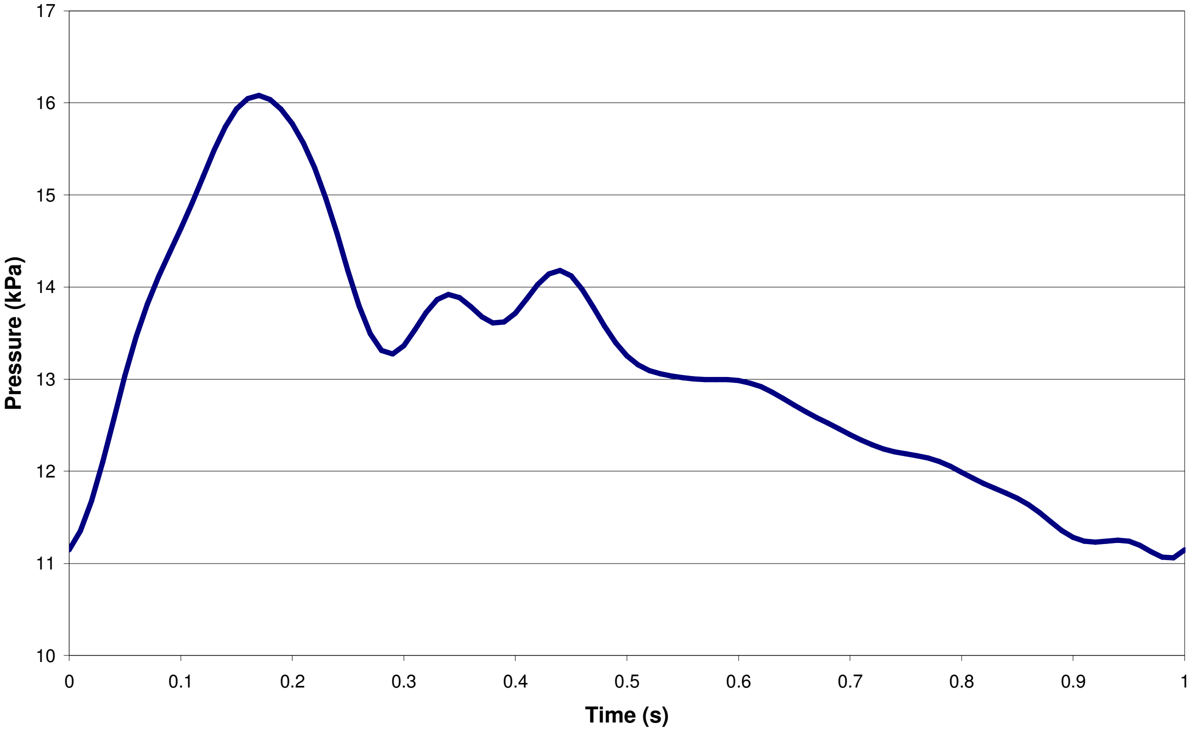

Figure 23: Outlet pressure profile used in simulations. Note the y-axis begins at 10kPa [116].

3.2.5 Initial Conditions

The CFX simulation was initialized with zero flow in the x, y and z directions along with zero relative pressure. The reference pressure was assumed to be one atmosphere.

3.2.6 Mesh

Fluids simulations were done with either fixed boundaries (rigid walls) or moving boundaries (compliant walls with fluid-structure interaction). The fluids meshes with fixed boundaries consisted of unstructured tetrahedral control volumes with hexahedral boundary cells near the walls. A 3 mm thick boundary cell region was used with 5 layers of cells and an expansion factor of 1.2. There were approximately 550 000 elements in the overall mesh as seen in Figure 24. A grid refinement study was done and it was found that grid independent results were obtained with a 1.35 mm average element edge length in the aorta itself and 0.5 mm edge length in the branch arteries. The fluids mesh was composed of SOLID186 elements.

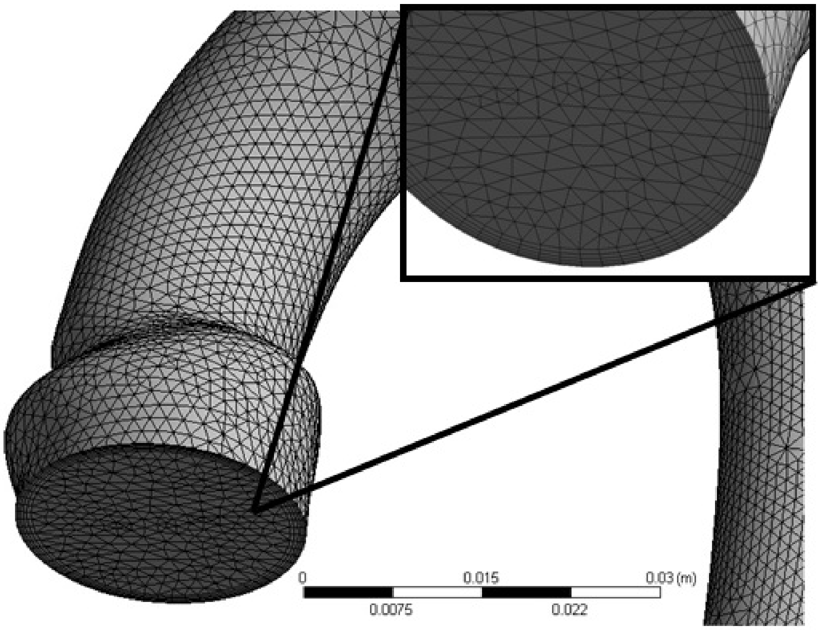

Figure 24: Tetrahedral fluids mesh enlarged to show boundary layers.

3.2.7 Numerics

The Navier-Stokes equations (conservation of mass and momentum) were solved on the mesh with the boundary and inlet condition discussed in Sections 3.2.3 and 3.2.4.

$$\frac{\partial \rho}{\partial t} + \frac{\partial}{\partial x_i}(\rho u_i) = 0 \tag{5}$$

$$\frac{\partial}{\partial t}(\rho u_j)+\frac{\partial}{\partial x_i}(\rho u_i u_j)=-\frac{\partial P}{\partial x_j}+\frac{\partial}{\partial x_i}\left[\mu\left(\frac{\partial u_j}{\partial x_i}+\frac{\partial u_i}{\partial x_j}\right)\right] \tag{6}$$

The conservation equations were solved using a scheme were a bending function switched between first- and second-order accurate advection schemes. In flow regions with low variable gradients, the blending function switched to a second-order scheme for accuracy, while in regions with higher variable gradients, the function switched to the more robust first-order scheme. This fluids Ansys CFX Solver code [136] was used to iteratively solve these governing mass and momentum equations at each timestep until the root mean square residuals fell below 1e-4.

3.3 Fluid Structure Interaction

Fluid structure interaction (FSI) modeling combined a CFD fluid domain with a FEA solid domain to couple fluid flow with a deformable structure. Fluid forces calculated in the CFD domain were passed to the FEA domain where those forces were imposed as loads on the solid structure. The deformation of the structure was then calculated and the new geometry was passed back to the CFD domain and the fluid flow and forces re-calculated, as shown in Figure 25.

Limitations in the FSI coupling of the CFD and FEA solvers were experienced in this work. With the addition of inlet motion, volume in the fluid domain was created and destroyed with each timestep, depending on the direction of motion applied. Compatibility with the inlet boundary conditions and the previous timestep's solution was difficult to enforce as the momentum of fluid in the created volume had to be specified (which was not just a simple plug at the inlet since the side walls of the domain were also moving laterally and radially). Discrepancies with the inlet BC and with the overall mass and momentum balances within the domain resulted in stability and convergence problems. Meshing problems were also created with mesh matching of the fluids and solids domain. This problem was especially magnified with the addition of inlet motion that was both tangential and perpendicular to the direction of inlet flow. Due to this limitation, when the effects of addition of inlet motion were investigated, a quasi steady (non FSI) approach was taken (see Section 3.4).

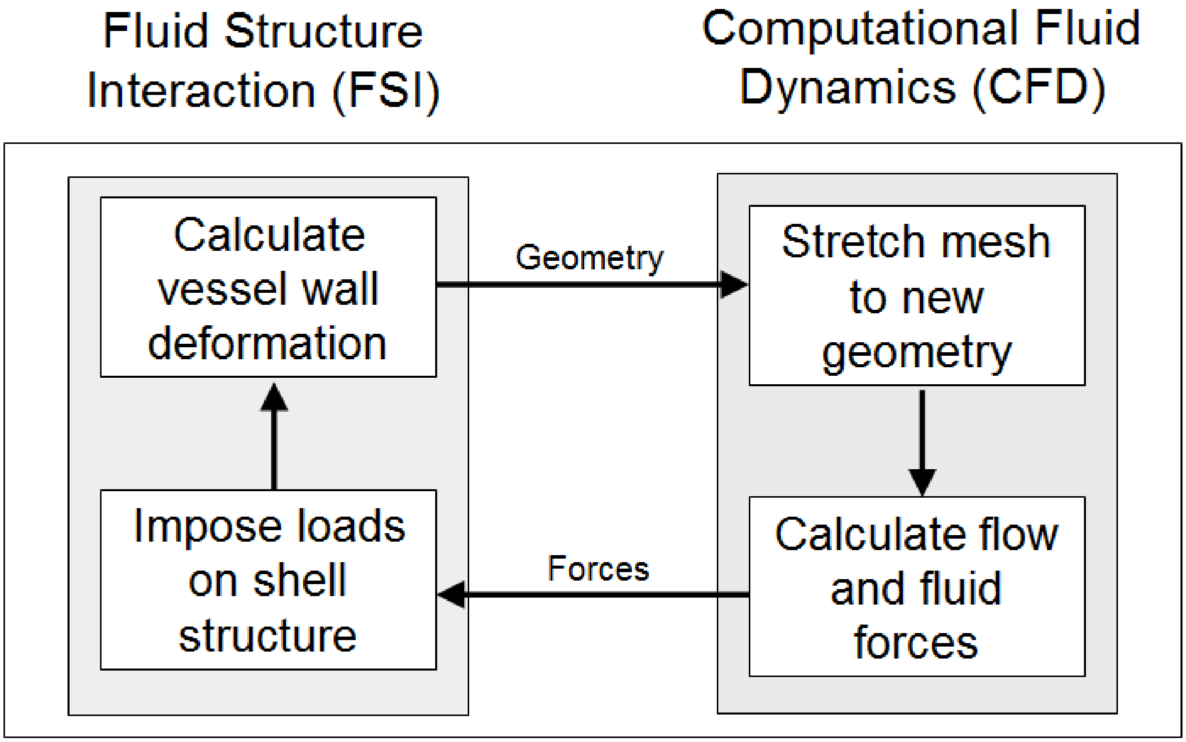

Figure 25: FSI Solver sequence showing transfer of forces from fluid to solid domains.

The fully coupled FSI simulations (used with stationary inlet conditions) were fully transient and solved in a time marching manner. Within each timestep, a series of iterations, or loops, coupling intermediate CFD and FEA solutions (as shown in Figure 25) are performed. The transfer of fluids loadings and domain deformations occurred at small enough intervals such that re-meshing of either model was not required. Convergence of the FSI model in the iterations was determined by a user set residual for both displacement and force values; in these simulations a residual threshold of 1E-4 was used. When the convergence criteria were met, the solution progressed to the subsequent timestep. The FSI numerical simulations were performed using the commercial FEA code, ANSYS 12.1, and CFD code, CFX, with FSI coupling done with the ANSYS available ADPL routines [136]. Post processing of results used Ansys CFD Post. FSI simulations were performed using stationary inlet geometries.

All of the FSI simulations were run for three seconds (3 cardiac cycles) with a time step of 0.03125 seconds. This timestep magnitude is commonly used in aortic blood flow studies [53, 116]. After two cardiac cycles the flow exhibited cycle to cycle consistency and the flow data from the third cardiac cycle was used for post processing.

3.4 Simulations

In order to investigate the effects of wall flexibility, a 3D inlet flow profile and inlet motion due to heart movement during the cardiac cycle, the following cases were simulated:

1. Rigid wall with uniform inlet flow
2. Compliant wall with uniform inlet flow (to be compared to Case 1)
3. Quasi Steady Flow Rigid wall (to be compared to Case 1)
4. Quasi Steady Flow Rigid wall with a moving inlet deformed geometry (to be compared to Case 3)
5. Compliant wall with MRI inlet flow (to be compared with Case 2)

3.4.1 Transient Flow, Rigid Wall

A rigid case was simulated using the abbreviated uniform profile at the inlet and the real time back pressure for the outlet condition. The wall of the aorta was fixed in space and all inlet and outlets were assumed to be fixed in all directions. The simulation was run for three pulses with a timestep of 0.03125 seconds. Results were taken from the third pulse sequence.

3.4.2 Fixed Inlet, Transient Flow, Compliant Wall

A compliant case was simulated using the same conditions as the rigid case, with the exception of the addition of a flexible wall. The wall was modeled with an elastic modulus of 0.17 MPa and an elastic foundation stiffness of 0.32 MPa was applied to mimic the surrounding tissues.

3.4.3 Quasi Steady Flow Rigid Wall

A quasi steady flow simulation with a rigid wall was run to compare to the transient rigid wall case. Three timesteps were chosen and used in the quasi steady flow case to correspond with early (0.0625 seconds), peak (0.125 seconds) and late (0.3125 seconds) systole. The quasi steady flow simulations were run with the time equivalent real time backpressure applied to all outlets. The walls of the aorta were assumed to be rigid.

3.4.4 Quasi Steady Flow Rigid Wall with a Moving Inlet Deformed Geometry

A second quasi steady flow case with a moving inlet was simulated using the same conditions as the case presented in Section 3.4.3, with the exception of the moving inlet. The deformed geometry was used to simulate the effects of inlet motion by stretching the original geometry to mimic the changes in aorta shape during early, peak and late systole resulting from heart motion at the inlet. To get the deformed geometry, an FEA simulation was run using the solid aorta model with inlet motion, flexible walls and specified EFS. The model was run until 0.0625, 0.125 and 0.3125 seconds with the nodal locations output at the end of each run. The node file was then exported into GeoMagic Studio 12 such that a geometry of the deformed aorta could be obtained by wrapping the points to form a solid. The deformed geometries were then imported into ANSYS CFX and run as quasi steady flow simulations at 0.0625, 0.125 and 0.3125 seconds.

3.4.5 Transient Flow, Compliant Wall with MRI Inlet Flow

A fixed inlet case was simulated using the inlet MRI velocity data provided from Markl [46]. The objective of this case was to investigate the effects of a non-uniform, spatially varying transient inlet flow profile. The real time outlet backpressure was applied to all outlets and the wall was assumed to be flexible as in the compliant wall case.

4 Results and Discussion

The effects of wall flexibility, addition of a 3D inlet flow profile and inlet motion on aortic flow are investigated. Wall flexibility and 3D inlet flow profile conditions are run as fully coupled FSI simulations and compared to rigid and uniform inlet profile simulations respectively. Due to modeling constraints, a fully coupled simulation incorporating inlet motion could not be completed. In order to investigate the effects of inlet motion, an FEA simulation is first run with inlet motion and compared to one with a stationary inlet condition. Once the effects of inlet motion on the aortic wall are determined, a quasi steady flow simulation with inlet motion is completed. The simulation is compared to a quasi steady flow simulation with a fixed inlet to determine the effects of adding inlet motion to the simulation. It is hypothesized that the effects of addition of inlet motion are more significant than that in previous work by Brown, Wang, et al and others [67, 89, 104, 116], which focused on wall flexibility based flow effects. Results and discussion of each comparison are presented in this section. A complete set of pictorial results for streamlines, transverse velocity profiles, wall shear stress, velocity and pressure profiles and mass flow over the cardiac cycle are presented in Appendices B-G.

4.1 Axis Definitions

It is important to establish orientation of the aorta and direction of the flow prior to investigating the simulation results. The orientation of the aortic inlet is described in Section 3.1.6, with the z direction defined as positive in the superior (up) direction. The y axis is positive towards the left arm and the x axis is defined as positive posteriorly (both when viewing the subject from the anterior (front) direction). These axis orientations can be seen in Figure 26.

Figure 26: Orientation of aorta for simulations with ascending aorta, descending aortic arch and descending aorta planes shown.

Flow patterns and velocity vectors are defined on planes in the ascending aorta, descending arch and descending aorta, as seen in Figure 26. Clockwise and counter clockwise flow orientations are dependent on the z direction the planes are viewed from. The ascending aorta and descending aorta are viewed looking in the positive z direction and hence have counter clockwise (or right hand flow) defined as the clockwise direction when looking at the plane. The descending arch is viewed from the negative z direction, looking down and has clockwise (or left hand flow) defined as the clockwise direction when looking at the plane. These conventions follow those used in the literature [68, 85, 87, 114] and can be seen in Figure 27.

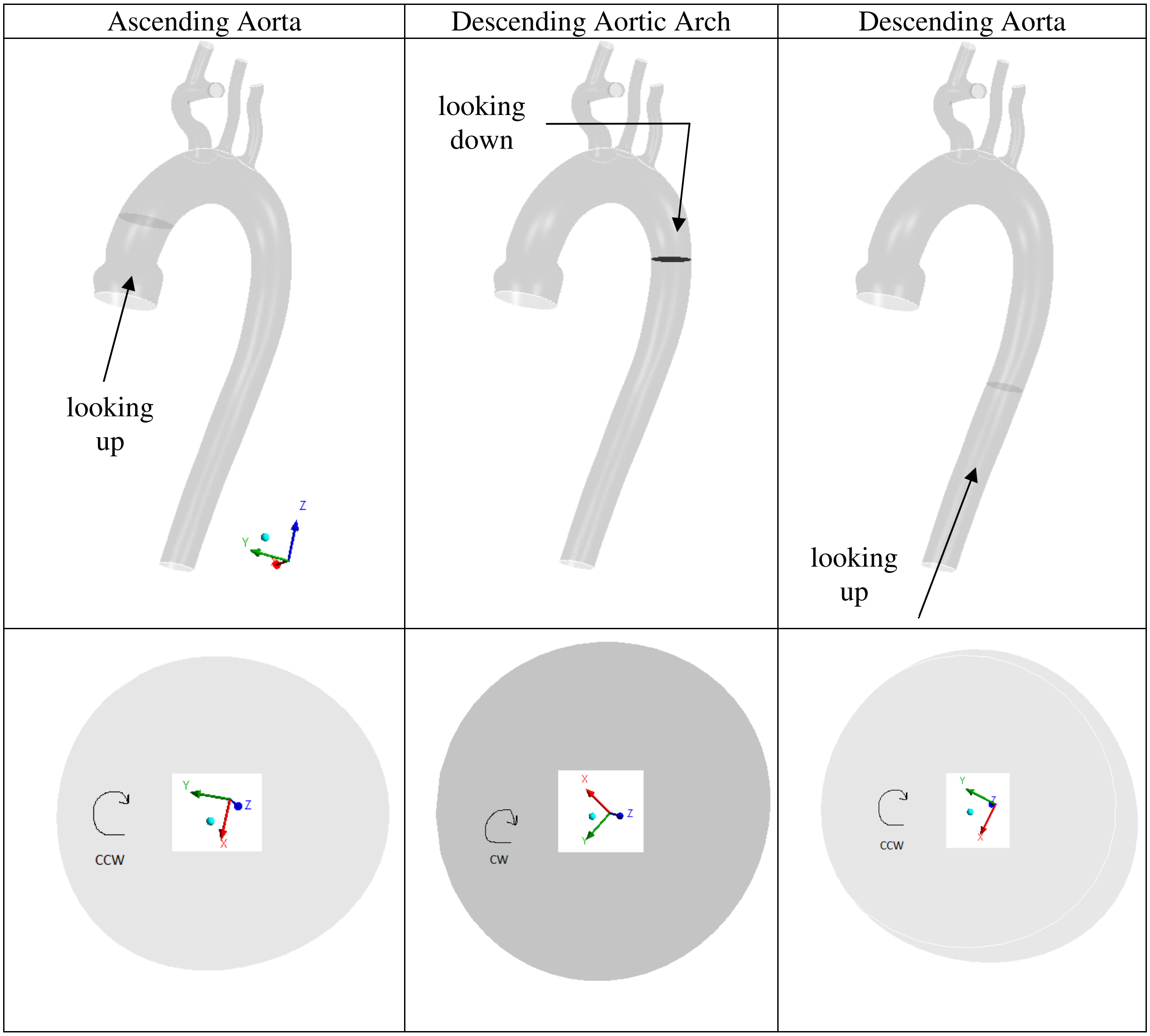

Figure 27: Orientation of flow and axis directions for ascending aorta, descending aortic arch and descending aorta planes.

4.2 Fixed Inlet, Transient Flow, with Rigid and Compliant Vessel Walls

To investigate the effect of wall compliance on aortic inlet flow, the results from the flexible wall and rigid wall cases are compared. Details of flow conditions for each case are listed in Section 3.

4.2.1 Wall Deformation

Addition of wall elasticity results in expansion of the aorta walls due to pressure along the cardiac cycle. Changes in diameter of 10% in the ascending aorta, 9% in the descending arch and 8% in the descending aorta are seen. These values agree well with results presented in literature [11],[12, 13]. Area changes corresponding to the diameter changes are shown in Figure 28, quantitatively showing the storage of blood in the aorta.

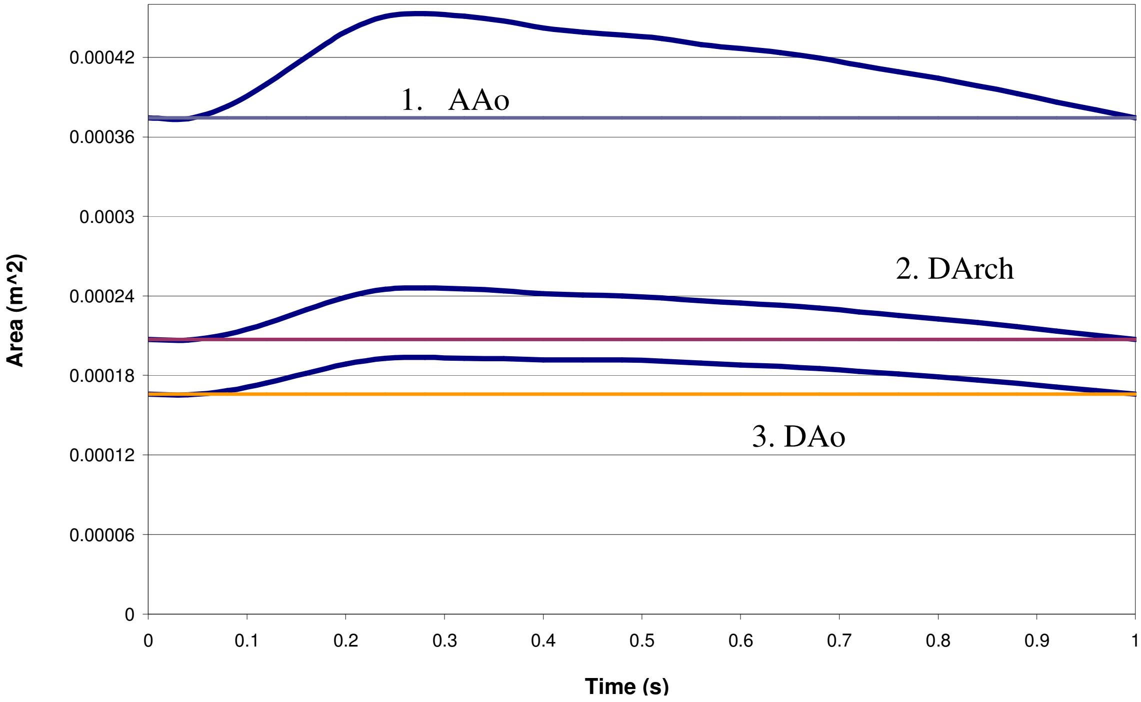

Figure 28: Area changes in the ascending and descending aorta and descending arch for compliant wall (blue) and rigid wall (purple, red, orange).

The maximum expansion occurs at approximately 0.27 seconds for all three locations. The time of peak wall expansion is significantly after the time of peak pressure (0.2 seconds, see Figure 23) and well after the time of peak flow (0.15 seconds, see Figure 19). Maximum deflection of the wall is approximately 1.25 mm in the ascending aorta and 0.58 mm in the descending aorta (radius change). This deflection is fairly small when compared to the motion of the heart at the aortic inlet which is up to 7 times larger (see section 4.4.2). The wall relaxes slowly over the course of diastole, returning to its un-deformed state at the end of the cardiac cycle.

4.2.2 Pressure

As expected, the pressure drops accordingly along the aorta and through the cardiac cycle. For both cases, the inlet pressure shows the trace of the 10^{th} order sinusoidal construction of the waveform. The rigid case experiences slightly higher outlet pressures than the flexible case, on the order of 10% higher, due to the lack of energy absorption from the rigid walls. A pressure plot through the cardiac cycle is presented for the inlet and outlet of both cases in Figure 29.

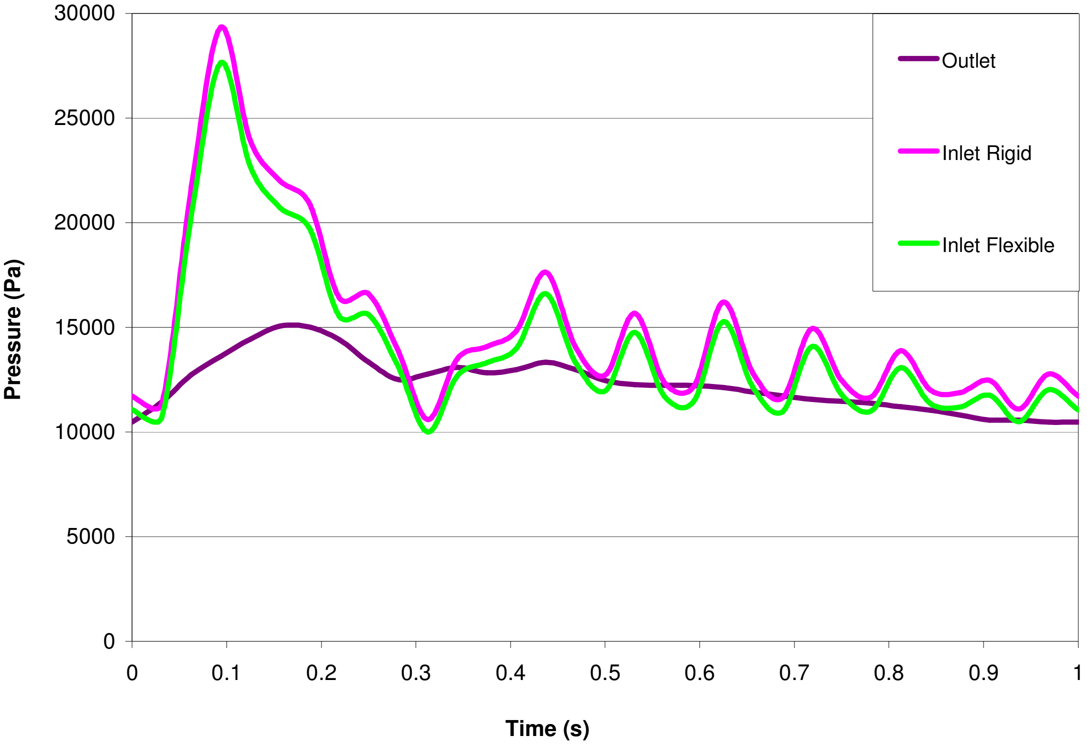

Figure 29: Pressure profile at inlet and outlet in the rigid and compliant cases, through one cardiac cycle.

4.2.3 Flow Patterns

Velocity magnitudes vary along the length of the aorta of the flexible wall case compared to the rigid wall case due to the expansion of the aorta, and subsequent area change. The greatest change is seen in the ascending aorta (Figure 30). This segment of the aorta experiences up to 20% lower velocity magnitudes that the rigid case. The descending arch and descending aorta also see lower velocities in comparison to the rigid case, slightly lower than the ascending aorta at 17% and 15% respectively.

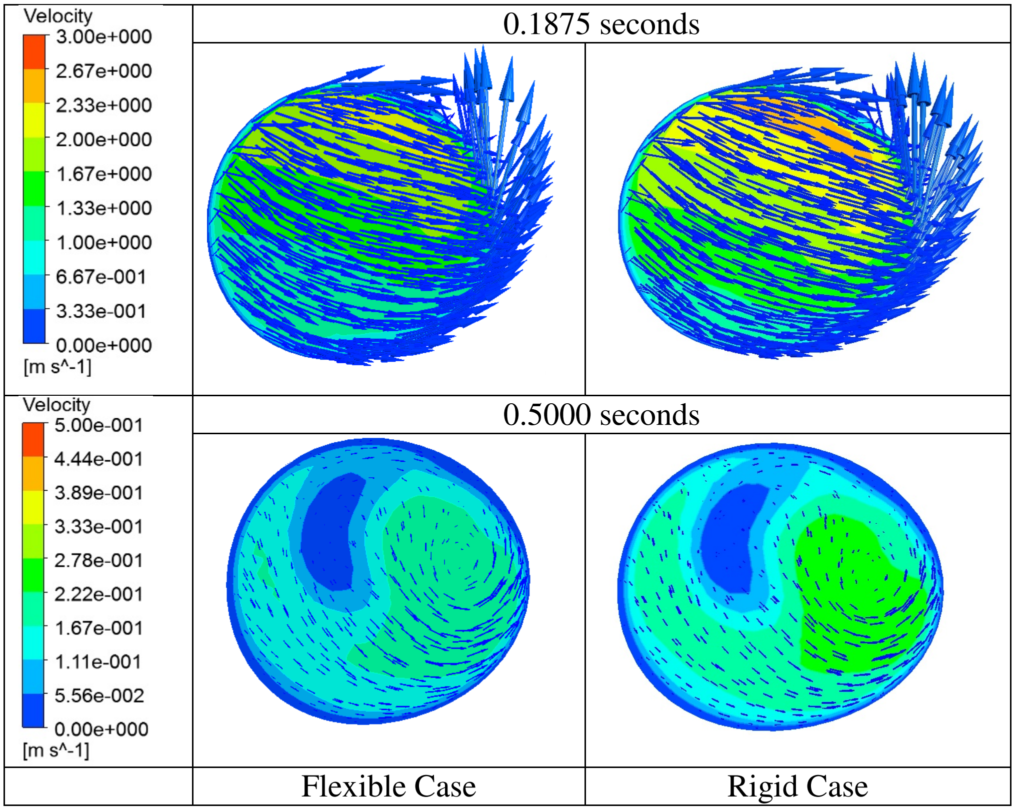

Figure 30: Velocity contours in the ascending aorta at 0.1875 and 0.5 seconds showing lower velocities in the flexible case (left) compared to the rigid case (right).

The rigid and flexible cases exhibit similar flow patterns along the length of the aorta through the entire cardiac cycle. The ascending aorta experiences parallel (straight) cross plane flow through early systole, continuing into peak systole. Helical flow patterns begin to develop during late systole with a large clockwise helix forming in the left posterior of the aorta. As the pulse progresses into early diastole, the helix moves forward to a more central position, still slightly to the left side. In late diastole, it moves backwards to the same left posterior position of late systole.

Helical flow in the descending arch develops much quicker than in the ascending aorta, with the transition from parallel flow occurring just after peak systole. The helix forms in a clockwise direction in the centre of the aorta. Through late systole it splits into a large clockwise helix in the centre, with a smaller counter clockwise helix forming at the posterior wall. This formation stays stable until mid-diastole when the central helix split again to form two smaller helices, bringing the total to three. The clockwise helix stays fairly central with the two counter clockwise helices forming right posterior and left central. During late diastole, the central clockwise helix is the single prominent structure in the flow. Clockwise helical flow patterns in the descending arch can be seen in Figure 31.

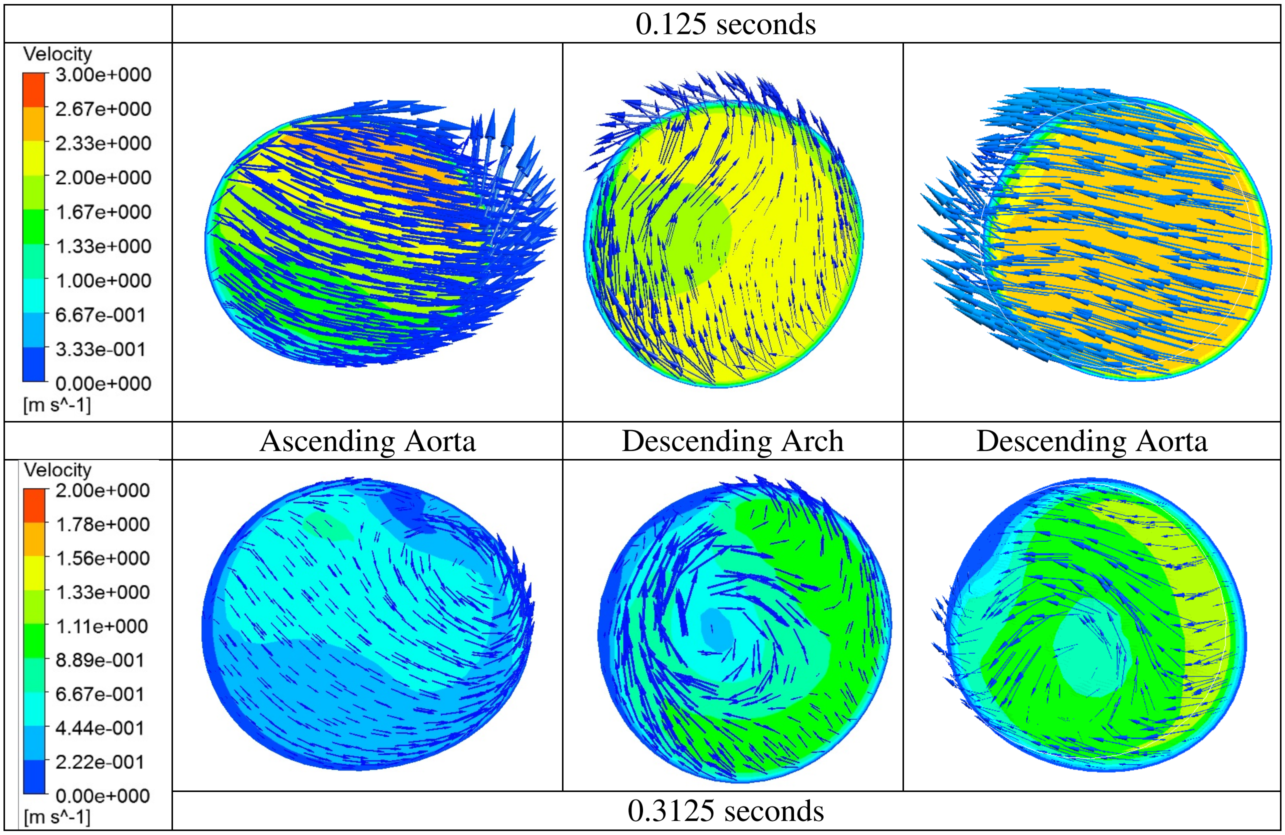

Figure 31: Helical flow patterns in the ascending aorta, descending arch and descending aorta in the rigid case during peak and late systole (see section 4.1 for plane locations). Colour contour corresponds to velocity magnitude.

Similar to the ascending aorta, parallel flow is seen in the descending aorta from the start of the pulse sequence to peak systole, where a small clockwise helix develops in the right, anterior aorta. This pattern persists to late diastole where it moves to a more central, slightly posterior location and changes direction of rotation to become counter clockwise. Flow development from parallel flow during early systole to helical flow during late systole can be seen in Figure 32.

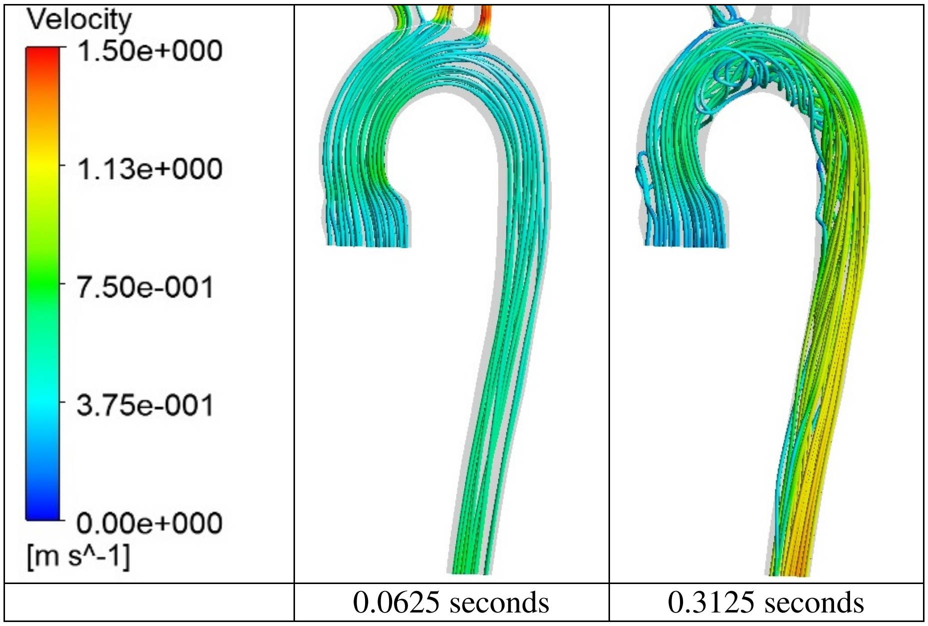

0.0625 seconds 0.3125 seconds

Figure 32: Flow development in the rigid simulation showing parallel flow during early systole (0.0625s) transitioning to helical flow in late systole (0.3125s).

Results from the rigid and flexible cases agree with rigid and flexible CFD studies presented in the literature review [27, 30, 33, 56, 67, 69, 139]. Helical flow patterns and locations in the ascending aorta, descending arch and descending aorta are identical through the entire pulse sequence. It is important to note that some of the plane orientations for helical flow defined in the literature are not clear, or well defined.

Velocity profiles through early, peak and late systole in the ascending aorta, descending arch and descending aorta are mapped and found to be the similar in both the rigid and flexible cases. M-shaped velocity profiles are observed in the descending arch and descending aorta through the duration of systole. Plug inlet flow rapidly becomes non-uniform in the ascending aorta and ascending arch. Velocity profile shapes are similar between flexible and rigid walls, with differences varying from decreased velocity and increased diameter in the flexible case. This agrees with results presented in literature from healthy patients as presented in [87]. A comparison of profiles in the descending aorta for the flexible and rigid cases is seen in Figure 33.

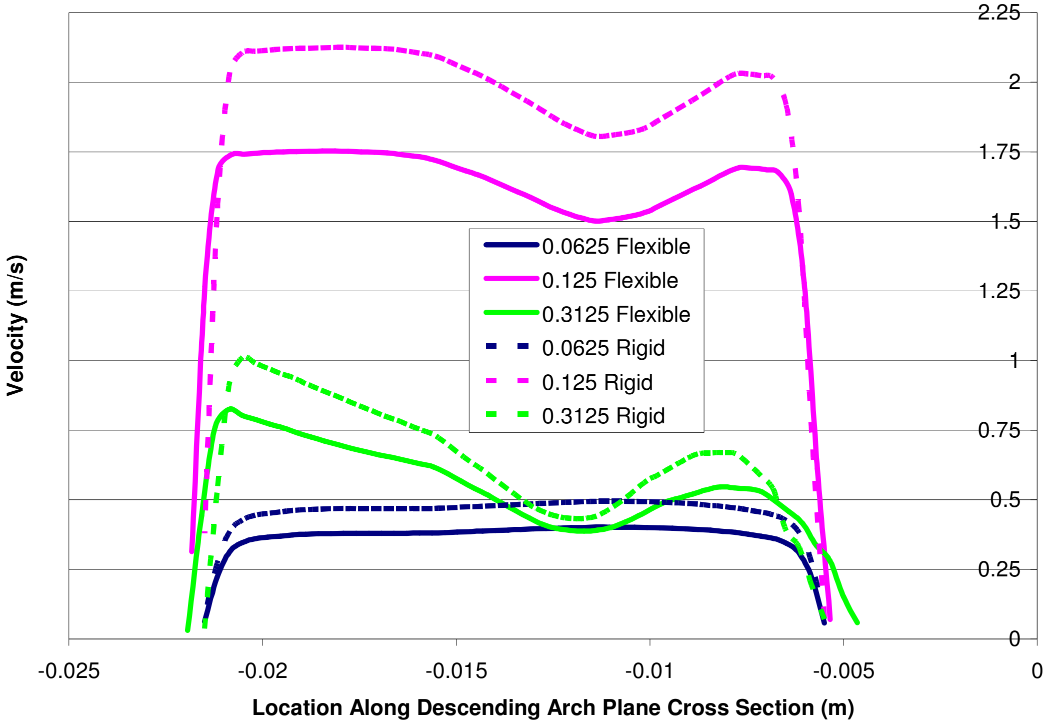

Figure 33: M-Shaped velocity profile seen in the descending arch in the rigid simulation showing profiles at three different time points in the cardiac cycle, with rigid case (dotted lines) and flexible case (solid lines).

4.2.4 Wall Shear Stress

WSS values for the rigid and flexible case vary by 10-12%, but are similar in locations for areas of high and low WSS. Areas of high WSS are observed in early and peak systole at the branch insertion points on the top of the aortic arch. These values are three times larger than peak WSS values seen by the main section of the aorta, experiencing values of 65 Pa, shown in Figure 34. Other areas of high WSS are seen at peak systole on the superior aortic sinus (50 Pa rigid case, 44 Pa compliant case), inner aortic arch (30 Pa rigid case, 26 Pa compliant case) and posterior descending aorta (35 Pa rigid case, 31 Pa compliant case). WSS is significantly diminished during late systole with peak values of 10 Pa in the rigid case and 9 Pa in the compliant wall case. The locations and values of WSS are similar to those found in the works of [69, 86, 87, 89, 90, 113].

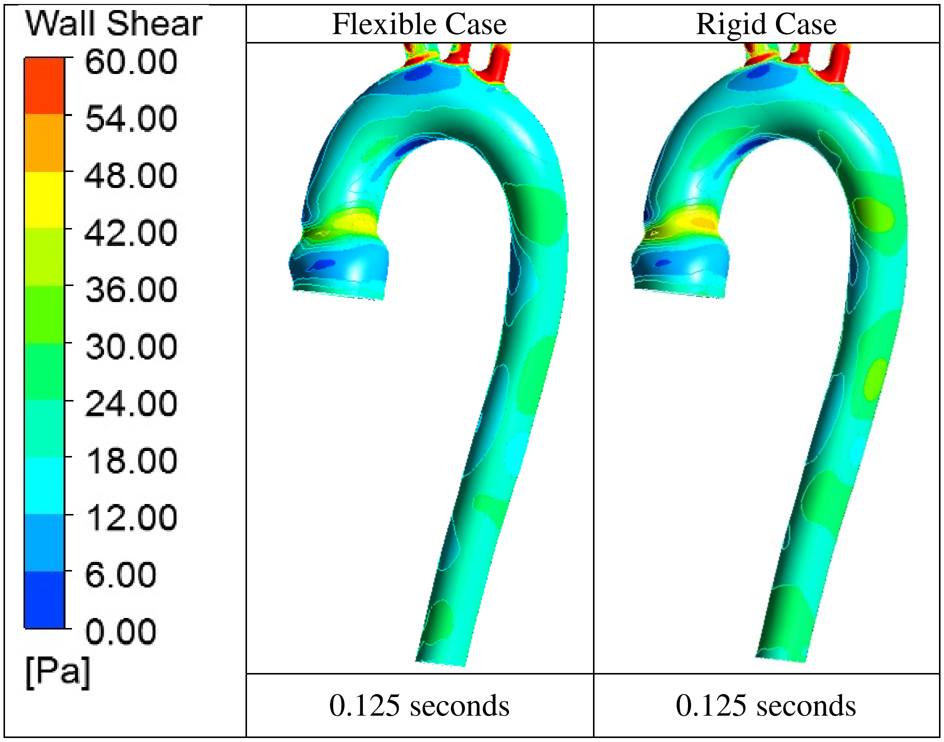

Figure 34: Peak wall shear stress values in the rigid case were seen during peak systole, reaching maximum values of 65 Pa at the branches. Views are anterior, flexible case (left) and rigid case (right). Values are 12% lower in the compliant case at this timestep.

4.3 Quasi Steady Flow, Rigid Vessel Wall

Quasi steady flow simulations with a rigid geometry are run to compare with the transient rigid case to see if a quasi steady flow case can be used for investigating inlet motion. Early, peak and late systole timestep (0.0625s, 0.125s, 0.3125s) quasi steady cases are investigated, as they are where the majority of flow occurs. Simulation details for each case can be seen in Sections 3.4.1 and 3.4.3.

4.3.1 Flow Patterns

The flow patterns in the quasi steady rigid wall cases are much more similar to each other than the fully transient case (Figure 35). The quasi steady t=0.3125 case is nearly identical to the quasi steady t=0.0625 second case as the inlet velocities are less than 0.1 m/s different. It is expected that the quasi steady results do not show the evolution of the transient flow, given the flow residence times in the aorta (at peak inlet flow, the mean residence time is about 0.15 s, comparable to the time from the start of the cycle to peak flow). The quasi steady cross-stream flow patterns are similar to those for the transient case around peak flow (0.125-0.25 s), as can be seen in Figure 36 (and in comparison of Figure 35 with Figure 32 and Appendix B - Transient Flow, Rigid Wall).

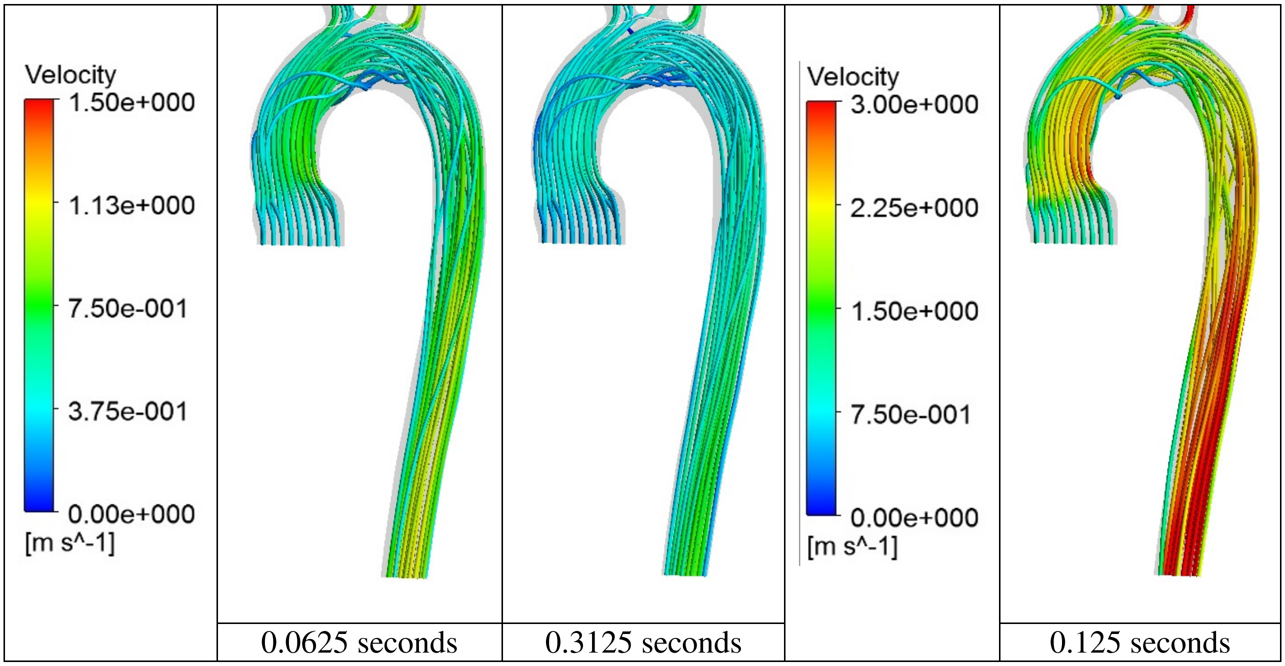

0.0625 seconds 0.3125 seconds 0.125 seconds

Figure 35: Flow patterns in the quasi steady, rigid wall case showing helical flow in the aortic arch and parallel flow near the aortic inlet.

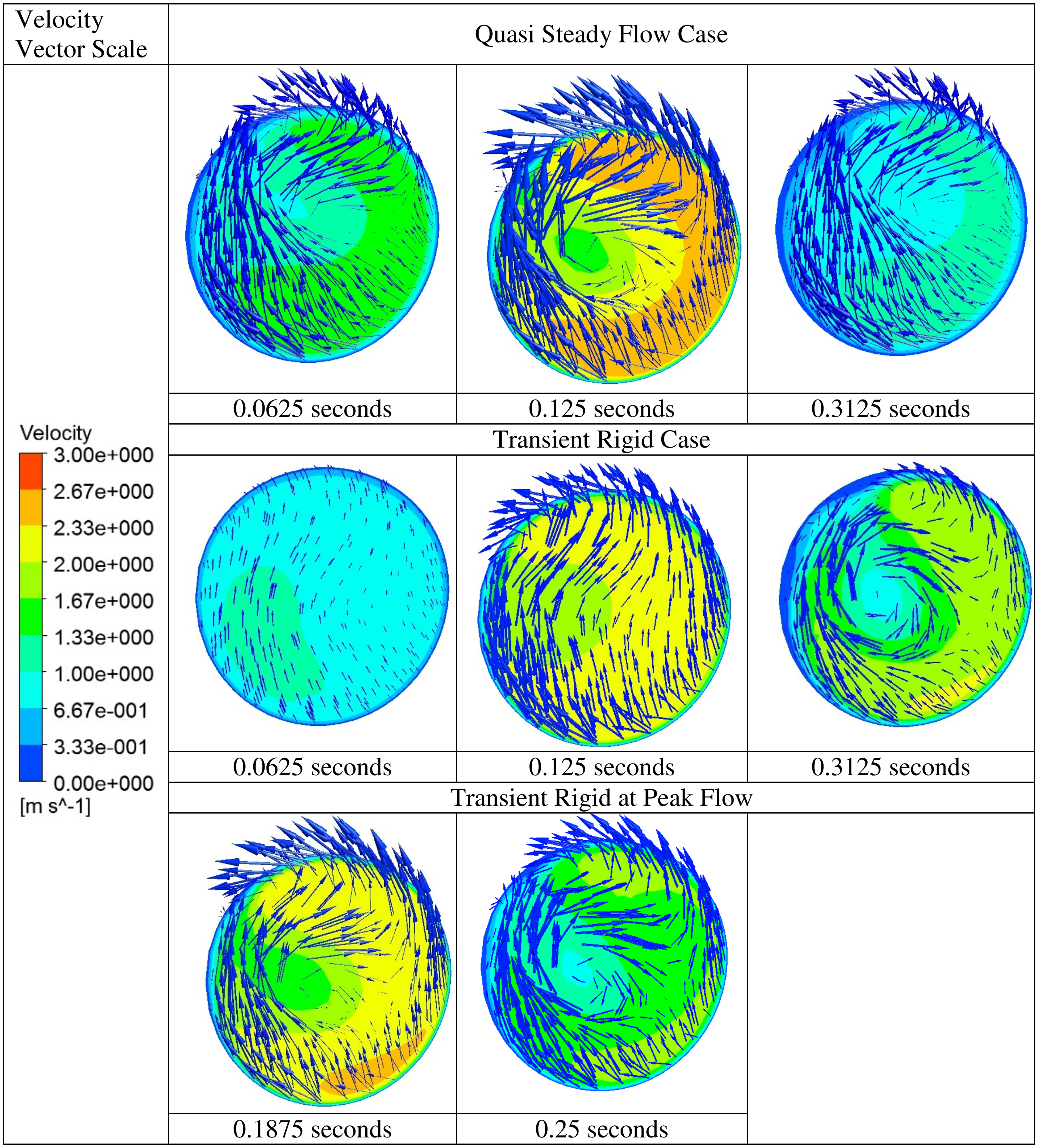

Figure 36: Velocity contour plots (scale showing total velocity) and profiles for each quasi steady flow timestep of the descending arch showing comparison to equal timesteps of the rigid case and also to corresponding lead timesteps of the rigid case.

Velocity profiles in the quasi steady flow case exhibit an M-shaped profile, similar to the transient case. All locations have slightly more non-uniform profiles during early and peak systole and more uniform in late systole in the quasi steady flow case, due to the quasi steady approach not capturing the development and growth of the helical and cross stream flows.

The quasi steady approach does capture the gross features of the transient flow (i.e. cross-sectional, helical flow). However, it is unable to resolve the transient development of these structures due to the rapid changes of the inlet flowrates in comparison to the overall residence times.

4.3.2 Wall Shear Stress

Values of WSS are slightly lower (5%) for the quasi steady flow case in both the 0.0625 (Figure 37) and 0.325 timesteps and slightly higher (5%) in the 0.125 timestep. This is again almost certainly due to the under-estimation of crossstream velocities by the quasi steady approach for the early and late systole, and the over-estimation of crossstream flows at t=0.125s. The locations of peak WSS remain the same for both the quasi steady flow and transient cases.

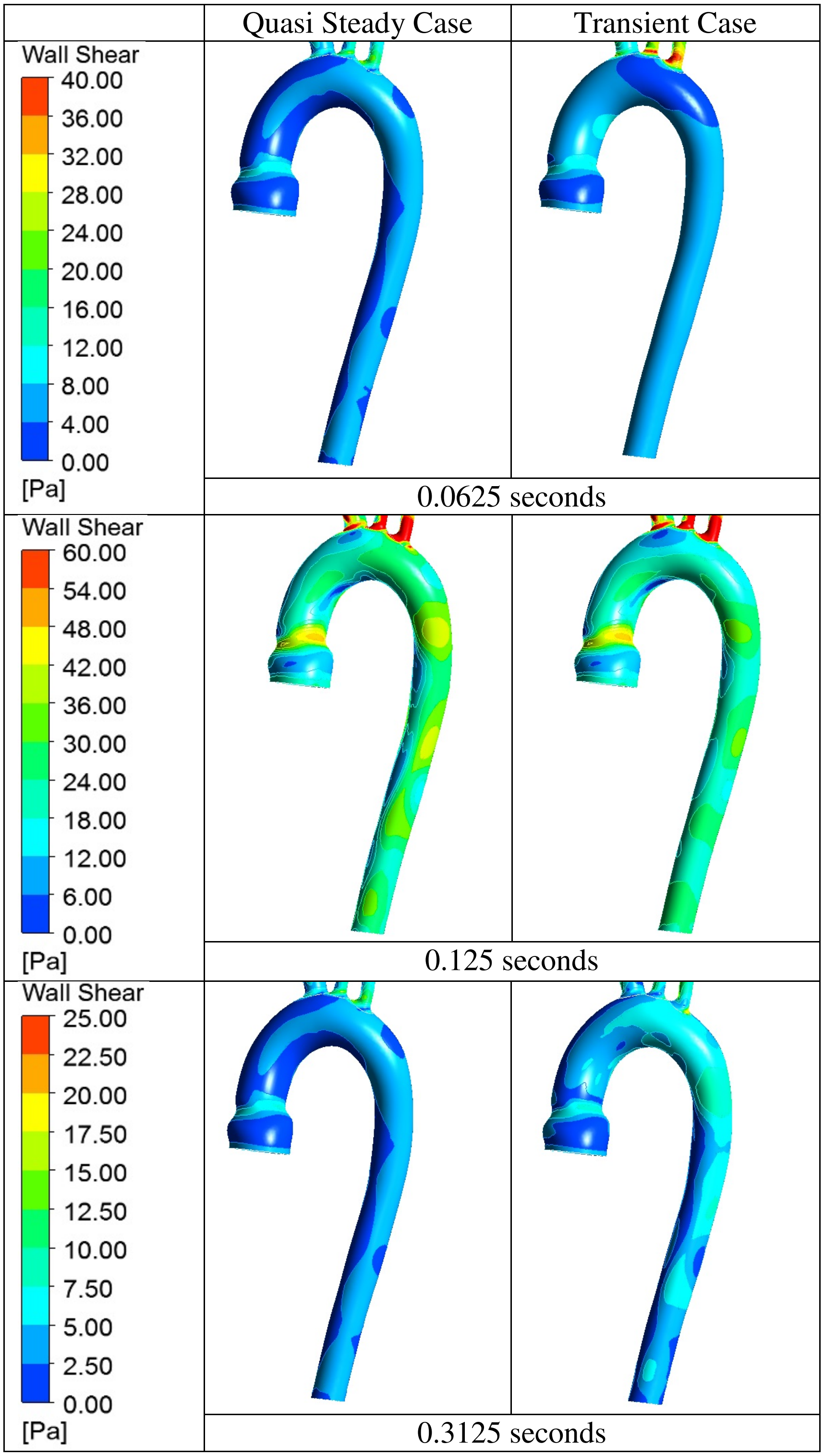

Figure 37: Wall shear stress values shown during early, peak and late systole for both the quasi steady case (left) and transient case (right), showing the slightly higher WSS in the quasi steady flow case during early and peak systole and slightly lower during later systole.

4.4 FEA Compliant Wall with Inlet Motion

Very little research has been conducted on the inclusion of inlet motion of the aorta in CFD studies, with only one work by Jin et al [14]. In this subsection, the total deformations resulting from the aortic pressure and addition of inlet motion are investigated to validate the reasoning behind the inclusion of inlet motion to aortic CFD models.

4.4.1 Deformation due to Pressure

The deformation of the transient flexible wall FSI case was discussed in Section 4.2.1. In this section, total deformation (i.e. displacement magnitude) is defined at each point around the ascending aorta, descending arch and descending aorta sections. Circumferential averages of this total displacement are show in Figure 38 through the cardiac cycle. The aorta expands the greatest amount in the ascending aorta, reaching a maximum of 0.55 mm. As expected, total deformation along the aorta decreases as the diameter decreases along the length travelling proximal to the heart, with deformations ranging from 8-10% of the diameter of the aorta.

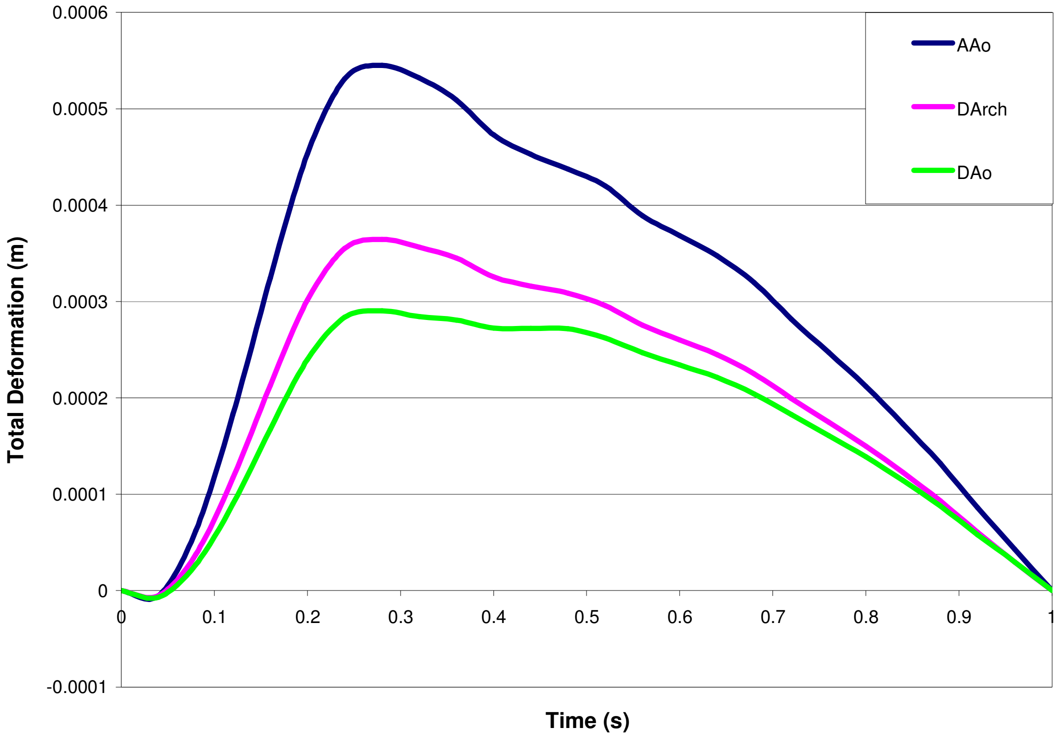

Figure 38: Total deformation (circumferential average) in the ascending aorta, descending aortic arch and descending aorta due to internal pressure and flow in the flexible wall simulation.

4.4.2 Deformation due to Inlet Motion

The results of the FEA simulation of the aorta wall with inlet heart motion as specified in Section 3.1.6 can be compared to the pressure/flow based deformations. Inlet motion results in much larger deformation of the aorta than the pressure/flow deformation in the ascending aorta and descending arch as seen in Figure 39 and Figure 40. With the addition of inlet motion, the ascending aorta experiences a total wall deformation up to 14.7 times larger than the fixed inlet pressure case. The descending arch also experiences much larger deformation change due to inlet motion, albeit slightly smaller, up to 4.7 times greater than the fixed inlet pressure case.

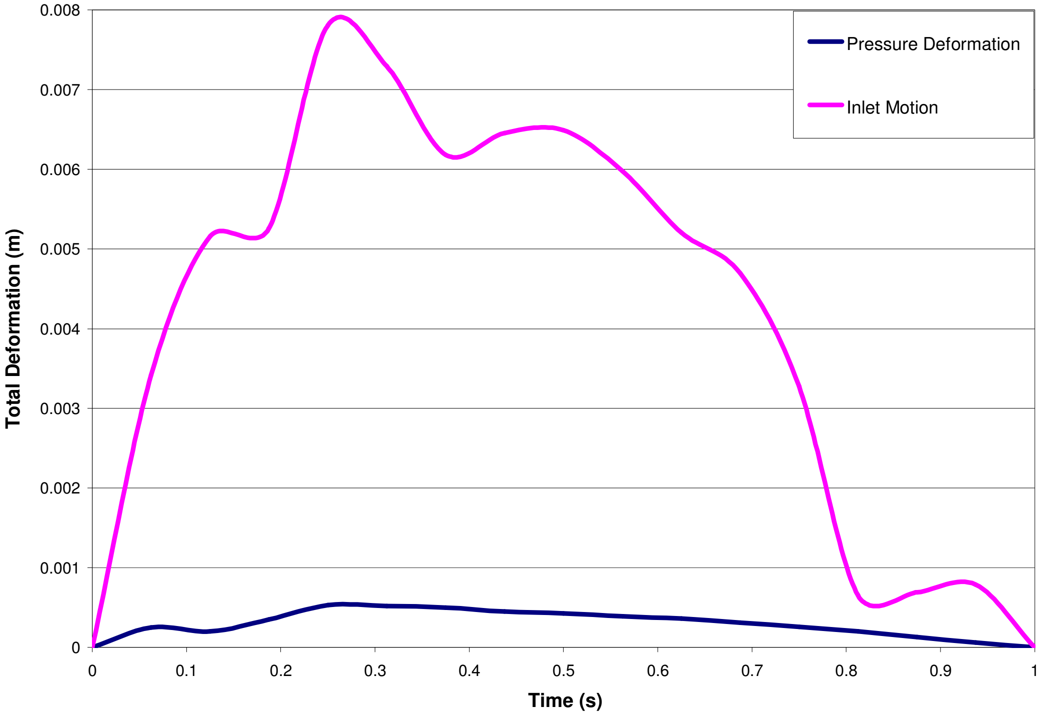

Figure 39: Total deformation in the ascending aorta due to pressure/flow (blue) and inlet motion (pink) for a flexible wall FEA simulation.

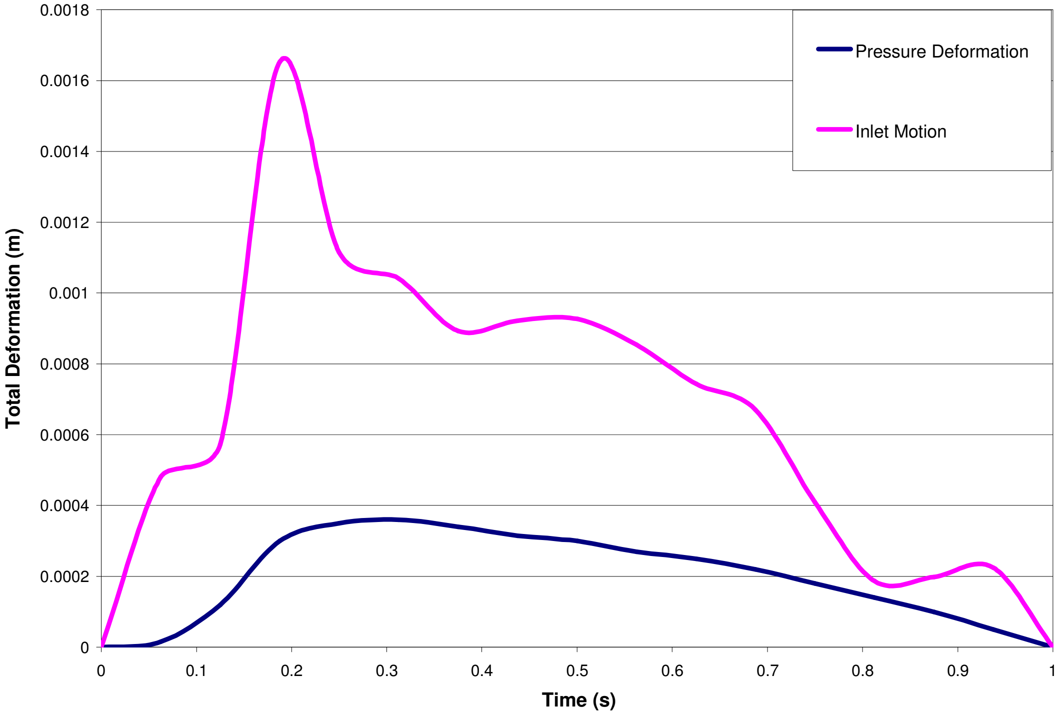

Figure 40: Total deformation in the descending arch due to pressure/flow (blue) and combined inlet motion (pink) for a flexible wall FEA simulation.

The descending aorta, unlike the ascending aorta and descending aortic arch experiences both increased and decreased total deformation over the cardiac cycle, as compared to the pressure/flow case. During systole, the descending aorta experiences up to 1.3 times larger total deformations as a result of the applied inlet motion when compared to the pressure/flow case. During diastole, the deformation from the inlet motion drops below that of the pressure/flow case by up to 1.5 times. From these FEA simulations, it is obvious that the addition of inlet motion results in a significant increase of total deformation of the aorta in the ascending aorta and ascending arch. Based on this finding, a CFD simulation including heart motion at the inlet of the aorta is deemed important to investigate the effects the increased deformation will have on the blood flow.

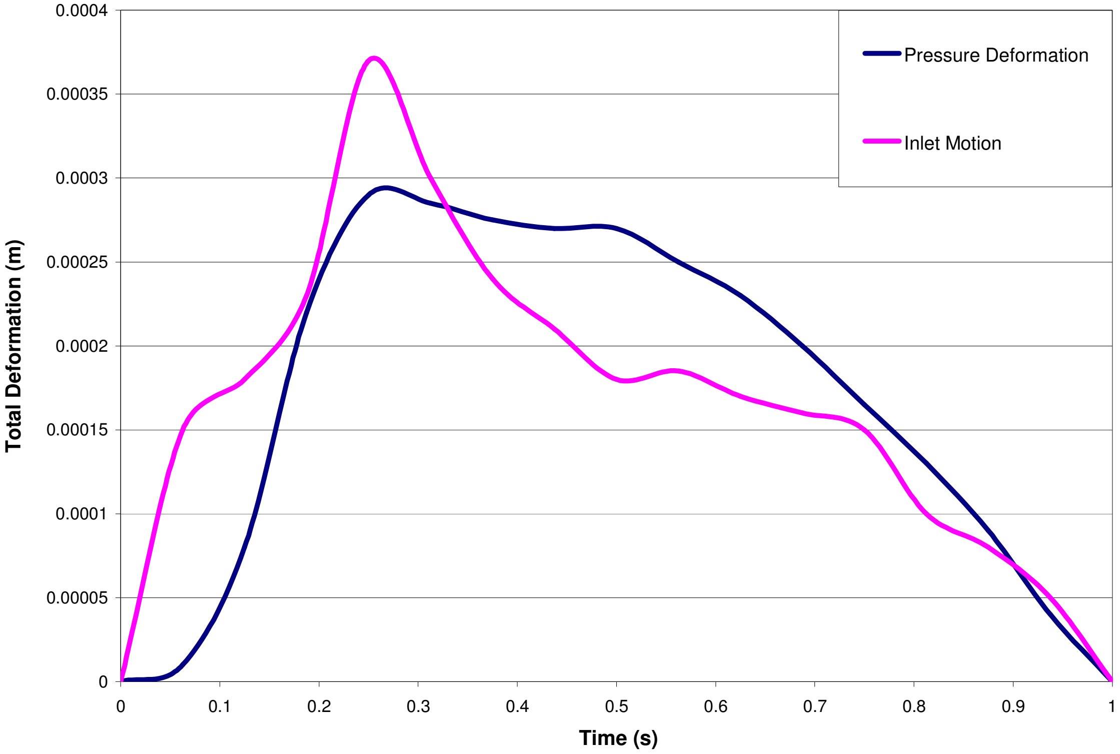

Figure 41: Total deformation in the descending aorta due to pressure/flow (blue) and inlet motion (pink) for a flexible wall FEA simulation.

4.5 Quasi Steady Flow, Inlet Motion

Quasi steady flow simulations using the deformed geometry are compared to a quasi steady flow simulation with the original geometry to investigate the effects of aortic inlet motion on the flow patterns in the aorta. Simulation details for each case are located in Section 3.4.3 and 3.4.4. Quasi steady flow simulations are used due to limitations in the FSI coupling of the CFD and FEA solvers with applied inlet motion, as described in Section 3.3. As discussed in Section 4.3, quasi steady flow cases cannot be directly compared to the corresponding transient cases. However, comparing the quasi steady case with inlet motion deformed geometry to the quasi steady rigid case should provide some rough indication of the effects of the inlet motion on the flow.

4.5.1 Flow Patterns

As discussed in the previous section, the inlet motion's primary effect is in deforming and elongating the ascending aorta and arch. Deformations in the descending aorta are much more limited due to its secure attachment to the spine and encasement by thoracic cavity tissues. This deformation and the resulting quasi steady flow can be seen in Figure 42. It should be noted that due to the deformation the late systole case (t=0.3125 s) does not match the early systole case (t=0.0625s) as was seen in the quasi steady rigid wall results.

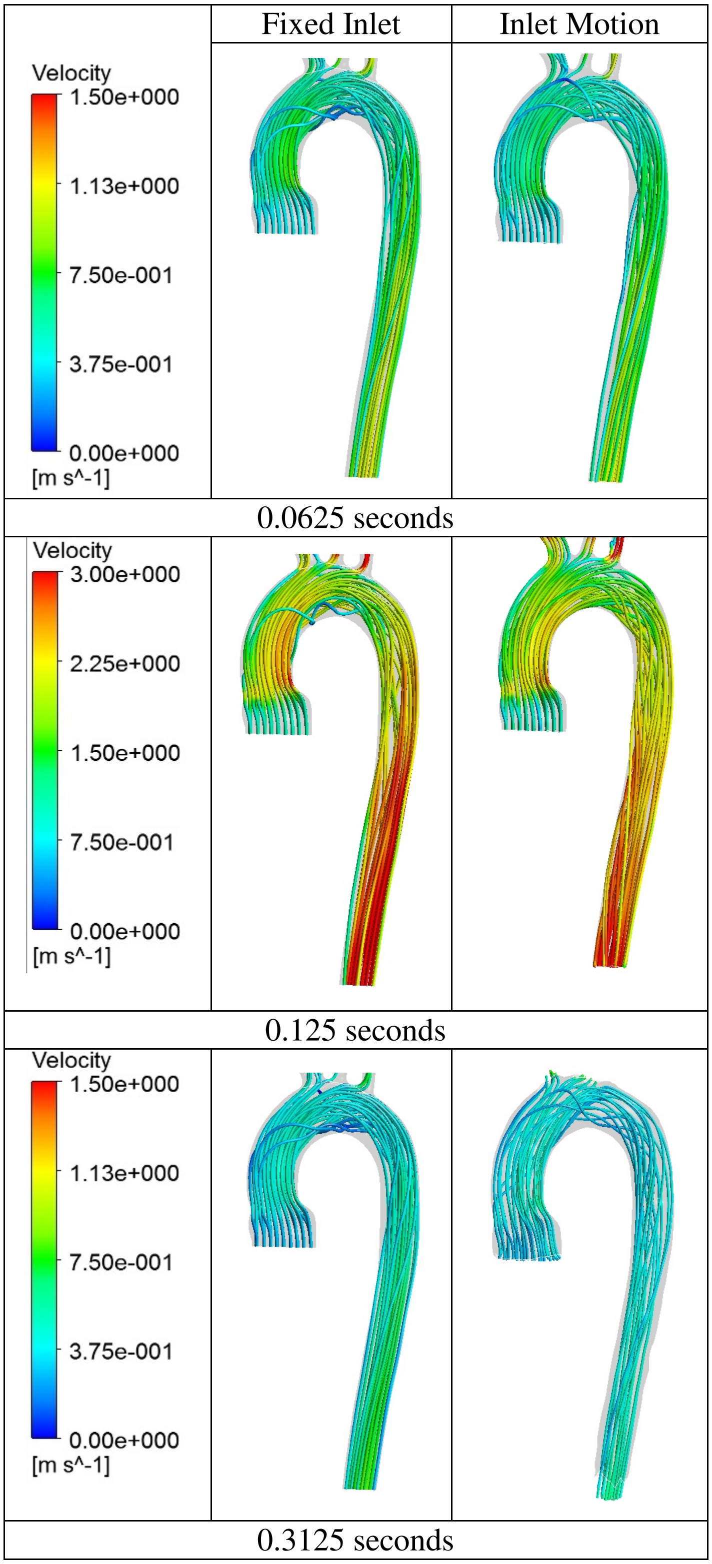

Figure 42: Streamlines for the quasi steady flow cases with a fixed inlet (left) and the deformed geometries due to inlet motion (right). Timesteps from top to bottom are0.0625s, 0.125s, 0.3125s. Streamlines are coloured by the total velocity magnitude. Note the change in scale at peak systole (t=0.125 s).

Figure 43 shows crossflow patterns comparing the quasi steady rigid and deformed cases. In general, the rigid and deformed flow patterns are very similar in early systole and late systole; however, in the quasi steady flow case with the deformed geometry, the crossflow velocity magnitudes are about 20% lower in the ascending aorta and descending arch. In the deformed elongated ascending aorta, the parallel flow from the uniform inlet is maintained considerably farther up (ending around the arch), a distance that is farther than the amount of the elongation.

At peak systole, velocity magnitudes and flow patterns are significantly different between the two cases. In the ascending aorta and descending aorta, the crossflow patterns are again similar but with reduced magnitudes in the deformed geometry case. However, in the arch, the helical flow seen in the rigid geometry (and in the fixed inlet fully transient case) is not present. This is significant as helical flow has been a key feature seen in previous CFD simulations, and if much of its presence relies on the fixed inlet geometries, this is an obvious limitation with the use of fixed inlet simulations. This important finding should be explored in future work involving aortic simulations.

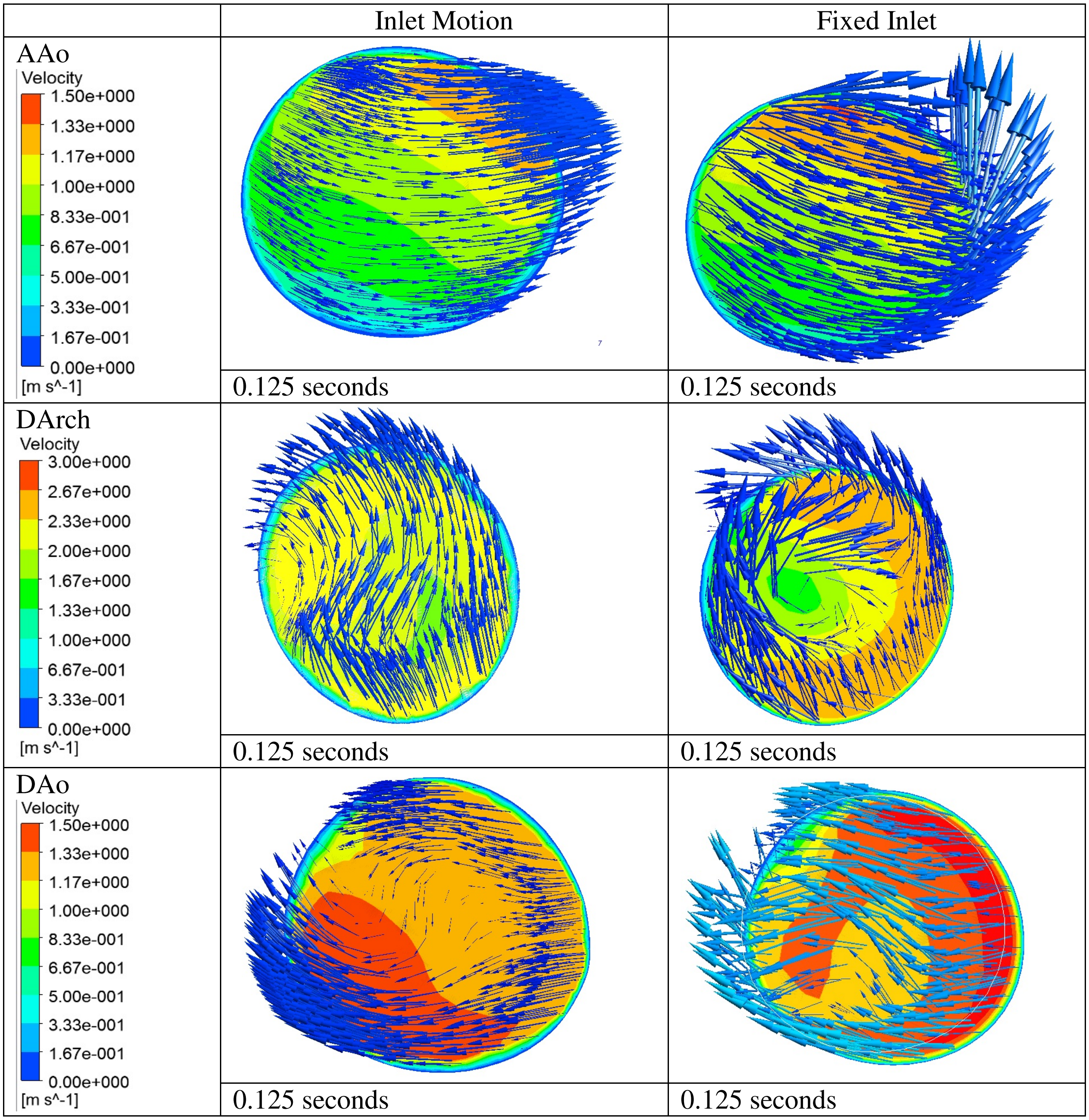

Figure 43: Flow patterns during peak systole for both quasi steady flow cases showing the lower velocity and slower helical flow development in the motion (deformed) case.

4.5.2 Wall Shear Stress

Differences in the wall shear stress can also be noted between the non-deformed and deformed quasi steady cases. The WSS is significantly lower in the deformed geometry case across all timesteps. This is expected as the total velocity magnitudes are lower across all timesteps due to lower cross flows. In early systole, WSS is 20% lower in the deformed case with peak values seen on the anterior ascending aorta and along the descending aorta. This is significantly different to the non-deformed case where values are higher on the anterior and posterior arch and along the descending aorta, again hypothesized to be due to the changes in the cross flows.

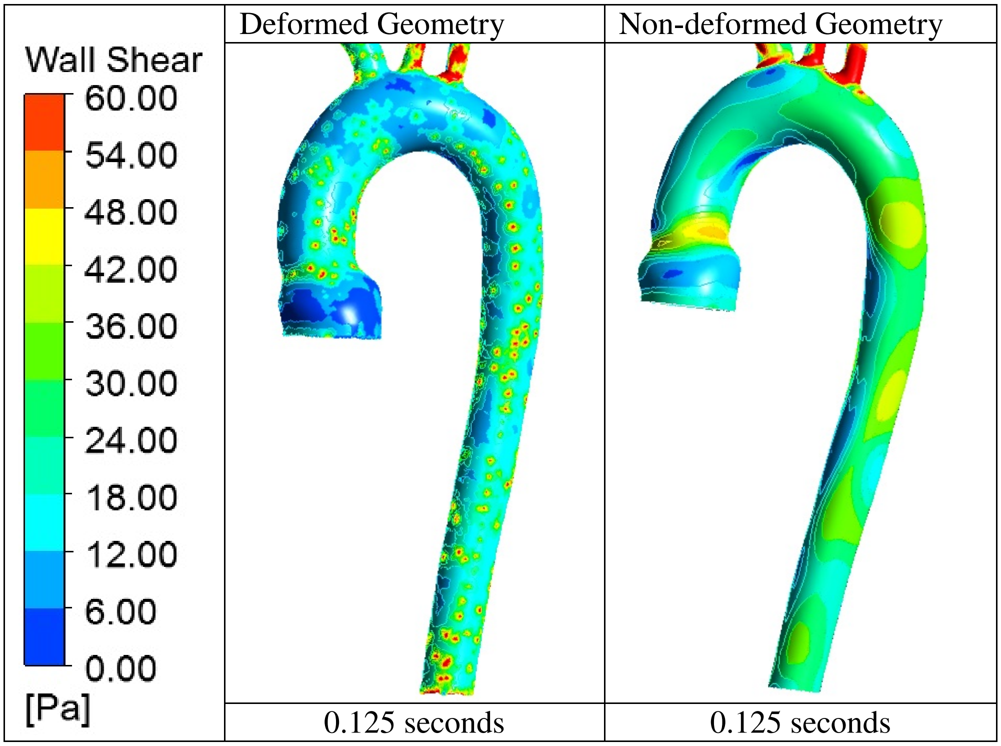

Figure 44: Wall shear stress values at peak systole for both the deformed and non-deformed cases showing higher values in the non-deformed case.

At peak systole in the deformed case, WSS is distributed fairly uniformly along the aorta with lower values seen on the posterior arch and posterior ascending aorta. In comparison the non-deformed case has significantly higher (40%) WSS values (Figure 44) that peak at the superior aortic sinus and along the anterior descending aorta. In late systole, WSS values are 30% lower in the deformed geometry case with peak values seen on the anterior ascending and descending aorta. In contrast, peak values in the original case occur along the aortic arch and descending aorta, on both the anterior and posterior aorta. It is important to note that the localized peaks in WSS in the deformed geometry case (e.g. in Figure 44) are due to non-smooth geometries resulting from taking the FEA calculated deformed geometry through triangular surface meshing (in GeoMagic) to create the fluids geometry. The surface peaks in these non-smooth geometries are small (0.15 mm max, [less than 1% of the aorta diameter]) so have little if any effect on the bulk flow patterns, but are clearly apparent in the WSS (these effects have been considered in the trends discussed above).

4.6 Transient Flow, Compliant Wall with MRI Inlet Flow

Work done previously has been limited to inlet flows that although time varying, are uniform over the inlet with the exception of recent work completed by Stalder et al [140] and Lantz et al [91]. The effects of changing inlet flow from a uniform profile to a 3D MRI inlet flow profile are investigated through comparing the compliant uniform profile case to the compliant case with MRI flow. This comparison highlights the importance of inlet flow non-uniformity. Simulation details for each case are located in Sections 3.4.2 and 3.4.5.

4.6.1 Flow Patterns

Comparing to in vivo MRI flow development patterns, the results from the MRI simulation agree through the entire pulse sequence for the ascending aorta, descending arch and descending aorta [41, 46]. In addition, the MRI simulation results for flow development and helical flow patterns compare well with CFD data presented in the ascending aorta simulation conducted by Leuprechet [90].

Helical flow development occurs much earlier in the cardiac cycle in the ascending aorta (Figure 45) and descending aortic arch compared to the uniform profile case, but is fairly consistent in location and direction. In the ascending aorta, strong clockwise helical flow develops in the centre of the aorta at peak systole, whereas with the uniform inlet, this occurs only late in systole (t~0.3 seconds). Thereafter, the crossflow patterns are roughly similar between the MRI and uniform inlet cases, although the crossstream velocities are lower for the uniform inlet case. This behaviour could be expected given the strong crossflows imposed at the inlet by the MRI data, in contrast to the zero crossflow velocities of the unrealistic uniform inlet.

	MRI Case	Uniform Profile Case
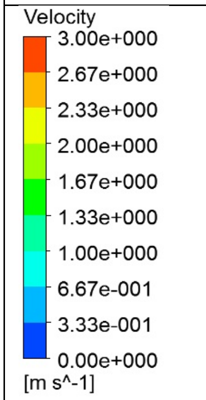Velocity 3.00e+000 2.67e+000 2.33e+000 2.00e+000 1.67e+000 1.33e+000 1.00e+000 6.67e-001 3.33e-001 0.00e+000 [m s^-1]	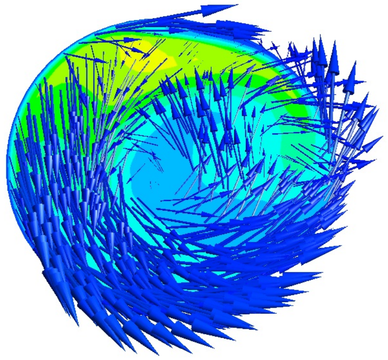	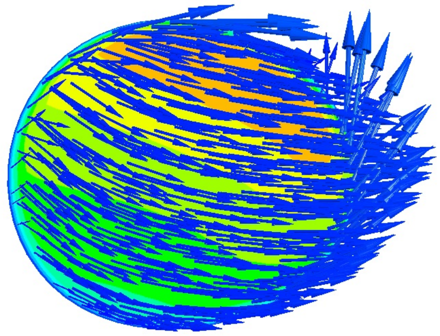
	0.1250 seconds	0.1250 seconds

Figure 45: Flow patterns showing earlier helical flow development in the ascending aorta in the MRI case.

Helical flow develops in the descending aortic arch at peak systole for both MRI and uniform inlet cases. For the MRI case, after peak systole clockwise helical flow develops in the middle of the aorta, unlike the uniform inlet case where the flow is more consistently counter clockwise. In the descending aorta the MRI and uniform inlet cases experience similar development of clockwise helical flow shortly after peak systole. The disintegration of the helical structure during late diastole is slightly different than the uniform profile case, where it persists through diastole.

The inlet velocity used in the MRI case exhibits a strong jet formation during early and peak systole; a result of the aortic valve leaflets opening. The peak flow in the jet is higher than the average flow in the uniform profile case; however, when averaged across the inlet plane, the MRI case has much lower normal velocity (~50% lower) than the uniform profile case. This results in lower streamwise velocity values in the MRI case along the length of the aorta for all timesteps, and, as the crossstream velocity decreases in the descending aorta, lower total velocities as shown in Figure 46.

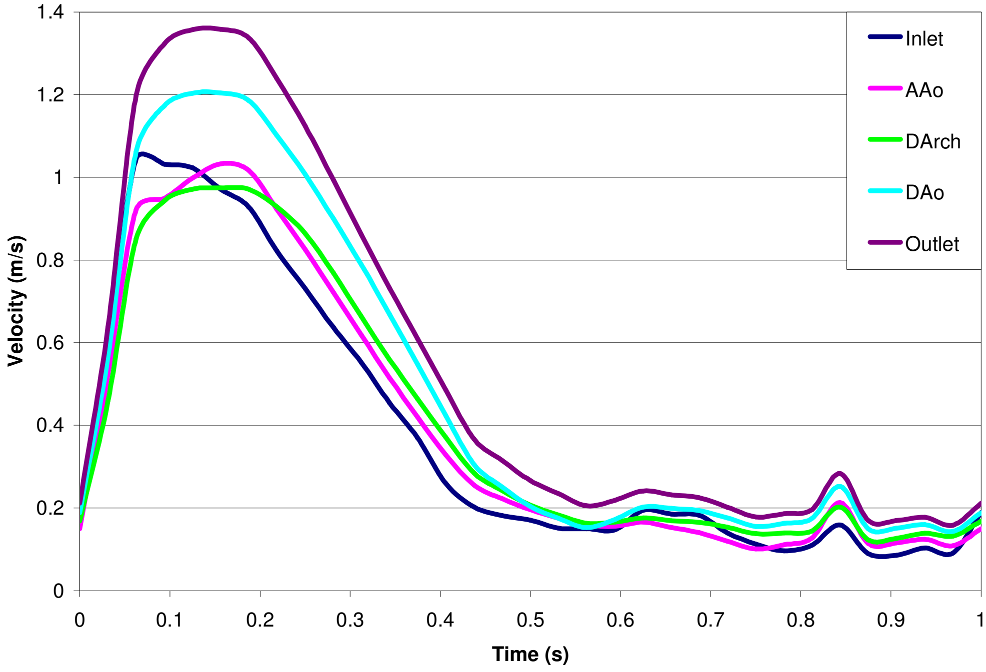

Figure 46: Velocity profiles at the inlet and all outlets of the aorta in the MRI case.

Velocity profiles at the ascending aorta, descending arch and descending aorta are investigated and compared to the uniform inlet case. It is found that the M shape is significantly more pronounced in the ascending aorta in the MRI case. This can be attributed to the non-uniform MRI data used at the inlet. The descending arch and descending aorta experienced similar profiles to the uniform profile case through early, peak and late systole.

4.6.2 Pressure

The pressure profile during late systole and diastole of the MRI case is similar to the uniform profile case; however, the fluctuations are significantly less in the MRI case during diastole. This difference could be the reason the helical flow development in diastole is significantly different in the uniform profile case compared to the MRI case. There is also a difference at peak systole, where the pressure is significantly lower in the MRI case by 15%. This is due to the difference in average inlet velocity between cases. In the MRI case, the average velocity at the inlet is lower (although the velocity of the jet is a lot higher) and results in a lower pressure profile.

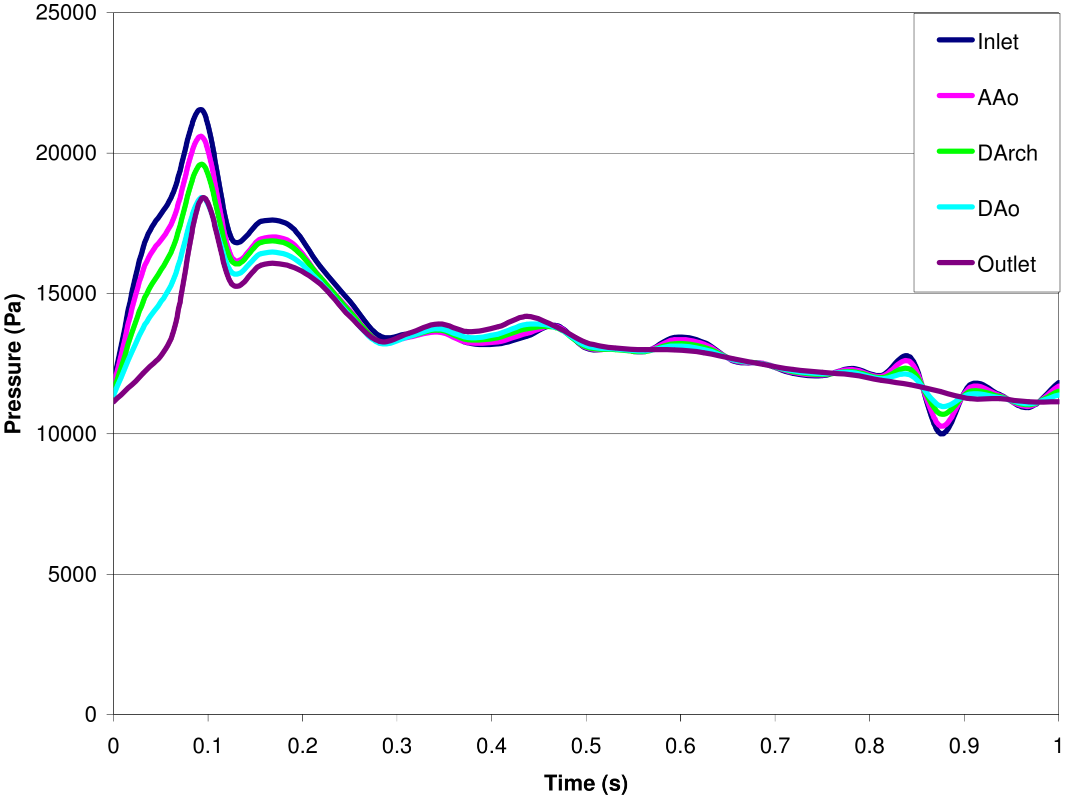

Figure 47: Pressure profile for the MRI flow case at select locations along the aorta through a full cardiac cycle.

4.6.3 Wall Shear Stress

Values of WSS are significantly different in the MRI case as compared to the uniform profile case. During early systole, the branch insertions, superior aortic sinus and anterior ascending aortic wall experience higher values of WSS in the MRI case, shown in Figure 48. The aortic sinus experiences nearly four times as high WSS, with the branches and ascending wall seeing one and a half times more. This can be attributed to the higher magnitude of the jet flow occurring in the MRI inlet flow during early systole.

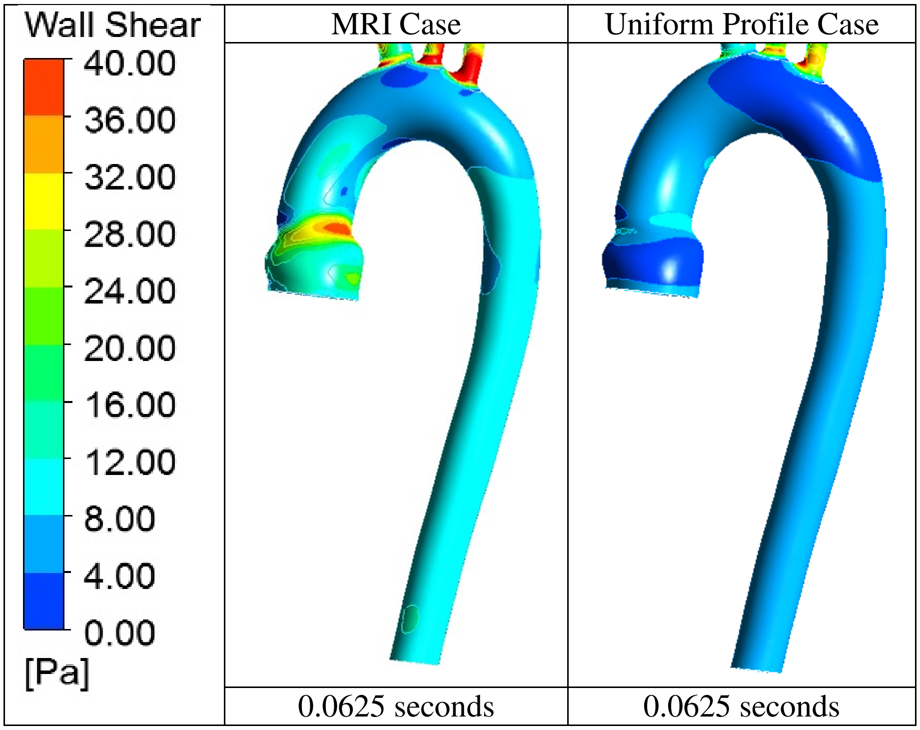

Figure 48: Wall shear stress values for both the MRI inlet and the uniform inlet cases showing increased values in the MRI case in early systole (0.0625s) due to jet flow.

At peak systole, slightly lower values were seen at all points along the aorta in the MRI case, due to the lower velocity gradient at the wall. In late systole, WSS values are similar in both MRI and uniform profile cases, with the only difference seen at the superior aortic sinus. WSS values for MRI results are limited in the literature; however, in comparison to the work of Frydrychowicz [48], the values of WSS are similar to the work in this thesis.

4.7 Outflow Validation

Outlet flow through the aorta exits through four outlets, the brachiocephalic artery, left common carotid artery, left subclavian artery and the aortic outlet in the descending aorta. The percentage outflow through the branches and outlet need to match physiologic data in order for the CFD model to be validated [117]. Several flow percentage data sets have been published [29, 67, 111] outlining outflow distribution per outlet. As can be seen from Table 12, the outlet takes the bulk of the flow at 70%, the brachiocephalic taking 17% and the left common carotid and left subclavian almost equally sharing the remain. Outflow data for each case presented in this thesis is listed in Table 12 and values agree with literature [48, 67, 82, 89] .

Brachiocephalic	Left Common Carotid	Left Subclavian	Outlet	Author	Year
-	-	-	80%	Wood [68]	2001
23.1%	8.3%	6.1%	62.5%	Mori [86]	2002
5%	5%	5%	85%	Shahcheraghi [87]	2002
15%	5%	10%	70%	Svensson [67]	2006
-	-	-	68%	Frydrychowicz [48]	2009
11.3%	6.8%	4.5%	77.4%	Wen [89]	2010
15%	7.5%	7.5%	70%	Benim [82]	2011
27%	6%	12%	55%	Brown, A. [29]	2011
13%	4%	5%	78%	Brown, S. [116]	2012
12%	9%	4%	76%	Current, Rigid Case	2013
12%	9%	4%	76%	Current, Flexible Case	2013
11%	10%	7%	72%	Current, MRI Case	2013
13%	10%	8%	69%	Current, Quasi steady flow	2013
13%	11%	9%	67%	Current, Quasi steady flow Motion	2013

Table 12: Percentage outflow distribution, averaged over one cardiac cycle.

When comparing mass outflow over time as a transient entity, the MRI case has more physiologically correct mass outflow in the branches and outlet as compared to cases run with the uniform inlet flow profile. This is due to the Fourier approximation of the uniform inlet flow that even with a 10th order approximation overestimates the outflow due to the harmonics visible in diastole. Flow in the MRI case matches more closely with the quasi steady flow states that use a constant inlet flow value taken from the Fourier series waveform during systole and are therefore independent from the harmonics.

5 Conclusions and Future Work

5.1 Conclusions

Wall flexibility, effects of heart motion and a physiologically relevant flow profile were investigated in this thesis, with the latter two found to have significant impact on blood flow in the aorta. The addition of wall flexibility resulted in diameter changes of 8-10% due to pressure expansion of the wall during the cardiac cycle. Closer to the heart the wall deformation was higher, reaching a maximum of 0.55 mm, while deformation fell slowly distally along the aorta reaching a minimum of 0.37 mm at the descending aorta. Outlet pressure was slightly lower (10%) than a rigid wall case, due to the energy absorption in the walls. Flow patterns and flow profile shapes were unchanged in comparison to the rigid case, while velocity magnitudes were 15-20% lower in the flexible case due to area increase from expansion of the wall, all of which agreed well with models reviewed in the literature [27, 30, 33, 56, 67, 69, 139].

In order to investigate the effects of heart motion on blood flow in the aorta, an FEA simulation was first conducted to compare the total wall deformation of a moving inlet case with a fixed inlet case. It was found that wall deformation in the ascending aorta of the moving inlet case was up to 14.7 times larger than that of the fixed inlet pressurized flow case. Motion effects continued into the descending arch, where wall deformation was up to 4.7 times larger in the moving inlet case. Wall deformation in the descending aorta was up to 1.3 times larger in systole, and then dropped to up to 1.5 times lower in diastole than the fixed inlet pressure/flow case. The significant increase in wall deformation in the ascending aorta and descending arch provided justification to explore a full FSI moving inlet aortic flow case. Due to difficulties with ANSYS and its current limited capability to perform FSI with moving inlets (combined movement in the transverse and perpendicular directions) and inlet flow, quasi steady flow cases were run to compare flow results between fixed and moving inlet aortic models. A quasi steady flow fixed inlet case was run to determine if flow patterns, flow development and flow profiles were similar to a corresponding transient case. Flow patterns in the quasi steady case were found to be more similar to each other than to the fully transient case due to similar inlet velocities applied at early and peak systole. The quasi steady cases also did not show the evolution of the transient flow as a result of the flow residence time in the aorta that was calculated to be approximately 0.15 seconds and was comparable to the start of the cardiac cycle to peak flow. At peak systole; however, the quasi steady flow patterns were similar to those of the transient case at peak flow. The quasi steady case captured the cross-sectional and helical flow features of the transient case, but was unable to resolve their transient development. A quasi steady case using a geometry deformed due to inlet motion was then run to compare to the quasi steady flow case with the fixed inlet. The deformed geometry flow patterns at early and late systole did not match, as was seen in the fixed inlet quasi steady case,, which was a result of the deformation in the aorta. Crossflow magnitudes were found to be 20% lower in the ascending aorta and descending arch in the deformed geometry case. At peak systole, parallel flow was maintained in the ascending aorta and up to the arch in the deformed case,, which was not seen in the fixed inlet case, or other fully transient cases. This is a significant finding as helical flow has been a key feature in previous CFD simulations using fixed inlet geometries and is an obvious limitation of the use of fixed inlets. This important finding should be investigated in future in a full FSI simulation to fully determine the effects of inlet motion on aortic blood flow across the entire cardiac cycle.

The effect of addition of a physiologically relevant inlet flow profile was also investigated. A 3D blood flow profile was taken from MRI data and added as a boundary condition to a flexible wall simulation to compare to a similar simulation with a uniform inlet profile. Helical flow development was found to occur earlier in both the ascending aorta and descending arch in the MRI case (peak systole vs. late systole in the uniform profile case). Crossflow velocities were lower for the uniform case, which was expected given the strong crossflows imposed at the inlet of the aorta by the MRI data. This inlet velocity exhibited a strong jet formation during early and peak systole that was higher than the average flow in the uniform case; however, when averaged across the inlet plane, the MRI case had a much lower normal velocity. This resulted in lower streamwise velocity values in the MRI case compared to the uniform profile case. WSS values were also lower as a result of the decreased streamwise velocity in the MRI case and contrastingly higher in the MRI case in the aortic sinus due to the jet profile of the flow. The velocity profile and geometry were not scaled for the MRI case and a direct comparison (transform non-uniform profile to plug flow and simulate with MRI geometry) was not made; however, the results of the MRI simulation agreed well with literature [41, 46] and demonstrated that addition of a non-uniform inlet flow profile that was physiologically relevant changes flow patterns, pressure profiles and WSS and should be included in future FSI simulations.

From the research conducted, it is clear that the addition of heart motion at the aortic inlet and 3D physiologically relevant inlet flow profiles result in significant changes to aortic blood flow patterns and flow development. It is recommended that both of these conditions are included in future FSI simulations to more accurately portray blood flow in the aorta.

5.2 Future Work

Although this work significantly advances aortic CFD studies with the addition of inlet motion in quasi steady flow results, it is strongly suggested that work be continued to include transient FSI cases. Other changes that may affect the flow include modeling turbulence, or transition to turbulence and using windkessel outlet conditions to include permeability and porosity of downstream arteries and arterioles. Addition of spring support stiffness variation along the length of the aorta wall and including a layered wall with a non-hookian assumption may also change the behaviour of the aorta wall structure with motion and in turn the flow development in the aorta. The addition of these suggestions to future simulations is currently hindered by present CFD software limitations and computational power; however, in future, software development and ease of complex simulation completion will enable more physiologically and anatomically correct simulations of blood flow in the aorta.

6 Terms

PWV - pulse wave velocimetry

Visceral - to the organs

Proximal - away from extremity

Distal - toward extremity

Posterior - back

Anterior - front

Superior - up

Inferior - down

Deep - within the body

Superficial - towards the surface

Artery - carry oxygenated blood away from the heart

Veins - return de-oxygenated blood to the heart

Elastin - elastic connective tissue

Collagen - fibrous connective tissue

Endothelium - continuous layer of cells lining the entire cardiovascular system

Pericardium - fluid filled sac containing the heart

Diastole - relaxation phase of the cardiac cycle

Systole - contraction phase of the cardiac cycle

Ex vivo - organs/tissues tested and examined external to the body, not in a cultured environment

In vivo - testing/examination of organs/tissues within the body

Ex vivo - testing/examining of organs external to the body in simulated body conditions

Aneurysm - blood filled balloon like swelling of the blood vessel wall.

Stenosis - abnormal vessel narrowing/constriction

Right hand flow - counter-clockwise when viewing the aorta from the anterior direction

Left hand flow - clockwise flow when viewing the aorta from the anterior direction

AAo - Ascending Aorta

DAo - Descending Aorta

DArch - Descending Arch

7 References

References

[1] W. O. Dictionary. (2013). *Definition of Aorta*. Available: http://www.websters-online-dictionary.org/definitions/Aorta.

[2] J. K. J. Li. Dynamics of the vascular system. pp. 257. 2004. Available: http://site.ebrary.com/lib/mcgill/Doc?id=10082175.

[3] H. Gray and C. D. Clemente. *Anatomy of the Human Body* 1985.

[4] MedFriendly. (2012). *Aorta*. Available: http://medfriendly.com/aorta.html.

[5] T. Poutanen, T. Tikanoja, H. Sairanen and E. Jokinen. Normal aortic dimensions and flow in 168 children and young adults. *Clin Physiol Funct Imaging. 23(4),* pp. 224-229. 2003.

[6] M. Cecconi, M. Manfrin, A. Moraca, R. Zanoli, P. L. Colonna, M. G. Bettuzzi, S. Moretti, D. Gabrielli and G. P. Perna. Aortic dimensions in patients with bicuspid aortic valve without significant valve dysfunction. *Am J Cardiol. 95(2),* pp. 292-294. 2005.

[7] H. Kahraman, M. Ozaydin, E. Varol, S. M. Aslan, A. Dogan, A. Altinbas, M. Demir, O. Gedikli, G. Acar and O. Ergene. The diameters of the aorta and its major branches in patients with isolated coronary artery ectasia. *Tex Heart Inst J. 33(4),* pp. 463-468. 2006.

[8] HowMed. (2009). *Aorta*. Available: http://howmed.net/anatomy/gross-anatomy/aorta/.

[9] H. Boudolas, C. Stefanadis and C. Machopoulos. *The Aorta: Structure, Function, Dysfunction and Diseases* 2008.

[10] G. J. Tortora and N. P. Anagnostakos. *Principles of Anatomy and Physiology* 1981.

[11] J. van Prehn, K. L. Vincken, S. M. Sprinkhuizen, M. A. Viergever, J. W. van Keulen, J. A. van Herwaarden, F. L. Moll and L. W. Bartels. Aortic pulsatile distention in young healthy volunteers is asymmetric: Analysis with ECG-gated MRI. *Eur J Vasc Endovasc Surg. 37(2),* pp. 168-174. 2009.

[12] S. Kozerke, M. B. Scheidegger, E. M. Pedersen and P. Boesiger. Heart motion adapted cine phase-contrast flow measurements through the aortic valve. *Magn Reson Med. 42(5),* pp. 970-978. 1999.

[13] L. M. de Heer, R. P. J. Budde, W. P. Mali, A. M. de Vos, L. A. van Herwerden and J. Kluin. Aortic root dimension changes during systole and diastole: Evaluation with ECG-gated multidetector row computed tomography. *Int J Cardiovasc Imaging. 27(8),* pp. 1195-1204. 2011.

[14] S. Jin, J. Oshinski and D. P. Giddens. Effects of wall motion and compliance on flow patterns in the ascending aorta. *J Biomech Eng. 125(3),* pp. 347-354. 2003.

[15] D. Mohan and J. W. Melvin. Failure properties of passive human aortic tissue .1. uniaxial tension tests. *J Biomech. 15(11),* pp. 887-902. 1982.

[16] D. Mohan and J. W. Melvin. Failure properties of passive human aortic tissue .2. biaxial tension tests. *J Biomech. 16(1),* pp. 31-44. 1983.

[17] C. S. Shah, M. J. Mason, K. H. Yang, W. N. Hardy, C. A. Van Ee, R. Morgan and K. Digges. High-speed biaxial tissue properties of the human cadaver aorta. Presented at ASME International Mechanical Engineering Congress and Exposition: Transportation. 2005, .

[18] C. S. Shah, W. N. Hardy, M. J. Mason, K. H. Yang, C. A. Van Ee, R. Morgan and K. Digges. Dynamic biaxial tissue properties of the human cadaver aorta. *Stapp Car Crash J 50*pp. 217-246. 2006.

[19] D. A. Vorp, B. J. Schiro, M. P. Ehrlich, T. S. Juvonen, M. A. Ergin and B. P. Griffith. Effect of aneurysm on the tensile strength and biomechanical behavior of the ascending thoracic aorta. *Ann Thorac Surg. 75(4),* pp. 1210-1214. 2003.

[20] W. W. Nichols, D. A. McDonald and M. F. O'Rourke. *McDonald's Blood Flow in Arteries: Theoretical, Experimental, and Clinical Principles* 2005.

[21] D. O. Craiem, F. J. Rojo, J. M. Atienza, G. V. Guinea and R. L. Armentano. Fractional calculus applied to model arterial viscoelasticity. *Latin American Applied Research 38(2),* pp. 141-145. 2008.

[22] N. Choudhury, O. Bouchot, L. Rouleau, D. Tremblay, R. Cartier, J. Butany, R. Mongrain and R. L. Leask. Local mechanical and structural properties of healthy and diseased human ascending aorta tissue. *Cardiovasc Pathol. 18(2),* pp. 83-91. 2009.

[23] D. Tremblay, T. Zigras, R. Cartier, L. Leduc, J. Butany, R. Mongrain and R. L. Leask. A comparison of mechanical properties of materials used in aortic arch reconstruction. *Ann Thorac Surg. 88(5),* pp. 1484-1491. 2009.

[24] J. P. Vande Geest, M. S. Sacks and D. A. Vorp. Age dependency of the biaxial biomechanical behavior of human abdominal aorta. *J Biomech Eng. 126(6),* pp. 815-822. 2004.

[25] J. P. Vande Geest, M. S. Sacks and D. A. Vorp. The effects of aneurysm on the biaxial mechanical behavior of human abdominal aorta. *J Biomech. 39(7),* pp. 1324-1334. 2006.

[26] J. Lantz, R. Gardhagen and M. Karlsson. Quantifying turbulent wall shear stress in a subject specific human aorta using large eddy simulation. *Med Eng Phys. 34(8),* pp. 1139-1148. 2012.

[27] C. A. Figueroa, I. E. Vignon-Clementel, K. E. Jansen, T. J. R. Hughes and C. A. Taylor. A coupled momentum method for modeling blood flow in three-dimensional deformable arteries. *Comput Method Appl M. 195(41-43),* pp. 5685-5706. 2006.

[28] W. B. Tay, Y. H. Tseng, L. Y. Lin and W. Y. Tseng. Towards patient-specific cardiovascular modeling system using the immersed boundary technique. *Biomed Eng Online 10(52),* pp. 1-17. 2011.

[29] A. G. Brown, Y. Shi, A. Marzo, C. Staicu, I. Valverde, P. Beerbaum, P. V. Lawford and D. R. Hose. Accuracy vs. computational time: Translating aortic simulations to the clinic. *J. Biomech. 45(3),* 2012. . DOI: 10.1016/j.jbiomech.2011.11.041.

[30] M. Bongert, M. Geller, W. Pennekamp, D. Roggenland and V. Nicolas. Transient simulation of the blood flow in the thoracic aorta based on MRI-data by fluid-structure-interaction. Presented at 4th European Conference of the International Federation for Medical and Biological Engineering (ECIFMBE). 2008, .

[31] M. Midulla, R. Moreno, A. Baali, M. Chau, A. Negre-Salvayre, F. Nicoud, J. Pruvo, S. Haulon and H. Rousseau. Haemodynamic imaging of thoracic stent-grafts by computational fluid dynamics (CFD): Presentation of a patient-specific method combining magnetic resonance imaging and numerical simulations. *22*2012.

[32] Y. Kim, S. Lim, S. V. Raman, O. P. Simonetti and A. Friedman. Blood flow in a compliant vessel by the immersed boundary method. *Ann Biomed Eng. 37(5),* pp. 927-942. 2009.

[33] F. Gao, Z. Guo, M. Watanabe and T. Matsuzawa. Loosely coupled simulation for aortic arch model under steady and pulsatile flow. *J Biomech Science and Eng. 1(2),* pp. 327-341. 2006.

[34] F. Gao, M. Watanabe and T. Matsuzawa. Stress analysis in a layered aortic arch model under pulsatile blood flow. *ICCES 1(1),* pp. 21-27. 2007.

[35] G. Xiong and C. A. Taylor. Physics-based modeling of aortic wall motion from ECG-gated 4D computed tomography. *Med Image Comput Assist Interv. 13(1),* pp. 426-434. 2010.

[36] Joei. Echocardiograph data. 2012.

[37] B. Wainman. Anatomy lab data. 2011.

[38] S. D. Qanadli, M. El Hajjam, B. Mesurolle, L. Lavisse, O. Jourdan, B. Randoux, S. Chagnon and P. Lacombe. Motion artifacts of the aorta simulating aortic dissection on spiral CT. *J Comput Assist Tomogr. 23(1),* pp. 1-6. 1999.

[39] H. V. Posniak, M. C. Olson and T. C. Demos. Aortic motion artifact simulating dissection on CT scans - elimination with reconstructive segmented images. *Am J Roentgenol. 161(3),* pp. 557-558. 1993.

[40] O. Duvernoy, R. Coulden and C. Ytterberg. Aortic motion - A potential pitfall in CT imaging of dissection in the ascending aorta. *J Comput Assist Tomogr. 19(4),* pp. 569-572. 1995.

[41] M. Markl, P. J. Kilner and T. Ebbers. Comprehensive 4D velocity mapping of the heart and great vessels by cardiovascular magnetic resonance. *J Cardiovasc Magn Reson. 13(7),* 2011.

[42] P. D. Stein and H. N. Sabbah. Turbulent blood-flow in the ascending aorta of humans with normal and diseased aortic valves. *Circulation Research 39*pp. 58-65. 1976.

[43] P. A. Stonebridge and C. M. Brophy. Spiral laminar-flow in arteries. *Lancet 338(8779),* pp. 1360-1361. 1991.

[44] P. A. Stonebridge, P. R. Hoskins, P. L. Allan and J. F. F. Belch. Spiral laminar flow in vivo. *Clin Sci (Lond). 91(1),* pp. 17-21. 1996.

[45] T. A. Hope and R. J. Herfkens. Imaging of the thoracic aorta with time-resolved three-dimensional phase-contrast MRI: A review. *Semin Thorac Cardiovasc Surg. 20(4),* pp. 358-364. 2008.

[46] M. Markl. EnSight MRI data. 2012.

[47] E. Weigang, F. A. Kari, F. Beyersdorf, M. Luehr, C. D. Etz, A. Frydrychowicz, A. Harloff and M. Markl. Flow-sensitive four-dimensional magnetic resonance imaging: Flow patterns in ascending aortic aneurysms. *Eur J Cardiothorac Surg. 34(1),* pp. 11-16. 2008.

[48] A. Frydrychowicz, A. F. Stalder, M. F. Russe, J. Bock, S. Bauer, A. Harloff, A. Berger, M. Langer, J. Hennig and M. Markl. Three-dimensional analysis of segmental wall shear stress in the aorta by flow-sensitive four-dimensional-MRI. *J Magn Reson Imaging. 30(1),* pp. 77-84. 2009.

[49] U. Morbiducci, R. Ponzini, G. Rizzo, M. Cadioli, A. Esposito, F. M. Montevecchi and A. Redaelli. Mechanistic insight into the physiological relevance of helical blood flow in the human aorta: An in vivo study. *Biomech Model Mechanobiol. 10(3),* pp. 339-355. 2011.

[50] Atlas of Echocardiography,. (2012). *Echocardiography Views*. Available: http://www.yale.edu/imaging/echo_atlas/views/.

[51] H. Tandon, M. Nwosu and A. F. LaSala. Aortic root motion: A marker of left ventricular diastolic dysfunction using M-mode echocardiography? an observational study. *Conn Med. 75(10),* pp. 591-598. 2011.

[52] K. Emilsson, R. Egerlid and B. M. Nygren. Comparison between aortic annulus motion and mitral annulus motion obtained using echocardiography. *Clin Physiol Funct Imaging. 26(5),* pp. 257-262. 2006.

[53] C. A. Taylor and M. T. Draney. Experimental and computational methods in cardiovascular fluid mechanics. *Annu Rev Fluid Mech. 36*pp. 197-231. 2004.

[54] I. E. Vignon-Clementel, C. A. Figueroa, K. E. Jansen and C. A. Taylor. Outflow boundary conditions for three-dimensional finite element modeling of blood flow and pressure in arteries. *Comput Method Appl M. 195(29-32),* pp. 3776-3796. 2006.

[55] E. O. Kung, A. S. Les, C. A. Figueroa, F. Medina, K. Arcaute, R. B. Wicker, M. V. McConnell and C. A. Taylor. In vitro validation of finite element analysis of blood flow in deformable models. *Ann. Biomed. Eng. 39(7),* 2011. . DOI: 10.1007/s10439-011-0284-7.

[56] R. L. Spilker, J. A. Feinstein, D. W. Parker, V. M. Reddy and C. A. Taylor. Morphometry-based impedance boundary conditions for patient-specific modeling of blood flow in pulmonary arteries. *Ann Biomed Eng. 35(4),* pp. 546-559. 2007.

[57] R. Fogliardi, M. Di Donfrancesco and R. Burattini. Comparison of linear and nonlinear formulations of the three-element windkessel model. *Am J Physiol. 271(6),* pp. 2661-2668. 1996.

[58] J. Y. Park, C. Y. Park, C. M. Hwang, K. Sun and B. G. Min. Pseudo-organ boundary conditions applied to a computational fluid dynamics model of the human aorta. *Comput Biol Med. 37(8),* pp. 1063-1072. 2007.

[59] Y. Shi, T. Korakianitis and C. Bowles. Numerical simulation of cardiovascular dynamics with different types of VAD assistance. *J Biomech. 40(13),* pp. 2919-2933. 2007.

[60] F. P. P. Tan, A. Borghi, R. H. Mohiaddin, N. B. Wood, S. Thom and X. Y. Xu. Analysis of flow patterns in a patient-specific thoracic aortic aneurysm model. *Computers and Structures 87(11-12),* pp. 680-690. 2009.

[61] Z. Cheng, F. P. P. Tan, C. V. Riga, C. D. Bicknell, M. S. Hamady, R. G. J. Gibbs, N. B. Wood and X. Y. Xu. Analysis of flow patterns in a patient-specific aortic dissection model. *J Biomech Eng. 132(5),* 2010.

[62] I. Borazjani, L. Ge and F. Sotiropoulos. High-resolution fluid-structure interaction simulations of flow through a bi-leaflet mechanical heart valve in an anatomic aorta. *Ann. Biomed. Eng. 38(2),* 2010. . DOI: 10.1007/s10439-009-9807-x.

[63] C. Canstein, P. Cachot, A. Faust, A. F. Stalder, J. Bock, A. Frydrychowicz, J. Kuffer, J. Hennig and M. Markl. 3D MR flow analysis in realistic rapid-prototyping model systems of the thoracic aorta: Comparison with in vivo data and computational fluid dynamics in identical vessel geometries. *Magn Reson Med. 59(3),* pp. 535-546. 2008.

[64] A. Cheer, H. A. Dwyer and T. Kim. New method for improved calculations of unsteady complex flows in large arteries. *Acta Mathematica Scientia 31(6),* pp. 2247-2264. 2011.

[65] W. Fu, B. Chu, Y. Chang and A. Qiao. Construction and analysis of human thoracic aorta based on CT images. Presented at World Congress on Medical Physics and Biomedical Engineering. 2009, .

[66] L. Morris, P. Delassus, A. Callanan, M. Walsh, F. Wallis, P. Grace and T. McGloughlin. 3-D numerical simulation of blood flow through models of the human aorta. *J Biomech Eng. 127(5),* pp. 767-775. 2005.

[67] J. Svensson, R. Gardhagen, E. Heiberg, T. Ebbers, D. Loyd, T. Lanne and M. Karlsson. Feasibility of patient specific aortic blood flow CFD simulation. *Med Image Comput Assist Interv. 9(1),* pp. 257-263. 2006.

[68] N. B. Wood, S. J. Weston, P. J. Kilner, A. D. Gosman and D. N. Firmin. Combined MR imaging and CFD simulation of flow in the human descending aorta. *J Magn Reson Imaging. 13(5),* pp. 699-713. 2001.

[69] A. S. Yang, C. Y. Wen and L. Y. Tseng. In vitro characterization of aortic flow using numerical simulation, phase-contrast magnetic resonance imaging, and particle tracking images. *P I Mech Eng C- J Mec. 222*pp. 2455-2462. 2008.

[70] J. Chen and X. Y. Lu. Numerical investigation of the non-newtonian blood flow in a bifurcation model with a non-planar branch. *J Biomech. 39(5),* pp. 818-832. 2006.

[71] S. U. Siddiqui, N. K. Verma, S. Mishra and R. S. Gupta. Mathematical modelling of pulsatile flow of casson's fluid in arterial stenosis. *Appl Math Comput. 210(1),* pp. 1-10. 2009.

[72] R. A. Sultanov and D. Guster. Full dimensional computer simulations to study pulsatile blood flow in vessels, aortic arch and bifurcated veins: Investigation of blood viscosity and turbulent effects. Presented at Engineering in Medicine and Biology Society. Annual International Conference of the IEEE. 2009, .

[73] P. Ternik and J. Marn. Numerical study of blood flow in stenotic artery. *Appl Rheol. 19(1),* pp. 17-27. 2009.

[74] H. Nygaard, J. M. Hasenkam, E. M. Pedersen, W. Y. Kim and P. K. Paulsen. A new perivascular multielement pulsed doppler ultrasound system for in-vivo studies of velocity-fields and turbulent stresses in large vessels. *Med Biol Eng Comput. 32(1),* pp. 55-62. 1994.

[75] E. Y. Wong, H. N. Nikolov, M. L. Thorne, T. L. Poepping, R. N. Rankin and D. W. Holdsworth. Clinical doppler ultrasound for the assessment of plaque ulceration in the stenosed carotid bifurcation by detection of distal turbulence intensity: A matched model study. *Eur Radiol. 19(11),* pp. 2739-2749. 2009.

[76] M. L. Thorne, R. N. Rankin, D. A. Steinman and D. W. Holdsworth. In vivo doppler ultrasound quantification of turbulence intensity using a high-pass frequency filter method. *Ultrasound Med Biol. 36(5),* pp. 761-771. 2010.

[77] J. N. Oshinski, D. N. Ku and R. I. Pettigrew. Turbulent fluctuation velocity - the most significant determinant of signal loss in stenotic vessels. *Magn Reson Med. 33(2),* pp. 193-199. 1995.

[78] P. Dyverfeldt, J. P. E. Kvitting, A. Sigfridsson, J. Engvall, A. F. Bolger and T. Ebbers. Assessment of fluctuating velocities in disturbed cardiovascular blood flow: In vivo feasibility of generalized phase-contrast MRI. *J Magn Reson Imaging. 28(3),* pp. 655-663. 2008.

[79] A. F. Stalder, A. Frydrychowicz, M. F. Russe, J. G. Korvink, J. Hennig, K. Li and M. Markl. Assessment of flow instabilities in the healthy aorta using flow-sensitive MRI. *J Magn Reson Imaging. 33(4),* pp. 839-846. 2011.

[80] E. L. Yellin. Laminar-turbulent transition process in pulsatile flow. *Circulation Research 19*pp. 791-804. 1966.

[81] I. Fukuda, S. Fujimori, K. Daitoku, H. Yanaoka and T. Inamura. Flow velocity and turbulence in the transverse aorta of a proximally directed aortic cannula: Hydrodynamic study in a transparent model. *Ann Thorac Surg. 87(6),* pp. 1866-1871. 2009.

[82] A. C. Benim, A. Nahavandi, A. Assmann, D. Schubert, P. Feindt and S. H. Suh. Simulation of blood flow in human aorta with emphasis on outlet boundary conditions. *Appl Math Model 35(7),* pp. 3175-3188. 2011.

[83] X. Liu, Y. Fan, X. Deng and F. Zhan. Effect of non-newtonian and pulsatile blood flow on mass transport in the human aorta. *J. Biomech. 44(6),* 2011.

[84] M. C. Paul, M. M. Molla and G. Roditi. Large-eddy simulation of pulsatile blood flow. *Med Eng Phys. 31(1),* pp. 153-159. 2009.

[85] M. Nakamura, S. Wada and T. Yamaguchi. Computational analysis of blood flow in an integrated model of the left ventricle and the aorta. *J Biomech Eng. 128(6),* pp. 837-843. 2006.

[86] D. Mori and T. Yamaguchi. Computational fluid dynamics modeling and analysis of the effect of 3-D distortion of the human aortic arch. *Comput Methods Biomech Biomed Engin. 5(3),* pp. 249-260. 2002.

[87] N. Shahcheraghi, H. A. Dwyer, A. Y. Cheer, A. I. Barakat and T. Rutaganira. Unsteady and three-dimensional simulation of blood flow in the human aortic arch. *J Biomech Eng. 124(4),* pp. 378-387. 2002.

[88] P. Vasava, P. Jalali and M. Dabagh. Computational study of pulstile blood flow in aortic arch: Effect of blood pressure. Presented at World Congress on Medical Physics and Biomedical Engineering. 2009, .

[89] C. Wen, A. Yang, L. Tseng and J. Chai. Investigation of pulsatile flowfield in healthy thoracic aorta models. *Ann Biomed Eng. 38(2),* pp. 391-402. 2010.

[90] A. Leuprecht, S. Kozerke, P. Boesiger and K. Perktold. Blood flow in the human ascending aorta: A combined MRI and CFD study. *J Eng Math. 47*pp. 387-404. 2003.

[91] J. Lantz, J. Renner and M. Karlsson. Wall shear stress in a subject specific human aorta - influence of fluid-structure interaction. *Int J Appl Mech. 3(4),* pp. 759-778. 2011.

[92] C. L. Bara and J. F. Verhey. Simulation of the fluid dynamics in artificial aortic roots: Comparison of two different types of prostheses. *J Artif Organs 11(3),* pp. 123-129. 2008.

[93] F. Sotiropoulos and I. Borazjani. A review of state-of-the-art numerical methods for simulating flow through mechanical heart valves. *Med Biol Eng Comput. 47(3),* pp. 245-256. 2009.

[94] L. P. Dasi, H. A. Simon, P. Sucosky and A. P. Yoganathan. Fluid mechancis of artificial heart valves. *Clin Exp Pharmacol Physiol. 36(2),* pp. 225-237. 2009.

[95] M. D. De Tullio, A. Cristallo, E. Balaras and R. Verzicco. Direct numerical simulation of the pulsatile flow through an aortic bileaflet mechanical heart valve. *J Fluid Mech. 622*pp. 259-290. 2009.

[96] A. Ranga, O. Bouchot, R. Mongrain, P. Ugolini and R. Cartier. Computational simulations of the aortic valve validated by imaging data: Evaluation of valve-sparing techniques. *Interact Cardiovasc Thorac Surg. 5*pp. 373-378. 2006.

[97] M. A. Nicosia, R. P. Cochran, D. R. Einstein, C. J. Rutland and K. S. Kunzelman. A coupled fluid-structure finite element model of the aortic valve and root. *J Heart Valve Dis. 12(6),* pp. 781-789. 2003.

[98] J. De Hart, G. W. M. Peters, P. J. G. Schreurs and F. P. T. Baaijens. A three-dimensional computational analysis of fluid-structure interaction in the aortic valve. *J Biomech. 36(1),* pp. 103-112. 2003.

[99] A. Ranga, R. Mongrain, Y. Biadilah and R. Cartier. A compliant dynamic FEA model of the aortic valve. Presented at 12th IFToMM World Congress. 2007, .

[100] E. J. Weinberg and M. R. Kaazempur Mofrad. Transient, three-dimensional, multiscale simulations of the human aortic valve. *Cardiovasc Eng. 7(4),* pp. 140-155. 2007.

[101] H. L. Leo, L. P. Dasi, J. Carberry, H. A. Simon and A. P. Yoganathan. Fluid dynamic assessment of three polymeric heart valves using particle image velocimetry. *Ann Biomed Eng. 34(6),* pp. 936-952. 2006.

[102] T. Akutsu and A. Matsumoto. Influence of three mechanical bileaflet prosthetic valve designs on the three-dimensional flow field inside a simulated aorta. *J Artif Organs 13(4),* pp. 207-217. 2010.

[103] T. Irvine, X. N. Li, Y. Mori, S. Wanitkun, X. K. Li, P. R. Detmer, R. W. Martin, A. Pope, G. A. Schwartz, R. A. Rusk, A. Kenny and D. J. Sahn. A digital 3-dimensional method for computing great artery flows: In vitro validation studies. *J Am Soc Echocardiogr. 13(9),* pp. 841-848. 2000.

[104] J. P. E. Kvitting, T. Ebbers, L. Wigstrom, J. Engvall, C. L. Olin and A. F. Bolger. Flow patterns in the aortic root and the aorta studied with time-resolved, 3-dimensional, phase-contrast magnetic resonance imaging: Implications for aortic valve-sparing surgery. *J Thorac Cardiovasc Surg. 127(6),* pp. 1602-1607. 2004.

[105] S. Canic, C. J. Hartley, D. Rosenstrauch, J. Tambaca, G. Guidoboni and A. Mikelic. Blood flow in compliant arteries: An effective viscoelastic reduced model, numerics, and experimental validation. *Ann Biomed Eng. 34(4),* pp. 575-592. 2006.

[106] Y. Huo and G. S. Kassab. A hybrid one-dimensional/womersley model of pulsatile blood flow in the entire coronary arterial tree. *Am J Physiol Heart Circ Physiol. 292(6),* pp. 2623-2633. 2007.

[107] K. S. Matthys, J. Alastruey, J. Peiro, A. W. Khir, P. Segers, P. R. Verdonck, K. H. Parker and S. J. Sherwin. Pulse wave propagation in a model human arterial network: Assessment of 1-D numerical simulations against in vitro measurements. *J Biomech. 40(15),* pp. 3476-3486. 2007.

[108] H. P. Fang, Z. F. Lin and Z. W. Wang. Lattice boltzmann simulation of viscous fluid systems with elastic boundaries. *Phys. Rev. E 57(1),* pp. 25-28. 1998.

[109] G. Pedrizzetti, F. Domenichini, A. Tortoriello and L. Zovatto. Pulsatile flow inside moderately eastic arteries, its modelling and effects of elasticity. *Comput Methods Biomech Biomed Engin. 5(3),* pp. 219-231. 2002.

[110] D. Mori and T. Yamaguchi. Computational fluid dynamics modeling and analysis of the effect of 3-D distortion of the human aortic arch. *Comput Methods Biomech Biomed Engin. 5(3),* pp. 249-260. 2002.

[111] D. Mori, T. Hayasaka and T. Yamaguchi. Modeling of the human aortic arch with its major branches for computational fluid dynamics simulation of the blood flow. *JSME Int J. , Ser. C 45(4),* pp. 997-1002. 2002.

[112] B. Xiao and Y. Zhang. Numerical simulation of pulsatile turbulent flow in tapering stenosed arteries. *Int J Heat Fluid Fl. 19(5),* pp. 561-573. 2009.

[113] P. Vasava, P. Jalali and M. Dabagh. Pulsatile blood flow simulations in aortic arch: Effects of blood pressure and the geometry of arch on wall shear stress. Presented at 4th European Conference of the International Federation for Medical and Biological Engineering (ECIFMBE). 2009, .

[114] S. J. Weston, N. B. Wood, G. Tabor, A. D. Gosman and D. N. Firmin. Combined MRI and CFD analysis of fully developed steady and pulsatile laminar flow through a bend. *J Magn Reson Imaging. 8(5),* pp. 1158-1171. 1998.

[115] X. Y. Xu, Q. Long, M. W. Collins, M. Bourne and T. M. Griffith. Reconstruction of blood flow patterns in human arteries. *Proc Inst Mech Eng H. 213(5),* pp. 411-421. 1999.

[116] S. Brown, J. Wang, H. Ho and S. Tullis. Numeric simulation of fluid structure interaction in the aortic arch. *Computational Biomechanics for Medicine* pp. 13-23. 2013.

[117] L. Grinberg, T. Anor, J. R. Madsen, A. Yakhot and G. E. Karniadakis. Large-scale simulation of the human arterial tree. *Clin Exp Pharmacol Physiol. 36(2),* pp. 194-205. 2009.

[118] (May, 2011). *Aorta Model*. Available: www.vascularmodel.org.

[119] J. Black and G. Hastings. *Handbook of Biomaterial Properties* 1998.

[120] L. Luzardo, I. Lujambio, M. Sottolano, A. Da Rosa, L. Thijs, O. Noboa, J. A. Staessen and J. Boggia. 24-H ambulatory recording of aortic pulse wave velocity and central systolic augmentation: A feasibility study. *Hypertens Res. 35(10),* pp. 980-987. 2012.

[121] T. W. Hansen, J. A. Staessen, C. Torp-Pedersen, S. Rasmussen, L. Thijs, H. Ibsen and J. Jeppesen. Prognostic value of aortic pulse wave velocity as index of arterial stiffness in the general population. *Circulation 113(5),* pp. 664-670. 2006.

[122] T. Shokawa, M. Imazu, H. Yamamoto, M. Toyofuku, N. Tasaki, T. Okimoto, K. Yamane and N. Kohno. Pulse wave velocity predicts cardiovascular mortality - findings from the hawaii-los angeles-hiroshima study. *Circ J. 69(3),* pp. 259-264. 2005.

[123] N. Inoue, R. Maeda, H. Kawakami, T. Shokawa, H. Yamamoto, C. Ito and H. Sasaki. Aortic pulse wave velocity predicts cardiovascular mortality in middle-aged and elderly japanese men. *Circ J. 73(3),* pp. 549-553. 2009.

[124] Y. Nagai, J. L. Fleg, M. K. Kemper, T. M. Rywik, C. J. Earley and E. J. Metter. Carotid arterial stiffness as a surrogate for aortic stiffness: Relationship between carotid artery pressure-strain elastic modulus and aortic pulse wave velocity. *Ultrasound Med Biol. 25(2),* pp. 181-188. 1999.

[125] G. G. Belz. Elastic properties and windkessel function of the human aorta. *Cardiovasc Drugs Ther. 9(1),* pp. 73-83. 1995.

[126] A. A. Laogun and R. G. Gosling. In vivo arterial compliance in man. *Clin Phys Physiol Meas. 3(3),* pp. 201-212. 1982.

[127] S. Radhakrishnan, D. N. Ghista, G. Jayaraman and K. M. Patil. Analysis for the in vivo determination of the non-linear elastic parameters of an artery. *Biomed Tech (Berl.) 26(6),* pp. 147-150. 1981.

[128] J. M. Cavanaugh, T. J. Walilko and A. e. a. Malhotra, "Biomechanical response and injury tolerance for the thorax in twelve sled side impacts," *SAE International,* vol. 23, pp. 23-38, 1990.

[129] A. M. Nahum and J. M. Melvin. "Biomechanics of abdominal trauma," in *Accidental Injury*Anonymous 2001, .

[130] C. G. Stephanis, D. E. Mourmouras and D. G. Tsagadopoulos. On the elastic properties of arteries. *J Biomech. 36(11),* pp. 1727-1731. 2003.

[131] M. l. Markl, W. Wallis, S. Brendecke, J. Simon, A. Frydrychowicz and A. Harloff. Estimation of global aortic pulse wave velocity by flow-sensitive 4D MRI. *Magn Reson Med. 63(6),* pp. 1575-1582. 2010.

[132] S. W. Fielden, B. K. Fornwalt, M. Jerosch-Herold, R. L. Eisner, A. E. Stillman and J. N. Oshinski. A new method for the determination of aortic pulse wave velocity using cross-correlation on 2D PCMR velocity data. *J Magn Reson Imaging. 27(6),* pp. 1382-1387. 2008.

[133] H. Y. Yu, H. H. Peng, J. L. Wang, C. Y. Wen and W. Y. I. Tseng. Quantification of the pulse wave velocity of the descending aorta using axial velocity profiles from phase-contrast magnetic resonance imaging. *Magn Reson Med. 56(4),* pp. 876-863. 2006.

[134] S. Vulliemoz, N. Stergiopulos and R. Meuli. Estimation of local aortic elastic properties with MRI. *Magn Reson Med. 47(4),* pp. 649-654. 2002.

[135] Y. Loren. Difficulty breathing throughout infancy. *Radiology Cases in Pediatric Emergency Medicine 6*2012.

[136] Anonymous (2013). *Ansys Inc.*

[137] P. Vasava, P. Jalali and M. Dabagh. Computational study of pulstile blood flow in aortic arch: Effect of blood pressure. Presented at World Congress on Medical Physics and Biomedical Engineering. 2010, .

[138] M. Olufsen, C. Peskin, W. Kim, E. Pedersen, A. Nadim and J. Larsen, "Numerical simulation and experimental validation of blood flow in arteries with structured-tree outflow conditions," *Ann Biomed Eng.,* vol. 28, pp. 1281-1299, 2000.

[139] C. Wen, A. Yang, L. Tseng and J. Chai. Investigation of pulsatile flowfield in healthy thoracic aorta models. *Ann Biomed Eng. 38(2),* pp. 391-402. 2010.

[140] A. F. Stalder, Z. Liu, J. Hennig, J. G. Korvink, K. C. Li and M. Markl. Patient specific hemodynamics: Combined 4D flow-sensitive MRI and CFD. *Computational Biomechanics for Medicine* pp. 27-38. 2011.

[141] (2012). *Tricuspid Valve Anatomy*. Available: http://emedicine.medscape.com/.

8 Appendix A - Echocardiographic Data

Short Axis Echocardiographic Data

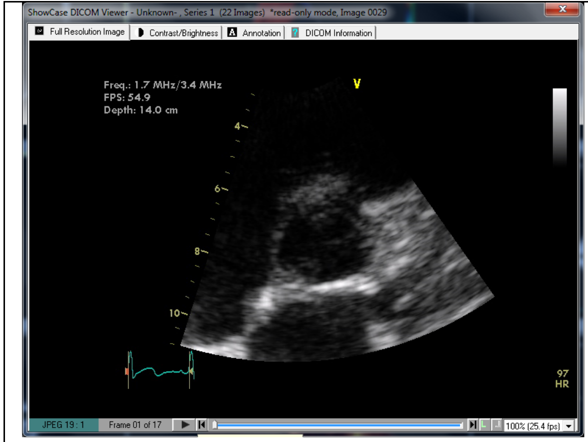

Freq.: 1.7 MHz/3.4 MHz
FPS: 54.9
Depth: 14.0 cm

0

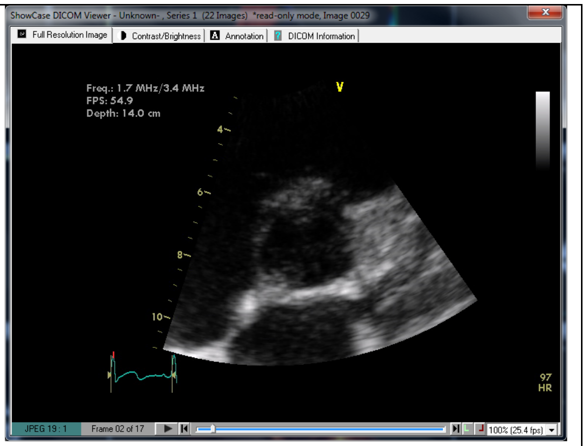

Freq.: 1.7 MHz/3.4 MHz
FPS: 54.9
Depth: 14.0 cm

0.0625

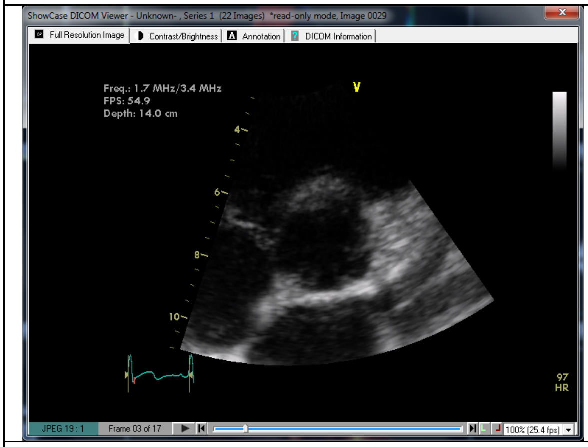

Freq.: 1.7 MHz/3.4 MHz
FPS: 54.9
Depth: 14.0 cm

0.125

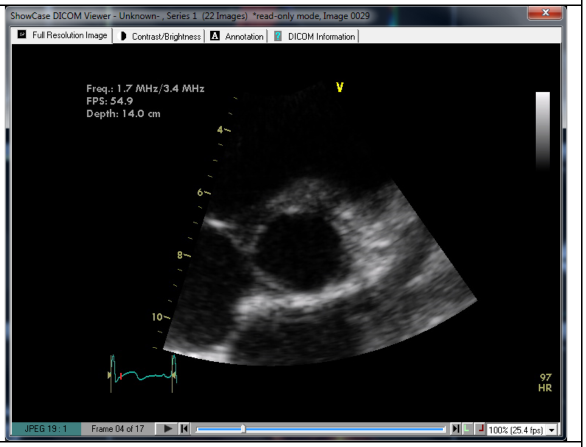

Freq.: 1.7 MHz/3.4 MHz
FPS: 54.9
Depth: 14.0 cm

0.1875

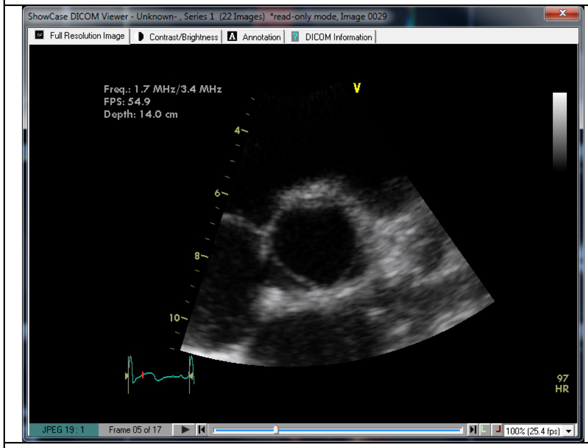

Freq.: 1.7 MHz/3.4 MHz
FPS: 54.9
Depth: 14.0 cm

0.25

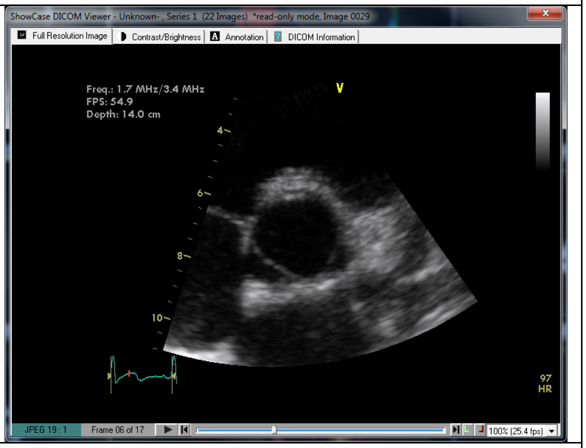

Freq.: 1.7 MHz/3.4 MHz
FPS: 54.9
Depth: 14.0 cm

0.3125

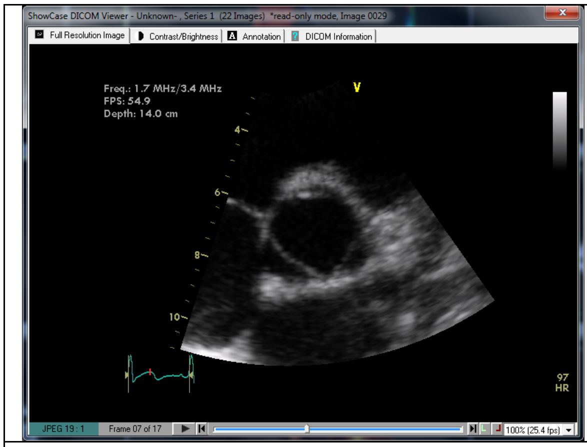

0.375

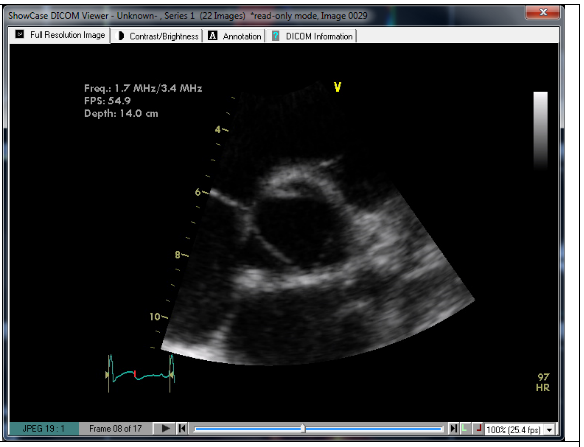

0.4375

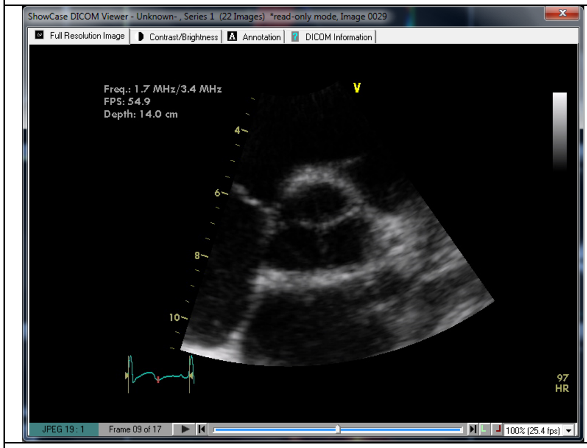

0.5

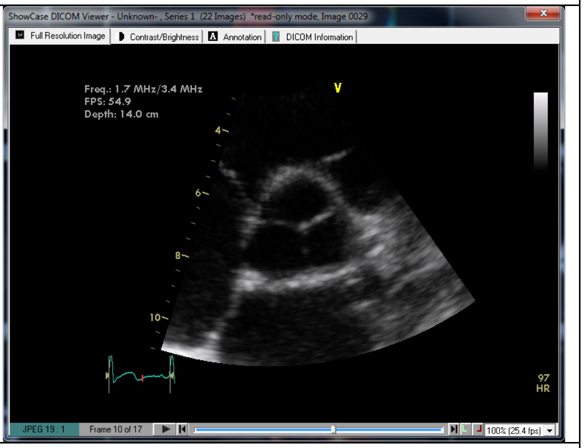

0.5625

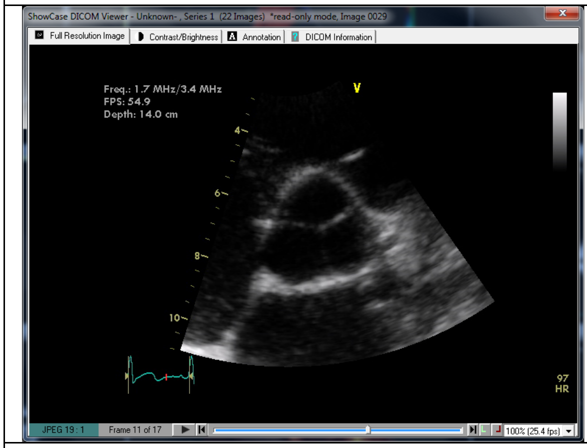

0.625

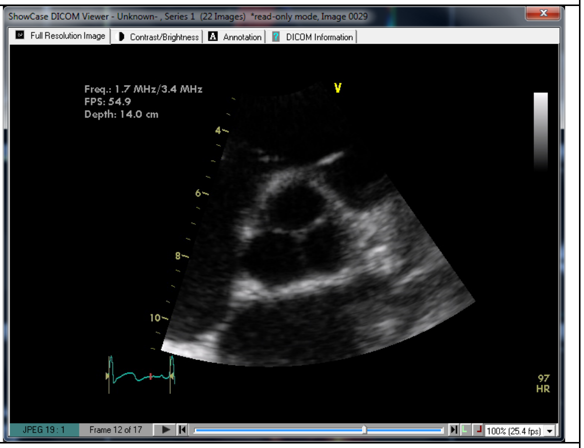

0.6875

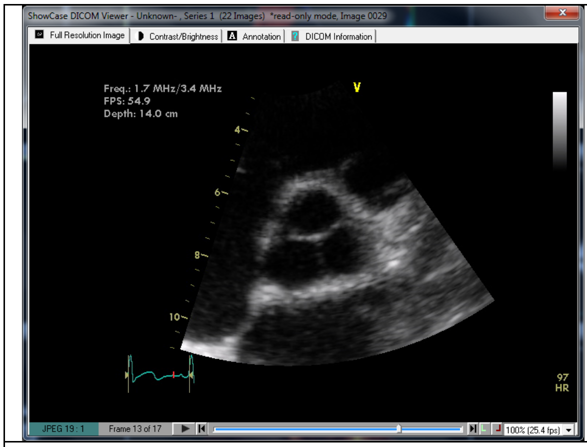	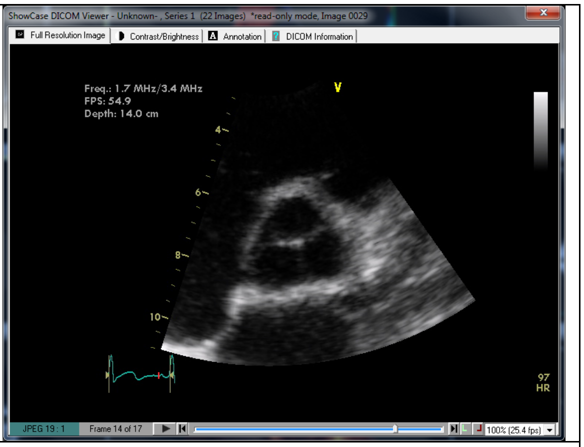
0.75	0.8125
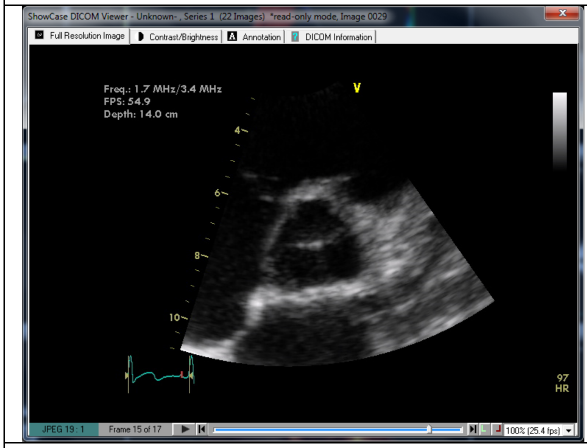	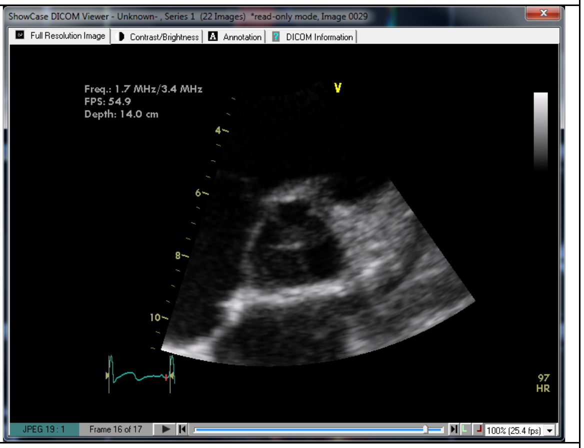
0.875	0.9375

LP Long Axis Echocardiographic Data

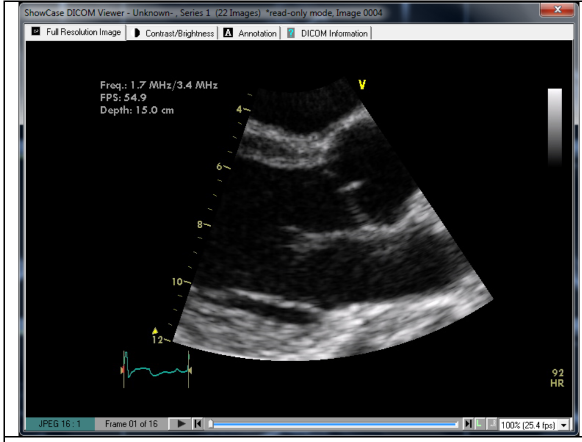

0

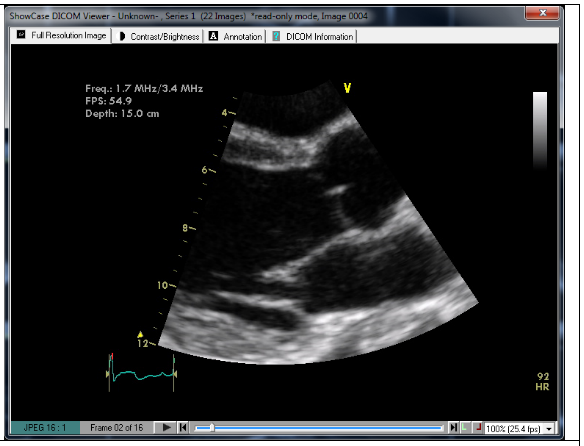

0.0625

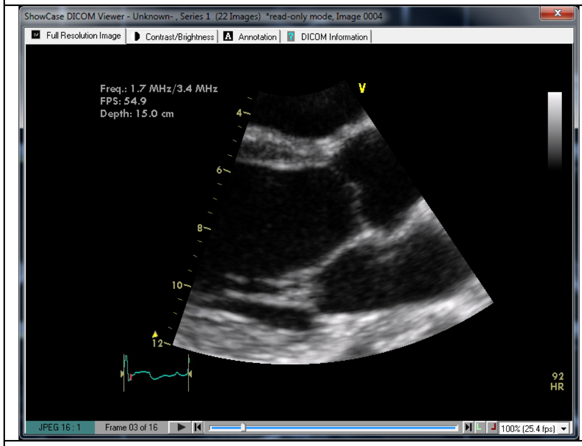

0.125

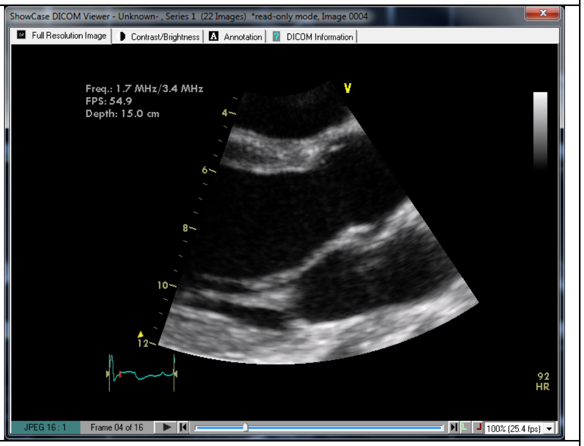

0.1875

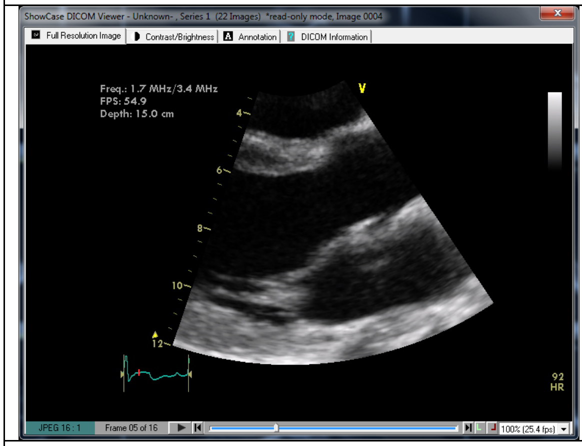

0.25

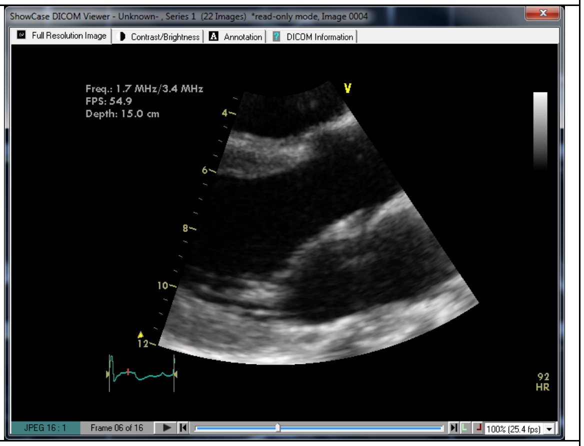

0.3125

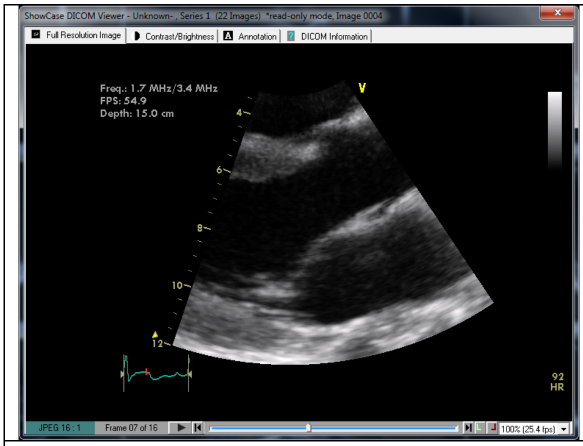
ShowCase DICOM Viewer - Unknown- , Series 1 (22 Images) *read-only mode, Image 0004

Freq.: 1.7 MHz/3.4 MHz
FPS: 54.9
Depth: 15.0 cm

0.375

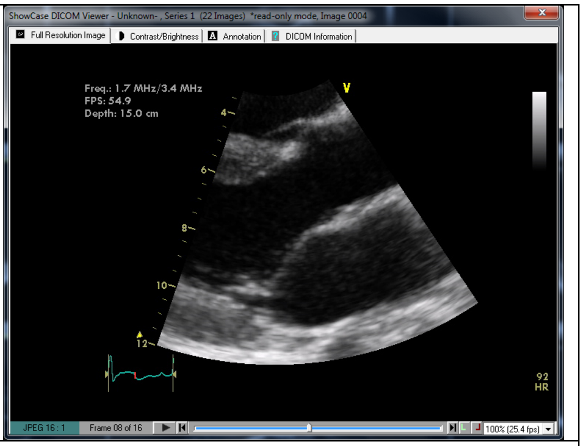
ShowCase DICOM Viewer - Unknown- , Series 1 (22 Images) *read-only mode, Image 0004

Freq.: 1.7 MHz/3.4 MHz
FPS: 54.9
Depth: 15.0 cm

0.4375

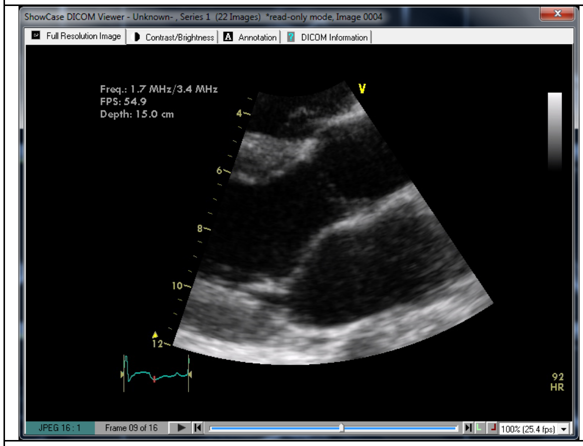
ShowCase DICOM Viewer - Unknown- , Series 1 (22 Images) *read-only mode, Image 0004

Freq.: 1.7 MHz/3.4 MHz
FPS: 54.9
Depth: 15.0 cm

0.5

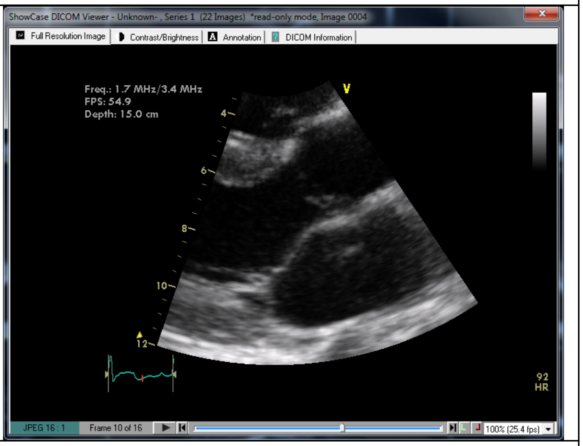
ShowCase DICOM Viewer - Unknown- , Series 1 (22 Images) *read-only mode, Image 0004

Freq.: 1.7 MHz/3.4 MHz
FPS: 54.9
Depth: 15.0 cm

0.5625

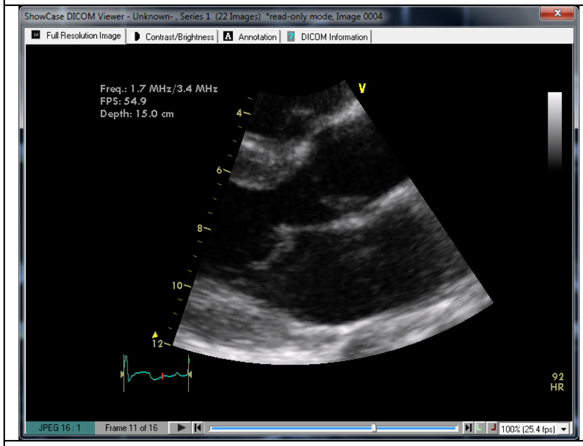
ShowCase DICOM Viewer - Unknown- , Series 1 (22 Images) *read-only mode, Image 0004

Freq.: 1.7 MHz/3.4 MHz
FPS: 54.9
Depth: 15.0 cm

0.625

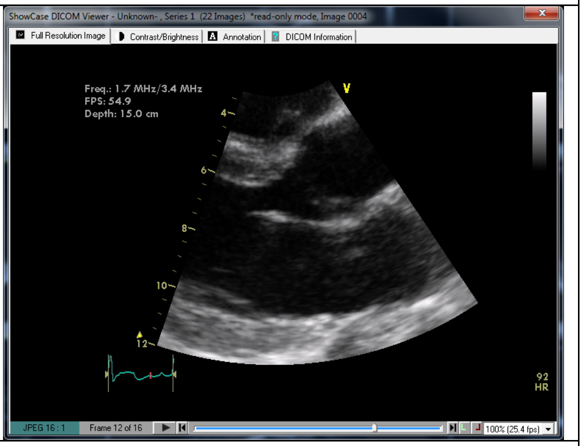
ShowCase DICOM Viewer - Unknown- , Series 1 (22 Images) *read-only mode, Image 0004

Freq.: 1.7 MHz/3.4 MHz
FPS: 54.9
Depth: 15.0 cm

0.6875

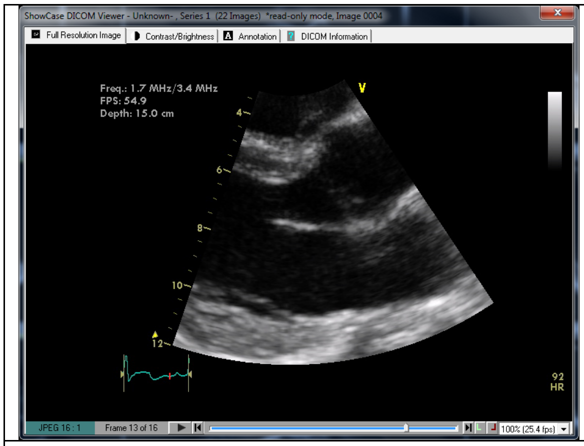 ShowCase DICOM Viewer - Unknown- , Series 1 (22 Images) *read-only mode, Image 0004 Freq.: 1.7 MHz/3.4 MHz FPS: 54.9 Depth: 15.0 cm 92 HR JPEG 16 : 1 Frame 13 of 16 100% (25.4 fps)	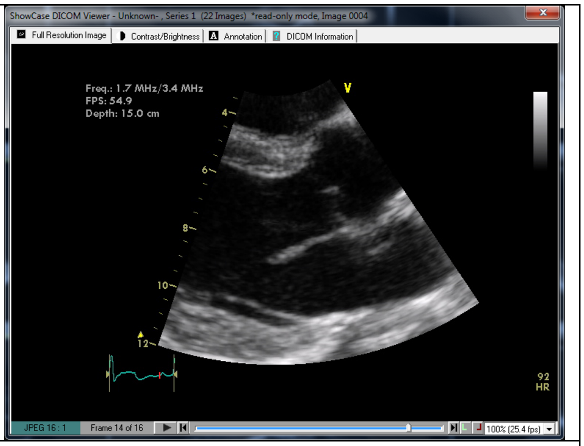 ShowCase DICOM Viewer - Unknown- , Series 1 (22 Images) *read-only mode, Image 0004 Freq.: 1.7 MHz/3.4 MHz FPS: 54.9 Depth: 15.0 cm 92 HR JPEG 16 : 1 Frame 14 of 16 100% (25.4 fps)
0.75	0.8125
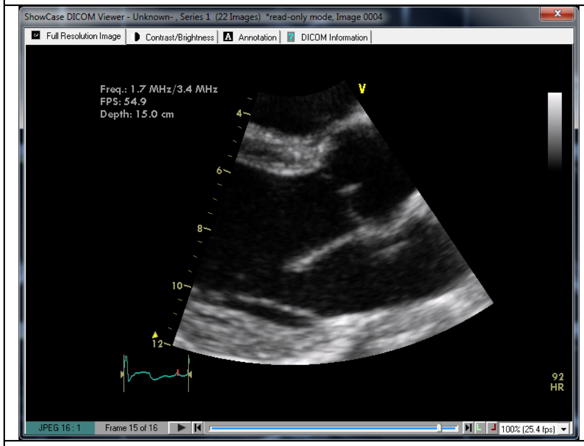 ShowCase DICOM Viewer - Unknown- , Series 1 (22 Images) *read-only mode, Image 0004 Freq.: 1.7 MHz/3.4 MHz FPS: 54.9 Depth: 15.0 cm 92 HR JPEG 16 : 1 Frame 15 of 16 100% (25.4 fps)	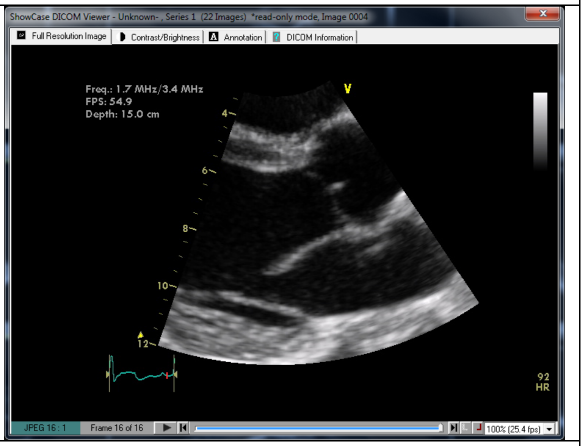 ShowCase DICOM Viewer - Unknown- , Series 1 (22 Images) *read-only mode, Image 0004 Freq.: 1.7 MHz/3.4 MHz FPS: 54.9 Depth: 15.0 cm 92 HR JPEG 16 : 1 Frame 16 of 16 100% (25.4 fps)
0.875	0.9375

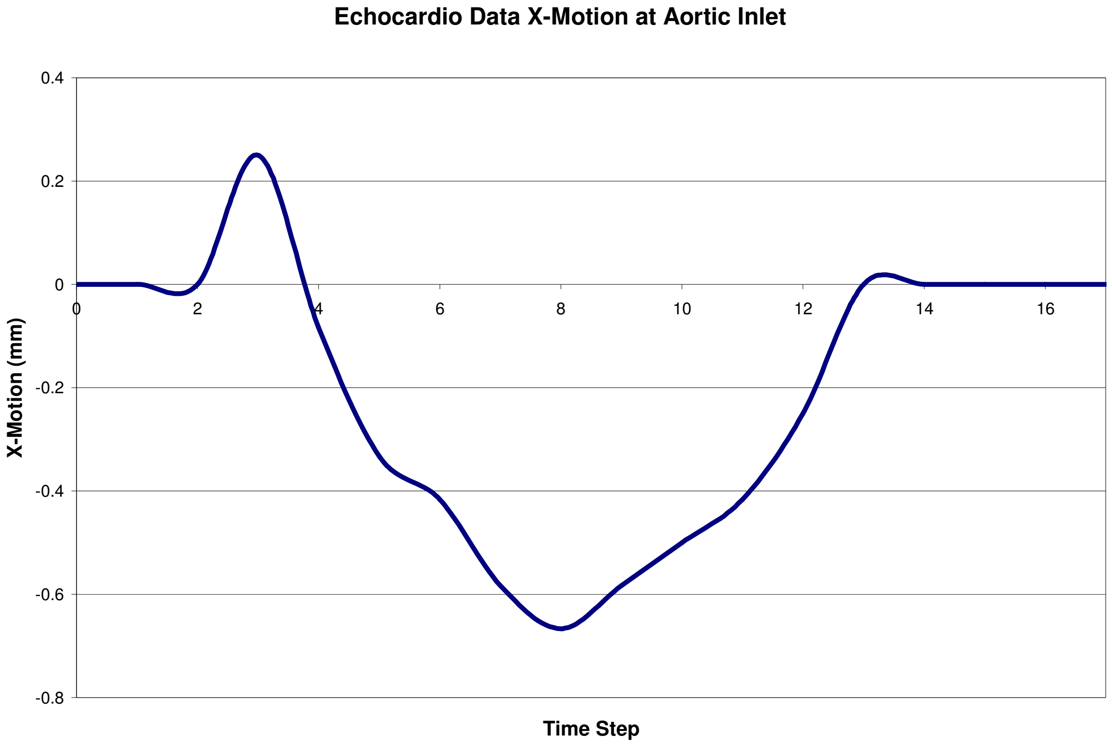
Echocardio Data X-Motion at Aortic Inlet
0.4
0.2
0
-0.2
-0.4
-0.6
-0.8
0
2
4
6
8
10
12
14
16
X-Motion (mm)
Time Step

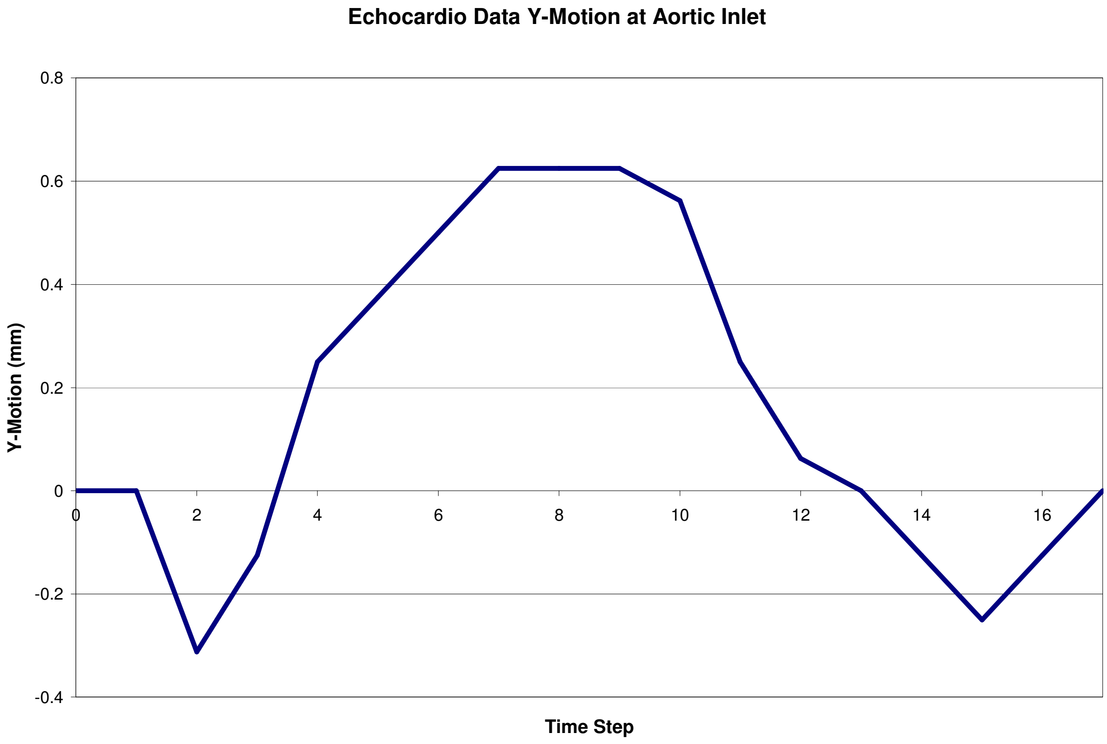
Echocardio Data Y-Motion at Aortic Inlet
0.8
0.6
0.4
0.2
0
-0.2
-0.4
0
2
4
6
8
10
12
14
16
Y-Motion (mm)
Time Step

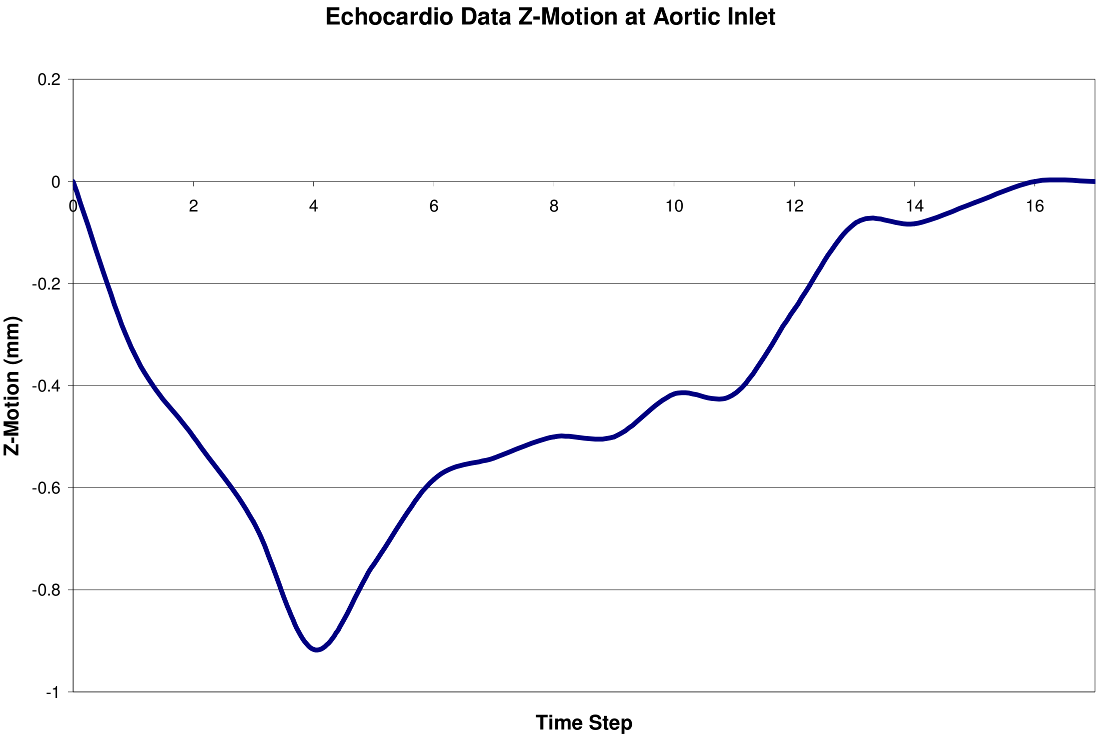
Echocardio Data Z-Motion at Aortic Inlet
0.2
0
-0.2
-0.4
-0.6
-0.8
-1
0
2
4
6
8
10
12
14
16
Z-Motion (mm)
Time Step

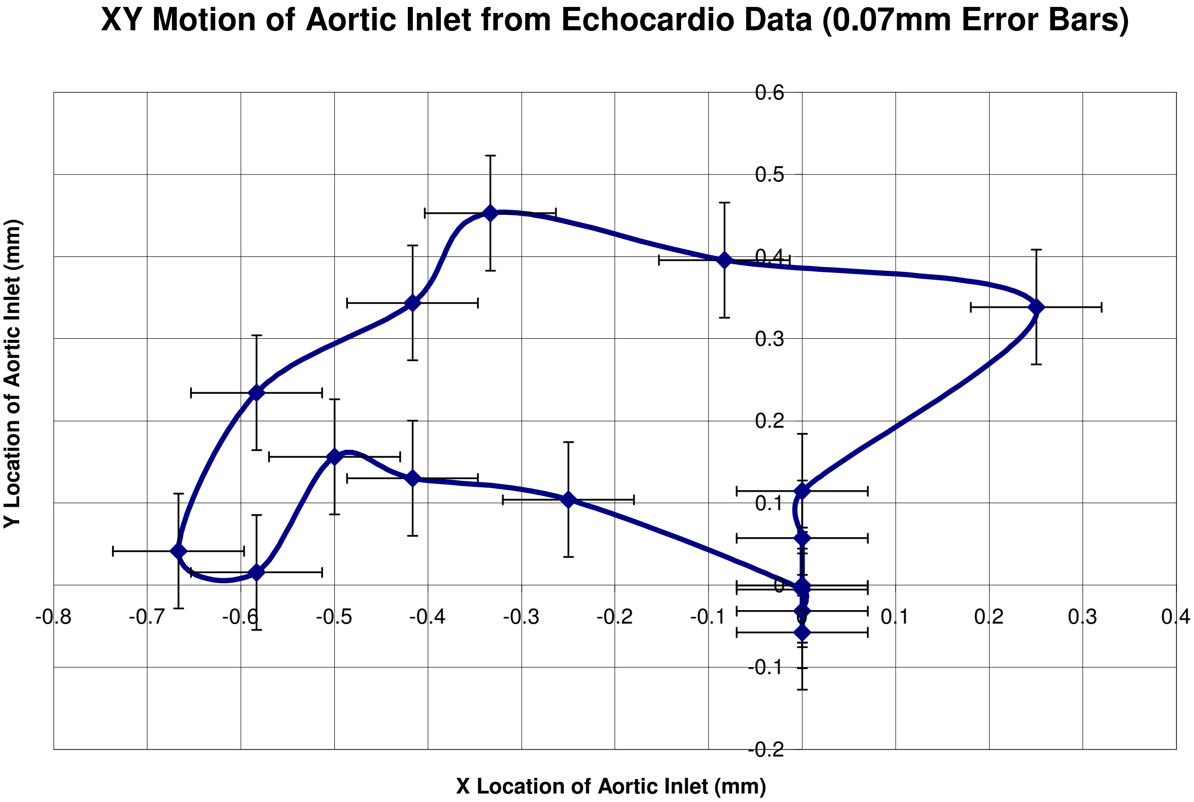
XY Motion of Aortic Inlet from Echocardio Data (0.07mm Error Bars)
0.6
0.5
0.4
0.3
0.2
0.1
0
-0.1
-0.2
-0.8
-0.7
-0.6
-0.5
-0.4
-0.3
-0.2
-0.1
0
0.1
0.2
0.3
0.4
Y Location of Aortic Inlet (mm)
X Location of Aortic Inlet (mm)

9 Appendix B - Transient Flow, Rigid Wall

Streamlines - Transient Flow, Rigid Wall Case

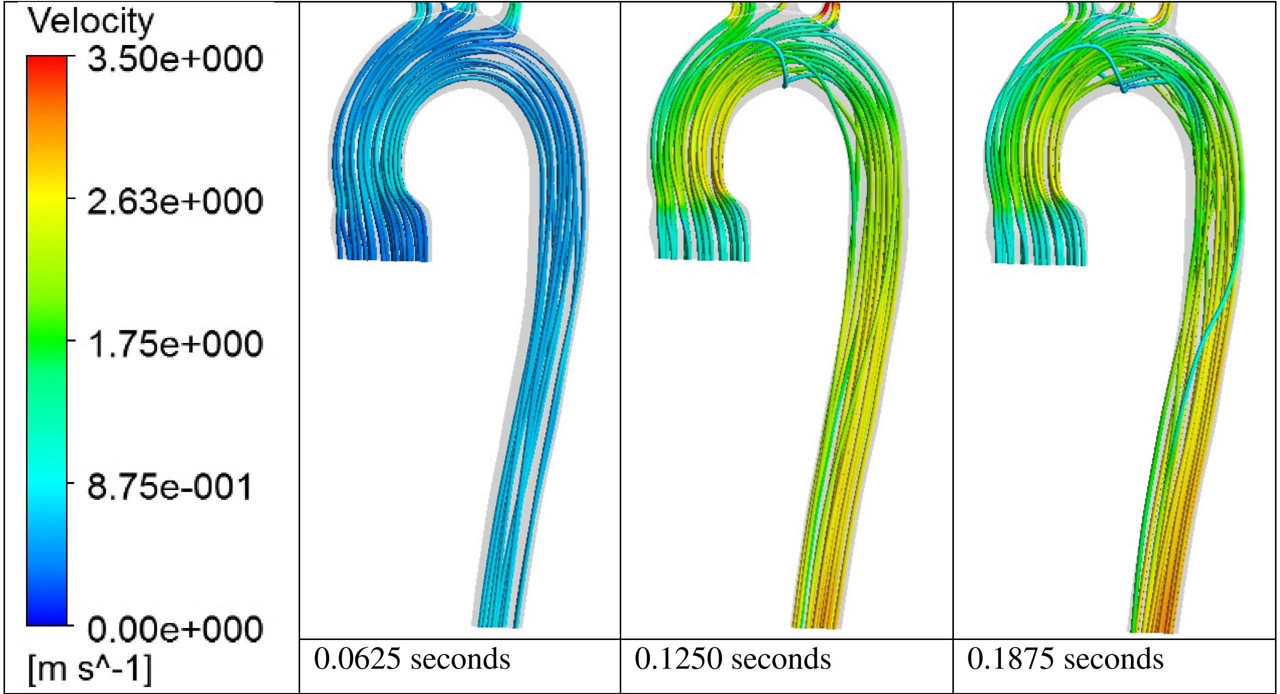

0.0625 seconds 0.1250 seconds 0.1875 seconds

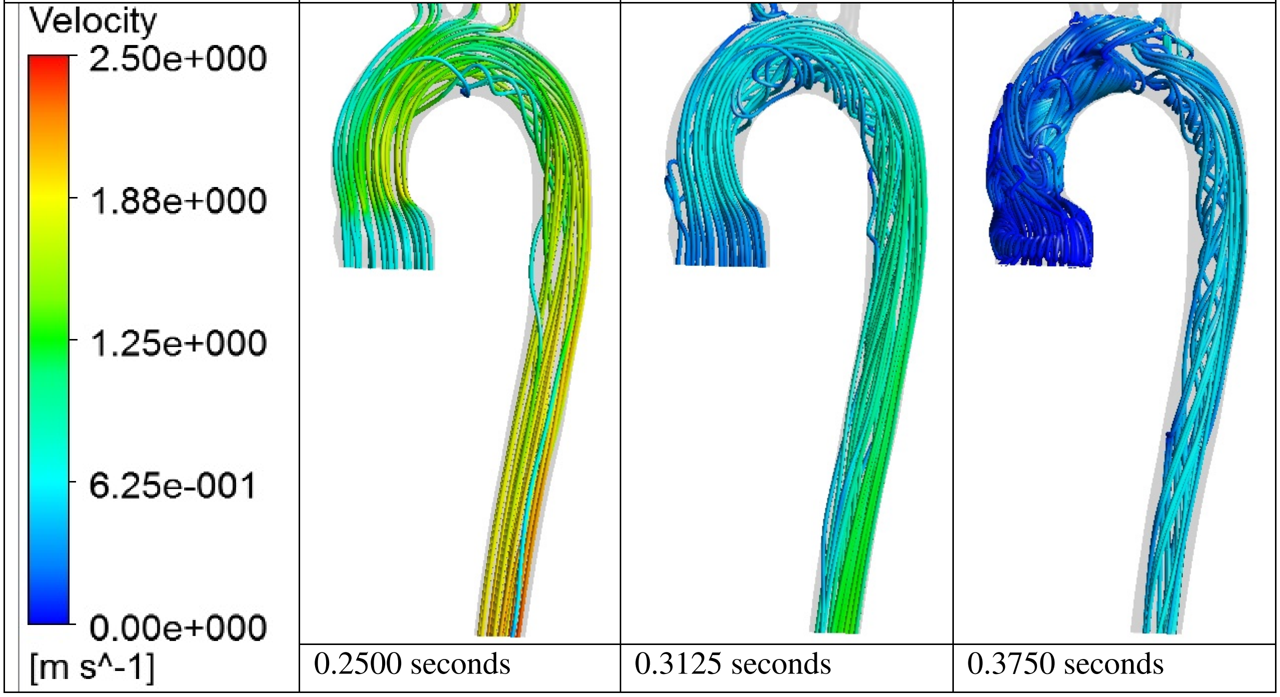

0.2500 seconds 0.3125 seconds 0.3750 seconds

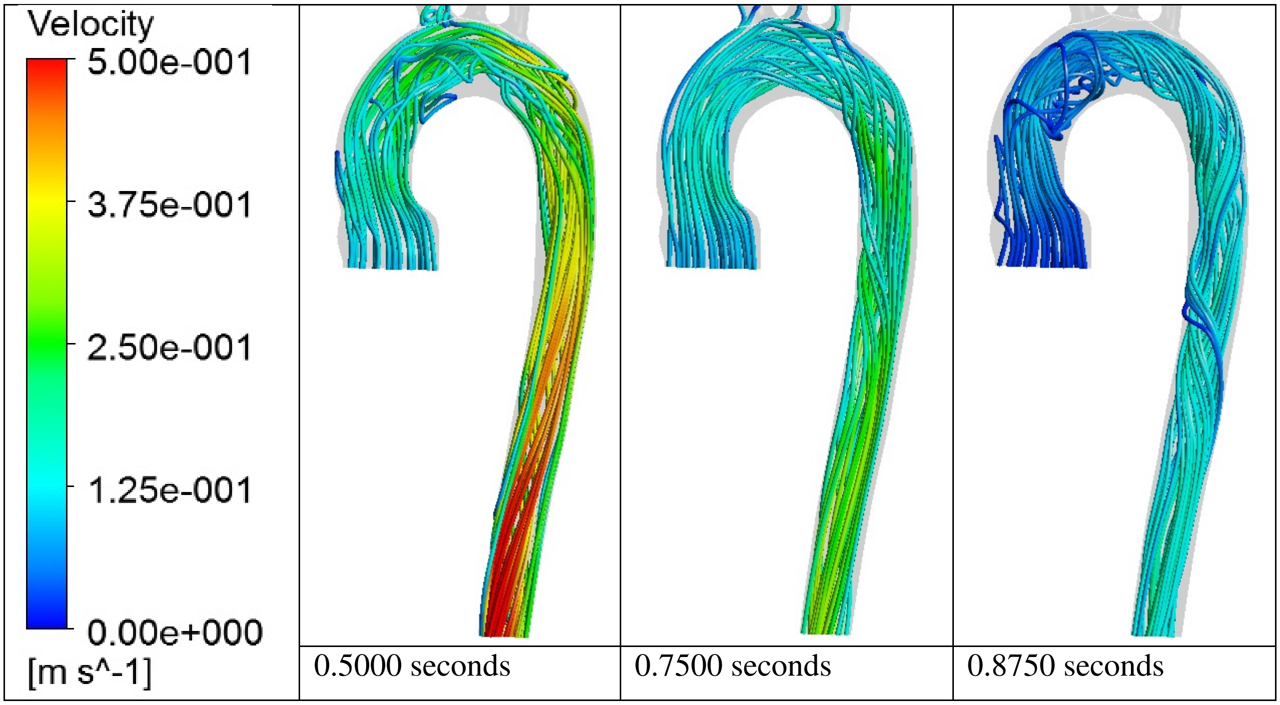

0.5000 seconds

0.7500 seconds

0.8750 seconds

Velocity Transverse - Ascending Aorta (Transient Flow, Rigid Wall Case)

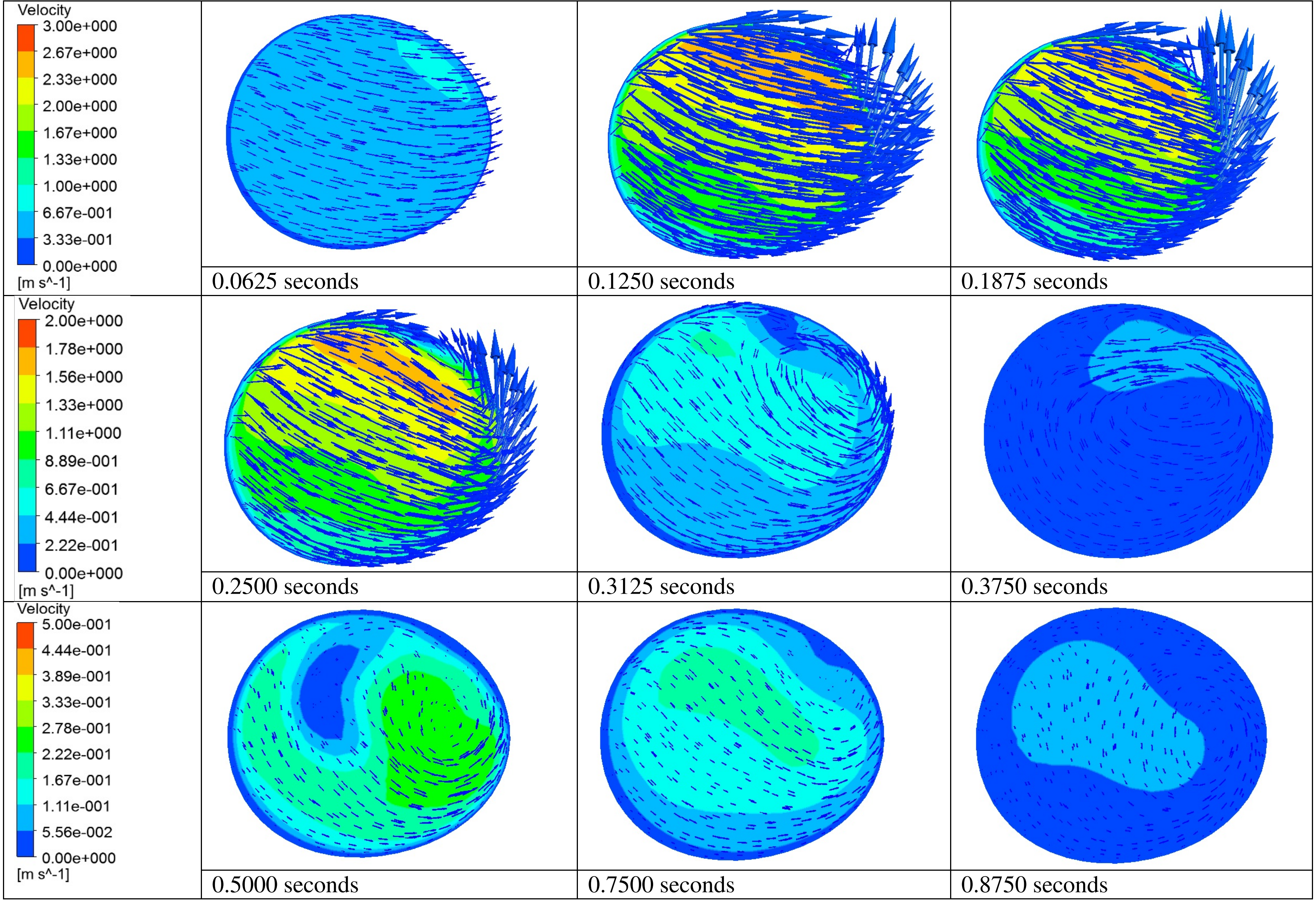

0.0625 seconds 0.1250 seconds 0.1875 seconds

0.2500 seconds 0.3125 seconds 0.3750 seconds

0.5000 seconds 0.7500 seconds 0.8750 seconds

Velocity Transverse - Descending Arch (Transient Flow, Rigid Wall Case)

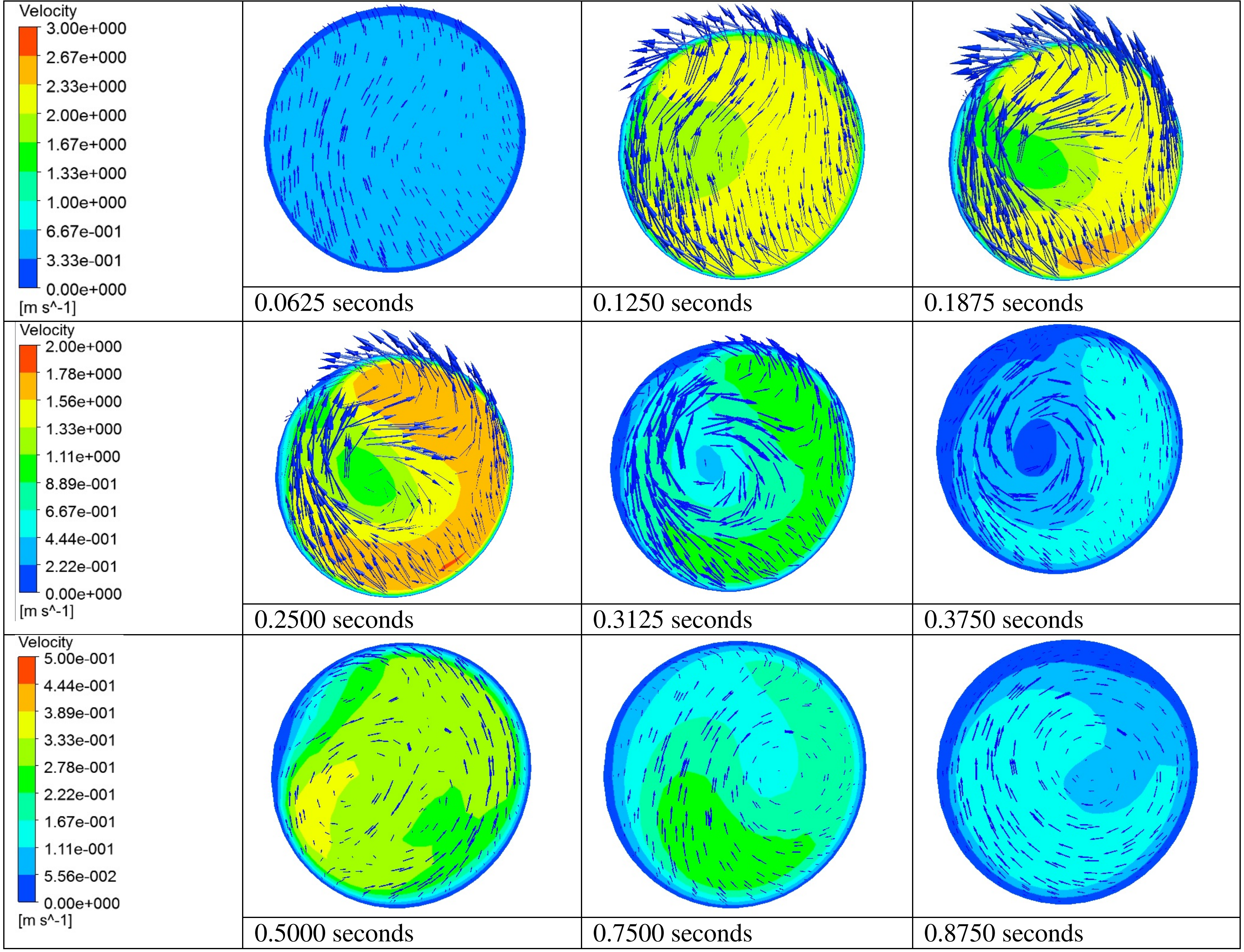

Velocity Transverse - Descending Aorta (Transient Flow, Rigid Wall Case)

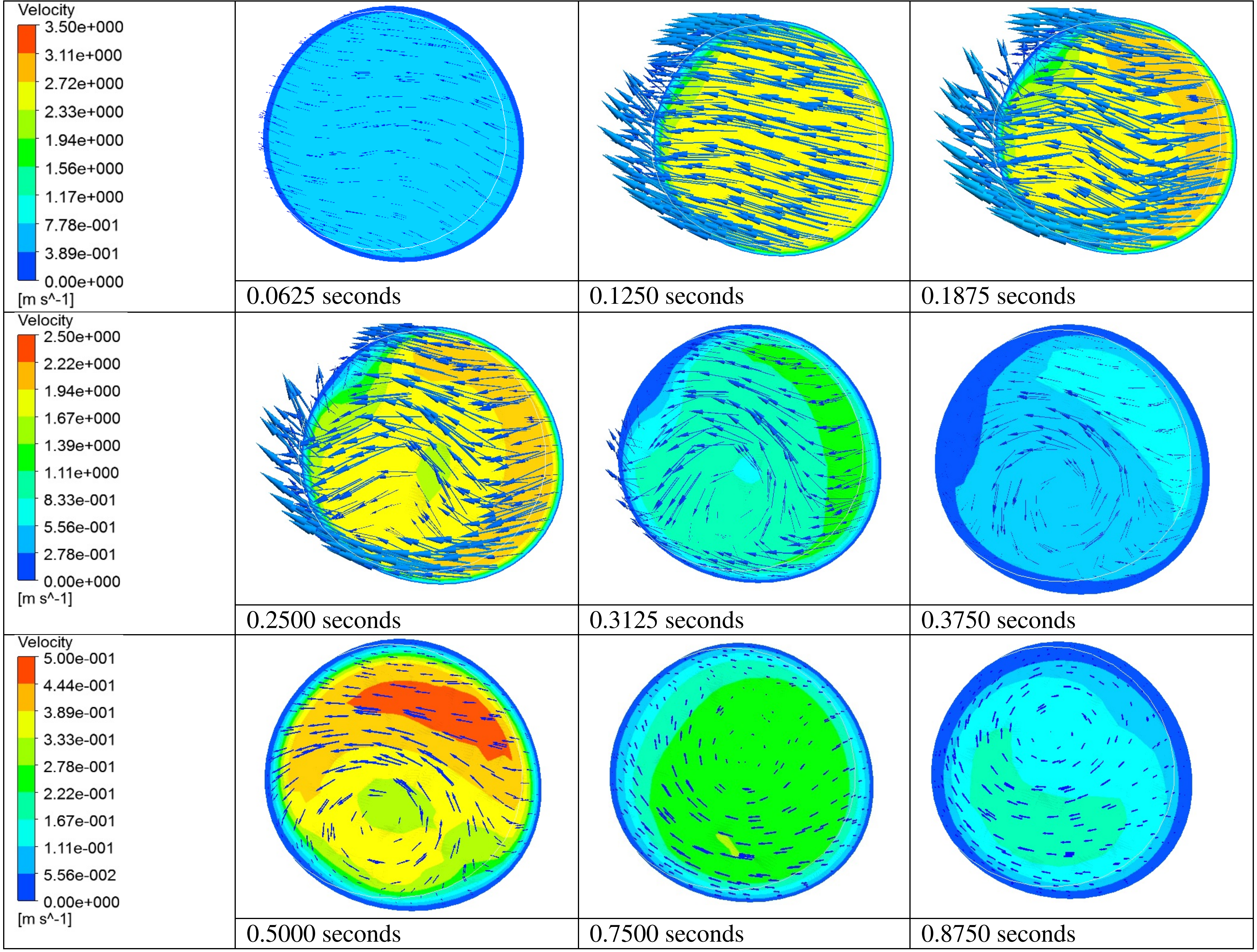

0.0625 seconds
0.1250 seconds
0.1875 seconds
0.2500 seconds
0.3125 seconds
0.3750 seconds
0.5000 seconds
0.7500 seconds
0.8750 seconds

WSS - Transient Flow, Rigid Wall Case

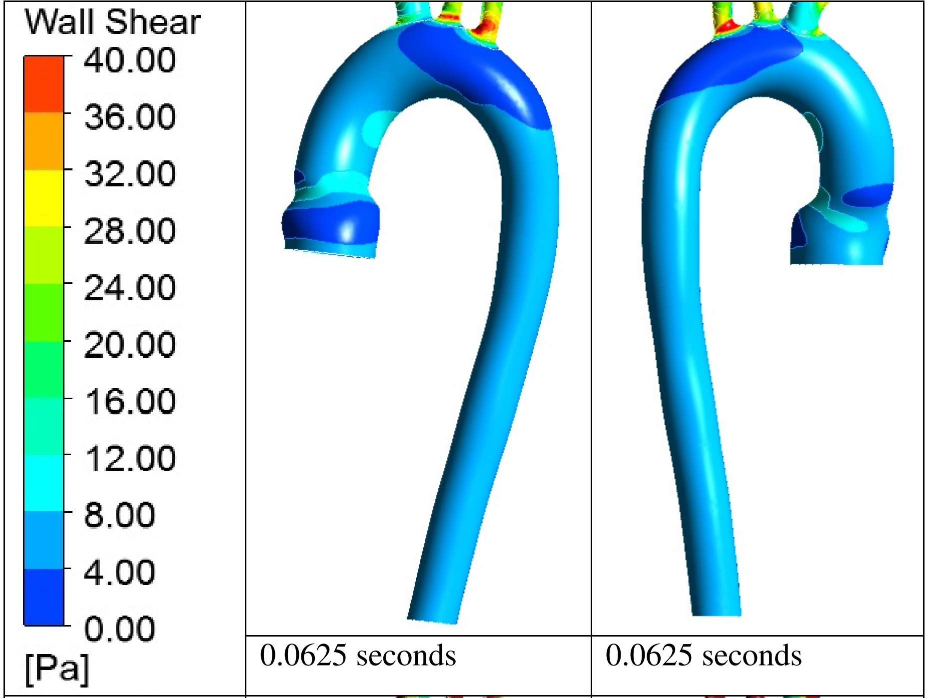

0.0625 seconds

0.0625 seconds

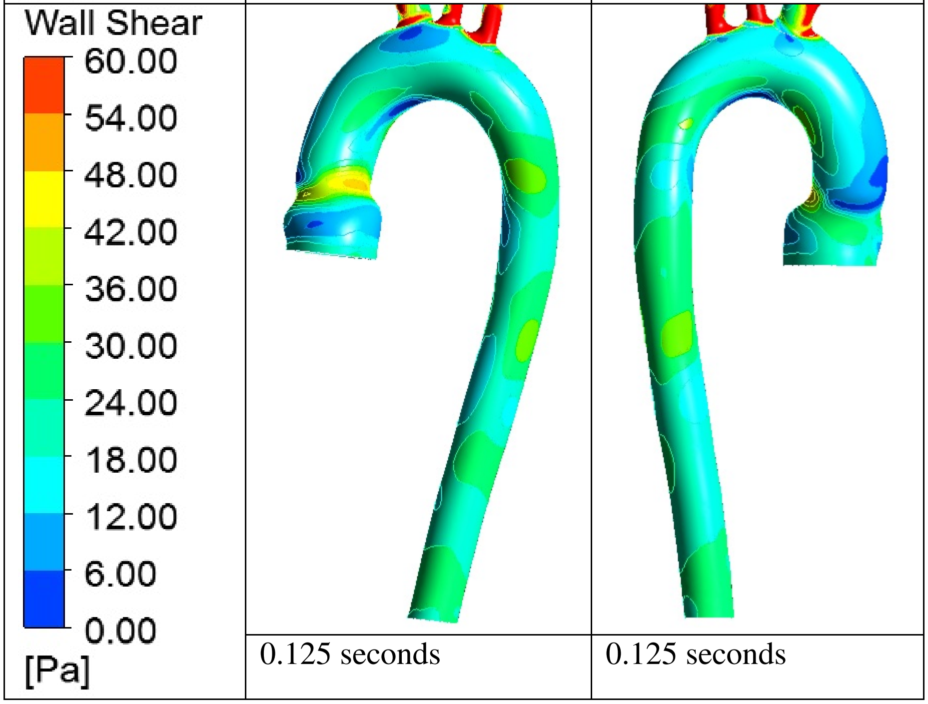

0.125 seconds

0.125 seconds

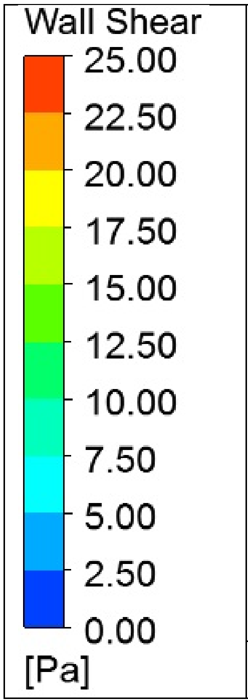

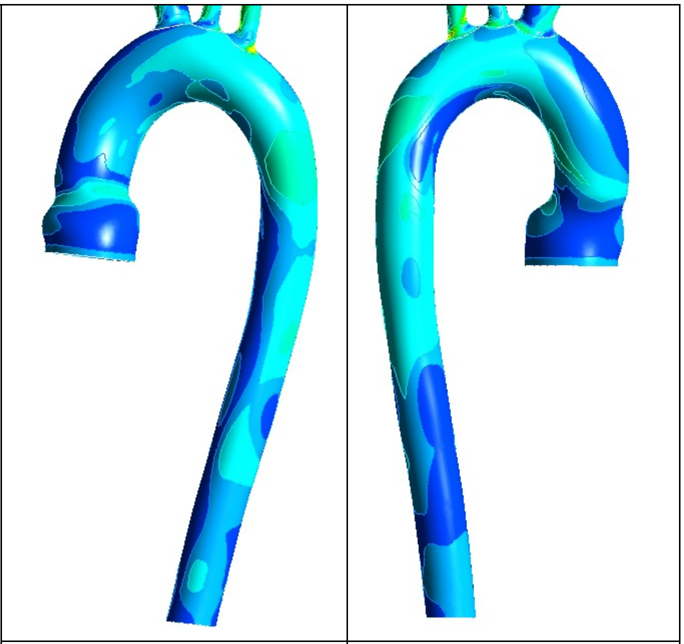

0.3125 seconds

0.3125 seconds

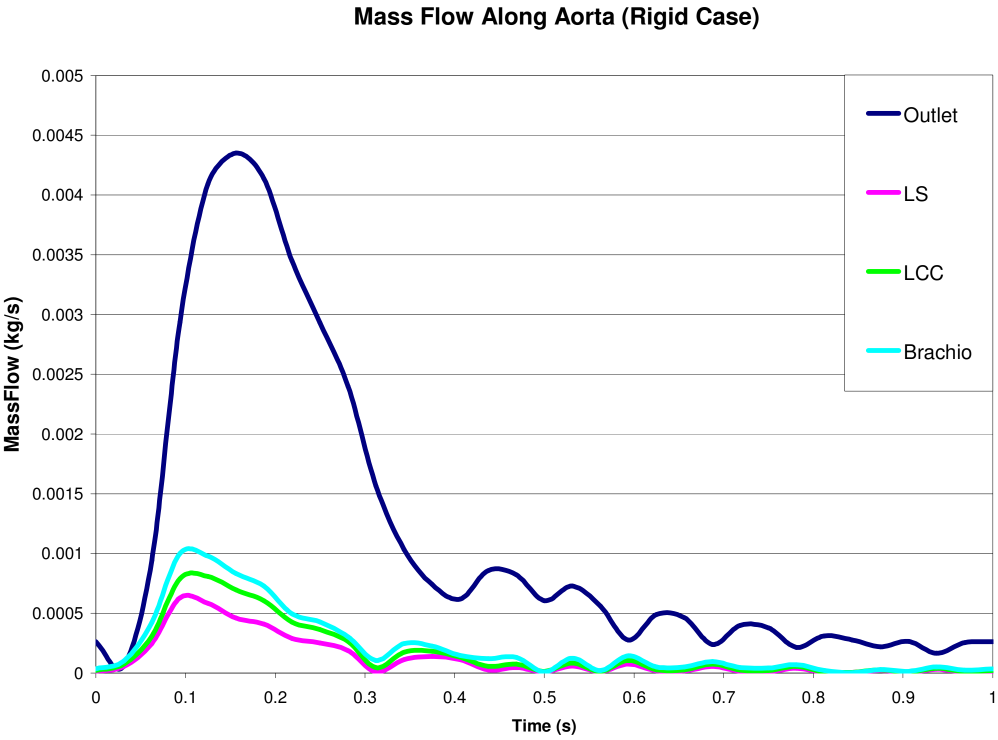
Mass Flow Along Aorta (Rigid Case)
MassFlow (kg/s)
0.005
0.0045
0.004
0.0035
0.003
0.0025
0.002
0.0015
0.001
0.0005
0
0
0.1
0.2
0.3
0.4
0.5
0.6
0.7
0.8
0.9
1
Time (s)
Outlet
LS
LCC
Brachio

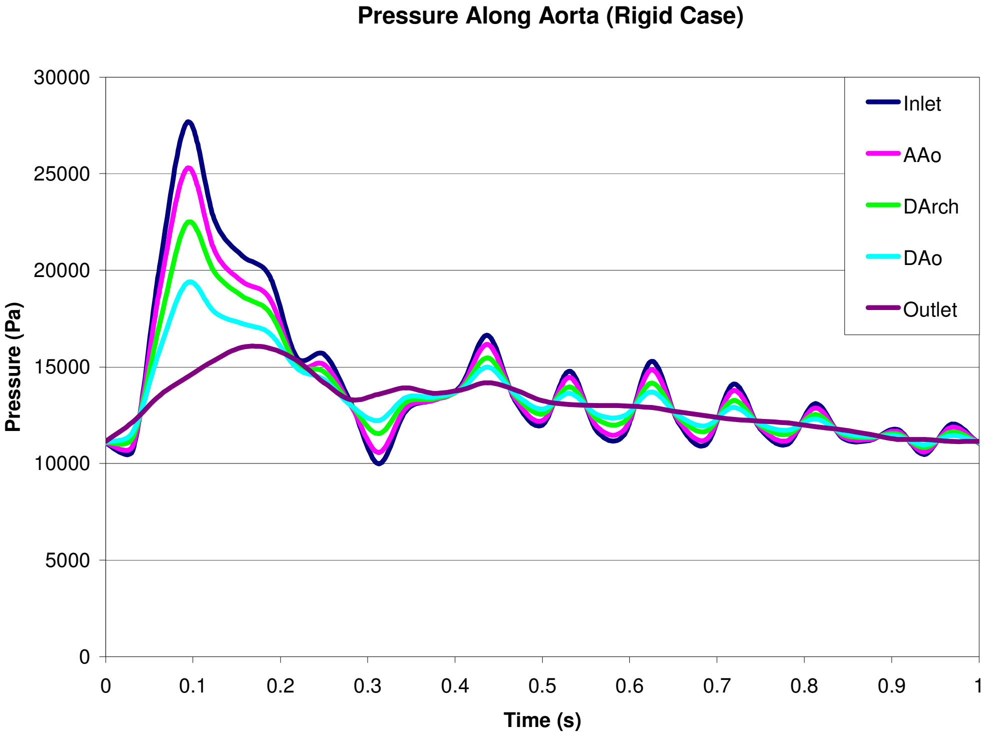
Pressure Along Aorta (Rigid Case)
Pressure (Pa)
30000
25000
20000
15000
10000
5000
0
0
0.1
0.2
0.3
0.4
0.5
0.6
0.7
0.8
0.9
1
Time (s)
Inlet
AAo
DArch
DAo
Outlet

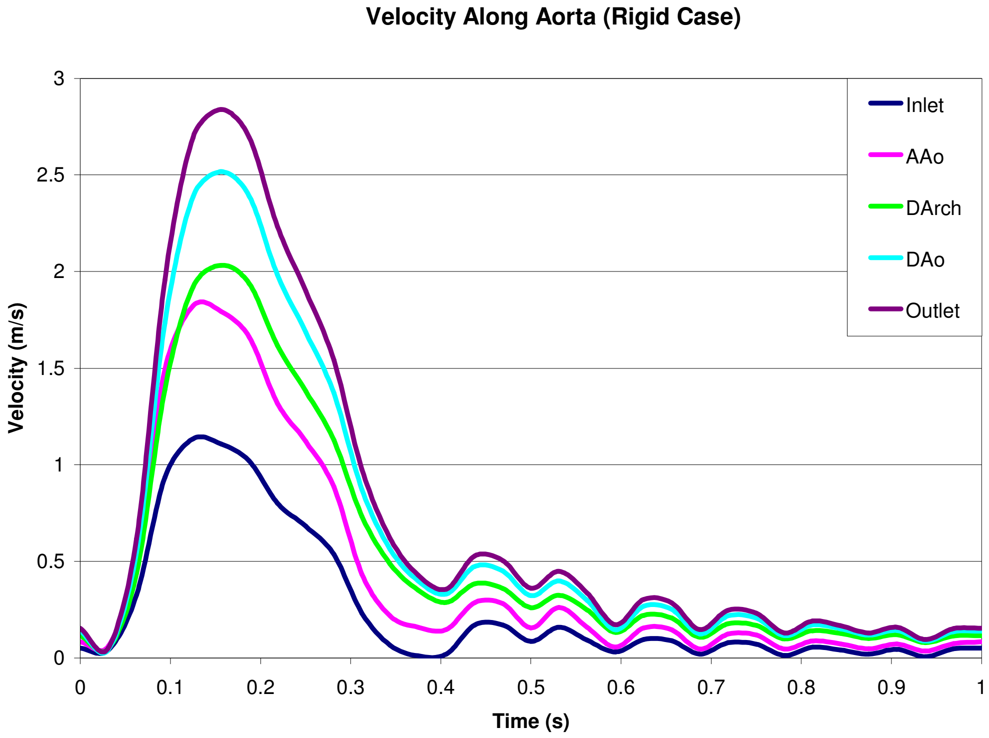
Velocity Along Aorta (Rigid Case)
Velocity (m/s)
3
2.5
2
1.5
1
0.5
0
0
0.1
0.2
0.3
0.4
0.5
0.6
0.7
0.8
0.9
1
Time (s)
Inlet
AAo
DArch
DAo
Outlet

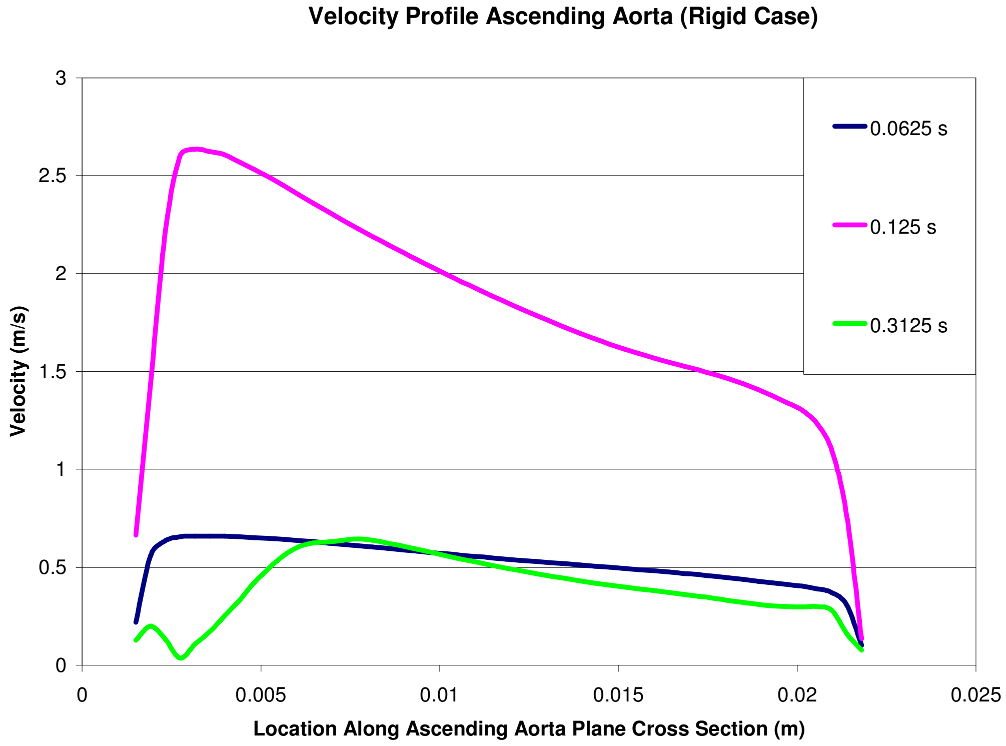
Velocity Profile Ascending Aorta (Rigid Case)
Velocity (m/s)
3
2.5
2
1.5
1
0.5
0
0
0.005
0.01
0.015
0.02
0.025
Location Along Ascending Aorta Plane Cross Section (m)
0.0625 s
0.125 s
0.3125 s

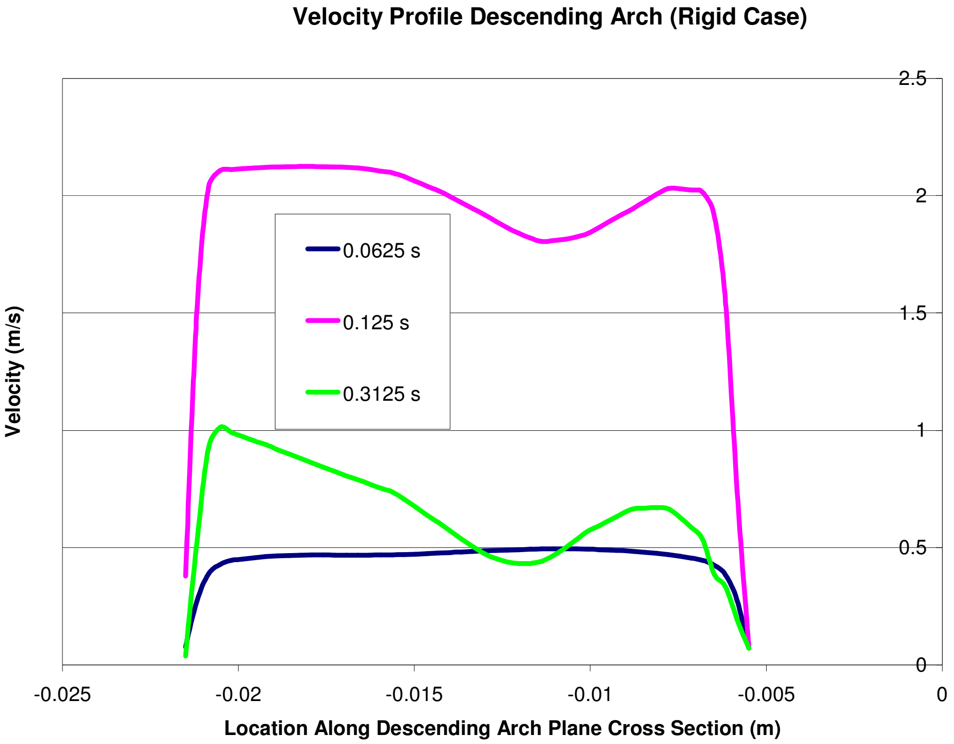
Velocity Profile Descending Arch (Rigid Case)
Velocity (m/s)
0.0625 s
0.125 s
0.3125 s
2.5
2
1.5
1
0.5
0
-0.025
-0.02
-0.015
-0.01
-0.005
0
Location Along Descending Arch Plane Cross Section (m)

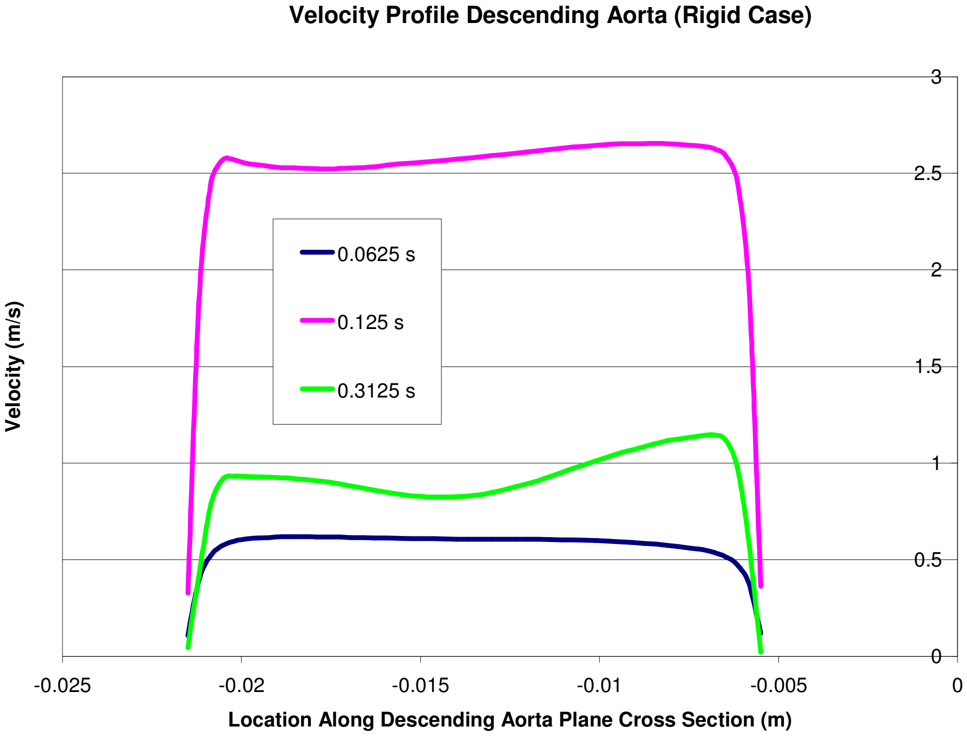
Velocity Profile Descending Aorta (Rigid Case)
Velocity (m/s)
0.0625 s
0.125 s
0.3125 s
3
2.5
2
1.5
1
0.5
0
-0.025
-0.02
-0.015
-0.01
-0.005
0
Location Along Descending Aorta Plane Cross Section (m)

10 Appendix C - Fixed Inlet, Transient Flow, Compliant Wall Results

Streamlines - Fixed Inlet, Transient Flow, Compliant Wall Case

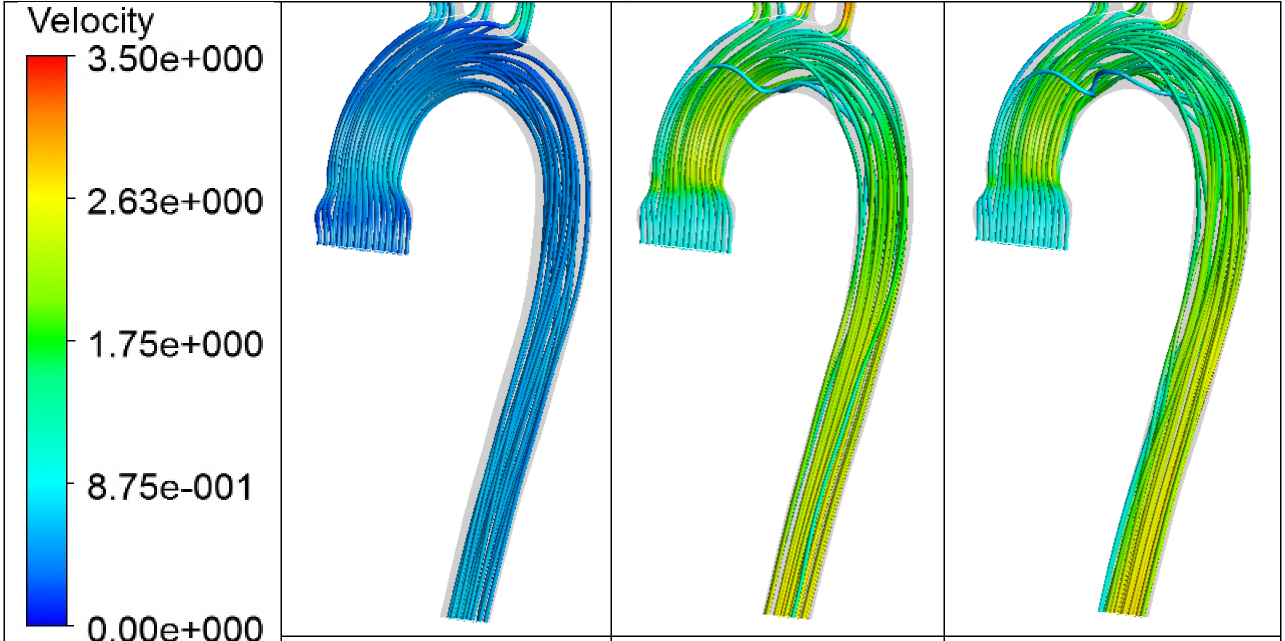

0.0625 seconds 0.1250 seconds 0.1875 seconds

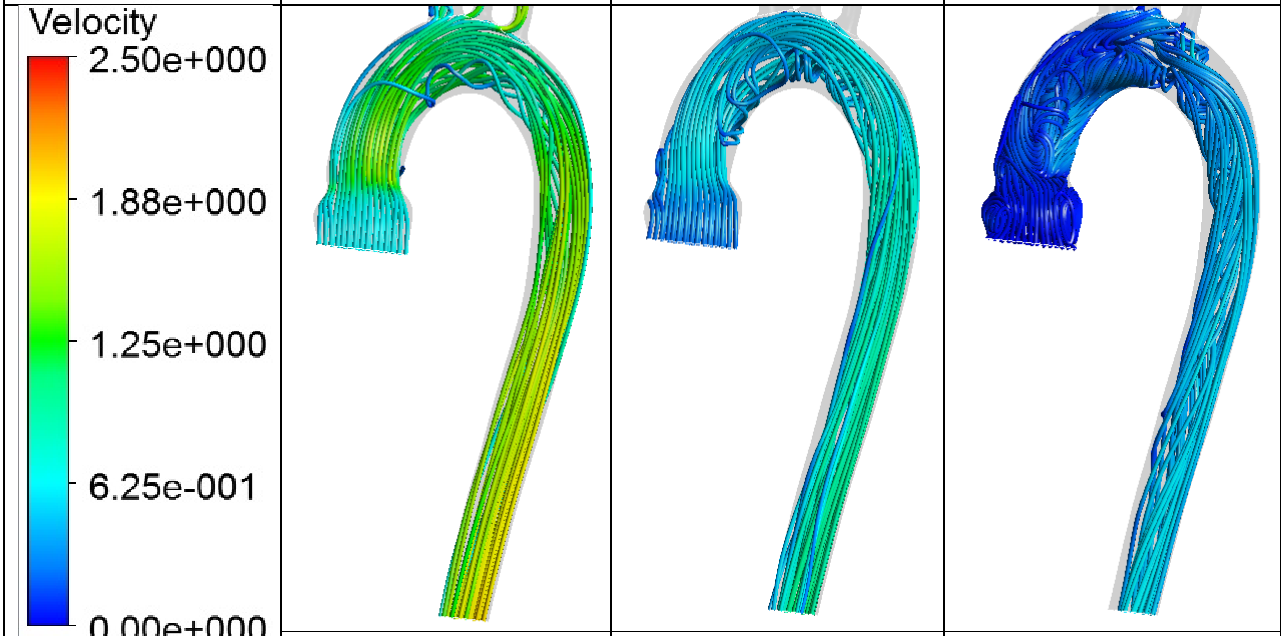

0.2500 seconds 0.3125 seconds 0.3750 seconds

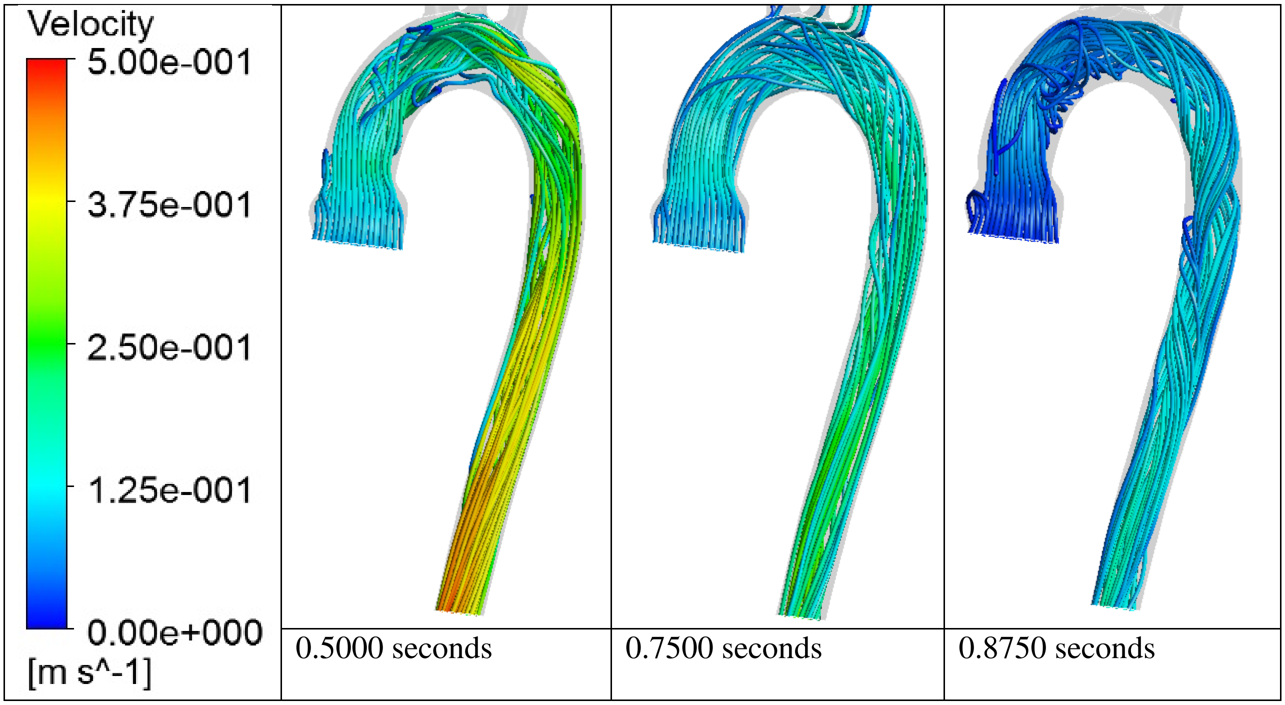

0.5000 seconds

0.7500 seconds

0.8750 seconds

Velocity Transverse - Ascending Aorta (Fixed Inlet, Transient Flow, Compliant Wall Case)

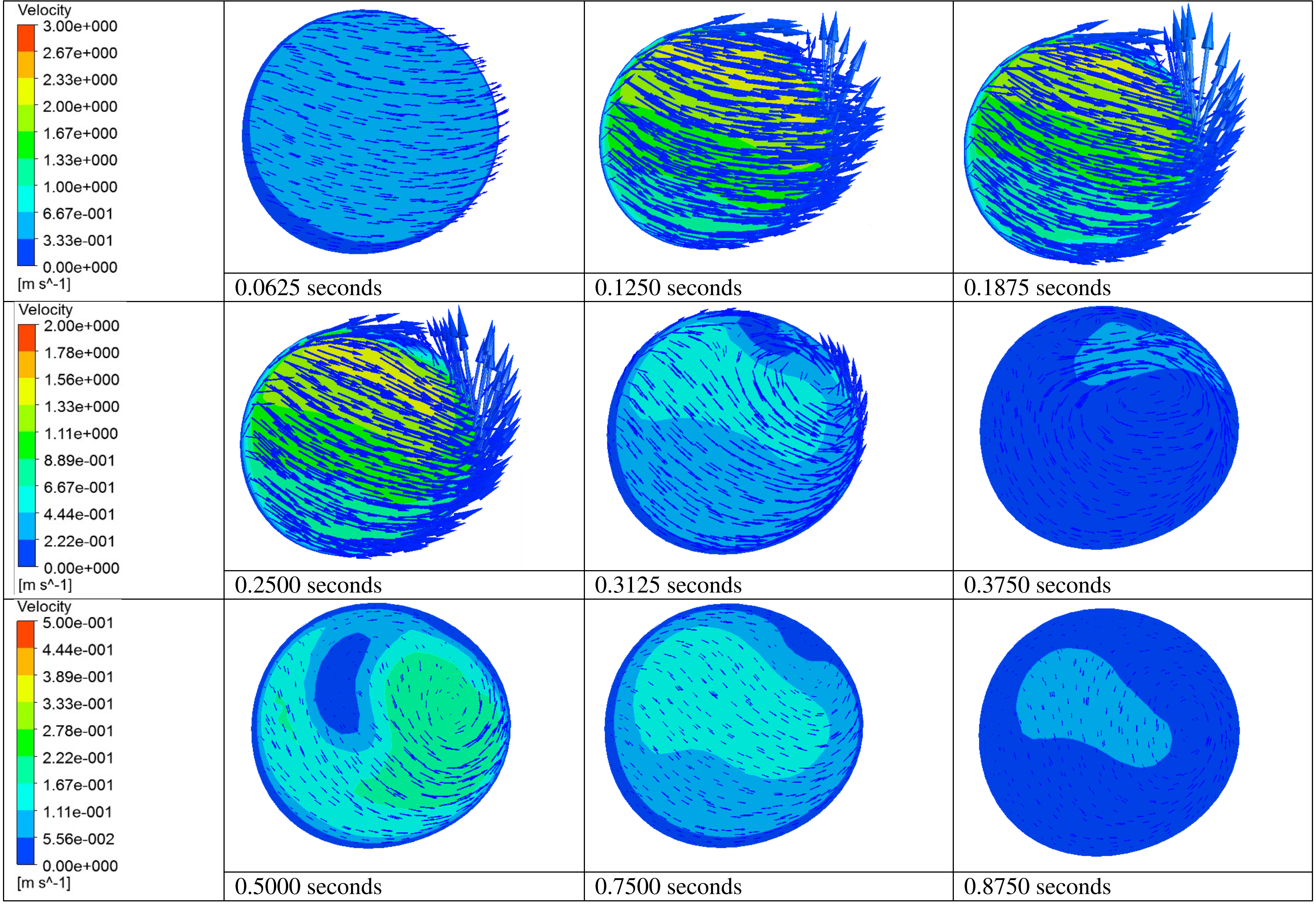

0.0625 seconds

0.1250 seconds

0.1875 seconds

0.2500 seconds

0.3125 seconds

0.3750 seconds

0.5000 seconds

0.7500 seconds

0.8750 seconds

Velocity Transverse - Descending Arch (Fixed Inlet, Transient Flow, Compliant Wall Case)

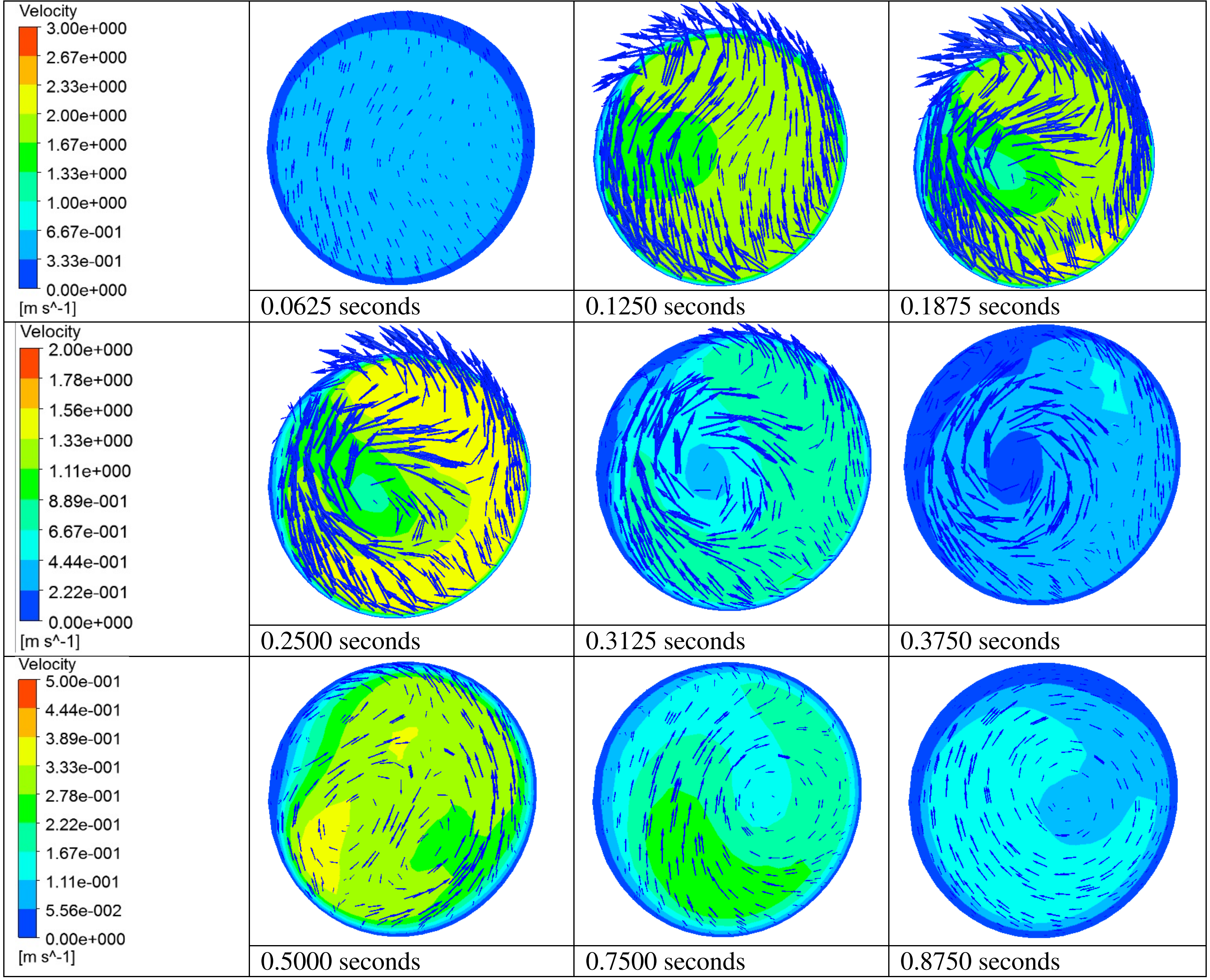

0.0625 seconds 0.1250 seconds 0.1875 seconds

0.2500 seconds 0.3125 seconds 0.3750 seconds

0.5000 seconds 0.7500 seconds 0.8750 seconds

Velocity Transverse - Descending Aorta (Fixed Inlet, Transient Flow, Compliant Wall Case)

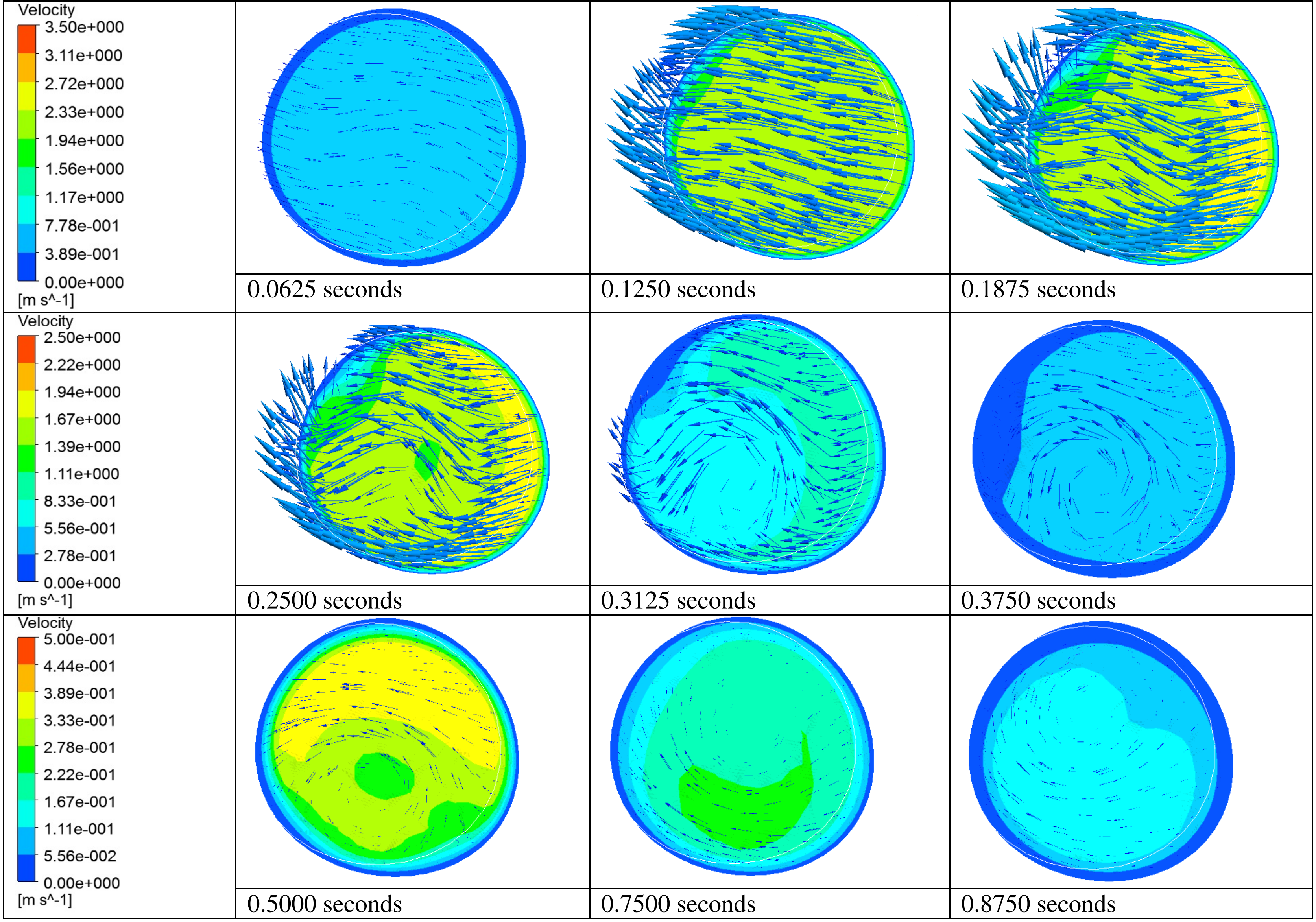

0.0625 seconds

0.1250 seconds

0.1875 seconds

0.2500 seconds

0.3125 seconds

0.3750 seconds

0.5000 seconds

0.7500 seconds

0.8750 seconds

WSS - Fixed Inlet, Transient Flow, Compliant Wall Case

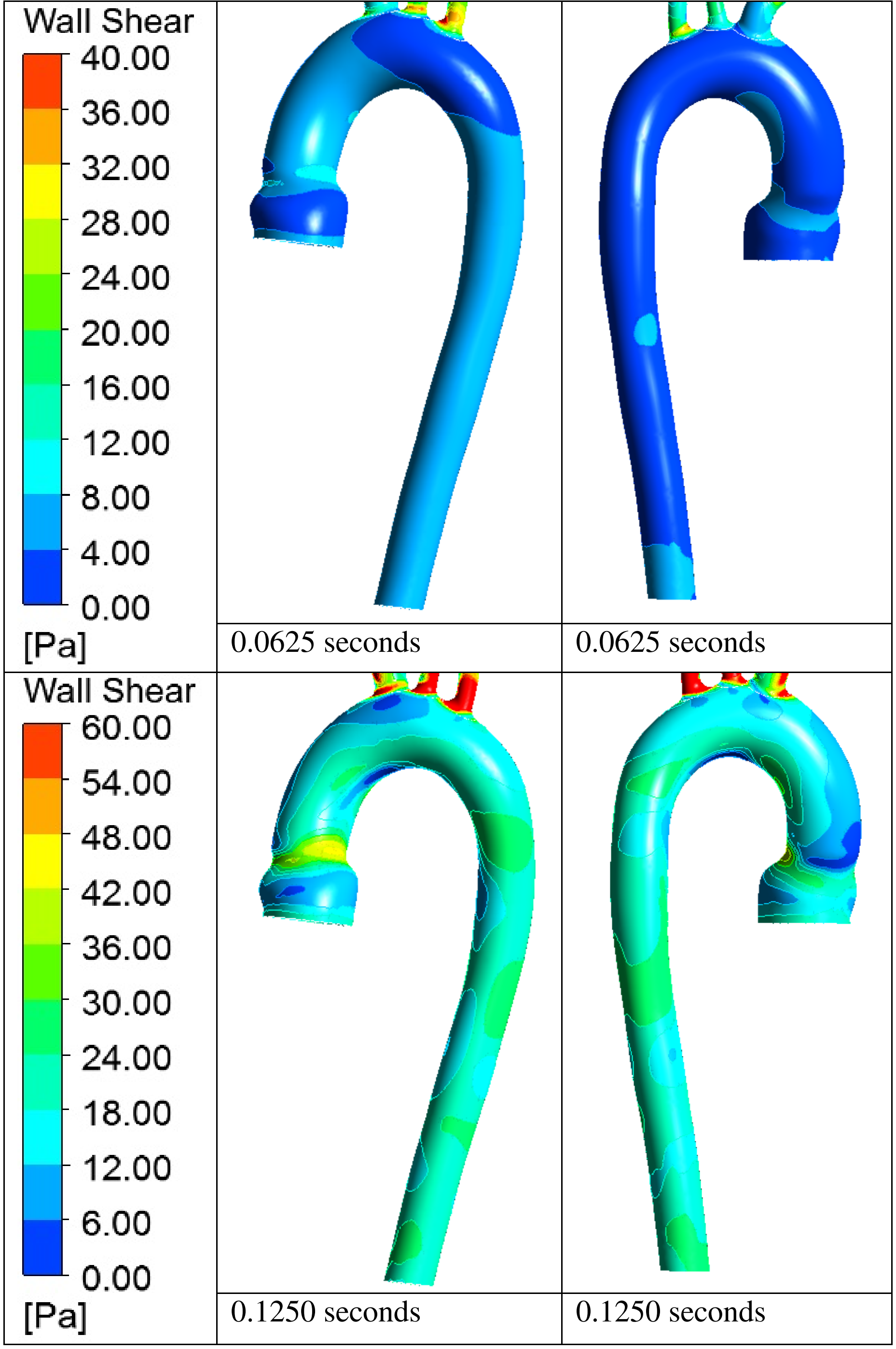

0.0625 seconds | 0.0625 seconds

0.1250 seconds | 0.1250 seconds

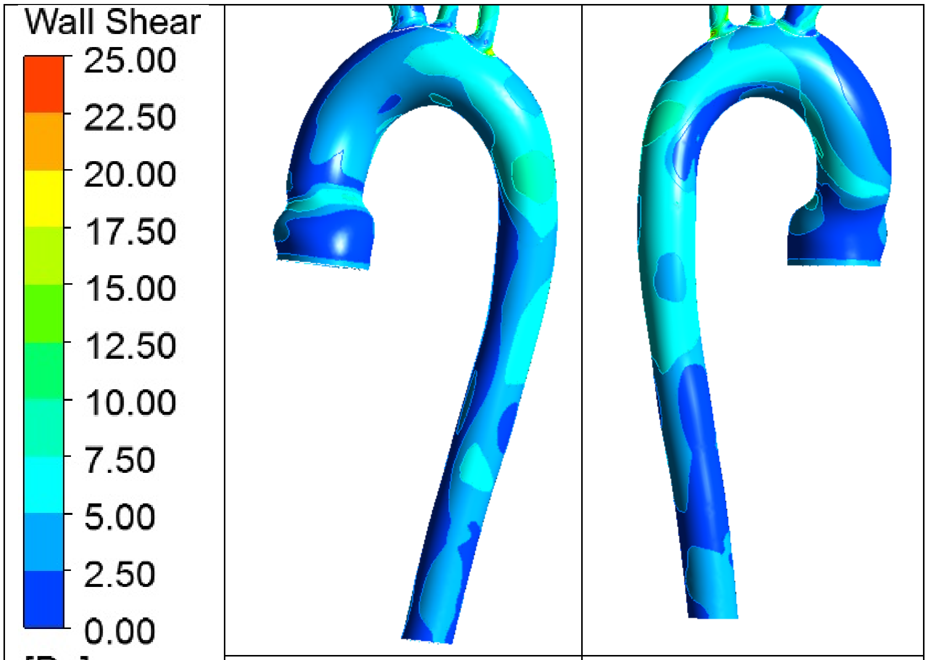

0.3125 seconds

0.3125 seconds

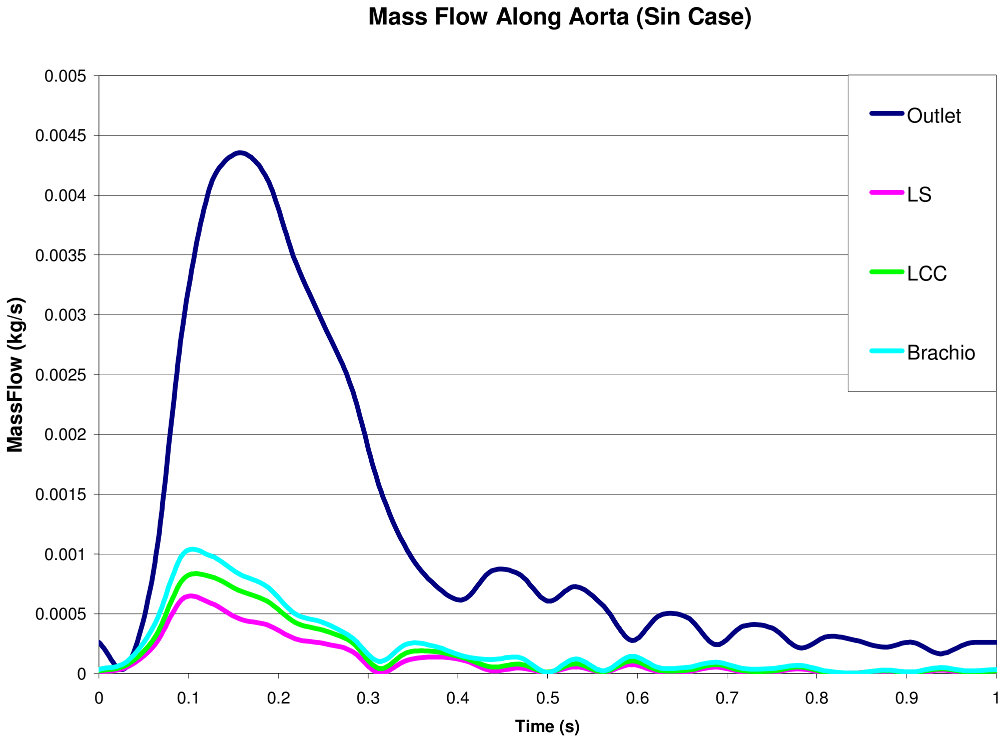
Mass Flow Along Aorta (Sin Case)
MassFlow (kg/s)
0.005
0.0045
0.004
0.0035
0.003
0.0025
0.002
0.0015
0.001
0.0005
0
0
0.1
0.2
0.3
0.4
0.5
0.6
0.7
0.8
0.9
1
Time (s)
Outlet
LS
LCC
Brachio

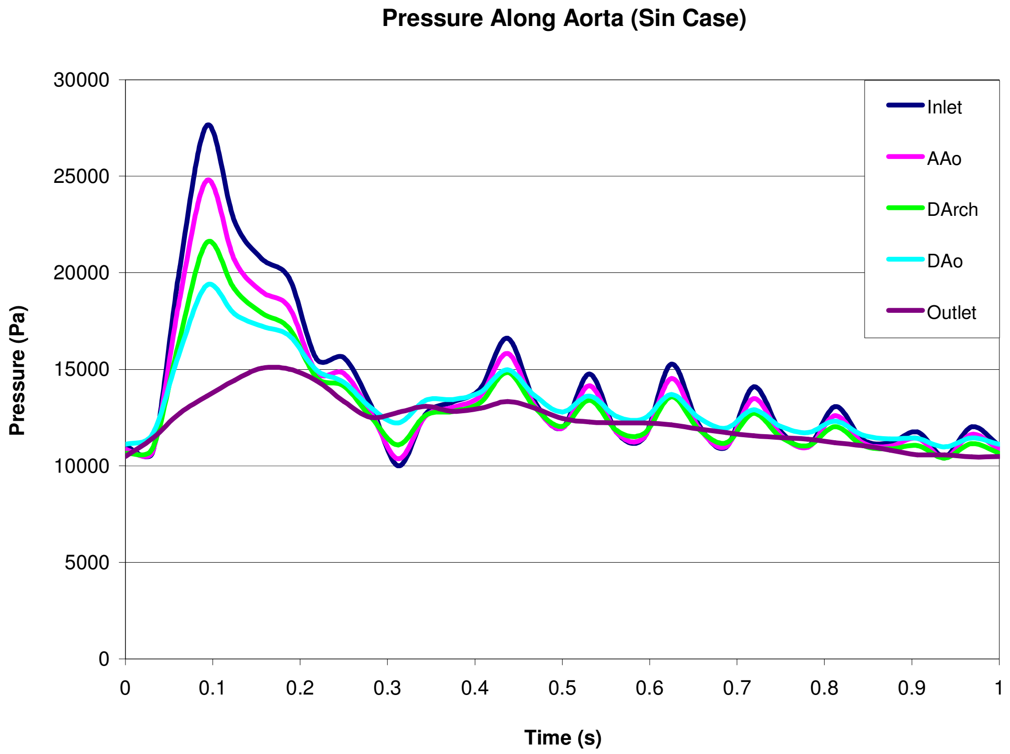
Pressure Along Aorta (Sin Case)
Pressure (Pa)
30000
25000
20000
15000
10000
5000
0
0
0.1
0.2
0.3
0.4
0.5
0.6
0.7
0.8
0.9
1
Time (s)
Inlet
AAo
DArch
DAo
Outlet

Velocity Along Aorta (Sin Case)

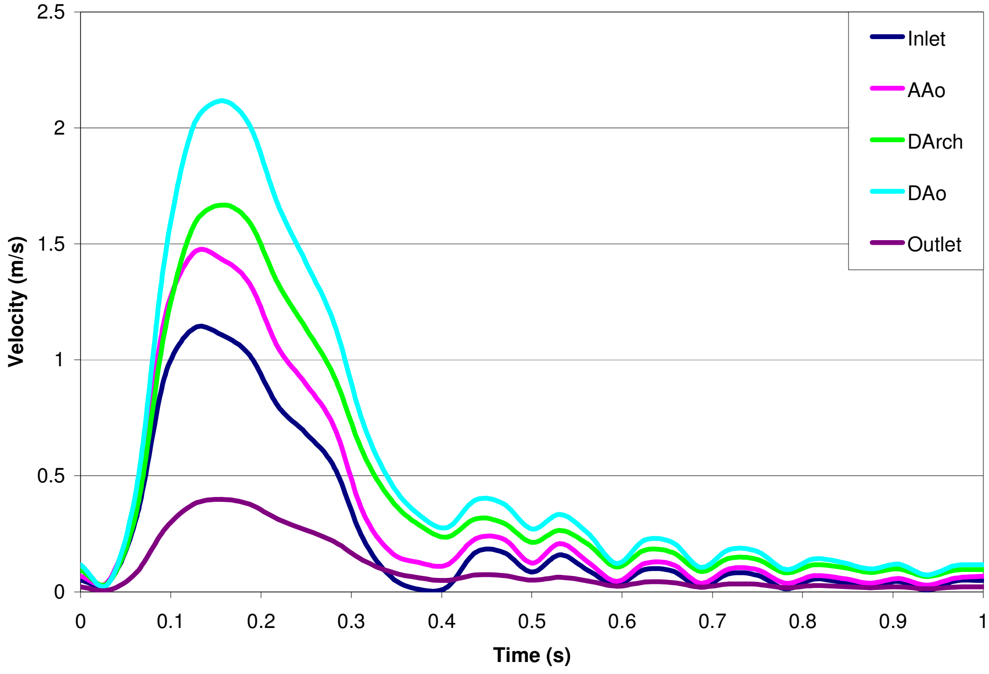

Velocity Profile Ascending Aorta (Sin Case)

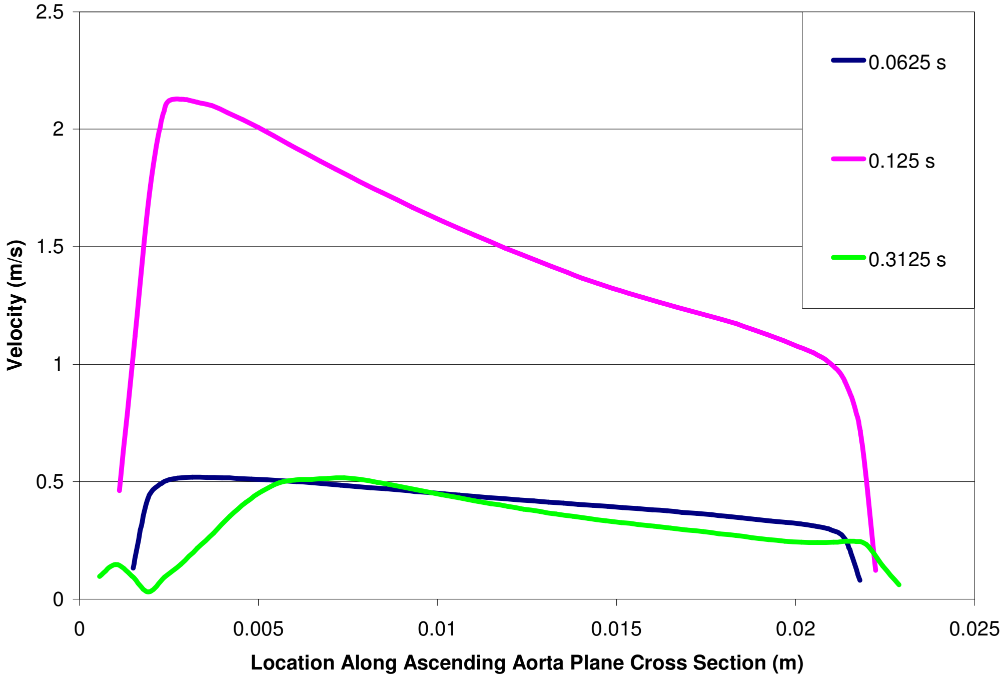

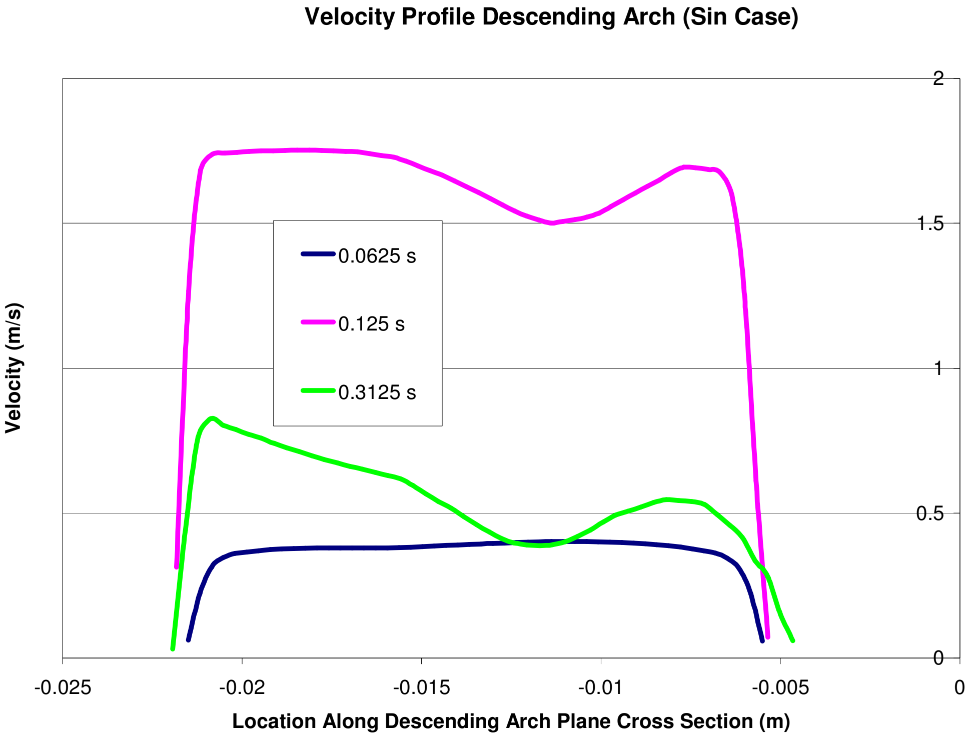
Velocity Profile Descending Arch (Sin Case)
Velocity (m/s)
2
1.5
1
0.5
0
-0.025
-0.02
-0.015
-0.01
-0.005
0
Location Along Descending Arch Plane Cross Section (m)
0.0625 s
0.125 s
0.3125 s

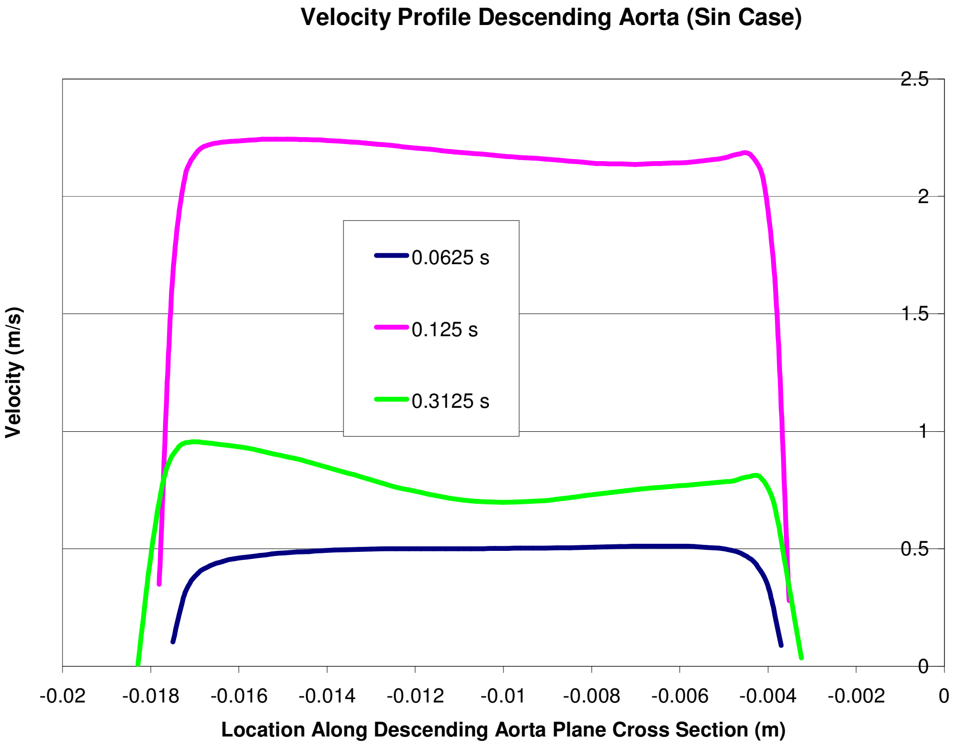
Velocity Profile Descending Aorta (Sin Case)
Velocity (m/s)
2.5
2
1.5
1
0.5
0
-0.02
-0.018
-0.016
-0.014
-0.012
-0.01
-0.008
-0.006
-0.004
-0.002
0
Location Along Descending Aorta Plane Cross Section (m)
0.0625 s
0.125 s
0.3125 s

11 Appendix D - Transient Flow, Compliant Wall with MRI Inlet Flow Results

Streamlines - Transient Flow, Compliant Wall with MRI Inlet Flow Case

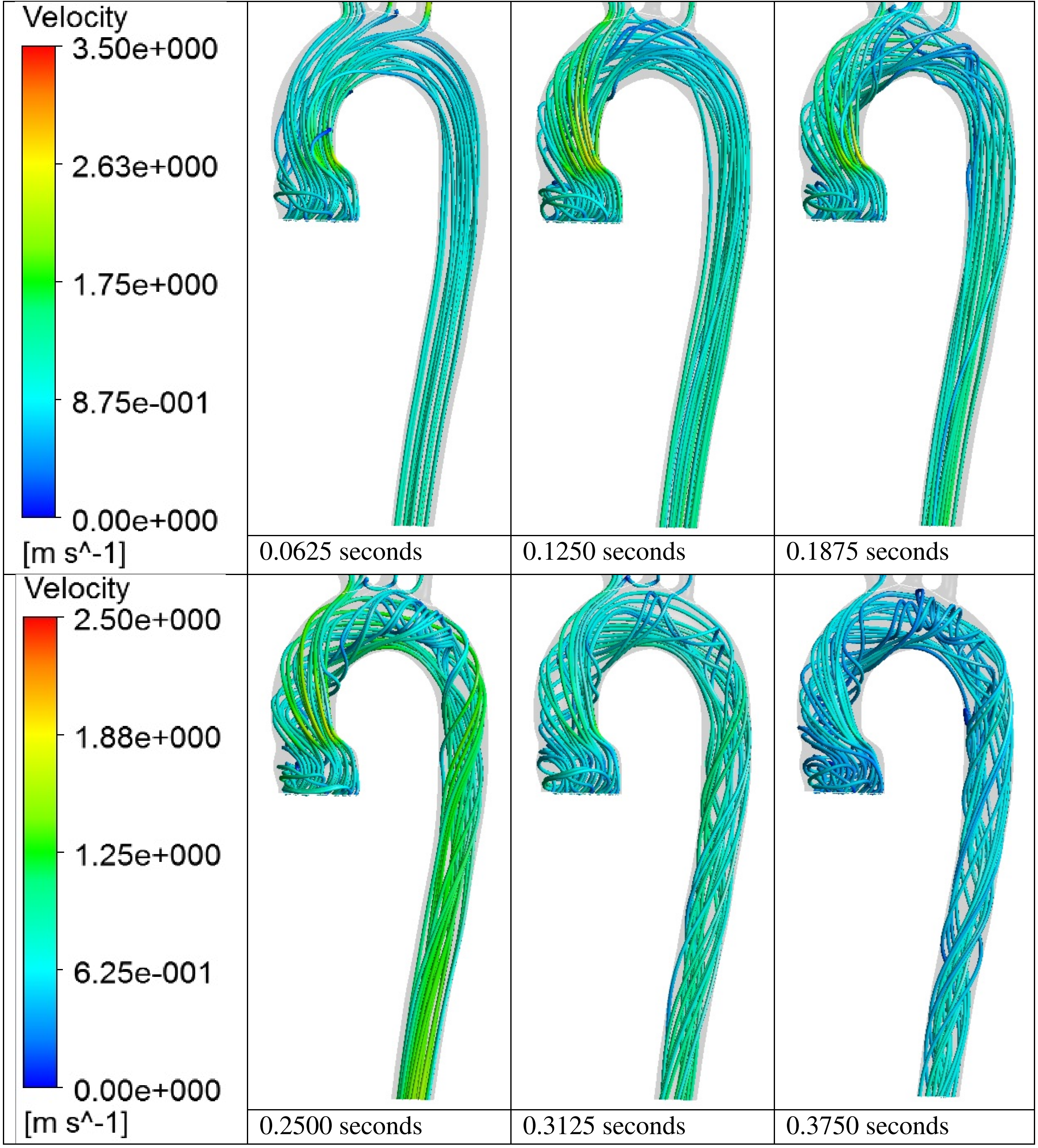

0.0625 seconds
0.1250 seconds
0.1875 seconds
0.2500 seconds
0.3125 seconds
0.3750 seconds

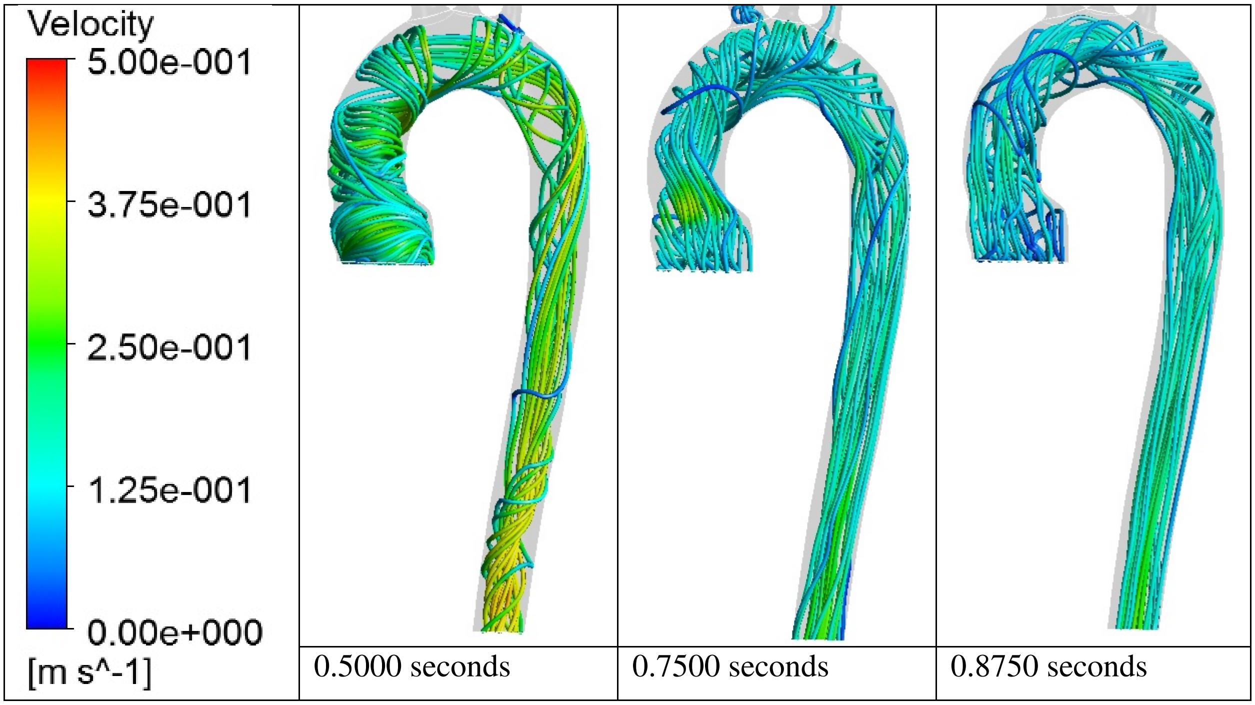

0.5000 seconds

0.7500 seconds

0.8750 seconds

Velocity Transverse - Ascending Aorta (Transient Flow, Compliant Wall with MRI Inlet Flow Case)

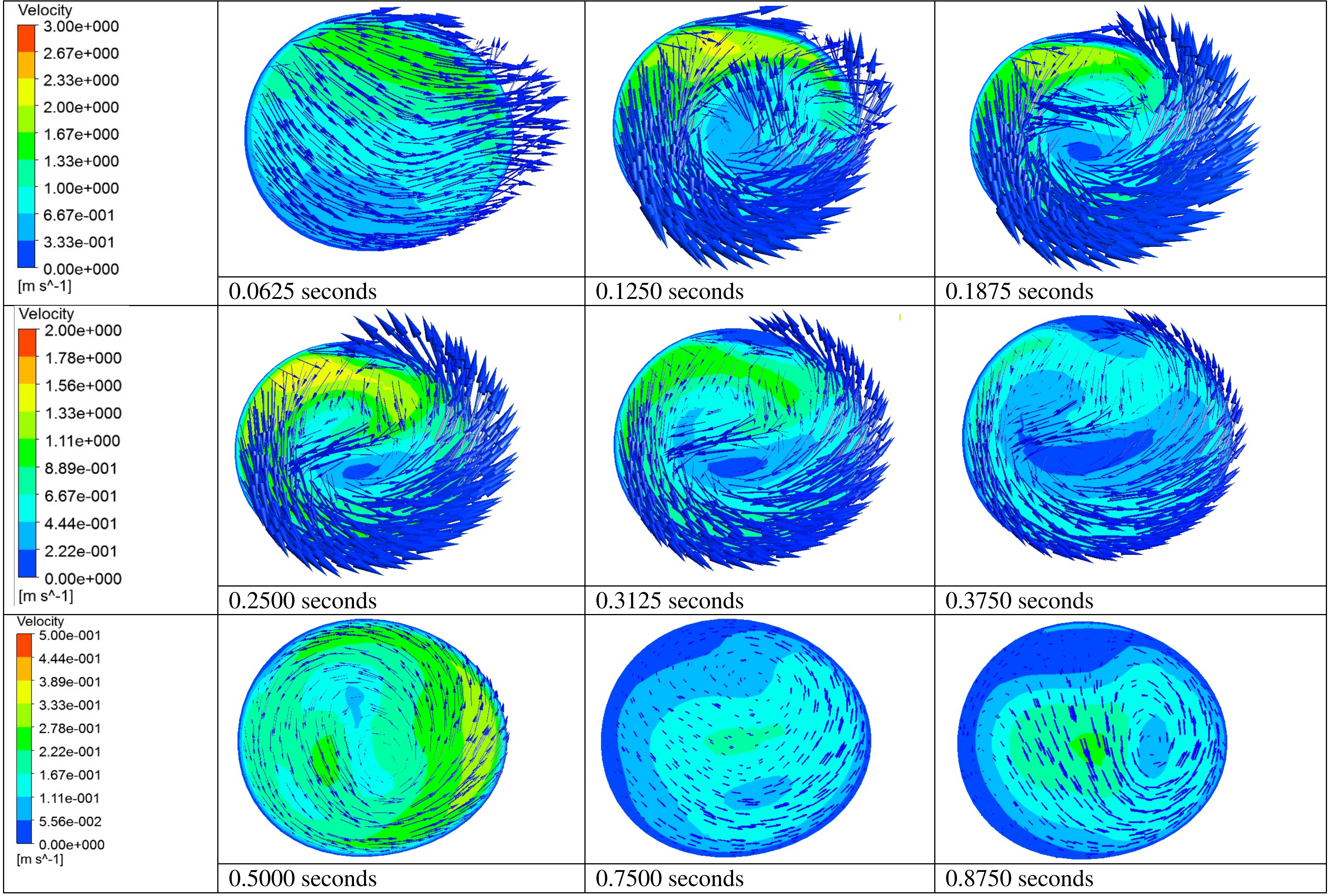

0.0625 seconds | 0.1250 seconds | 0.1875 seconds

0.2500 seconds | 0.3125 seconds | 0.3750 seconds

0.5000 seconds | 0.7500 seconds | 0.8750 seconds

Velocity Transverse - Descending Arch (Transient Flow, Compliant Wall with MRI Inlet Flow Case)

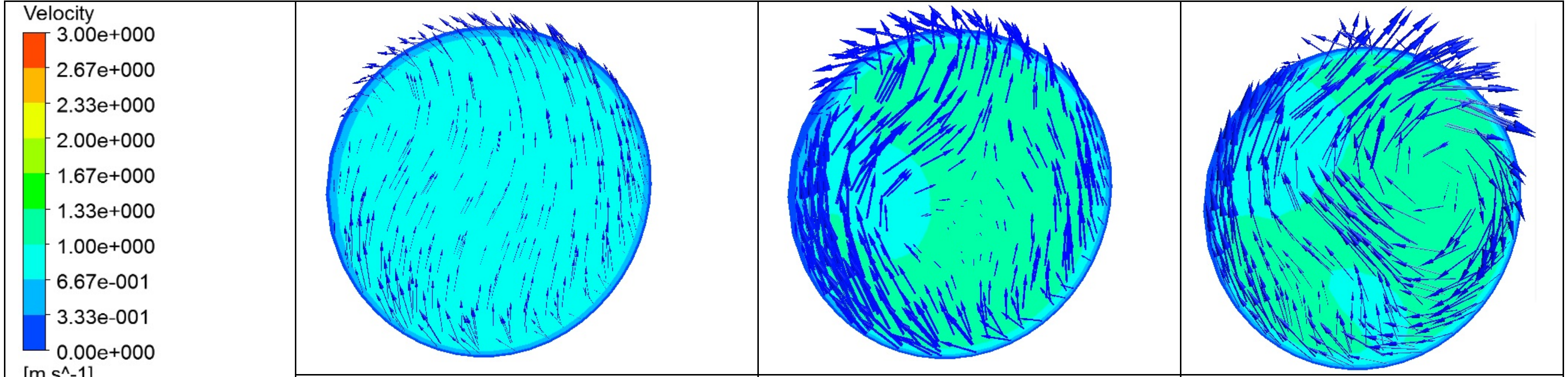

0.0625 seconds | 0.1250 seconds | 0.1875 seconds

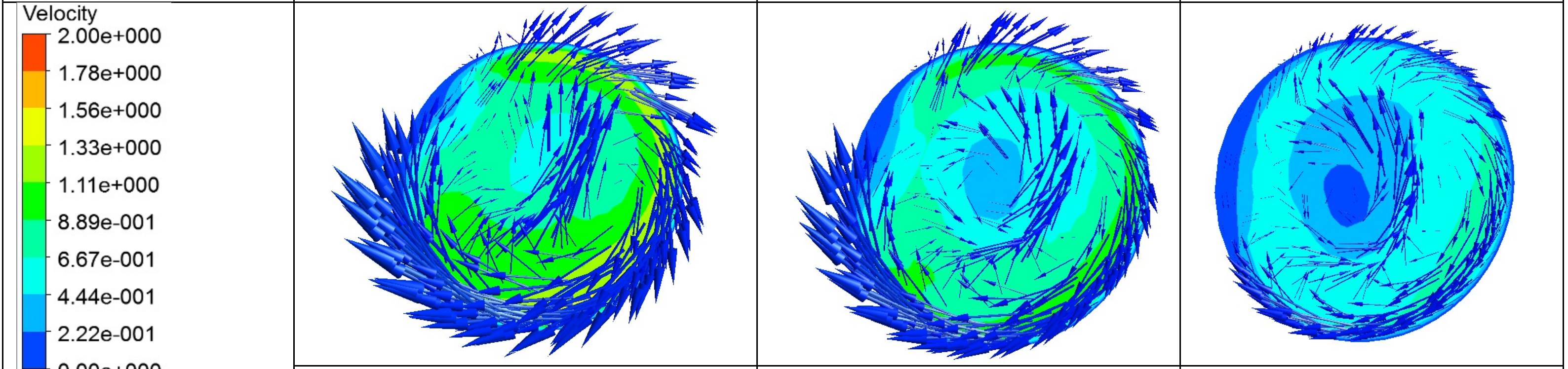

0.2500 seconds | 0.3125 seconds | 0.3750 seconds

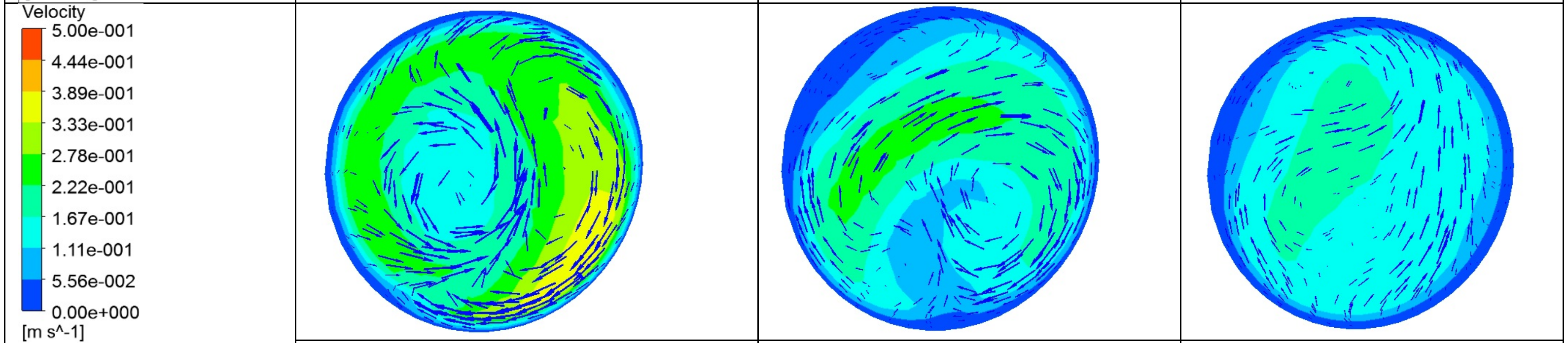

0.5000 seconds | 0.7500 seconds | 0.8750 seconds

Velocity Transverse - Descending Aorta (Transient Flow, Compliant Wall with MRI Inlet Flow Case)

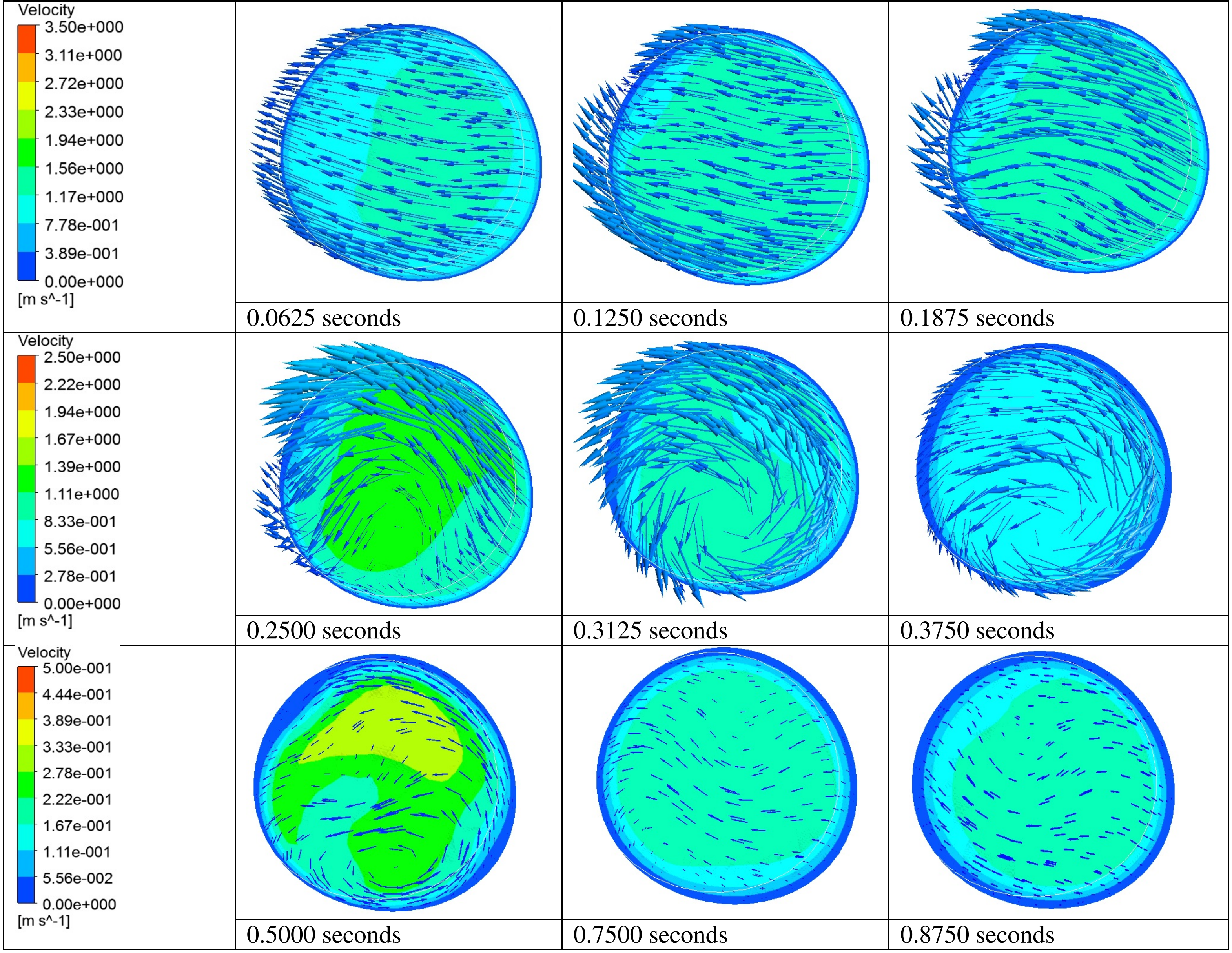

WSS - Transient Flow, Compliant Wall with MRI Inlet Flow Case

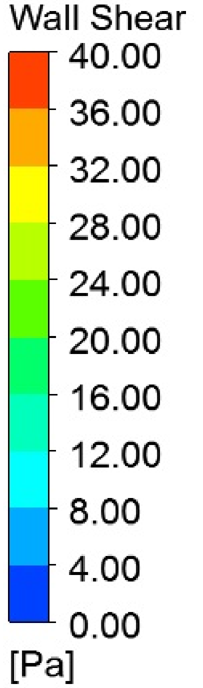	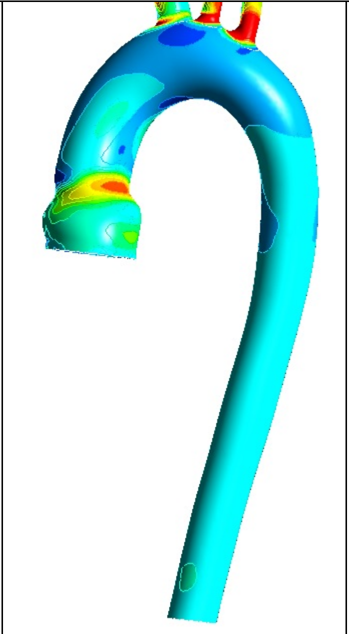	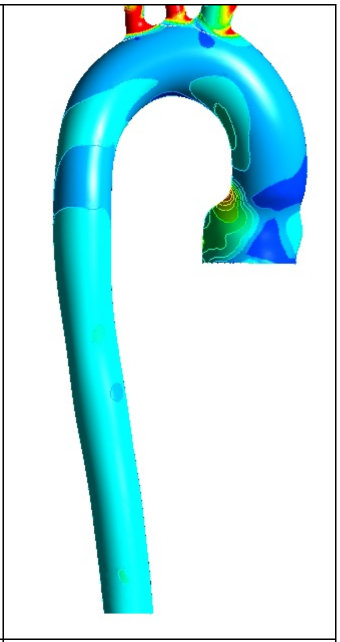
	0.0625 seconds	0.0625 seconds
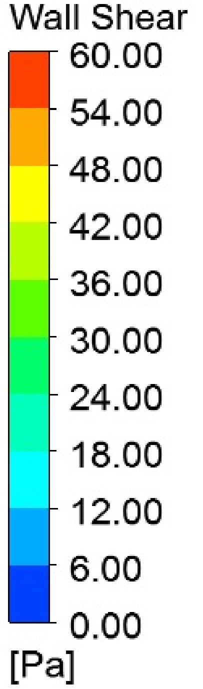	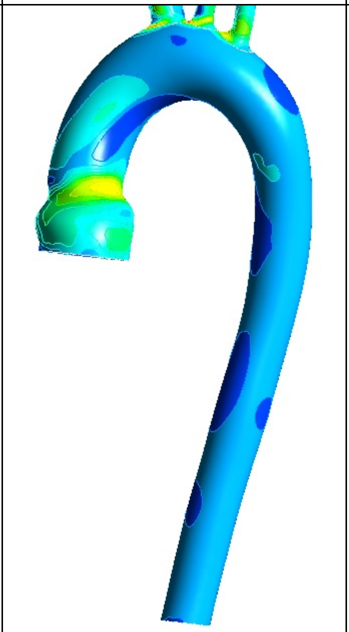	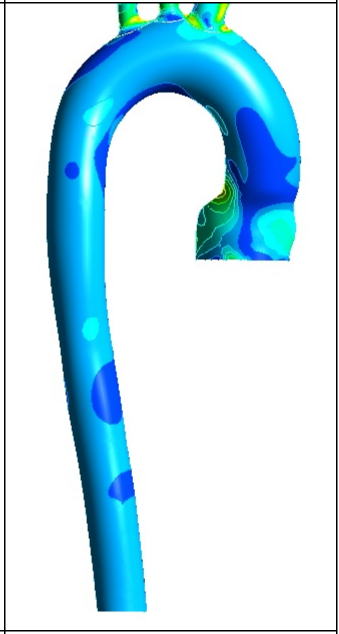
	0.1250 seconds	0.1250 seconds

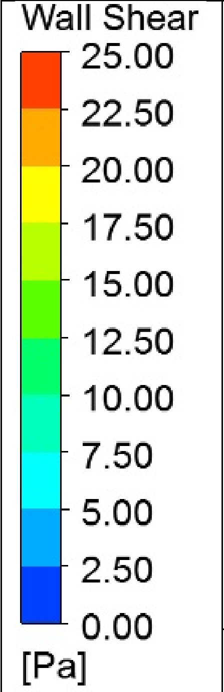	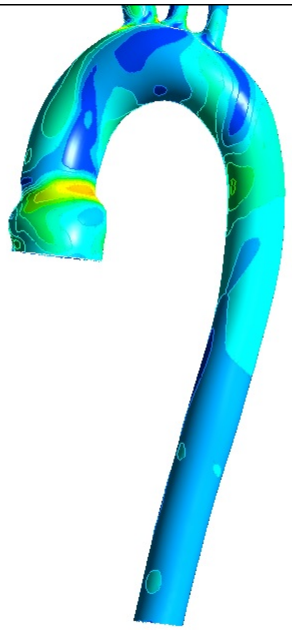	
	0.3125 seconds	0.3125 seconds

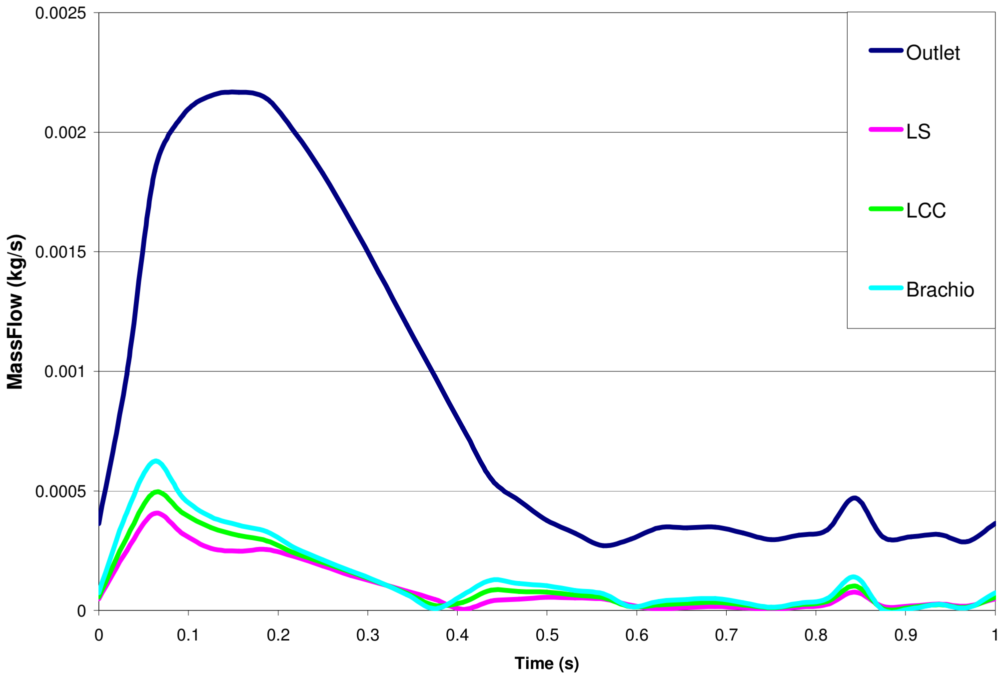

Mass Flow Along Aorta (MRI Case)

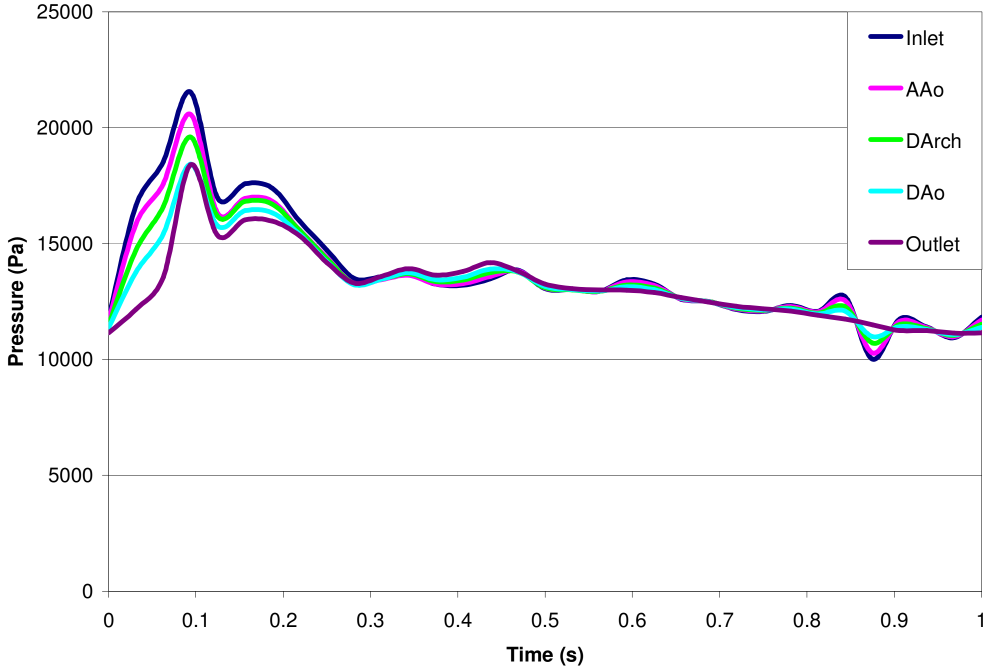

Pressure Along Aorta (MRI Case)

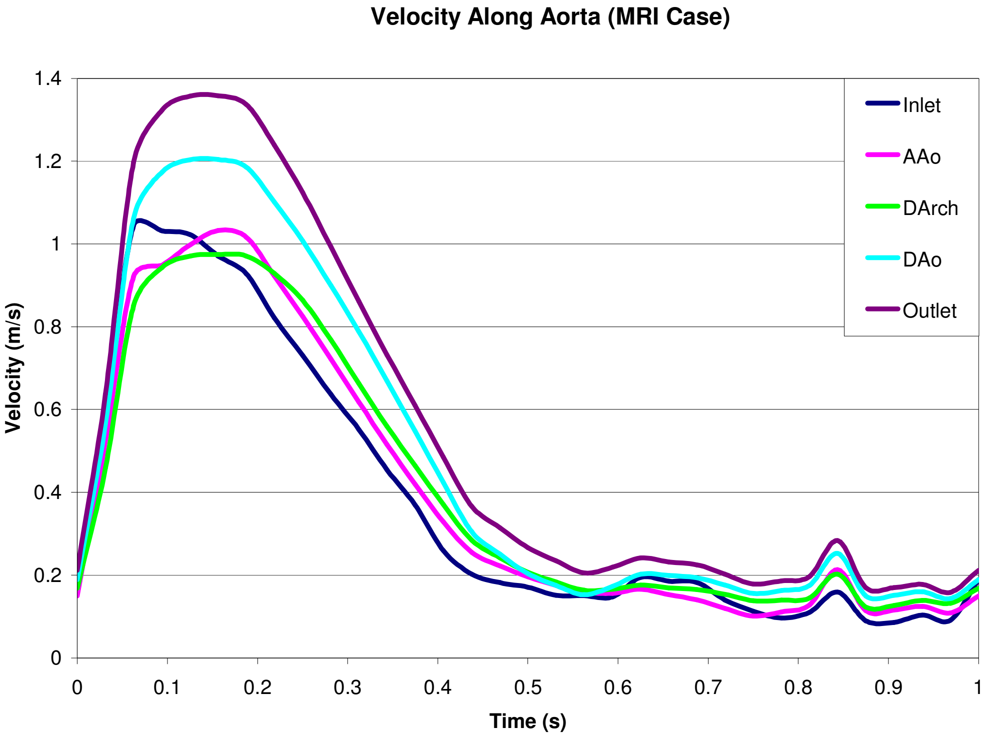
Velocity Along Aorta (MRI Case)
Velocity (m/s)
Time (s)
1.4
1.2
1
0.8
0.6
0.4
0.2
0
0.1
0.2
0.3
0.4
0.5
0.6
0.7
0.8
0.9
1
Inlet
AAo
DArch
DAo
Outlet

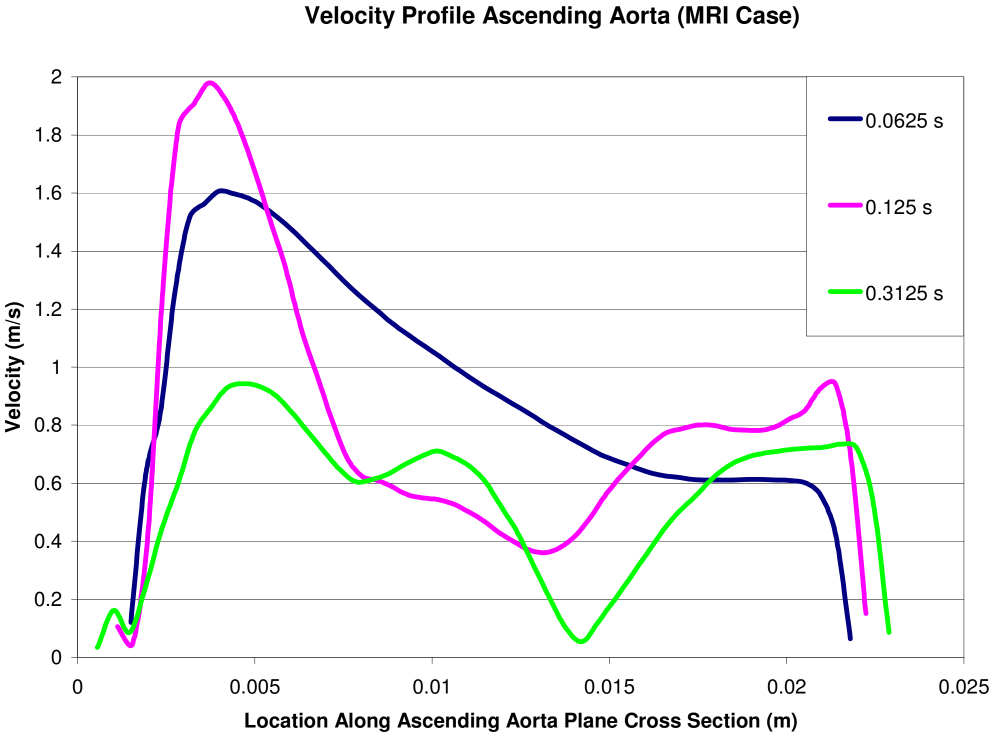
Velocity Profile Ascending Aorta (MRI Case)
Velocity (m/s)
Location Along Ascending Aorta Plane Cross Section (m)
2
1.8
1.6
1.4
1.2
1
0.8
0.6
0.4
0.2
0
0.005
0.01
0.015
0.02
0.025
0.0625 s
0.125 s
0.3125 s

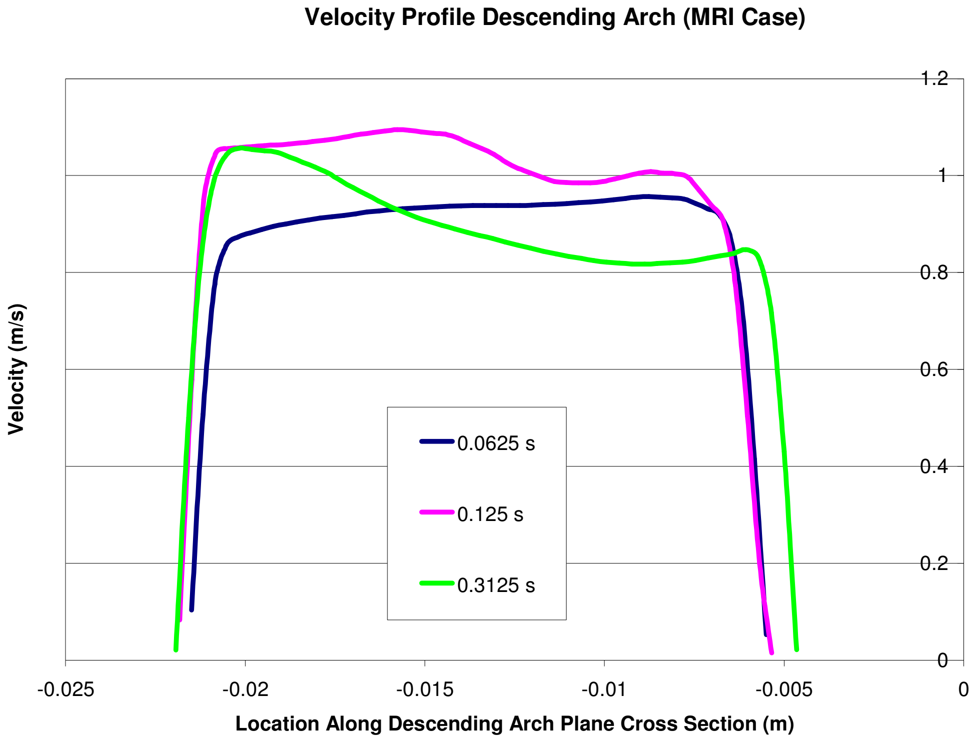
Velocity Profile Descending Arch (MRI Case)
Velocity (m/s)
1.2
1
0.8
0.6
0.4
0.2
0
-0.025
-0.02
-0.015
-0.01
-0.005
0
Location Along Descending Arch Plane Cross Section (m)
0.0625 s
0.125 s
0.3125 s

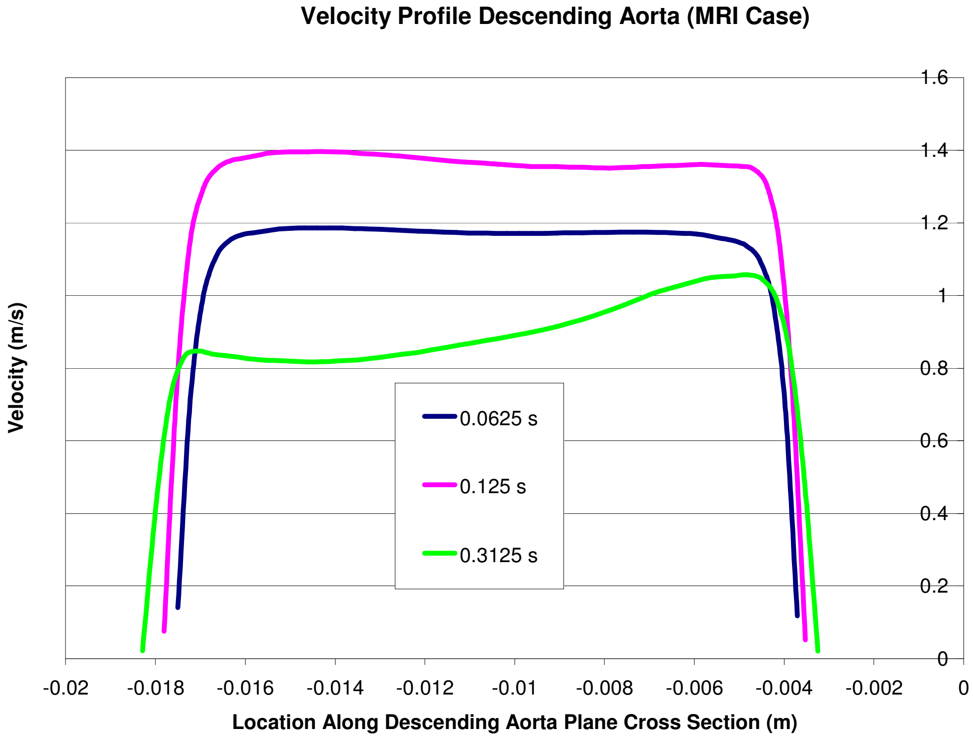
Velocity Profile Descending Aorta (MRI Case)
Velocity (m/s)
1.6
1.4
1.2
1
0.8
0.6
0.4
0.2
0
-0.02
-0.018
-0.016
-0.014
-0.012
-0.01
-0.008
-0.006
-0.004
-0.002
0
Location Along Descending Aorta Plane Cross Section (m)
0.0625 s
0.125 s
0.3125 s

12 Appendix E - Quasi Steady Flow, Rigid Wall Results

Streamlines - Quasi Steady Flow, Rigid Wall Case

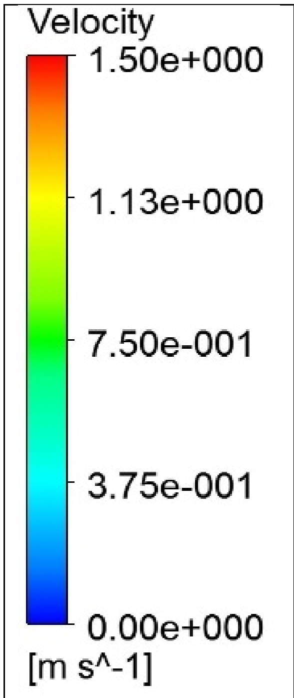

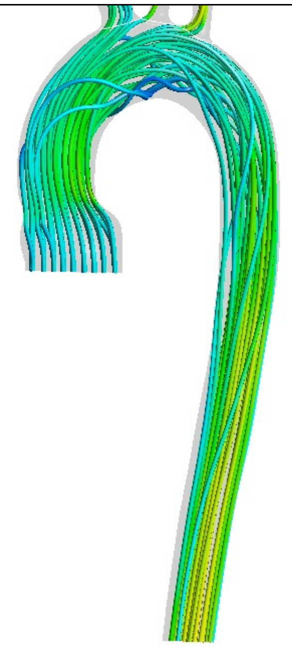

0.0625 seconds

0.3125 seconds

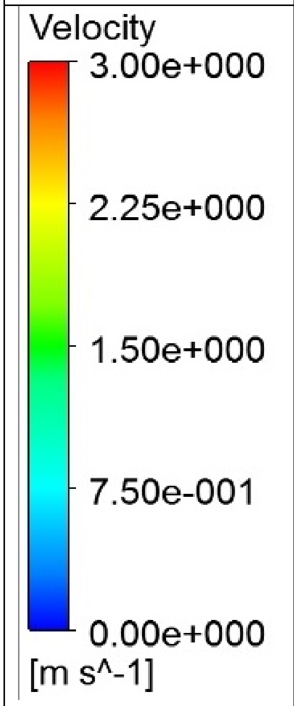

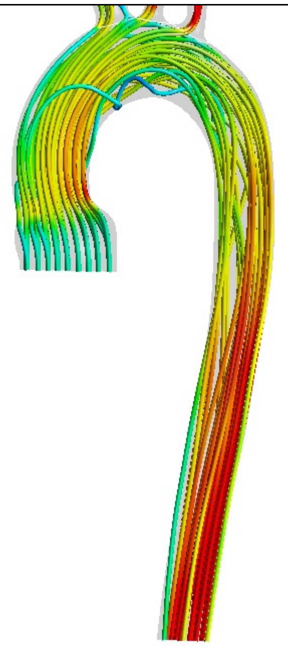

0.125 seconds

Velocity Transverse - Quasi Steady Flow, Rigid Wall

AAo

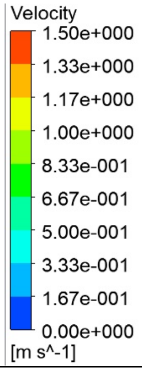

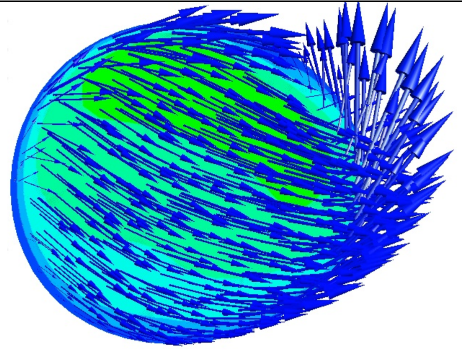
0.0625 seconds

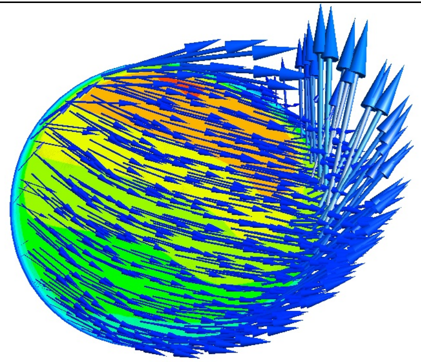
0.125 seconds

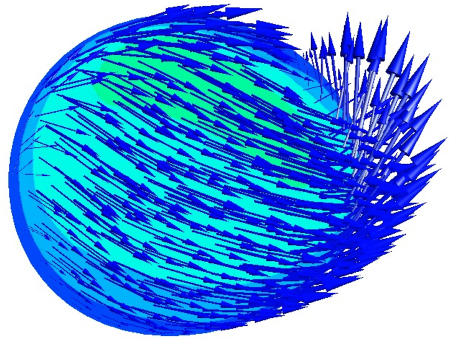
0.3125 seconds

DArch

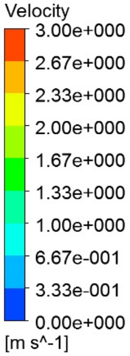

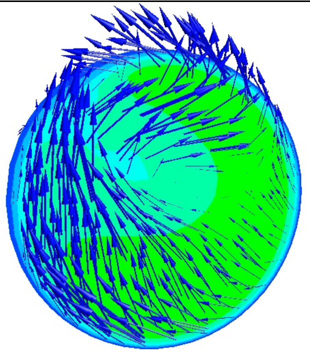
0.0625 seconds

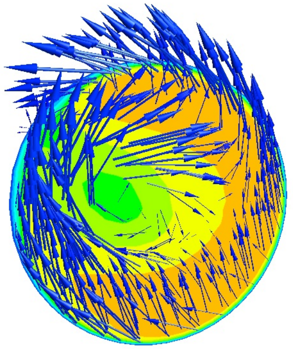
0.125 seconds

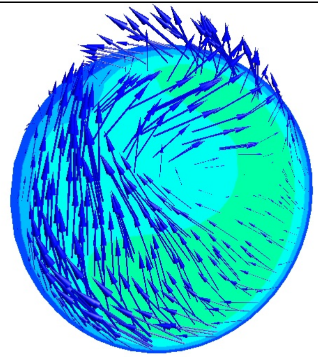
0.3125 seconds

DAo

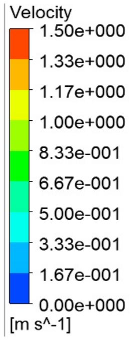

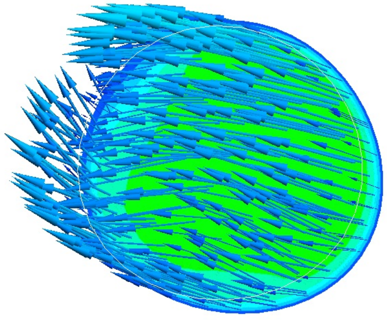
0.0625 seconds

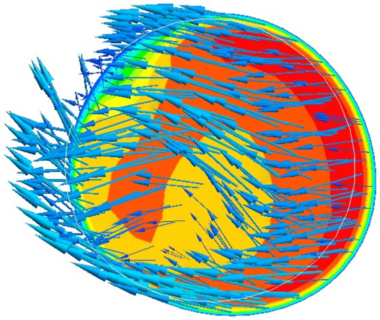
0.125 seconds

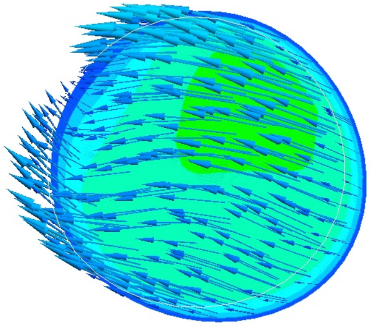
0.3125 seconds

WSS - Quasi Steady Flow, Rigid Wall Case

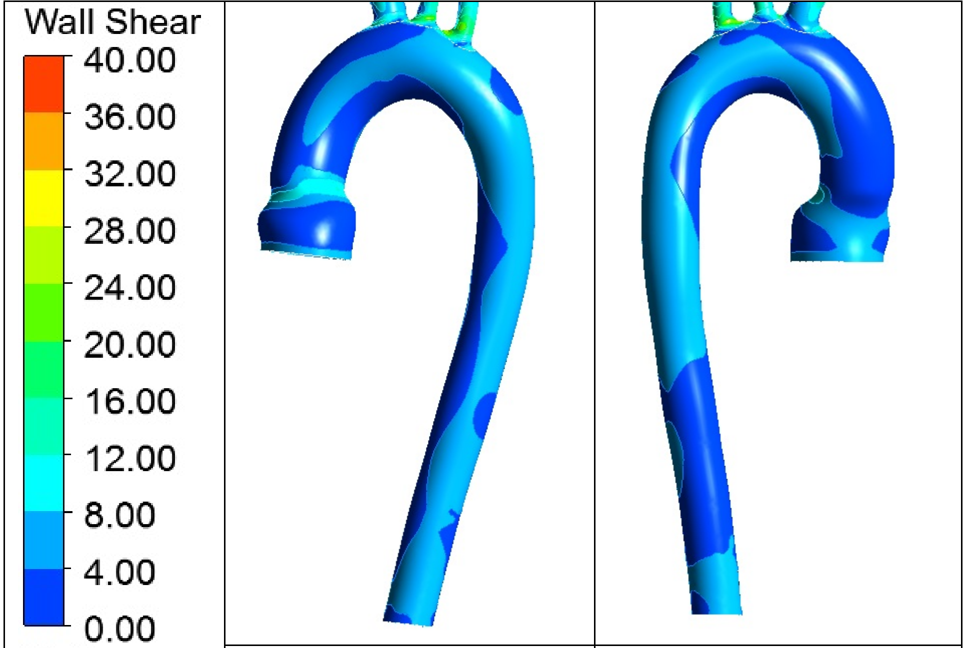

0.0625 seconds

0.0625 seconds

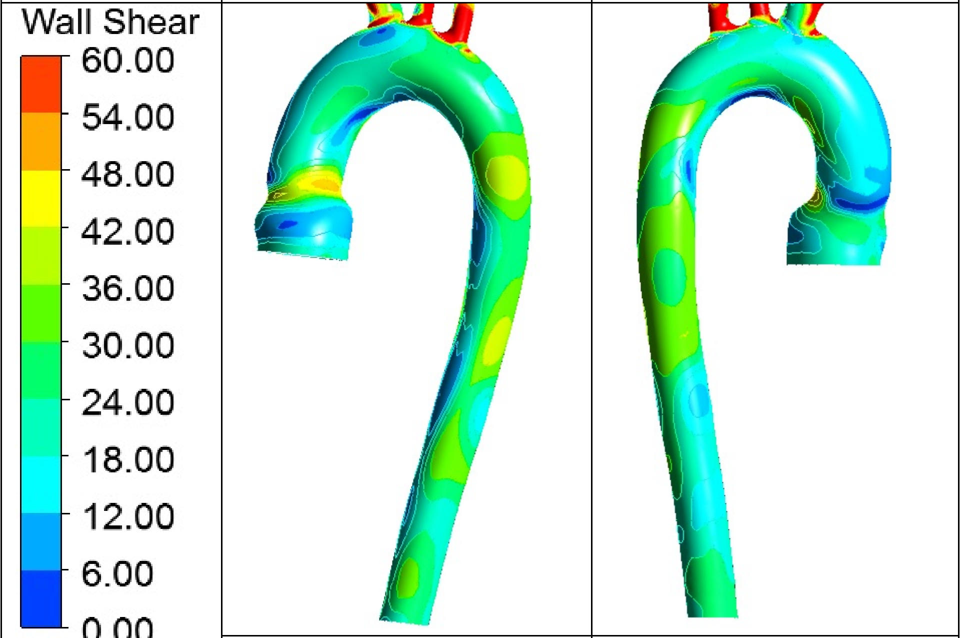

0.125 seconds

0.125 seconds

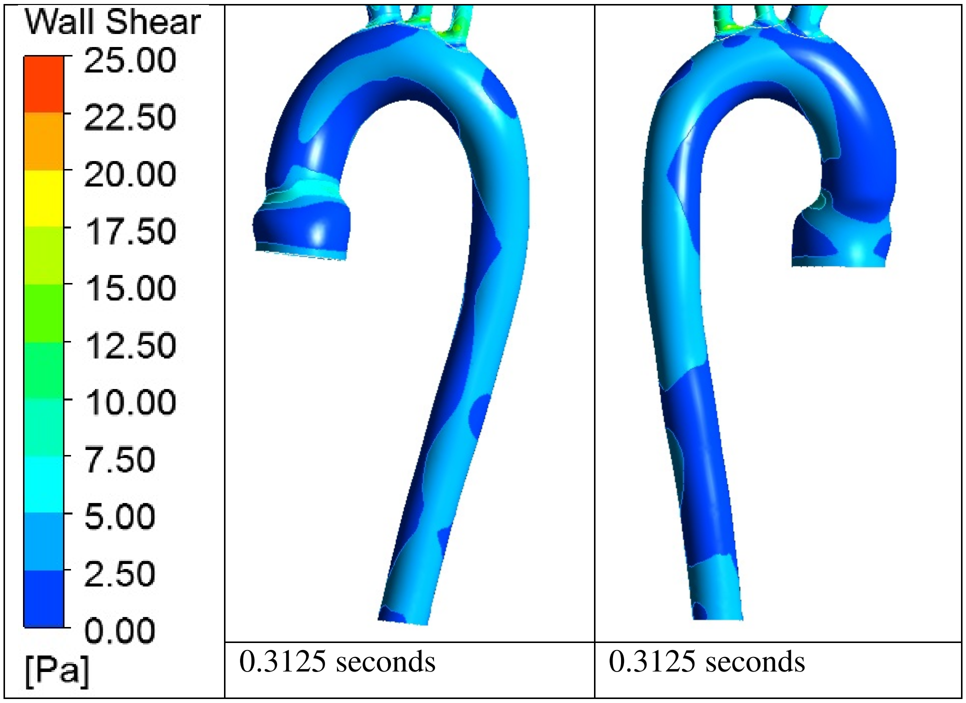

0.3125 seconds

0.3125 seconds

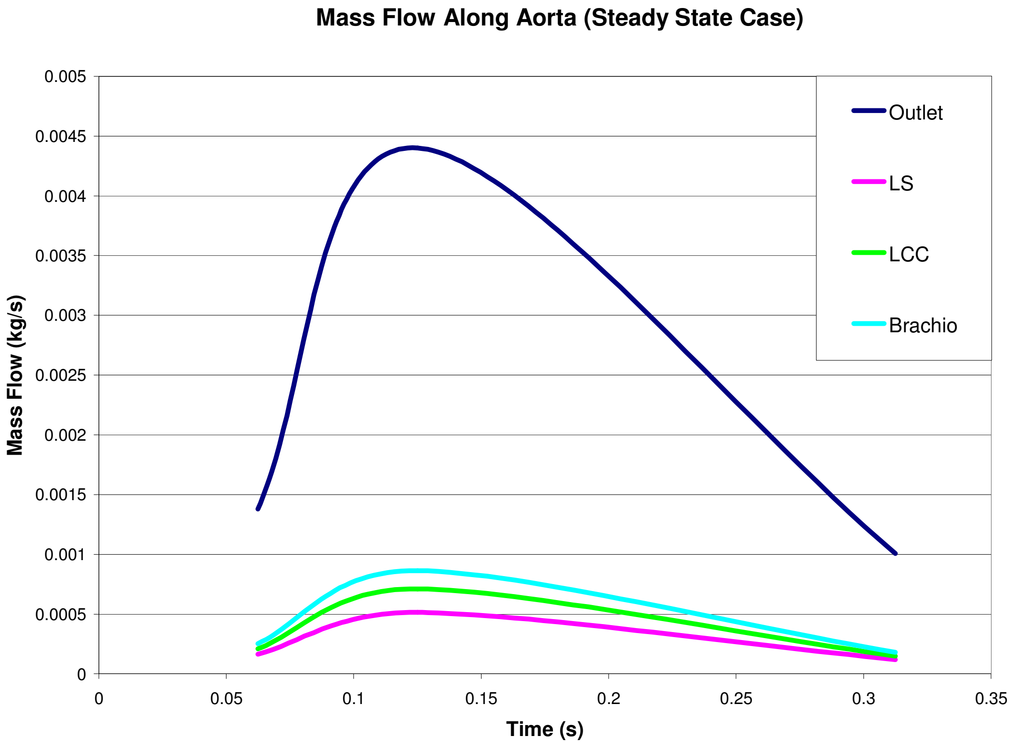
Mass Flow Along Aorta (Steady State Case)
Mass Flow (kg/s)
0.005
0.0045
0.004
0.0035
0.003
0.0025
0.002
0.0015
0.001
0.0005
0
0
0.05
0.1
0.15
0.2
0.25
0.3
0.35
Time (s)
Outlet
LS
LCC
Brachio

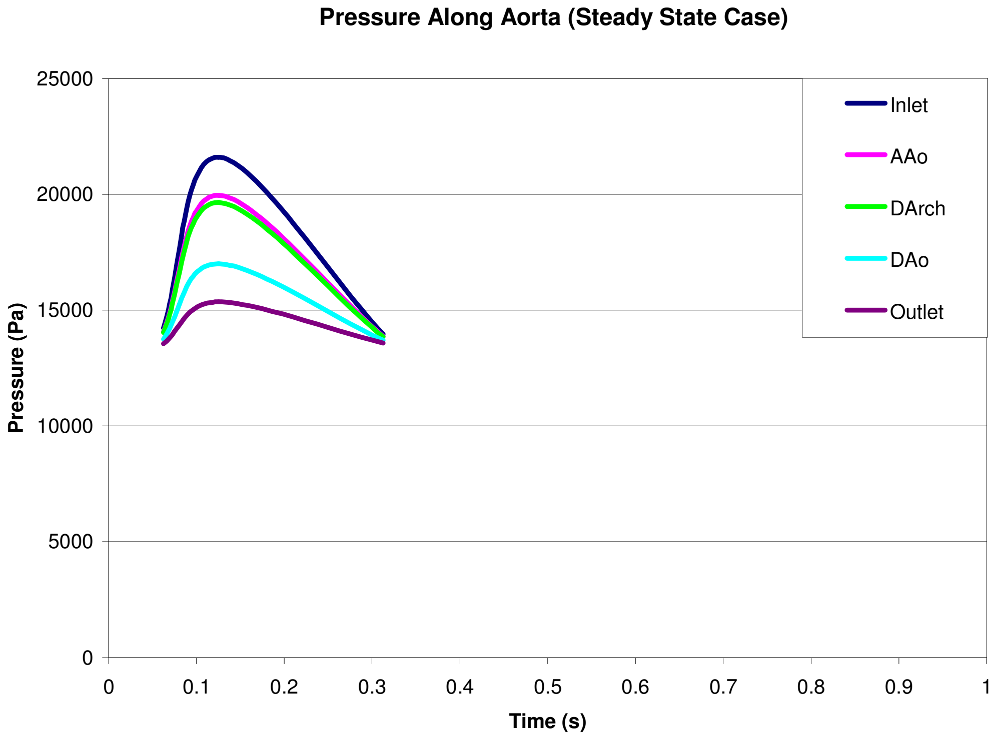
Pressure Along Aorta (Steady State Case)
Pressure (Pa)
25000
20000
15000
10000
5000
0
0
0.1
0.2
0.3
0.4
0.5
0.6
0.7
0.8
0.9
1
Time (s)
Inlet
AAo
DArch
DAo
Outlet

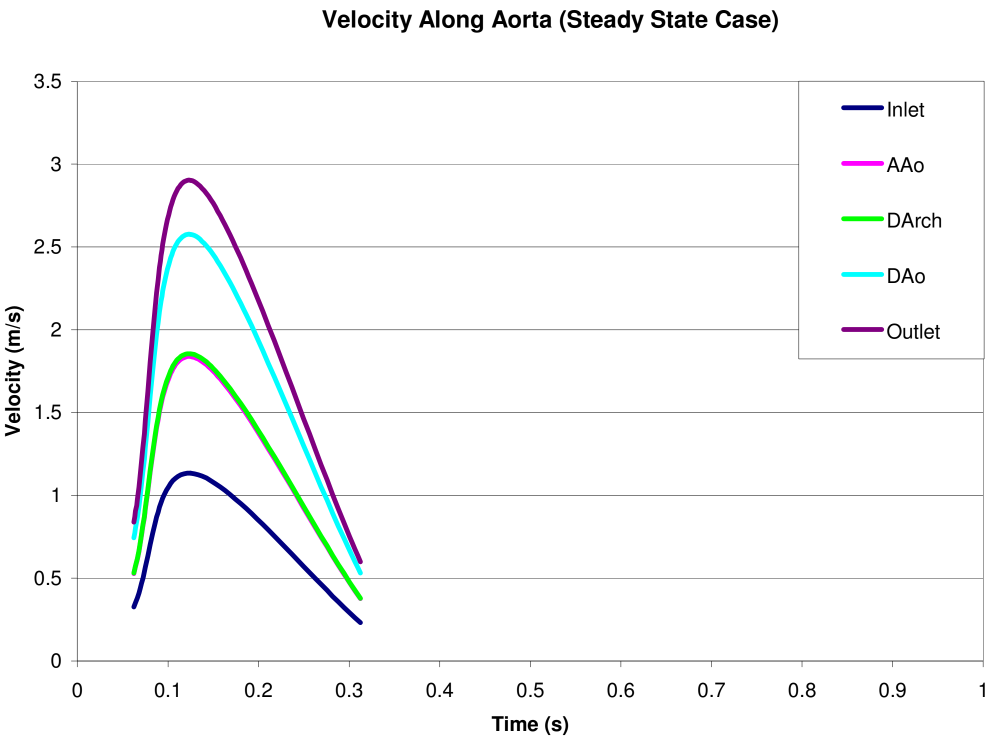
Velocity Along Aorta (Steady State Case)
Velocity (m/s)
3.5
3
2.5
2
1.5
1
0.5
0
0
0.1
0.2
0.3
0.4
0.5
0.6
0.7
0.8
0.9
1
Time (s)
Inlet
AAo
DArch
DAo
Outlet

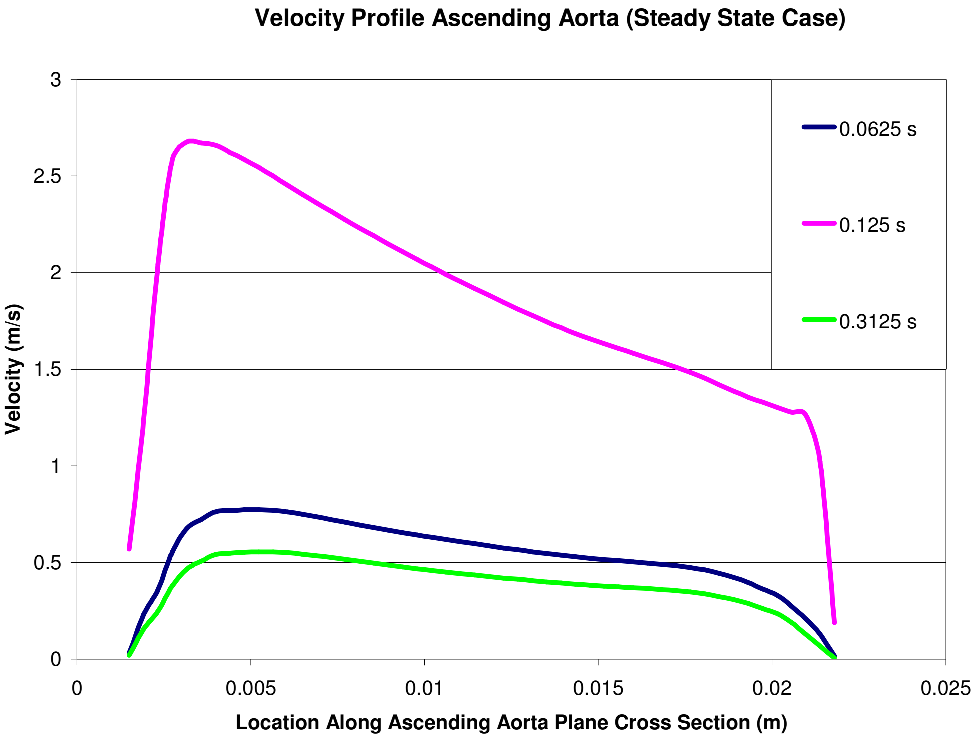
Velocity Profile Ascending Aorta (Steady State Case)
Velocity (m/s)
3
2.5
2
1.5
1
0.5
0
0
0.005
0.01
0.015
0.02
0.025
Location Along Ascending Aorta Plane Cross Section (m)
0.0625 s
0.125 s
0.3125 s


Velocity Profile Descending Arch (Steady State Case)
Velocity (m/s)
Location Along Descending Arch Plane Cross Section (m)
0.0625 s
0.125 s
0.3125 s
3
2.5
2
1.5
1
0.5
0
-0.025
-0.02
-0.015
-0.01
-0.005
0

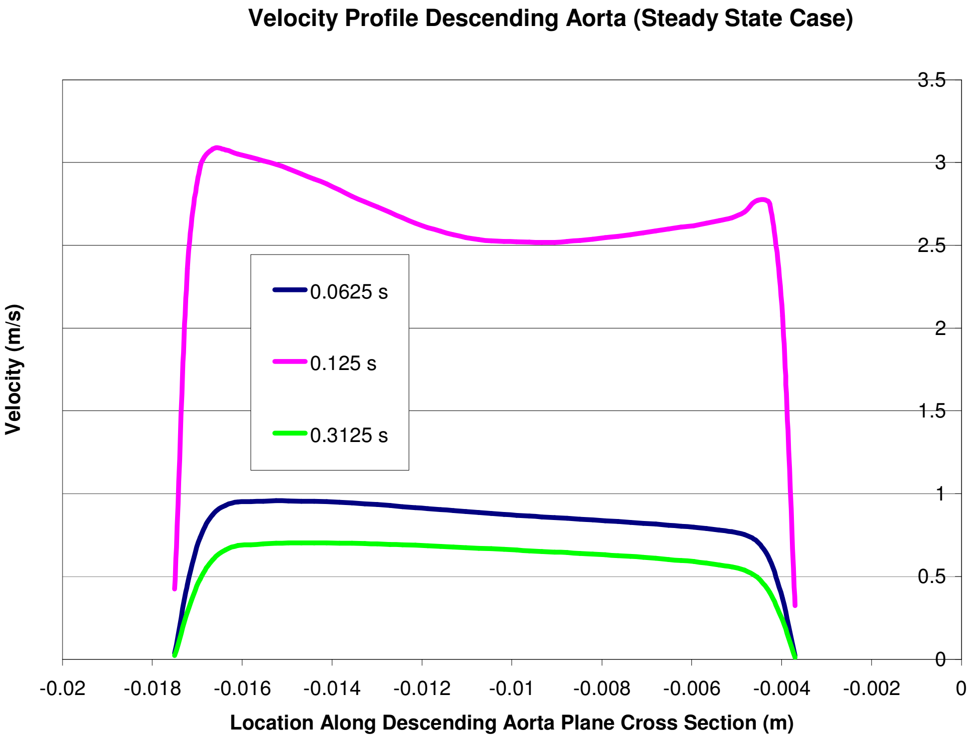
Velocity Profile Descending Aorta (Steady State Case)
Velocity (m/s)
Location Along Descending Aorta Plane Cross Section (m)
0.0625 s
0.125 s
0.3125 s
3.5
3
2.5
2
1.5
1
0.5
0
-0.02
-0.018
-0.016
-0.014
-0.012
-0.01
-0.008
-0.006
-0.004
-0.002
0

13 Appendix F - Rigid Wall Transient Comparison Results

Streamlines - Rigid Wall Transient Comparison

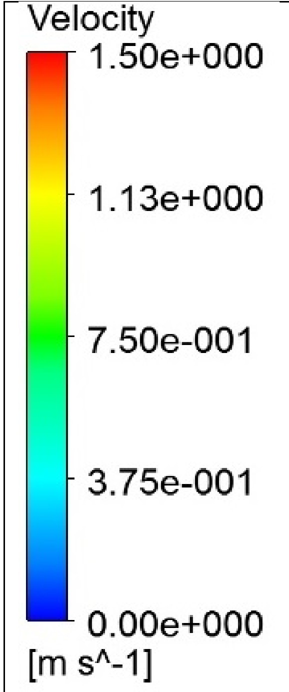

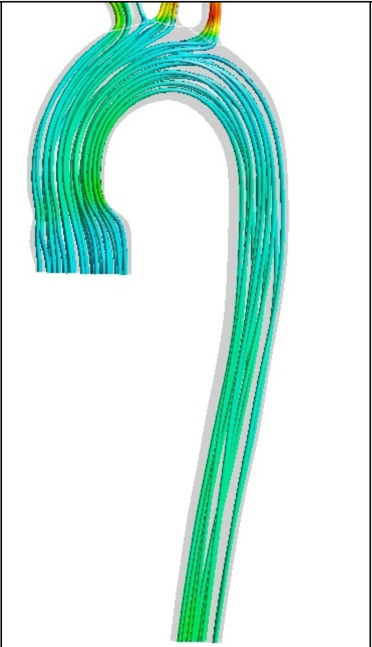

0.0625 seconds

0.3125 seconds

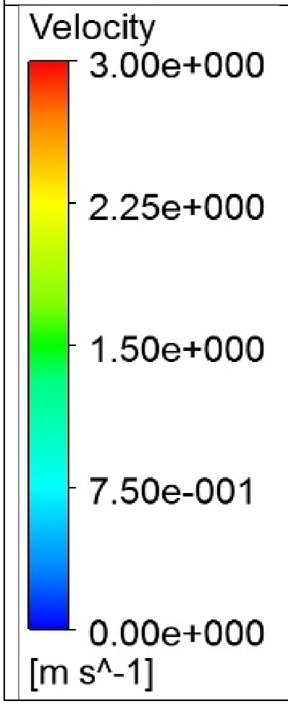

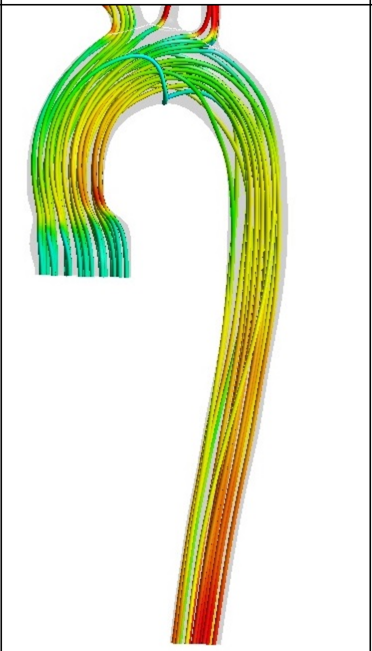

0.125 seconds

Velocity Transverse - Rigid Wall Transient Comparison

AAo 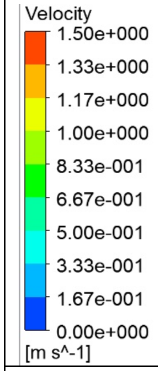	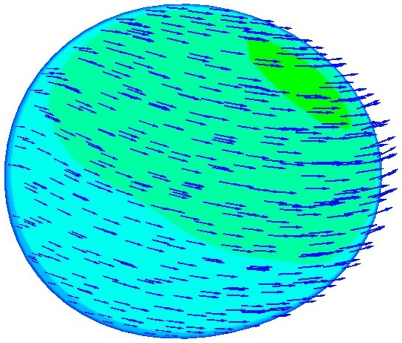	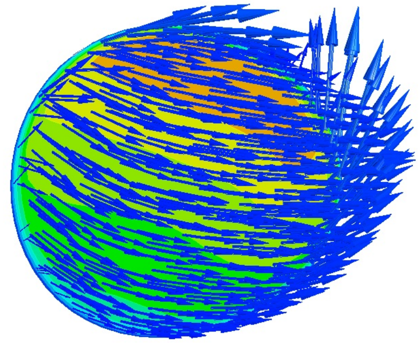	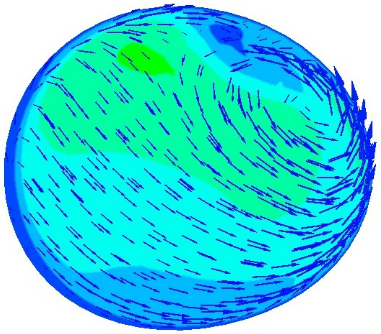
	0.0625 seconds	0.125 seconds	0.3125 seconds
DArch 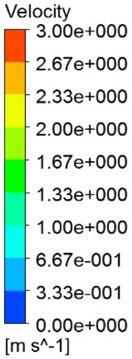	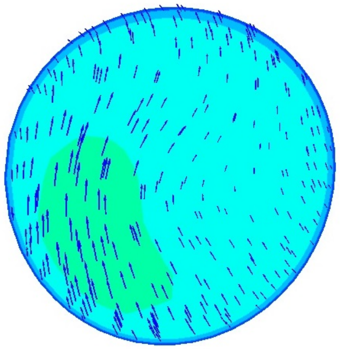	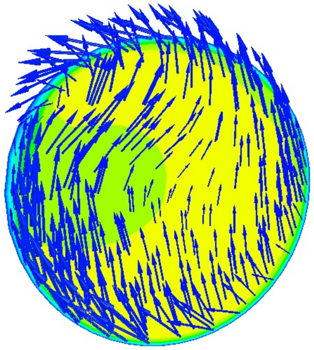	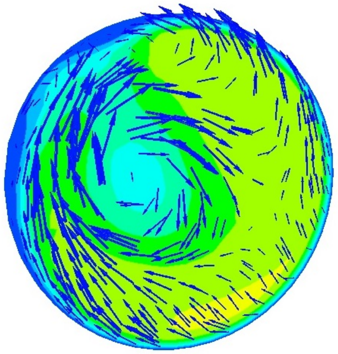
	0.0625 seconds	0.125 seconds	0.3125 seconds
DAo 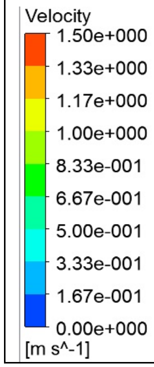	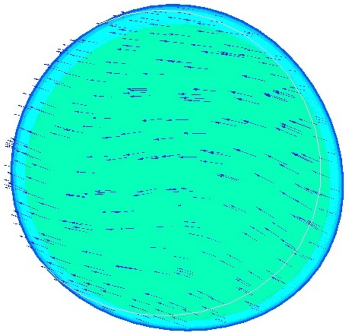	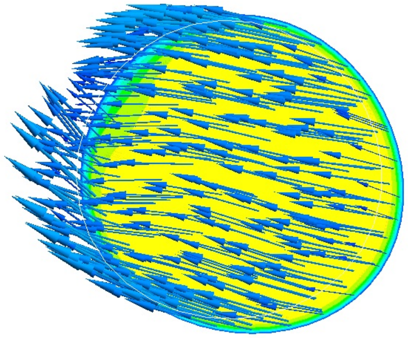	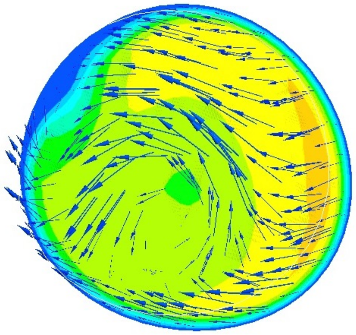
	0.0625 seconds	0.125 seconds	0.3125 seconds

WSS - Rigid Wall Transient Comparison

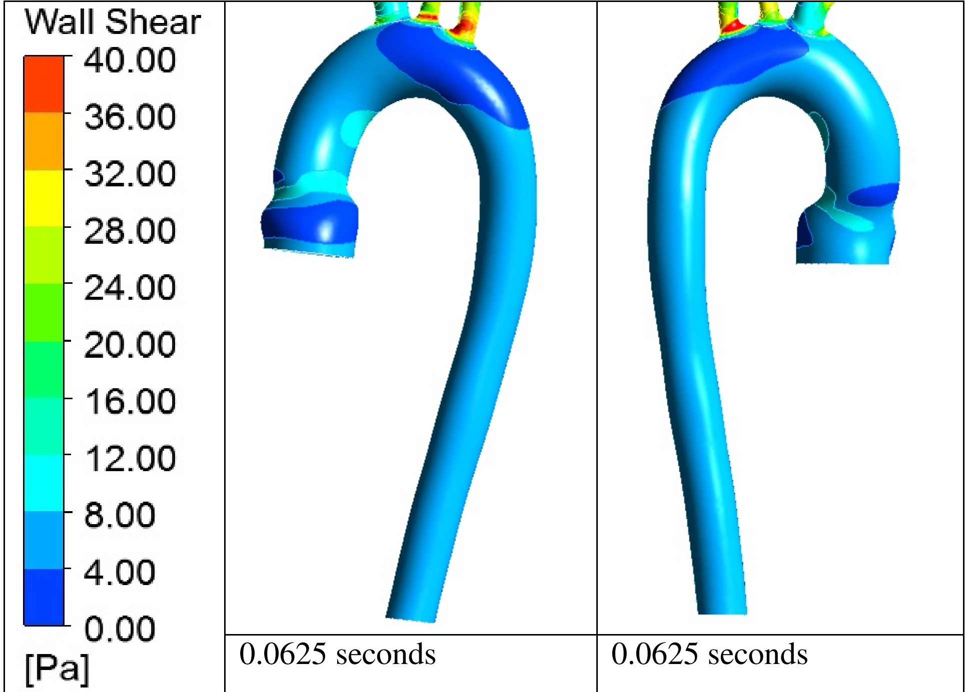

0.0625 seconds

0.0625 seconds

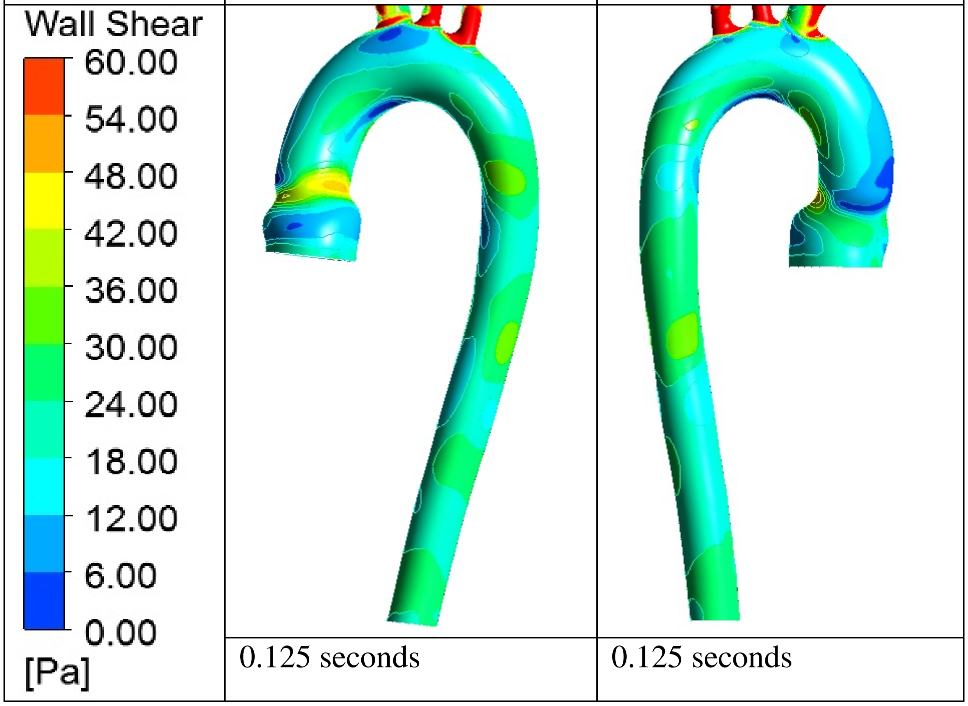

0.125 seconds

0.125 seconds

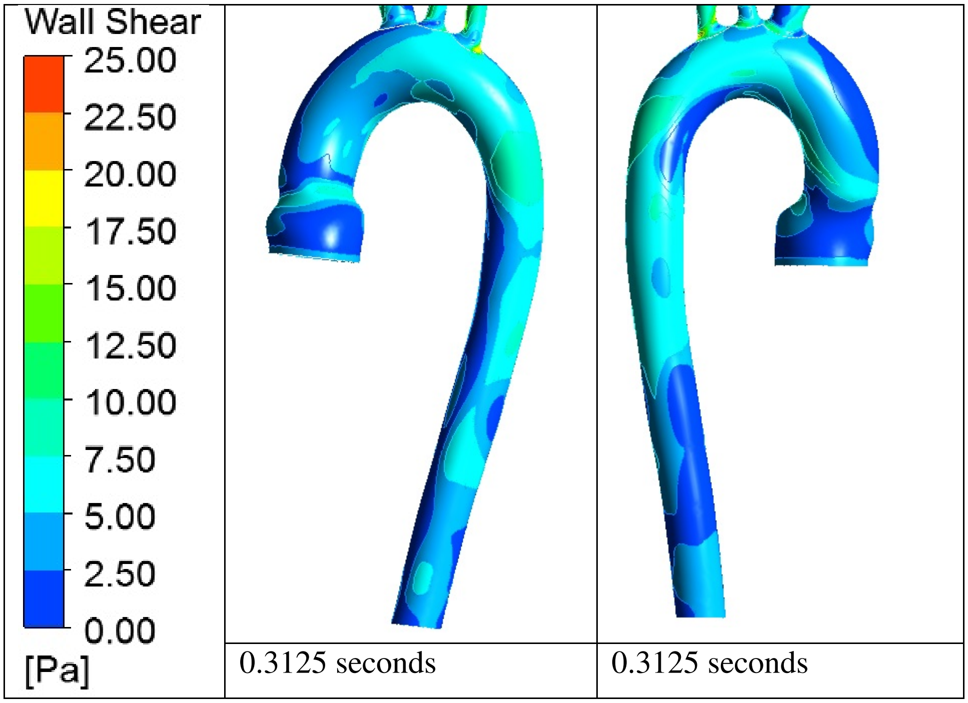

0.3125 seconds

0.3125 seconds

14 Appendix G - Quasi Steady Flow Deformed Geometry Results

Streamlines - Quasi Steady Flow Deformed Geometry Case

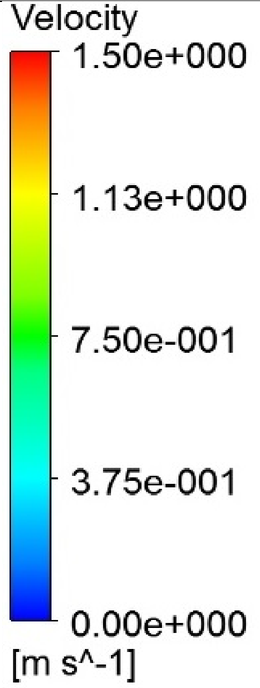	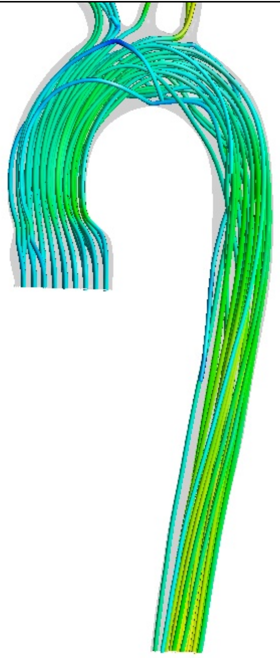	
	0.0625 seconds	0.3125 seconds
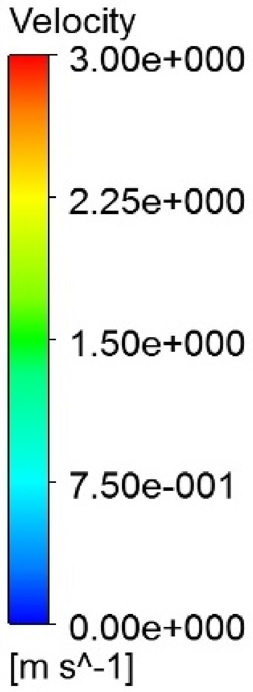	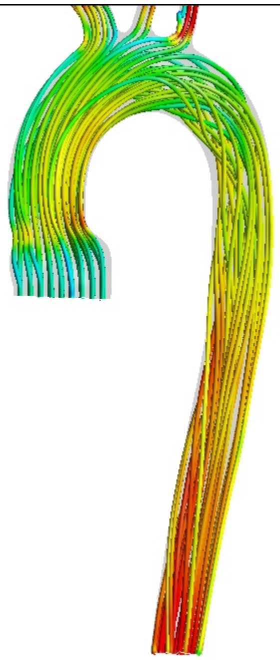	
	0.125 seconds	

Velocity Transverse - Quasi Steady Flow Deformed Geometry Case

AAo Velocity 1.50e+000 1.33e+000 1.17e+000 1.00e+000 8.33e-001 6.67e-001 5.00e-001 3.33e-001 1.67e-001 0.00e+000 [m s^-1]	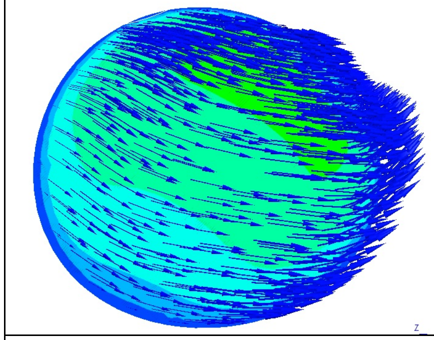	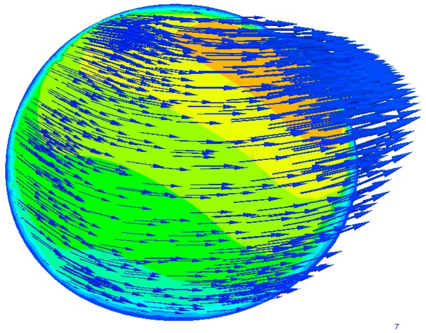	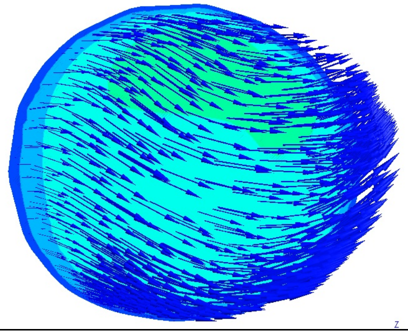
	0.0625 seconds	0.125 seconds	0.3125 seconds
DArch Velocity 3.00e+000 2.67e+000 2.33e+000 2.00e+000 1.67e+000 1.33e+000 1.00e+000 6.67e-001 3.33e-001 0.00e+000 [m s^-1]	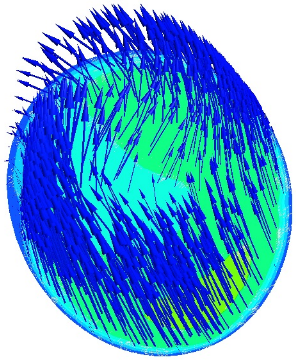	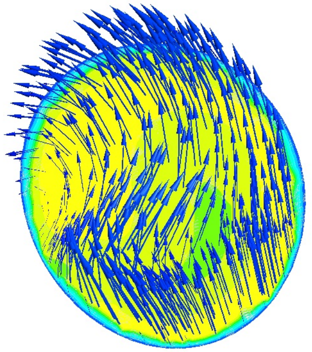	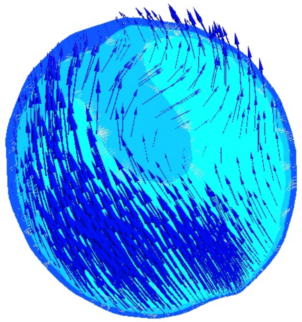
	0.0625 seconds	0.125 seconds	0.3125 seconds
DAo Velocity 1.50e+000 1.33e+000 1.17e+000 1.00e+000 8.33e-001 6.67e-001 5.00e-001 3.33e-001 1.67e-001 0.00e+000 [m s^-1]	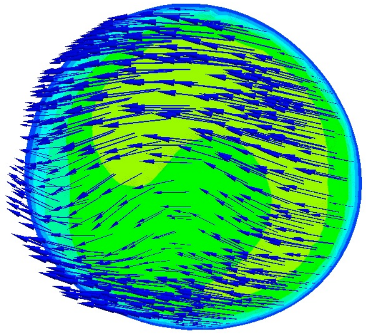	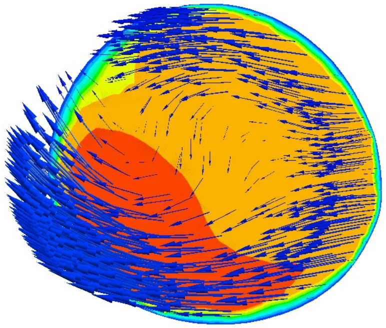	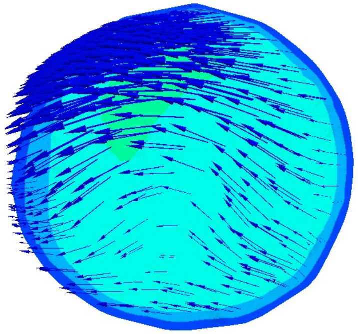
	0.0625 seconds	0.125 seconds	0.3125 seconds

WSS - Quasi Steady Flow Deformed Geometry Case

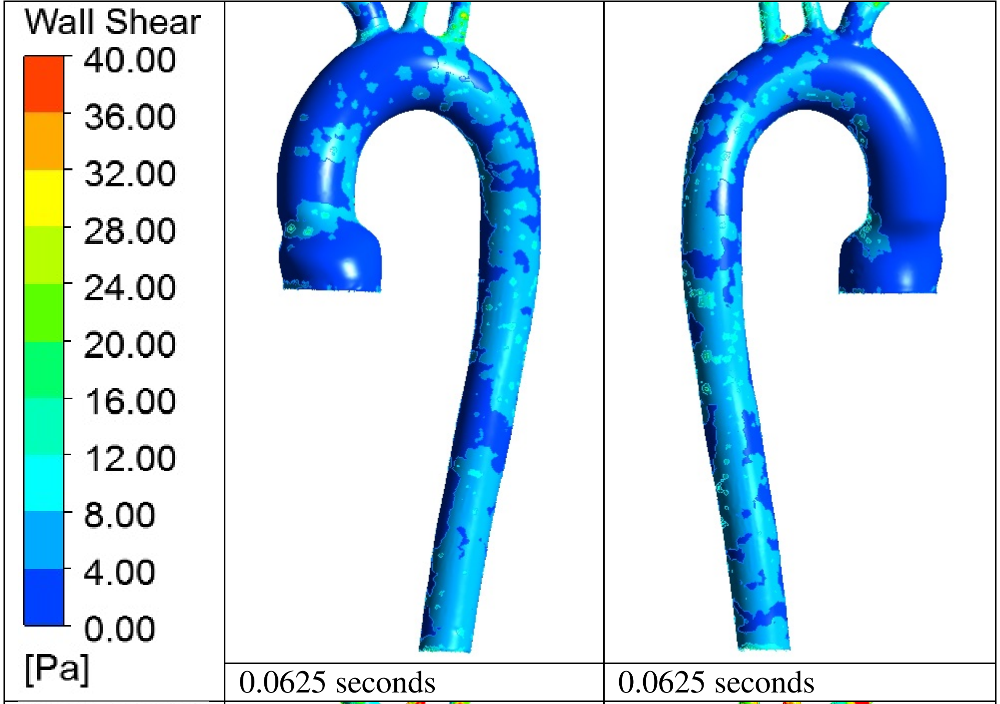

0.0625 seconds 0.0625 seconds

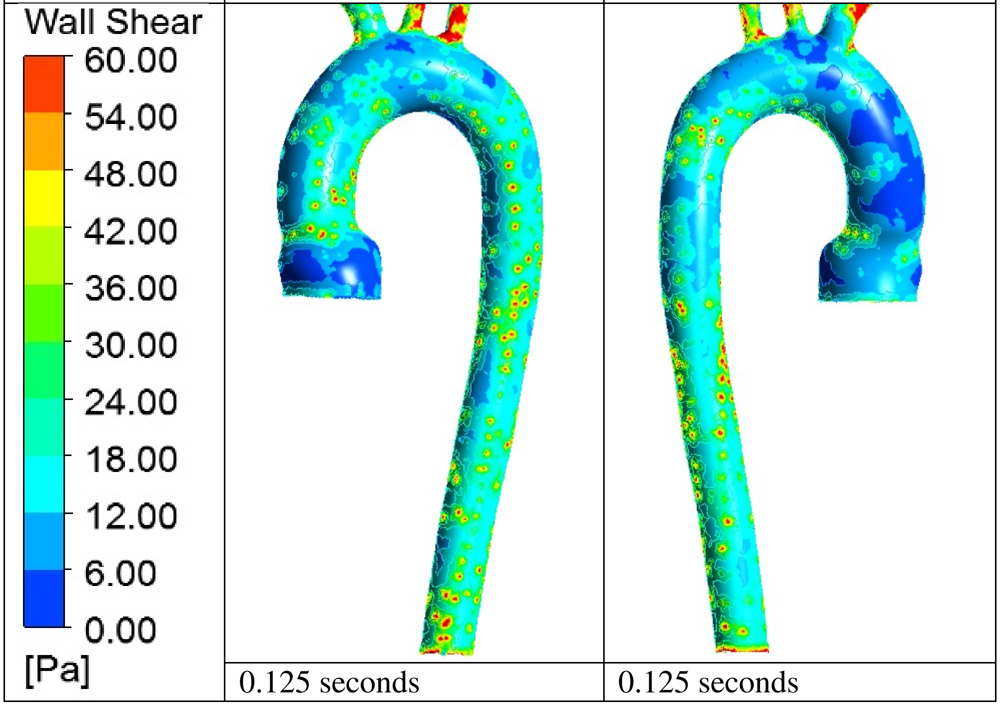

0.125 seconds 0.125 seconds

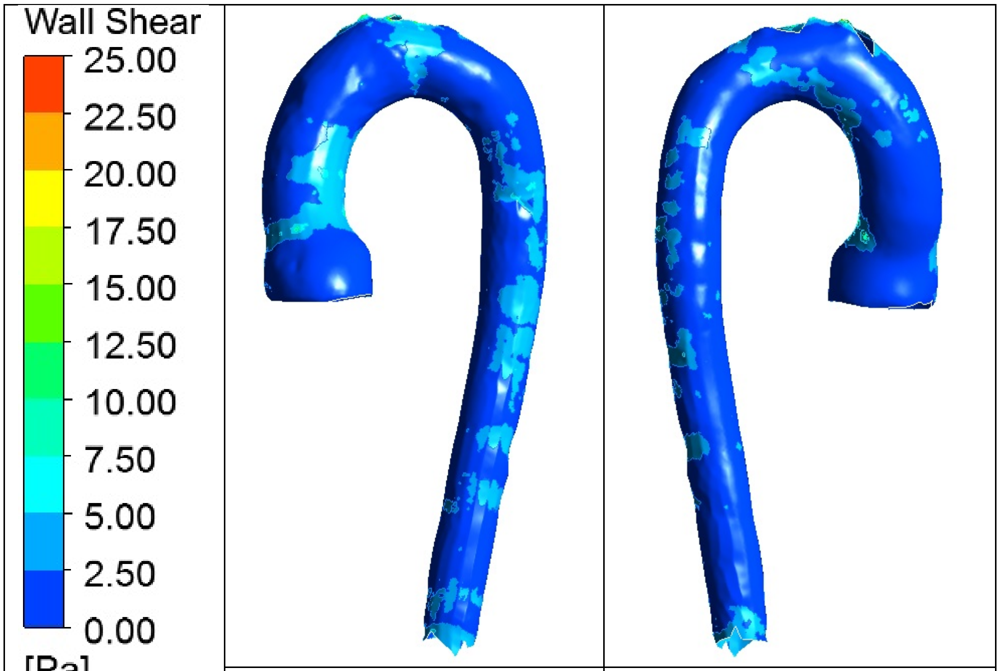

0.3125 seconds

0.3125 seconds

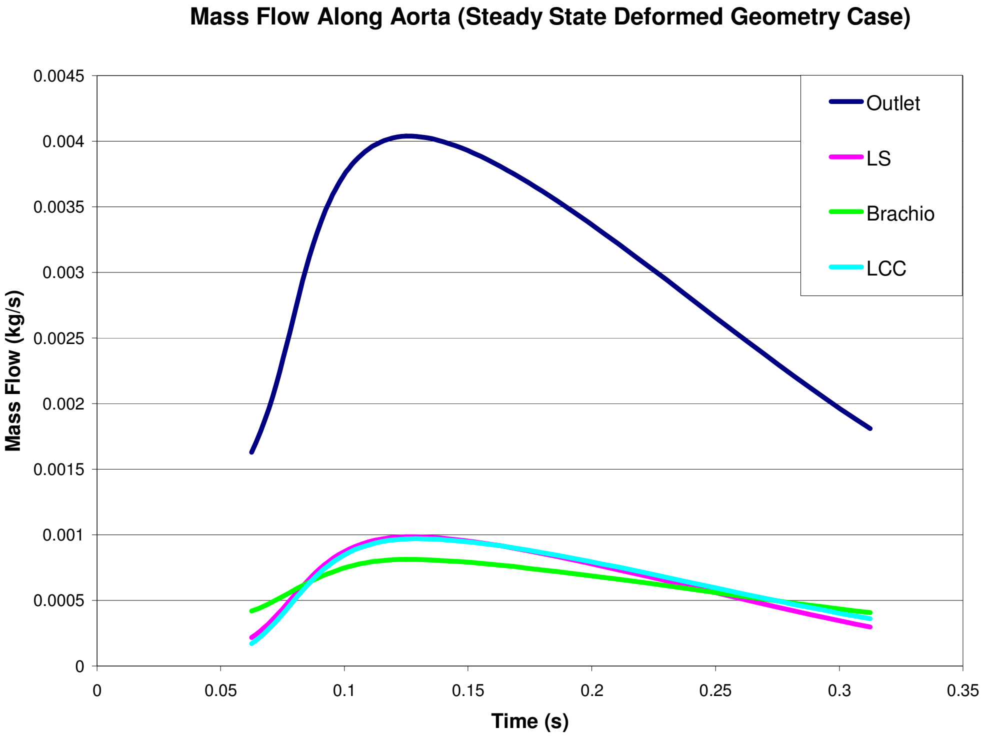
Mass Flow Along Aorta (Steady State Deformed Geometry Case)
Mass Flow (kg/s)
0.0045
0.004
0.0035
0.003
0.0025
0.002
0.0015
0.001
0.0005
0
0
0.05
0.1
0.15
0.2
0.25
0.3
0.35
Time (s)
Outlet
LS
Brachio
LCC

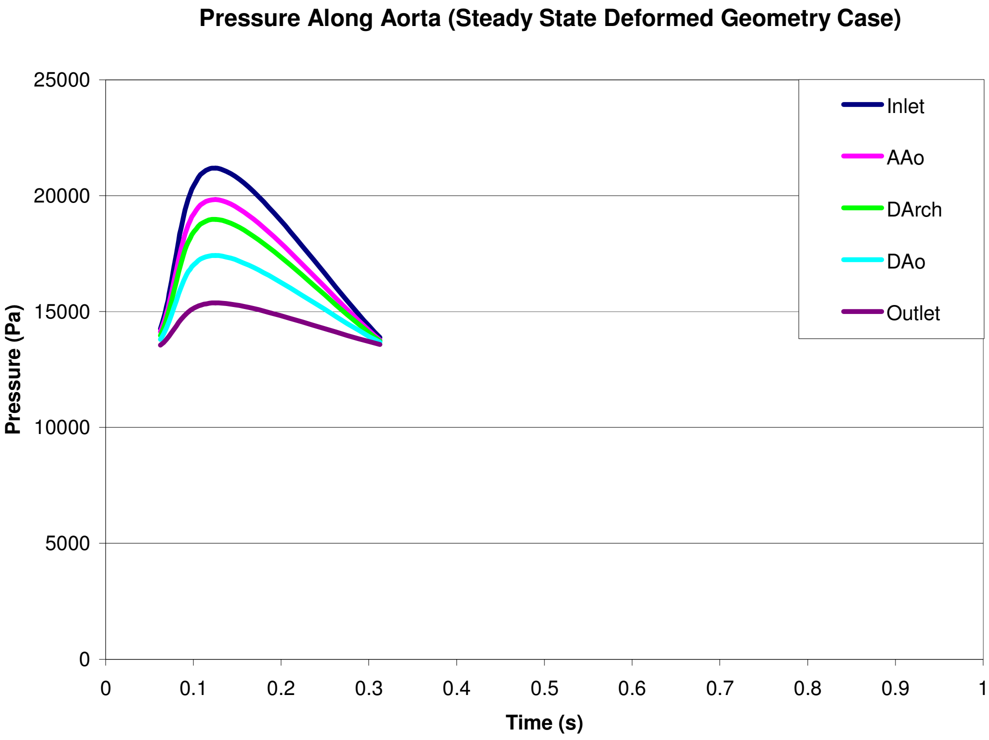
Pressure Along Aorta (Steady State Deformed Geometry Case)
Pressure (Pa)
25000
20000
15000
10000
5000
0
0
0.1
0.2
0.3
0.4
0.5
0.6
0.7
0.8
0.9
1
Time (s)
Inlet
AAo
DArch
DAo
Outlet

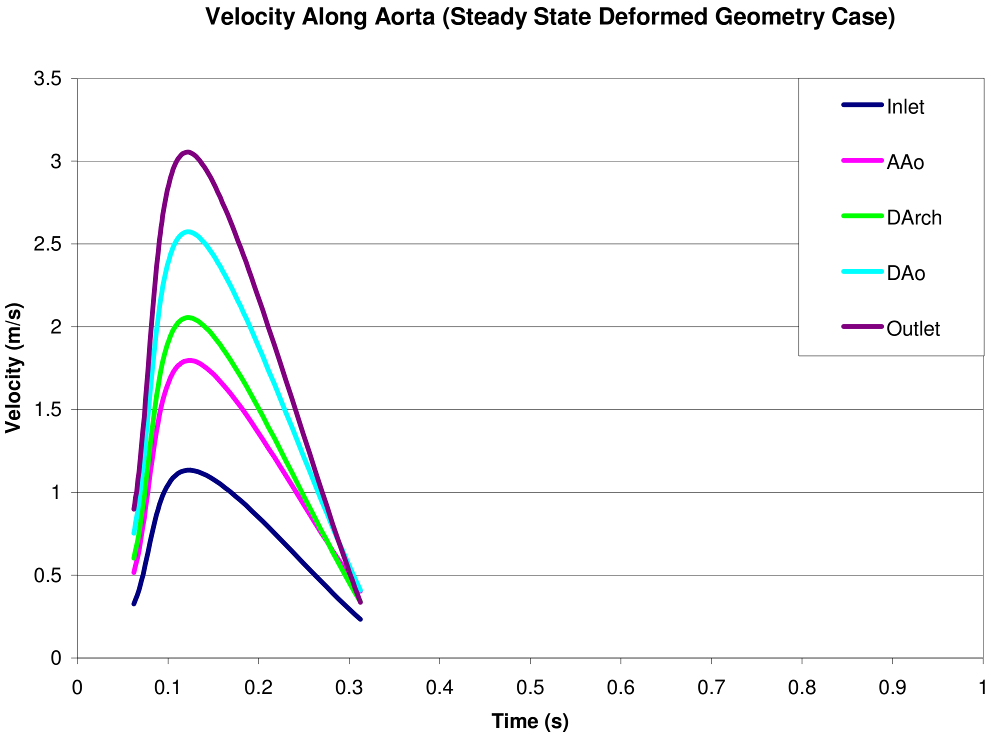
Velocity Along Aorta (Steady State Deformed Geometry Case)
Velocity (m/s)
Time (s)
0
0.5
1
1.5
2
2.5
3
3.5
0
0.1
0.2
0.3
0.4
0.5
0.6
0.7
0.8
0.9
1
Inlet
AAo
DArch
DAo
Outlet

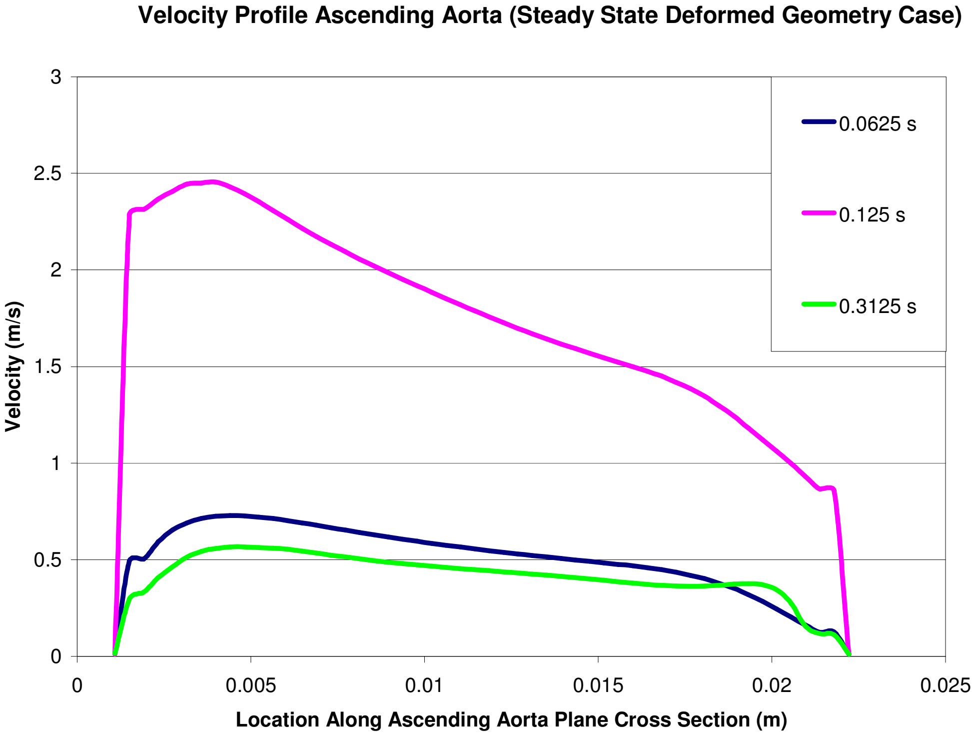
Velocity Profile Ascending Aorta (Steady State Deformed Geometry Case)
Velocity (m/s)
Location Along Ascending Aorta Plane Cross Section (m)
0
0.5
1
1.5
2
2.5
3
0
0.005
0.01
0.015
0.02
0.025
0.0625 s
0.125 s
0.3125 s

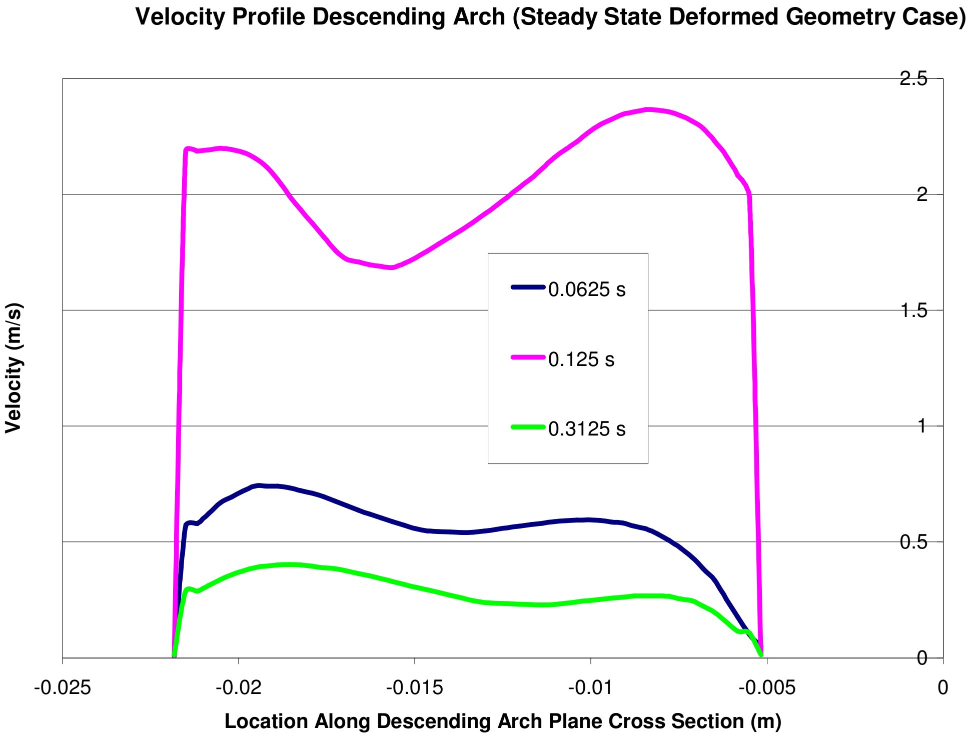
Velocity Profile Descending Arch (Steady State Deformed Geometry Case)
Velocity (m/s)
Location Along Descending Arch Plane Cross Section (m)
0.0625 s
0.125 s
0.3125 s
2.5
2
1.5
1
0.5
0
-0.025
-0.02
-0.015
-0.01
-0.005
0

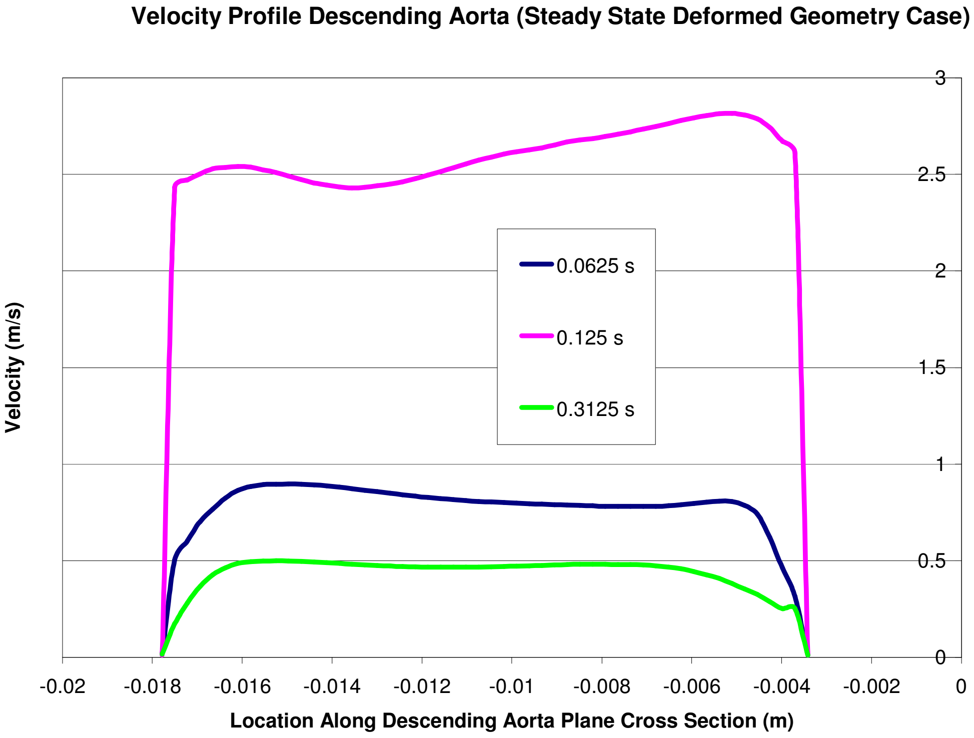
Velocity Profile Descending Aorta (Steady State Deformed Geometry Case)
Velocity (m/s)
Location Along Descending Aorta Plane Cross Section (m)
0.0625 s
0.125 s
0.3125 s
3
2.5
2
1.5
1
0.5
0
-0.02
-0.018
-0.016
-0.014
-0.012
-0.01
-0.008
-0.006
-0.004
-0.002
0